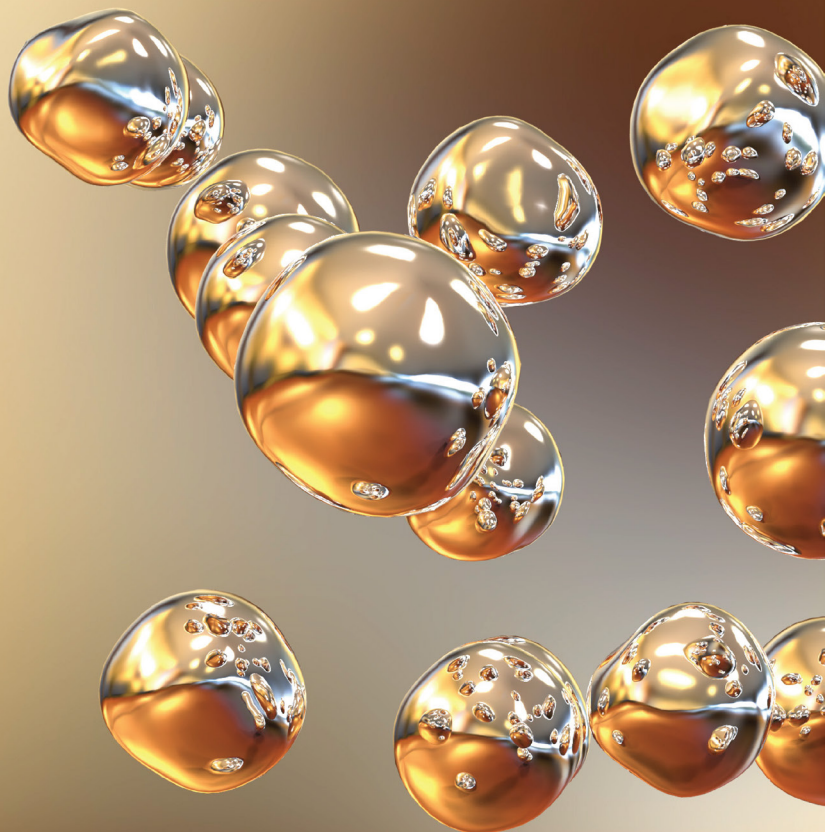


THE GREAT WORLD OF NANOTECHNOLOGY



Marcos Augusto de Lima Nobre
(Organizador)

VOL II

 EDITORA
ARTEMIS
2021

THE GREAT WORLD OF NANOTECHNOLOGY

Marcos Augusto de Lima Nobre
(Organizador)

VOL II

 EDITORA
ARTEMIS
2021



O conteúdo deste livro está licenciado sob uma Licença de Atribuição Creative Commons Atribuição- Não-Comercial NãoDerivativos 4.0 Internacional (CC BY-NC-ND 4.0). Direitos para esta edição cedidos à Editora Artemis pelos autores. Permitido o download da obra e o compartilhamento, desde que sejam atribuídos créditos aos autores, e sem a possibilidade de alterá-la de nenhuma forma ou utilizá-la para fins comercial. A responsabilidade pelo conteúdo dos artigos e seus dados, em sua forma, correção e confiabilidade é exclusiva dos autores. A Editora Artemis, em seu compromisso de manter e aperfeiçoar a qualidade e confiabilidade dos trabalhos que publica, conduz a avaliação cega pelos pares de todos manuscritos publicados, com base em critérios de neutralidade e imparcialidade acadêmica.

Editora Chefe	Prof. ^a Dr. ^a Antonella Carvalho de Oliveira
Editora Executiva	M. ^a Viviane Carvalho Mocellin
Direção de Arte	M. ^a Bruna Bejarano
Diagramação	Elisangela Abreu
Organizadoras	Prof. Dr. Marcos Augusto de Lima Nobre
Imagem da Capa	Kateryna Kon
Bibliotecário	Maurício Amormino Júnior – CRB6/2422

Conselho Editorial

Prof.^a Dr.^a Ada Esther Portero Ricol, *Universidad Tecnológica de La Habana “José Antonio Echeverría”, Cuba*
Prof. Dr. Adalberto de Paula Paranhos, *Universidade Federal de Uberlândia*
Prof.^a Dr.^a Amanda Ramalho de Freitas Brito, *Universidade Federal da Paraíba*
Prof.^a Dr.^a Ana Clara Monteverde, *Universidad de Buenos Aires, Argentina*
Prof. Dr. Ángel Mujica Sánchez, *Universidad Nacional del Altiplano, Peru*
Prof.^a Dr.^a Angela Ester Mallmann Centenaro, *Universidade do Estado de Mato Grosso*
Prof.^a Dr.^a Begoña Blandón González, *Universidad de Sevilla, Espanha*
Prof.^a Dr.^a Carmen Pimentel, *Universidade Federal Rural do Rio de Janeiro*
Prof.^a Dr.^a Catarina Castro, *Universidade Nova de Lisboa, Portugal*
Prof.^a Dr.^a Cláudia Neves, *Universidade Aberta de Portugal*
Prof. Dr. Cleberton Correia Santos, *Universidade Federal da Grande Dourados*
Prof.^a Dr.^a Deuzimar Costa Serra, *Universidade Estadual do Maranhão*
Prof.^a Dr.^a Eduarda Maria Rocha Teles de Castro Coelho, *Universidade de Trás-os-Montes e Alto Douro, Portugal*
Prof. Dr. Eduardo Eugênio Spers, *Universidade de São Paulo*
Prof. Dr. Eloi Martins Senhoras, *Universidade Federal de Roraima*
Prof.^a Dr.^a Elvira Laura Hernández Carballedo, *Universidad Autónoma del Estado de Hidalgo, México*
Prof.^a Dr.^a Emilas Darlene Carmen Lebus, *Universidad Nacional del Nordeste/ Universidad Tecnológica Nacional, Argentina*
Prof.^a Dr.^a Erla Mariela Morales Morgado, *Universidad de Salamanca, Espanha*
Prof. Dr. Ernesto Cristina, *Universidad de la República, Uruguay*
Prof. Dr. Ernesto Ramírez-Briones, *Universidad de Guadalajara, México*
Prof. Dr. Gabriel Díaz Cobos, *Universitat de Barcelona, Espanha*
Prof. Dr. Geoffroy Roger Pointer Malpass, *Universidade Federal do Triângulo Mineiro*
Prof.^a Dr.^a Gladys Esther Leoz, *Universidad Nacional de San Luis, Argentina*
Prof.^a Dr.^a Glória Beatriz Álvarez, *Universidad de Buenos Aires, Argentina*
Prof. Dr. Gonçalo Poeta Fernandes, *Instituto Politécnico da Guarda, Portugal*
Prof. Dr. Gustavo Adolfo Juarez, *Universidad Nacional de Catamarca, Argentina*
Prof.^a Dr.^a Iara Lúcia Tescarollo Dias, *Universidade São Francisco*
Prof.^a Dr.^a Isabel del Rosario Chiyon Carrasco, *Universidad de Piura, Peru*
Prof.^a Dr.^a Isabel Yohena, *Universidad de Buenos Aires, Argentina*
Prof. Dr. Ivan Amaro, *Universidade do Estado do Rio de Janeiro*
Prof. Dr. Iván Ramon Sánchez Soto, *Universidad del Bio-Bío, Chile*



Prof.ª Dr.ª Ivânia Maria Carneiro Vieira, Universidade Federal do Amazonas
 Prof. Me. Javier Antonio Albornoz, *University of Miami and Miami Dade College*, USA
 Prof. Dr. Jesús Montero Martínez, *Universidad de Castilla - La Mancha*, Espanha
 Prof. Dr. Joaquim Júlio Almeida Júnior, UniFIMES - Centro Universitário de Mineiros
 Prof. Dr. Juan Carlos Mosquera Feijoo, *Universidad Politécnica de Madrid*, Espanha
 Prof. Dr. Juan Diego Parra Valencia, *Instituto Tecnológico Metropolitano de Medellín*, Colômbia
 Prof. Dr. Júlio César Ribeiro, Universidade Federal Rural do Rio de Janeiro
 Prof. Dr. Leinig Antonio Perazolli, Universidade Estadual Paulista
 Prof.ª Dr.ª Livia do Carmo, Universidade Federal de Goiás
 Prof.ª Dr.ª Luciane Spanhol Bordignon, Universidade de Passo Fundo
 Prof. Dr. Manuel Ramiro Rodriguez, *Universidad Santiago de Compostela*, Espanha
 Prof. Dr. Marcos Augusto de Lima Nobre, Universidade Estadual Paulista
 Prof. Dr. Marcos Vinicius Meiado, Universidade Federal de Sergipe
 Prof.ª Dr.ª Margarida Márcia Fernandes Lima, Universidade Federal de Ouro Preto
 Prof.ª Dr.ª Maria Aparecida José de Oliveira, Universidade Federal da Bahia
 Prof.ª Dr.ª Maria do Céu Caetano, Universidade Nova de Lisboa, Portugal
 Prof.ª Dr.ª Maria do Socorro Saraiva Pinheiro, Universidade Federal do Maranhão
 Prof.ª Dr.ª Maria Lúcia Pato, Instituto Politécnico de Viseu, Portugal
 Prof.ª Dr.ª Maritza González Moreno, *Universidad Tecnológica de La Habana "José Antonio Echeverría"*, Cuba
 Prof.ª Dr.ª Mauriceia Silva de Paula Vieira, Universidade Federal de Lavras
 Prof.ª Dr.ª Odara Horta Boscolo, Universidade Federal Fluminense
 Prof.ª Dr.ª Patrícia Vasconcelos Almeida, Universidade Federal de Lavras
 Prof.ª Dr.ª Paula Arcoverde Cavalcanti, Universidade do Estado da Bahia
 Prof. Dr. Rodrigo Marques de Almeida Guerra, Universidade Federal do Pará
 Prof. Dr. Saulo Cerqueira de Aguiar Soares, Universidade Federal do Piauí
 Prof. Dr. Sergio Bitencourt Araújo Barros, Universidade Federal do Piauí
 Prof. Dr. Sérgio Luiz do Amaral Moretti, Universidade Federal de Uberlândia
 Prof.ª Dr.ª Silvia Inés del Valle Navarro, *Universidad Nacional de Catamarca*, Argentina
 Prof.ª Dr.ª Teresa Cardoso, Universidade Aberta de Portugal
 Prof.ª Dr.ª Teresa Monteiro Seixas, Universidade do Porto, Portugal
 Prof. Dr. Turpo Gebera Osbaldo Washington, *Universidad Nacional de San Agustín de Arequipa*, Peru
 Prof. Dr. Valter Machado da Fonseca, Universidade Federal de Viçosa
 Prof.ª Dr.ª Vanessa Bordin Viera, Universidade Federal de Campina Grande
 Prof.ª Dr.ª Vera Lúcia Vasilévski dos Santos Araújo, Universidade Tecnológica Federal do Paraná
 Prof. Dr. Wilson Noé Garcés Aguilár, *Corporación Universitaria Autónoma del Cauca*, Colômbia

Dados Internacionais de Catalogação na Publicação (CIP)
(eDOC BRASIL, Belo Horizonte/MG)

G786 The great world of nanotechnology [livro eletrônico] : vol. II /
 Organizador Marcos Augusto de Lima Nobre. – Curitiba, PR: Artemis, 2021.

Formato: PDF
 Requisitos de sistema: Adobe Acrobat Reader
 Modo de acesso: World Wide Web
 Inclui bibliografia
 Edição bilíngue
 ISBN 978-65-87396-36-1
 DOI 10.37572/EdArt_300621361

1. Nanociência. 2. Nanotecnologia. I. Nobre, Marcos Augusto Lima.

CDD 620.5

Elaborado por Maurício Amormino Júnior – CRB6/2422



PREFACE

The insertion of new and enhanced materials based on materials belonging to the Nano scale in the day-by-day has growth up in a silent way. In part, a number of works in the nanotechnology stemming of theoretical research using Density Functional Theory (DFT) and sophisticated simulation methods; another part is associated to the protected technologies associated to the military and patented nanomaterial and its process. In this sense, open access to recent aspects on the nanostructures application and properties can be reached in this book. Here, an interesting set of chapters gives opportunity of access texts that reach process and processing of nanostructures, applications of nanotechnology, advanced techniques to theoretical development. A broad set of nanostructures are here covered such as, nanocrystal, superficial nanograins, inner microstructures with nanograins, nanoaggregates, nanoshells, nanotubes, nanoflowers, nanoroad, nanosheets, Also, reveals new investigations areas as grainboundary of nanograins in ceramics and metals. A great number of software has been used as a tool of development of Science and Technologies for nanotechnology COMSOL Multiphysics 5.2. Phenomena and properties has been investigated by recent or classical techniques of materials characterization as Localized Surface Plasmon Resonance (LSPR), X-ray photoelectron spectroscopy (XPS), Field Emission Gun Scanning Electron Microscopy (FEG-SEM) with Energy Dispersive Spectroscopy (EDS), Raman Scattering Spectroscopy (RSS), X ray diffraction (XRD), ⁵⁷Fe Mössbauer spectroscopy, UV-vis spectroscopy, dynamic light scattering (DLS), Atomic Force Microscopy (AFM), and Field Emission Gun Scanning Electron Microscopy (FEG-SEM). In this sense, collections of spectra from Mössbauer spectroscopy, UV-vis spectroscopy and Infrared spectroscopy can be found. As a matter of fact, some chapter's item can be seemed as specific protocols for synthesis, preparations and measurements in the nanotechnology.

I hope you enjoy your reading.

Prof. Dr. Marcos Augusto Lima Nobre

TABLE OF CONTENTS

CHAPTER 1..... 1

ROLLING OF 316L STAINLESS STEEL WITH ROUGH ROLLS: A POSSIBLE TECHNIQUE TO OBTAIN SUPERFICIAL NANOGRAINS

Carlos Camurri

Alejo Gallegos

DOI 10.37572/EdArt_3006213611

CHAPTER 2..... 11

EFFECTS OF DIFFERENT ASPECT RATIOS AND JUNCTION LENGTHS ON THE COUPLED PLASMON GOLD NANOROD DIMERS

Hafiz Zeeshan Mahmood

Umer Farooq

Usman Rasool

Noor ul Huda

Sana Gulzar

Mahmood Ali

Maryam Iftikhar

Yasir Javed

Sajid Farooq

DOI 10.37572/EdArt_3006213612

CHAPTER 3.....21

AB-INITIO STUDY OF ELECTRONIC AND MAGNETIC PROPERTIES OF ZnO NANOCRYSTALS CAPPED WITH ORGANIC MOLECULES

Aline L. Schoenhalz

Paulo Piquini

DOI 10.37572/EdArt_3006213613

CHAPTER 439

CONFINED WATER CHEMISTRY: THE CASE OF NANOCHANNELS GOLD OXIDATION

André Mourão Batista

Herculano da Silva Martinho

DOI 10.37572/EdArt_3006213614

CHAPTER 5..... 67

PLASMONIC RESPONSE OF GOLD- SILICA AND SILVER- SILICA METAL CORE NANOSHHELLS BY OPTIMIZING THE FIGURE OF MERIT

Hafiz Zeeshan Mahmood

Zainab Shahid

Alina Talat

Imama Irfan

Bushra Arif

Sana Habib

Saba Munawar

Yasir Javed

Shaukat Ali Shahid

Sajid Farooq

DOI 10.37572/EdArt_3006213615

CHAPTER 6 76

AMORPHOUS MICRO AND NANO SILICA EXTRACTED FROM RICE HUSKS AND OBTAINED BY ACIDIC PREHYDROLYSIS AND CALCINATION: PREPARATION ROUTE AND CHARACTERIZATION

Eduardo Roque Budenberg

Eilton Aparecido Prado dos Reis

Deuber Lincon da Silva Agostini

Renivaldo José dos Santos

Felipe Silva Bellucci

Aldo Eloizo Job

Daltro Garcia Pinatti

Rosa Ana Conte

DOI 10.37572/EdArt_3006213616

CHAPTER 7..... 92

FORMATION OF METAL NANOPARTICLES BY SPUTTER DEPOSITION ON UNCD FILMS BY NPIII INSIDE CONDUCTIVE TUBES

Nazir Monteiro dos Santos

Divani Carvalho Barbosa

Evaldo José Corat

Mario Ueda

DOI 10.37572/EdArt_3006213617

CHAPTER 8 109

X-RAY PHOTOELECTRON SPECTROSCOPY (XPS) STUDY OF CONDUCTIVE TUBE AFTER NITROGEN PIII

Nazir Monteiro dos Santos
Elver Juan de Dios Mitma Pillaca
Mario Ueda
Steven Frederick Durrant
Pericles Lopes Sant'Ana

DOI 10.37572/EdArt_3006213618

CHAPTER 9 125

APPLICATION OF CLAY-CARBOXIMETHYLCHITOSANE NANOCOMPOSITE-SILVER NANOPARTICLES IN FILTERS TO TREAT CONSUMPTION WATER IN RURAL AREAS OF CAMANA - AREQUIPA-PERU

Maria Elena Talavera Nuñez
Irene Zea Apaza
Corina Vera Gonzales
Julia Zea Alvarez
Luis Rodrigo Benavente Talavera

DOI 10.37572/EdArt_3006213619

CHAPTER 10..... 138

NANOGRAIN BOUNDARY PHENOMENON IN CERAMIC NANOMETRIC MICROSTRUCTURE

Marcos Augusto Lima Nobre
Silvania Lanfredi

DOI 10.37572/EdArt_30062136110

CHAPTER 11..... 150

ON SPIN HAMILTONIAN FITS TO MÖSSBAUER SPECTRA OF NIFE₂O₄ NANOPARTICLES SYNTHESIZED BY CO-PRECIPIATION

Jose Higinio Dias Filho
Jorge Luis Lopez
Adriana Silva de Albuquerque
Renato Dourado Maia
Wesley de Oliveira Barbosa
Ernando Campos Ferreira
Fellipe Silva Pereira
Kátia Guimarães Benfica

DOI 10.37572/EdArt_30062136111

CHAPTER 12..... 162

EFFECT OF GRAPHITE NANOSTRUTURES ON THE VISCOSITY PROPERTIES OF BLENDS DIESEL-S10 AND BIODIESEL

Túlio Begena Araújo

Marcos Augusto Lima Nobre

DOI 10.37572/EdArt_30062136112

CHAPTER 13..... 172

REMOCIÓN DE ARSÉNICO DE EFLUENTES ACUOSOS EMPLEANDO COMO ADSORBENTE MAGNETITA NANOESTRUCTURADA

Orfelinda Avalo Cortez

Luis Jean Carlo Cisneros García

David Pedro Martínez Aguilar

DOI 10.37572/EdArt_30062136113

CHAPTER 14..... 182

AVALIAÇÃO DA MICRODUREZA DE NANOCOMPÓSITOS DE MATRIZ DE ALUMÍNIO REFORÇADOS COM ÓXIDO DE GRAFENO REDUZIDO

Daniel Andrada Maria

Andreza de Sousa Andrada Jordânio

Samuel Siqueira

Adelina Pinheiro Santos

Clascídia Aparecida Furtado

DOI 10.37572/EdArt_30062136114

CHAPTER 15..... 197

ROTA ECOLOGIA PARA SINTESE DE ELETRODO NANOESTRUTURADO DE ZnO PARA SUPERCAPACITOR

Eguiberto Galego

Marilene Morelli Serna

Tatiane Yumi Tatei

Bruna Rodrigues de Lima

Rubens Nunes de Faria Junior

DOI 10.37572/EdArt_30062136115

CHAPTER 16.....	212
MORFOLOGIA DE FILMES FINOS NANOESTRUTURADOS DE ZnO PRODUZIDOS PELO MÉTODO SILAR	
Eguiberto Galego	
Marilene Morelli Serna	
Lalgudi Venkataraman Ramanathan	
Rubens Nunes de Faria Junior	
DOI 10.37572/EdArt_30062136116	
CHAPTER 17.....	228
OBTENÇÃO E CARACTERIZAÇÃO DE NANOCRISTAIS DE CELULOSE A PARTIR DE PAPEL RECICLADO VIRGEM E PÓS-CONSUMO	
Jean Brito Santos	
Emanoel Igor da Silva Oliveira	
Nádia Mamede José	
DOI 10.37572/EdArt_30062136117	
ABOUT THE ORGANIZER.....	234
INDEX.....	236

ROLLING OF 316L STAINLESS STEEL WITH ROUGH ROLLS: A POSSIBLE TECHNIQUE TO OBTAIN SUPERFICIAL NANOGRAINS

Data de submissão: 17/03/2021

Data de aceite: 06/04/2021

Carlos Camurri

University of Concepción
Department of Materials Engineering
Concepción, Chile

Alejo Gallegos

University of Concepción
Department of Materials Engineering
Concepción, Chile

ABSTRACT: 316L stainless steel plates of 5 mm thickness, normalized at 900°C, were cold rolled with different reductions and number of passes by using rolls with three different surface roughnesses: grain heights of 0.17 and 0.33 mm and romboid-shaped grains of 1.5 mm height. Subsequently, the rolled samples were annealed at 275°C for 1 h in an effort to achieve superficial nanograins. The plates laminated by using low-roughness rolls had continuous superficial microcrystallization when they were rolled for at least 26 passes. For samples made with rougher rolls, the recrystallized superficial grains formed on the surface (sized ~10–15 μm) were smaller than those below the surface; this behavior was caused by the major deformation induced by repeated indentations. The superficial recrystallization of the sample also tended

to be more continuous for higher number of passes; micrographs of the penetration profiles of indentation in the samples rolled with high roughness rolls revealed that a sample rolled 24 times had not yet reached the steady surface topology. As a conclusion, in order to successfully form superficial nanograins, very low roughness rolls must be used as well as a small absolute reduction per pass, followed by annealing. These rolling conditions generate a continuous field of highly superficial deformations, which act as nucleation centers for nanograins during annealing.

KEYWORDS: Surface. Nanograins. Rolling. Rough rolls. Annealing.

1 INTRODUCTION

The development of the economy, with an annual increase of 3.7% on the global growth product since 2003, has generated an increasing demand for metals, which have risen in price, sometimes drastically; for example, the price of copper has increased by 409.5%. In that context, the international scientific community has made efforts to improve the mechanical and chemical performance of metals in order to optimize their use and widen their range of applications. In that sense, it is known that the presence of small grains favors

the mechanical resistance of metallic materials. This phenomenon can be observed from the classic Hall–Petch equation, which indicates that smaller grain sizes produce higher yield strengths. This relationship has led to several investigations on refining the grain size of metallic materials. The methods used to refine the grain size to microscale and nanoscale regimes can be classified into three groups depending on the phases involved in the process: solid-state methods, solidification methods, and condensation/solidification methods. A number of studies have analyzed the deformation-recrystallization sequence of solid-state methods, a sequence which causes severe plastic deformation to the grain structure 3. This methodology has industrial limitations because of the size of the pieces and the high amounts of energy needed process the entire bulk structure instead of only its surface.

Other investigations have developed means of refining surface grains by inducing highly peripheral deformation and then recrystallizing the material; these deformation methods include sandblasting, shot-blasting, ultrasound pulses, wire-brushing and, more recently, high-speed waterjet deformation. For example, a previous report demonstrated the generation of a nanocrystalline surface layer on AISI 316 stainless steel by sandblasting with 0.75-mm alumina grains followed by annealing; this process refined the grains and increased hardness to a depth of 200- μm . Similar results have been obtained on AISI 304 stainless steel by sandblasting with 0.21–0.30-mm silica grains followed by annealing; this process produced 20-nm grains; the presence of this surface layer considerably improved the steel's corrosion resistance and mechanical properties.

Another technique that has been used to obtain superficial nanograins is superficial deformation/recrystallization induced by wire brushing. In fact, a previous study demonstrated the generation of 20–300-nm superficial equiaxed grains on low-carbon steel alloys, austenitic stainless steel, commercial aluminum, Al-Mg, Al-4% Cu, pure Cu, Cu-Zn, and Pb-Sn; the authors of that study indicated that this technique can easily generate superficial nanostructures on any metallic alloy.

Additionally, several authors have reported the presence of nanocrystals in metallic surface layers after pin-on-disk tests performed on train rails or induced by friction. Nonetheless, none of these techniques are compatible with ongoing processes or for processing large surfaces, because they are slow and have low operative speed.

Because of these limitations, in this work the possibility of generating superficial nanostructures by other means is addressed. Specifically, cold rolling with rough rolls, thus simulating the superficial deformation processes occurring in sandblasting, could generate a dense, complex, high field of superficial deformations in a 316L stainless steel, and with a subsequent low-temperature annealing would induce the desired superficial nanostructures.

In effect, the application of a strong microcontinuous deformation field in a certain volume near the roll accumulates enough energy that new crystals can form at temperatures as low as 275°C. These new grains will be smaller than the original grains, given that a higher amount of energy can enter in the original network and that more nucleation centers are generated. Sandblasting and shot-blasting have produced positive results, but they cannot be used to treat large surfaces while maintaining proper dimensional control. The methodology proposed in this report simulates the deformation generated by these processes while allowing for better dimensional control and the possibility of treating larger surfaces.

2 EXPERIMENTAL DETAILS

A 316L austenitic stainless steel sheet with a nominal thickness h_0 of 5 mm, previously normalized at 900°C for 12 h, was considered as a raw material. To cold roll the sheet, was used a 7.5 kW Joliot two-high reversible rolling mill, equipped with rolls that were 200 mm wide and 127 mm in diameter. Based on the grain sizes of alumina and silica (between 0.21 and 0.75 mm) used for sandblasting samples of stainless steel in previous reports, three rolls with varying degrees of roughness were used in this work, between one half of the minimum to twice the maximum of the roughness considered by the cited references. The three rolls used are as follows: rolls with 0.17-mm and 0.33-mm average height surface grains (from ten measurements with standard deviation of 0.05 and 0.08 mm respectively), referred to as low-roughness rolls, and a roll with rhomboid-shaped base pyramids of 2.08-mm length, 1.04-mm width, and 1.5 -mm height on its surface, referred to as the high-roughness roll. The surface heights size of grains of the rough rolls were obtained by measuring it with a probe on a micrometer screw of 0.01 mm sensibility.

The 316L stainless steel normalized at 900°C was cold rolled first with the low-roughness rolls; the relative reduction was varied as well as the number of passes, up to 107. These variations were introduced in order to study the real effect on the generation of surface nanograins of the total reduction and that of repeated indentation induced by roll roughness. From the first set of results, obtained with low-roughness roll, it was deduced that the most important variable for generating new recrystallized grains was the number of passes; thus, when the high-roughness roll was used, the sheet was rolled in four different ways while keeping a fixed total reduction of 26%, reaching the final nominal thickness h_f of 3.7 mm but varying the number of passes and the absolute reduction per pass. Then, the cold-rolled samples were annealed at 275°C for 1 h. In the pattern samples (normalized) and those cold rolled and annealed, the Vickers microhardness (HV) - with a

load of 30 Kg- using a Struers Duramin equipment was measured, and microstructures by optical microscopy were determined.

3 RESULTS

Figure 1 shows a typical micrograph of 316L stainless steel normalized at 900°C for 12 h and cooled in the furnace. The central zone of the sample shows 150- μm recrystallized grains; also, the formation of a fragile oxide layer with 50- μm grains was detected.

Figure 1. Micrograph of a 316L stainless steel sheet normalized at 900°C for 12 h.

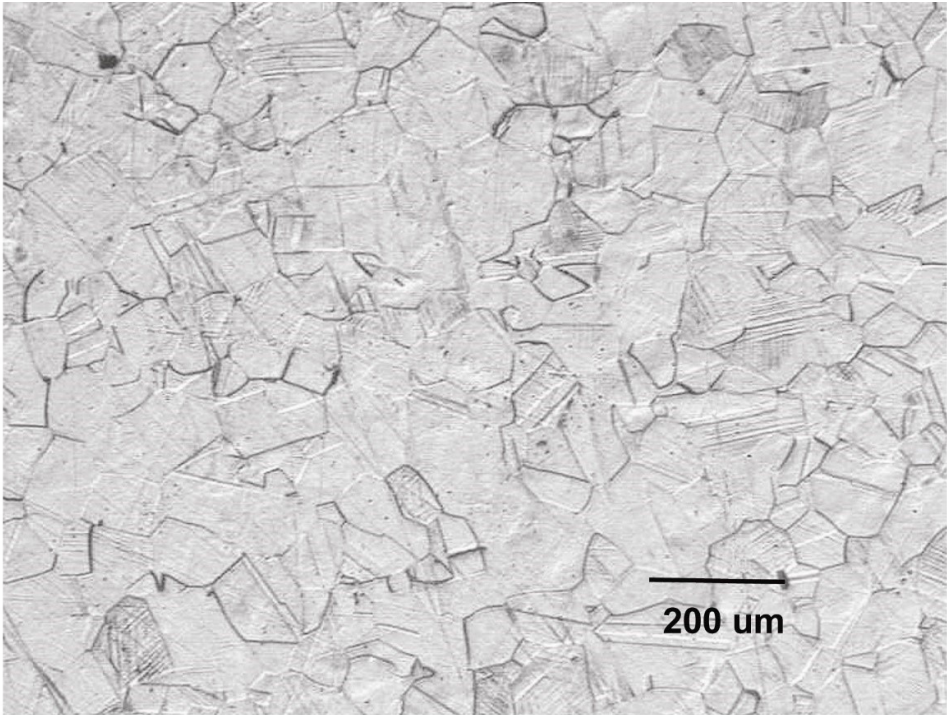


Table I shows the absolute reductions, numbers of passes, and characteristics of recrystallization obtained after annealing in the rolling assays with low-roughness rolls.

Table I. Characteristics of the assays made with low-roughness rolls.

Sample	Height grains (mm)	h_o (mm)	Number of passes	h_f (mm)	Results	Location
r18	0.33	4.94	18	4.69	Partial recryst.	surface
r12	0.33	4.92	12	4.46	No recryst.	
r26	0.33	4.94	26	4.73	Continuous.	surface
r7	0.17	4.81	7	4.64	No recryst.	

Sample	Height grains (mm)	h_o (mm)	Number of passes	h_f (mm)	Results	Location
r22	0.17	4.77	22	3.92	Partial recryst.	surface
r107	0.17	4.93	107	4.03	Continuous.	surface
r54	0.17	4.95	54	3.68	Continuous.	surface
r3	0.17	4.78	3	3.48	Partial recryst.	internal

In Table I and then in Table II, surface recrystallization refers to that from the surface to a 50- μm depth, while internal recrystallization refers to that from a 600- μm depth and below; partial recrystallization refers to that associated with zones of maximal deformation in the indentation marks or the planes of highest deformation. Also, in those tables the rolled samples were named r (number of pass) or R (number of pass) when low or high roughness rolls were used respectively.

Table I shows that continuous recrystallization on the surface is only achieved when the sample is rolled at least 26 times, independent of the total reduction. It is necessary to create a high and tangled density of deformations at the surface of the steel induced by the continuous indentation of the rough roll; these deformations will act as preferential nucleation sites during subsequent heating. Sticking friction is produced at the interface of the steel and roll as well as through some depth because of the indenter effect of the roll roughness, the latter of which increases with absolute reduction and the roughness itself; thus, it is deduced that global or bulk deformation does not affect surface recrystallization. In other words, the surface of the steel deforms mainly because of the indentation and not because of the deformation of the rolling itself.

Table II shows the absolute reductions, number of passes, and characteristics of recrystallization obtained after annealing in the rolling assays with high-roughness rolls.

Table II. Characteristics of the assays made with high-roughness rolls.

Sample	h_o (mm)	Number of passes	h_f (mm)	Results	Location
R06	4.96	6	3.66	Partial recryst.	Int. – ext.
R10	4.96	10	3.79	Partial recryst.	Int. – ext.
R19	4.95	19	3.59	Partial recryst.	Int. – ext.
R24	4.96	24	3.62	Continuous	Int. – ext.

As shown in Table II, the assays with high-roughness rolls exhibited partial or continuous internal and superficial recrystallization after annealing at 275°C for 1 h, based

on the number of passes and independent of the absolute reduction imposed. Figure 2 shows that samples rolled with 6 and 10 passes have certain sections on the surface with no new grains as well as other zones with smaller recrystallized grains of 10–15 μm . For the sample cold rolled with 24 passes, these small recrystallized grains appear over the entire surface, a behavior which highlights the cumulative effect of deformations by indentation based on the number of rolling passes.

Figure 2. Micrographs of the four different cold rolled samples annealed at 275°C for 1 h.

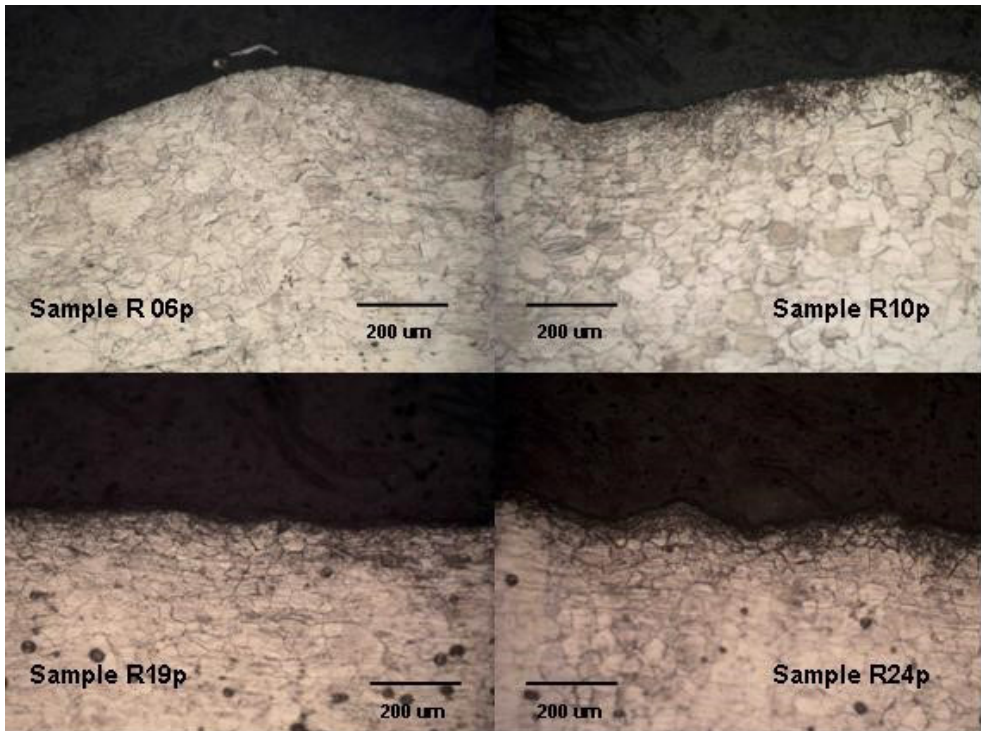


Figure 3 shows that preferential recrystallization with smaller (10–15 μm) grains can be observed from the surface. Zone 1 (to depth of 100 μm) is mostly affected by the indentation deformation caused by shear, which is imposed by the roughness of the roll. The recrystallized surface grains of 10–15 μm appear in this zone at a depth of 35–50 μm ; these grains are considerably smaller than the remaining recrystallized grains in this sample. This behavior suggests a preferential indentation effect imposed by the roughness on this superficial deformation and the subsequent recrystallization. Zone 2 is located deeper in the sample; this zone contains larger recrystallized grains, which are produced by deformation from slip associated with the rolling itself and from some shear strain due to the effect of indentations that can reach such a depth. Zone

3, starting from a 600- μm depth, has recrystallization associated only with the rolling deformation from slip on bulk.

Figure 3: Micrograph of the R10 sample after rolling and annealing.

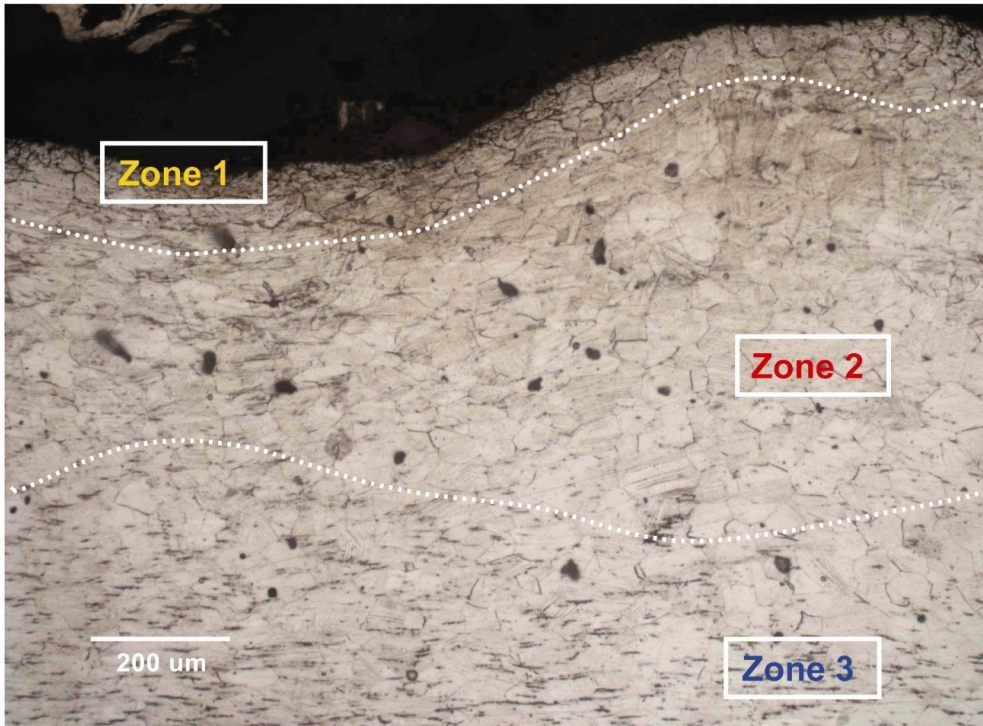


Figure 4 shows the microhardness profiles of two of the samples cold rolled with high-roughness rolls and then annealed; they are compared with those normalized at 900°C for 12 h and then sandblasted with granulometry sand of 0.21–0.30 mm for 20 min, followed by annealing at 275°C for 1 h with furnace cooling.

The hardnesses of the sandblasted and rolled samples at $50\ \mu\text{m}$ from the surface are 240 and 210 HV, respectively. As previously mentioned, the grain size and hardness in this zone are associated only with the deformation caused by indentation. At greater depths, the hardness of the sandblasted sample decreases greatly to about 60 HV, the same as stainless steel annealed at 900°C . This phenomenon does not occur in the rolled stainless steel R06 and R24 in whose there is an increase of hardness to the deeper Zone 2 shown in Figure 3; this region shows a combination of the effects of the deformations by rolling and by indentation. From $600\text{-}\mu\text{m}$ depth, zone 3 of Figure 3, the hardness tends toward a stable value due to the only effect of the volume deformation by rolling.

Figure 4. Volumetric hardness's in samples that were cold-rolled or sandblasted and subsequently annealed.

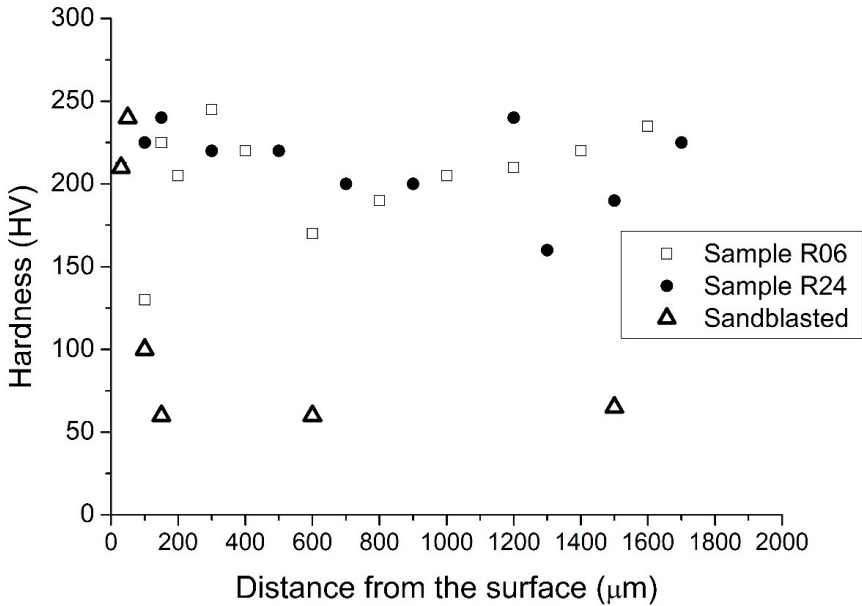
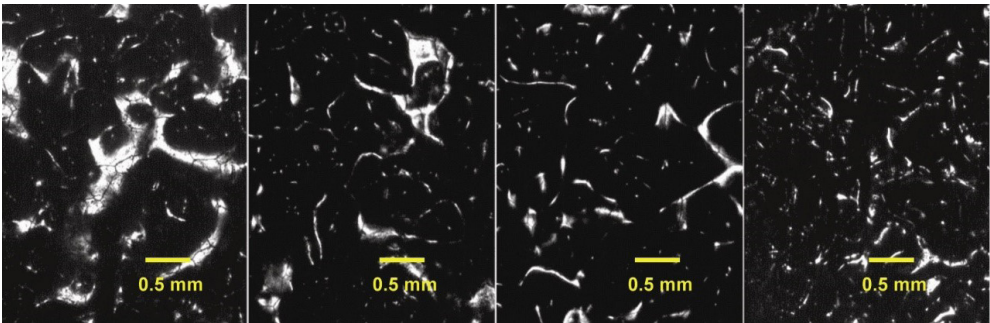


Figure 5 shows how the number of passes affects the indentation imposed in the sample cold rolled with high-roughness rolls.

Figure 5. Micrographs of the superficial topography of samples after 6, 11, 19 and 24 passes respectively from left to right, with high-roughness rolls.



In each micrograph from Figure 5, the large white areas represent higher zones or plateaus from the material removed by indentation from the rough rolls. As the number of passes increases, these plateaus continue to interact with the roughness of the roll; this behavior tends to cause the surface of the steel to flatten, reducing the macroscopic effect of the indentation and diminishing the visibility of these plateaus in the micrographs. Nevertheless, the sample with 24 passes still exhibits visible white zones, although many fewer than the other samples. Studying the morphological evolution of the surface as the number of passes increases, as shown in Figure 6, a continuous increase of the density

of concave regions and a decrease of the plateaus was found; thus, with respect to the studied roughness, the superficial deformation by indentation did not reach its steady topology conditions. This behavior coincides with the results of cold rolling with low-roughness rolls, as shown in Table I which both indicate the need of at least 26 passes to achieve a stable superficial imposition and, after annealing, continuous recrystallization of the surface.

4 CONCLUSION

The roughness of the roll imposes on the surface of the samples sticking friction and to avoid this surface adherence it is necessary to use rolls with lower roughness than those used in this work.

Cold rolling the sheet with rough rolls up to 24 passes did not produce a steady topology by indentation; wide plateaus visible on the surface, indicators of non-deformed material, progressively disappeared but did not do completely.

The industrial applicability of this process demands that the number of passes should be as low as possible, ideally between 5 and 10, when obtaining proper surface indentation. Thus, rolls with much lower superficial roughness than those used in this work should be considered; doing so will produce a much higher concentration of superficial points with high deformation, thus generating more nucleation centers during the annealing, producing more desirable superficial nanostructures.

The hardness at a depth of 50 μm achieved in the samples rolled with high roughness rolls is of the same order of that for the reference sandblasted sample. Nonetheless, the same recrystallization uniformity or grain size obtained from the sandblasted sample was not achieved. This result is caused by the differences in the complexity and homogeneity of the deformations imposed, a higher density of which can be obtained from sandblasting. Because of roughness of the rolls used, this effect was not reached in the samples of this report. A roll with lower roughness will cause the surface of the steel, over many rolling passes, to accumulate a tangle of indentation deformations, which is a necessary phenomenon not obtained in this work. Thus, only having a good hardness is not sufficient evidence of a structure with good conditions to generate nanograins after thermal treatment.

REFERENCES

Azushima, Severe plastic deformations (SPD) for Metals, *CIRP Ann.-Manuf. Techn.* 57, (2008): 716–735.

A. Gallegos, “Nuevas Técnicas de nanoestructuración superficial en un acero inoxidable 316L (New techniques for obtaining surface nanostructures on a 316L stainless steel)” (PhD diss., Universidad de Concepción, 2012).

- C.T. Kwok, Corrosion characteristics of nanostructured layer on 316L stainless steel fabricated by cavitation- annealing, *Mater. Lett.* 60, (2006): 2419–2422.
- H.A. Yun-wei, The wear and corrosion resistance of shot peened-nitrided 316L austenitic stainless steel, *J. Iron Steel Res. Int.* 16, (2009): 68–72.
- Ministerio Economía y Finanzas Peru, marco macroeconomico trianual 2014-2016 (Economy and Finance Ministry of Peru, Triennial annual macro economy projection 2014-2016), 2013. <http://www.bcrp.gob.pe/docs/Publicaciones/Programa-Economico/mmm-2014-2016-mayo.pdf>. Accessed September 2013.
- M. Multigner, Influence of the sandblasting on the subsurface microstructure of 316LVM stainless steel: Implications on the magnetic and mechanical properties, *Mat. Sci. Eng. C* 29(4), (2009): p. 1357–1360.
- M. Sato, N. Tsuji, Y. Minamino, and Y. Koizumi, in High Performance structures and materials, *Technol. Adv. Mat.* 5(1–2), January-March (2004): 145–152.
- N. Tsuji, Y. Saito, H. Utsunomiya, and S. Tanigawa, Ultra-fine grained bulk steel produced by accumulative roll- bonding (ARB) Process, *Scripta Mater.* 40(7), (1999): 795–800.
- Rezaee, The influence of reversion annealing behavior on the formation of nanograined structure in AISI 201L austenitic stainless steel through martensite treatment, *Mater. Design* 32, (2011): 4437–4442.
- S. Barriuso, Roughening of metallic biomaterial by abrasive less water jet penning characterization and viability, *Wear* 270, (2011): 634–639.
- S. Emgea, D. Karthikeyanb, and A. Rigney, Effect of the boronizing on the dry wear behaviour of DC53/0.45 mass % C steel, *Wear* 267, (2009): 562–567.
- X.H. Chen, Tensile properties of a nanocrystalline 316L austenite stainless steel, *Scripta Mater.* 52, (2005): 1039–1044.
- X.Y. Wang, Mechanical and electrochemical behavior of nanocrystalline surface of 304 stainless steel, *Electrochim. Acta* 47, (2002): 3939–3947.
- X.Y. Wang, Mechanical, electrochemical and tribological properties of nanocrystalline surface of 304 stainless steel, *Wear* 255, (2003): 836–845.
- X.Y. Wang, Mechanical, electrochemical and tribological properties of nanocrystalline surface of brass produced by sandblasting and annealing, *Surf. Coat. Technol.* 167, (2003): 188–196.

CHAPTER 2

EFFECTS OF DIFFERENT ASPECT RATIOS AND JUNCTION LENGTHS ON THE COUPLED PLASMON GOLD NANOROD DIMERS

Data de submissão: 05/04/2021

Data de aceite: 28/04/2021

Hafiz Zeeshan Mahmood

PhD Electrical Engineering
University of Central Punjab
Faisalabad Campus, Pakistan
<https://www.researchgate.net/profile/H-Zeeshan-Mahmood>

Umer Farooq

University of Central Punjab
Faisalabad Campus, Pakistan

Usman Rasool

University of Central Punjab
Faisalabad Campus, Pakistan

Noor ul Huda

University of Central Punjab
Faisalabad Campus, Pakistan

Sana Gulzar

University of Central Punjab
Faisalabad Campus, Pakistan

Mahmood Ali

University of Central Punjab
Faisalabad Campus, Pakistan

Maryam Iftikhar

University of Central Punjab
Faisalabad Campus, Pakistan

Yasir Javed

Assistant Professor, PhD
University of Agriculture Faisalabad, Pakistan
Department of Physics
<https://www.researchgate.net/profile/Yasir-Javed-6>

Sajid Farooq

Doctor of Philosophy
Universidade de Pernambuco, UPE
50950-050, Recife, Brazil
Institute of Innovation and Technology
Escola Politécnica de Pernambuco - POLI
<https://www.researchgate.net/profile/Sajid-Farooq>

ABSTRACT: We have explored the optical behaviour in dimer of gold nanorod (AuNR) bridge by thin silica cylinder to sub-nanometre regime. To probe this model, Computational simulations were carried out to investigate the nanorod surface which was divided into small tetrahedral mesh with finer size. Furthermore, perfectly matched layer (PML) around the nanorod surface was applied to avoid any reflection artifacts on the simulation. The amplitude of the background oscillating field was one (1) Vm^{-1} . Our results reveal that an increase in aspect ratio causes a red shift in dimer connected mode, leading to significantly higher sensitivity 717 nm/RIU and figure of merit 16.9 compared to a single dimer having 300 nm/RIU sensitivity with similar dimensions. These findings suggest that using end to end

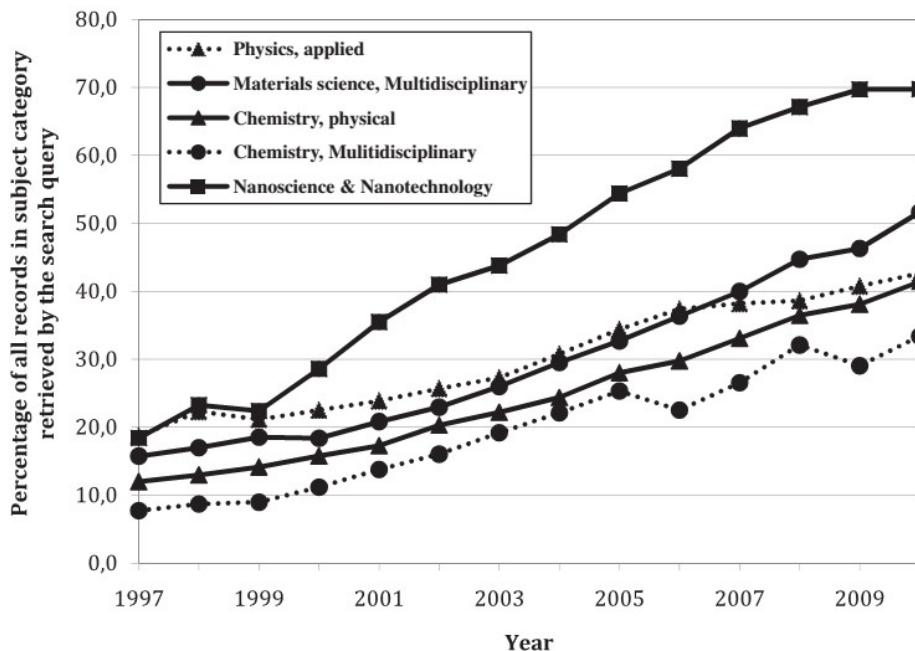
linked nanoscale structures could significantly play an important role in tuning far field spectral responses of plasmonic metal nanostructures for applications in LSPR sensing.

KEYWORDS: AuNR dimer. Figure of merit. Bulk Sensitivity. Perfectly matched layer.

1 INTRODUCTION

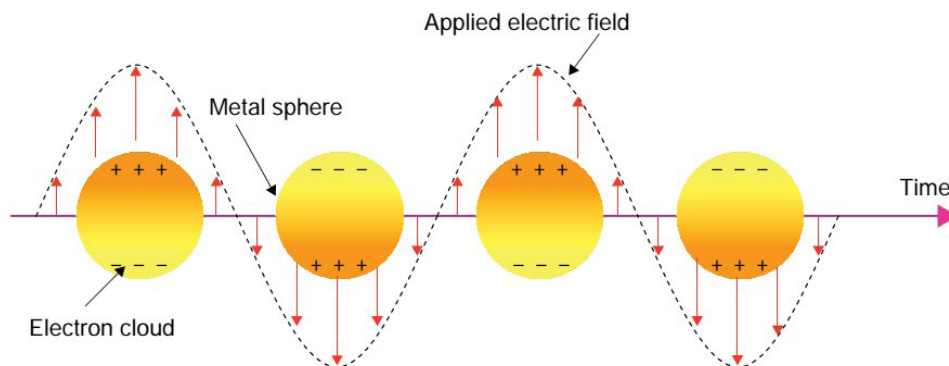
Modern civilization growth relies upon three pillars: materials, energy sources and information technology. Out of these three resources, materials are the basis for advancement in energy and information technology (Zhang et al., 2018). In past, each era was named after the material most dominant at that time e.g., Stone age, Bronze age, Iron age, polymer age etc. Thus, present era can be attributed as the Nanomaterial age. Nanotechnology is the study of the behavior of objects which fall between 10^{-9} to 10^{-6} meters regime (roughly 1 nm to 100 nm) (Grieneisen et al., 2011). When matter is reduced from its bulk to nanoscale, high surface-to-volume ratio, a key parameter of nanostructure plays a significant role to explore the novel and intriguing properties of the nanoparticles begin to emerge. Arguably “beginning” with the discovery of fullerenes, the last three decades have seen an expeditious investigation in nanoscience (Kroto et al., 1985). Due to the technology advancement in synthesis, control, and characterization of materials, the field of nanotechnology has seen tremendous growth. A brief description of rapidly growing field of nanotechnology in last decade is illustrated in Figure 1.

Figure. 1 - Graph displaying the proliferation of journals in the field of “nanoscience and nanotechnology” over the last decade. (Source: Adapted from (Grieneisen & Zhang, 2011).



As the name implies, nanoplasmonics is the study of plasmon resonance that occurs within nanostructures. In brief, the free electrons in a metal can be excited by the presence of an external electromagnetic (EM) field. This EM field displaces the electrons from their neutral orientation with respect to the fixed positive nuclei, and the resulting coulombic restorative force causes the electron cloud to oscillate at the system's natural frequency as a result of collective oscillations of the conduction electrons (Non-Propagating) prompted by electromagnetic radiation having a pertinent wavelength which is referred as Localized Surface Plasmon Resonance (LSPR) as depicted in Figure 2.

Figure. 2 - Schematic representation of the interaction of EM radiation and metallic nanostructure. (Source: Adapted from Zalevsky, Z. & Abdulhalim 2010).



Plasmonic nanostructures strongly interact with light resulting in size-dependent scattering, absorption and large enhancement in near electric field. These optical mechanisms of nanoscale particles have led to remarkable potential applications. A plethora of studies reveal that plasmonic properties of the metallic nanostructures have been demonstrated by controlling the geometry (size, shape), composition and the refractive index of their surrounding medium (Farooq and Araujo, 2018, Kelly *et al.*, 2003).

The spectrum of LSPR excitations have been the subject of intensive research efforts and encourage researchers to synthesize the growth of complex shapes nanostructures such as nanoshells, nanorice, nanocages, nanostars, nanorods and nanopyramids (Lee *et al.*, 2009), which shows plasmon peaks in various spectral regions.

Moreover, gold nanostructures are increasingly receiving attention as an important starting point for label-free sensing. LSPR sensors can be explored as fast, reliable, cheap and fairly facile tool for medical diagnosis. Various examples of LSPR biosensors were attributed to the diagnosis of relevant medical disease, as Alzheimer (Haes *et al.*, 2005), preeclampsia (Hammond *et al.*, 2005), influenza (Takemura *et al.*, 2017) Dengue virus (Camara *et al.*, 2013) and *Candida albicans* (Farooq *et al.*, 2018) as well as for intracellular protein sensing (Jain *et al.*, 2006).

El-Sayed and coworkers have theoretically suggested the use of coupled gold nanostructures for sensing (Hong et al., 2014). Several structural aspects of a nanochain rules the plasmonic features of coupled gold nanorods. Moreover, Pramod et al have investigated the effects of molecular link orientation on the optical properties of gold nanorod (AuNR) dimers (Pramod et al., 2008).

The basis of plasmonic sensors is the resonant coupling between the oscillations of free electrons, called plasmons, and incident visible light waves. By confining these oscillations within a nanostructure, the coupling efficiency is enhanced by the creation of LSPR states.

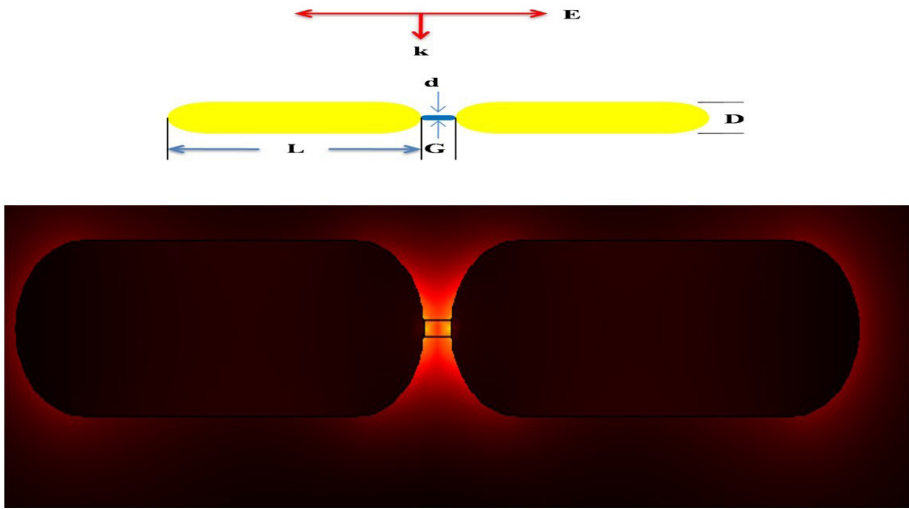
In this study, we evaluate the use of gold nanorod dimer as a sensing platform. Analyses of LSPR behavior of gold nanorod dimers, connected with silica nano-cylinder, with several aspect ratios and silica junction thickness, were investigated. In this work, crucial parameters that govern the LSPR molecular sensor performance, in particular figure of merit and bulk sensitivity was evaluated. Moreover, this work provides insights on the LSPR behavior due to embedding AuNR dimer in several surrounding media.

The performance of gold nanorod (AuNR) dimer linked end-to-end by thin dielectric junction, as a sensor platform has been investigated. Three-dimensional finite element simulations (COMSOL Multiphysics) in frequency domain were carried out to study the influence of local environment on the optical features of AuNR dimer, with different junction lengths and aspect ratios. This computational approach focused on understanding the LSPR spectral peak position and spatial distribution of electromagnetic field enhancement near the surface of individual gold nanorod dimer, in order to reveal the behavior of crucial parameters such as figure of merit and bulk sensitivity, which predicts the LSPR sensor performance. We find the plasmon peak position of end-to-end connected Au nanorod dimer exhibited red shift by at least 60 nm from single Au nanorod. The simulations reveal that silica linked dimer of gold nanorod sensing platform shows higher sensitivity (717 nm/RIU) as compared to individual gold nanorod. We observed that silica bridge dimer also exhibits a high figure of merit value, up to 16.9. Our proposed model put forth a new paradigm in LSPR based sensing applications.

2 SIMULATED MODEL ANALYSES

Finite Element Method (FEM) calculations were used to predict the plasmonic properties of the gold nanorod (AuNR) dimers which are linked with a thin silica cylinder. In the 3D simulations, the AuNR dimer surface was divided into small tetrahedral mesh elements with size 'extremely fine'. The dimers were modeled as shown in Figure. 3. The plasmonic dimers consist of two hemispherically-capped cylinders forming the gold nanorod (AuNRs) dimer with length = L , diameter = D and connected by a silica cylinder (length = G , diameter = d).

Figure. 3. 3D simulations model region composed of model nanostructure in embedding medium and PML layers.



The nanostructures geometry consisting of hemispherical capped cylinders of AuNR and linked through a silica cylinder. The plasmonic structure was probed by linearly polarized light along the long axis of dimer. Furthermore, perfectly matched layer (PML) around the nanoparticle was used to avoid any kind of reflection artifacts on the simulations. We have performed a plane wave electromagnetic field for the numerical model analysis using COMSOL Multiphysics software, Electromagnetic Waves and Frequency Domain interface, where the Electric field within the domain explores Maxwell's equations. The radius and thickness of the PML spheres were chosen, depending on the NPs diameter, such that further NPs size variations would not influence the simulation results as well as minimizing the reflection effects. To simulate the probe model, a background electric field 1 Vm^{-1} was applied. The data of the metal dielectric functions (real and imaginary) for Au were obtained from Johnson and Christy (Johnson et al., 1972). To investigate which metal nanostructures is a good candidate for bio or chemical sensing applications as well as their efficiency can be characterized by measuring their RI based sensitivity. Bulk sensitivity (η_b), A sensing parameter which qualitatively analyse the sensing efficiency and correlates the change in LSPR wavelength as function of varying refractive index of the surrounding medium has been evaluated i.e: $\eta_b = \Delta\lambda_{\text{LSPR}} / \Delta n$. Figure of Merit (FoM) is second analytical parameter which elucidate well sensor reliability by, $\text{FoM} = \eta_b / \text{FWHM}$, where (FWHM) is full width at half maximum or line width of the LSPR peak (Mahmood et al., 2019).

2.1 BULK SENSITIVITY

Sensitivity is one of the important parameters to characterize a sensor. For LSPR based sensors, bulk sensitivity is termed as the variation of LSPR peak position with

respect to the change in RI unit (RIU) of the medium, and its unit is eV/RIU or nm/RIU (Farooq, and Araujo 2018). The most commonly employed equation for refractive index (RI) based sensitivity or bulk sensitivity can be written as:

$$\eta_B = \frac{\Delta\lambda}{\Delta n} \quad (1)$$

where η_B represents bulk sensitivity, while $\Delta\lambda$ and Δn are respectively, Shift in LSPR peak wavelength and the refractive index change of a medium.

2.2 FIGURE OF MERIT

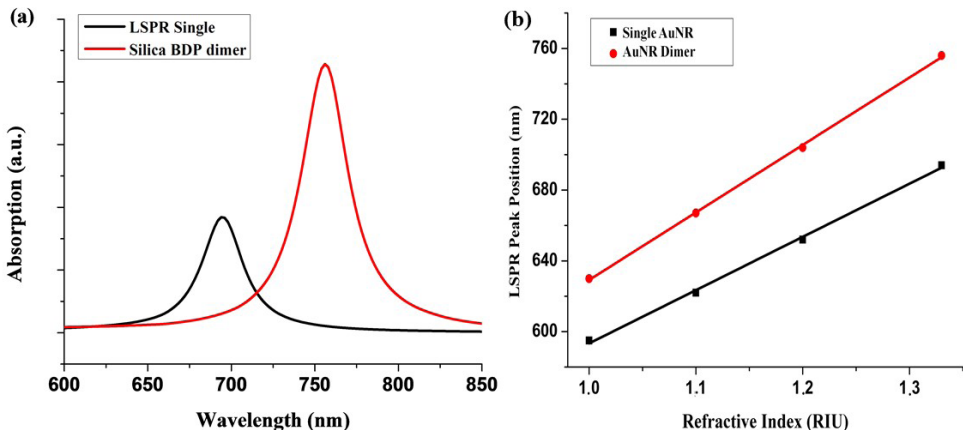
Sensing performance can also be evaluated by exploring the Figure of Merit (*FoM*) factor. The *FoM* is defined as the ratio of bulk sensitivity to the full width at half maximum (FWHM) (Farooq, and Araujo 2018), and is expressed as:

$$FoM = \eta_B / FWHM \quad (2)$$

3 RESULTS AND DISCUSSIONS

The LSPR peak shift of single AuNR and silica connected AuNR dimer in various surrounding mediums with different RI values are presented in Figure. 4. LSPR peak position is linearly dependent on the variations of the surrounding medium RI, as shown in Figure.4 for Au single rod and AuNR dimer. For gold dimer bridged by silica cylinder having length $G = 2$ nm and thickness $d = 1$ nm, LSPR peak position can shift from 630 to 756 nm with RI increasing from 1.0 to 1.33, as depicted in Figure 4.

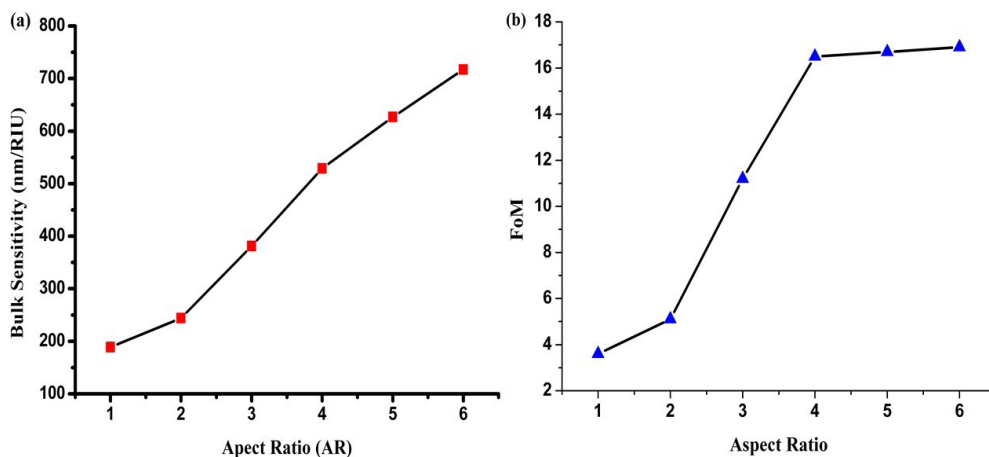
Figure. 4. LSPR peak shift of single AuNR and AuNR dimer connected with silica cylinder on changing the the refractive index of the surrounding Medium.



Numerical values for the bulk sensitivity of AuNR dimer were identified as 381 nm/RIU, which is higher than single nanorod value (300 nm/RIU). The AuNR dimer also presents a higher figure of merit (11.7) after linked by silica cylinder with appropriate aspect ratio (AR = 3).

As depicted in Figure. 5a, the aspect ratio of silica linked AuNR dimer increase, the bulk sensitivity of gold nanostructures enhances accordingly. The higher value of bulk sensitivity obtained at aspect ratio 6 (L = 30 nm, D = 5 nm), and the lower value at aspect ratio 1.

Figure. 5. The bulk sensitivity (a) and FoM (b) of AuNR dimer with various aspect ratios, keeping constant silica connection length (G = 1 nm) and thickness (d = 1 nm).



Therefore, FoM of AuNR dimer also varies as a function of aspect ratio as shown in Figure 5b. The maximum value of FoM calculated in this work is 16.9, for aspect ratio equals to 6. This calculated value of FoM (16.9) of gold rod dimer is higher than the reported values of several nanostructures with different shapes, such as Au nanorod (1.3) (Mayer et al, 2008), Au nanosphere (1.5) (Underwood and Mulvaney, 1994), Au nano-crescent (2.4) (Bukasov, and Shumaker-Parry, 2007), Au nanoshells (0.9) [14], Au bipyramide (4.5) (Burgin and Guyot-Sionnest, 2008) and Ag Nanoplate (2.5). Table 1 indicates the figure of merit and bulk sensitivity of different nanostructures (ensemble).

Table 1. The survey of bulk sensitivity and figure of merit of plasmonic nanostructures of various shapes

Nanostructures	Types	η_B (nm/RIU)	FoM	References
Au NR-dimer	---	717	16.9	Calculated
Au Nanoshells	Ensemble	314	0.9	Pramod et al, 2008

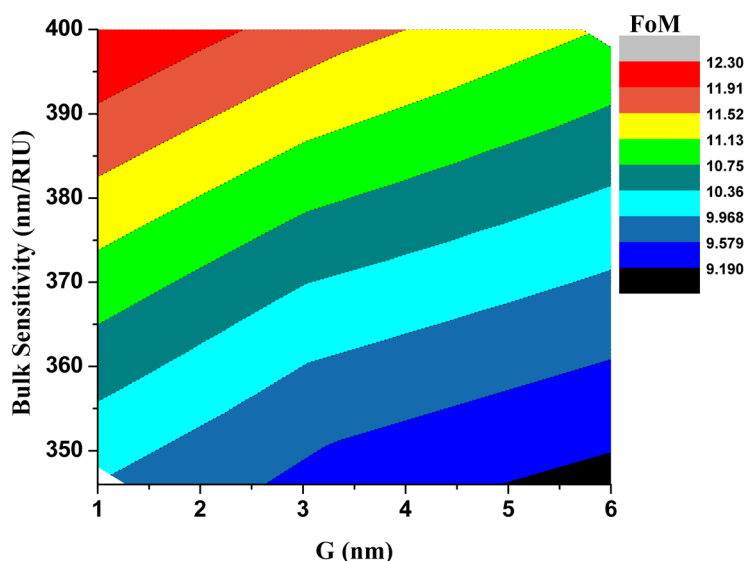
Nanostructures	Types	η_B (nm/RIU)	FoM	References
Au Nanospheres	Ensemble	90	1.5	Mulvaney et al, 1994
Au Nanorods	Ensemble	170	1.3	Mayer et al., 2008
Au Nano-Crescent	Ensemble	596	2.4	Bukasov et al, 2007
Au bipyramid	Ensemble	352	4.5	Burgin et al, 2008
Ag Nanoplate	Ensemble	406	2.5	Farooq et al., 2018

The FWHM of gold dimer spectrum is not so affected by increasing the aspect ratios, as compared to other ensemble shapes like spheres, shells etc. However, varying the AuNR aspect ratios of gold dimer can also affect the FoM due to change in radiation damping. Therefore, the FoM response of AuNR dimer is mainly dependent on the variations in bulk sensitivity and FWHM.

The impact of silica nano-cylinder junction length (G), connecting end-to-end gold nanorods, on the bulk sensitivity and FoM can be observed in fig 4. AuNR dimers with silica junction lengths from 1 to 5 nm were analyzed.

As silica linked cylinder length increases, the sensitivity and FoM of the nanostructured platform reduces. As FWHM of gold dimer spectrum is not so affected by the junction length FoM and bulk sensitivity presents similar behavior, as shown in Figure 6.

Figure.6. The bulk sensitivity and FoM of 30nmx10nm AuNR dimer as a function of silica nano-cylinder with different lengths (G); L= 30nm; D=10nm and d = 1 nm.



The higher FoM and sensitivity values were obtained for 1 nm junction length, Which was 12.25 and 397 nm/RIU respectively.

4 CONCLUSION

Localized Surface Plasmon Resonance phenomenon can drive the development of low-cost and accurate sensing. The establishment of high performance AuNR dimer LSPR sensor requires the description of sensing parameters (sensitivity and FoM) as a function of the AuNR aspect ratios and silica connection length.

The obtained computational results present a potential of the bulk sensitivity and FoM as function of the AuNR dimer connected end-to-end by silica nano-cylinder. By tuning the dimer aspect ratio from 1 to 6, substantial bulk sensitivity (717 nm/RIU) was obtained by embedding the nanostructure into several media. Moreover, higher FoM (16.9) was achieved by keeping the dimer aspect ratio 6.

Besides, the approach used in this work provides insight on the dimer LSPR behavior due to tuning the NR aspect ratio and silica junction length, establishing a new paradigm for engineering LSPR based sensor. The proposed approached can be extended to engineer an efficient and precise nanoscale sensor in molecular biosensing.

5 ACKNOWLEDGEMENT

This work was supported by the Brazilian Agencies: Coordination for the Improvement of Higher Education Personnel (CAPES), the Brazilian National Council for Scientific and Technological Development (CNPQ), the Polytechnic School of Pernambuco, and authors are also grateful to University of Central Punjab, Faisalabad Campus, Pakistan.

REFERENCES

- Bukasov R, Shumaker-Parry JS. Highly tunable infrared extinction properties of gold nanocrescents. *Nano letters*. 2007 May 9;7(5):1113-8.
- Burgin J, Liu M, Guyot-Sionnest P. Dielectric sensing with deposited gold bipyramids. *The Journal of Physical Chemistry C*. 2008 Dec 11;112(49):19279-82.
- Camara AR, Gouvêa PM, Dias AC, Braga AM, Dutra RF, de Araujo RE, Carvalho IC. Dengue immunoassay with an LSPR fiber optic sensor. *Optics express*. 2013 Nov 4;21(22):27023-31.
- Farooq S, Neves WW, Pandoli O, Del Rosso T, de Lima LM, Dutra RF, de Araujo RE. Engineering a plasmonic sensing platform for *Candida albicans* antigen identification. *Journal of Nanophotonics*. 2018 May;12(3):033003.
- Farooq S, Nunes FD, de Araujo RE. Optical properties of silver nanoplates and perspectives for biomedical applications. *Photonics and Nanostructures-Fundamentals and Applications*. 2018 Sep 1;31:160-7.

- Farooq S, D. Rativa and R. E. de Araujo, "High performance gold dimeric nanorods for plasmonic molecular sensing," in *IEEE Sensors Journal*, doi: 10.1109/JSEN.2021.3064648.
- Farooq, Sajid, and Renato E. de Araujo. "Engineering a localized surface plasmon resonance platform for molecular biosensing." *Open Journal of Applied Sciences* 8.3 (2018): 126-139.
- Grieneisen, M. L. & Zhang, M. Nanoscience and Nanotechnology: Evolving Definitions and Growing Footprint on the Scientific Landscape. *Small* 7, 2836–2839 (2011).
- Haes AJ, Chang L, Klein WL, Van Duyne RP. Detection of a biomarker for Alzheimer's disease from synthetic and clinical samples using a nanoscale optical biosensor. *Journal of the American Chemical Society*. 2005 Feb 23;127(7):2264-71.
- Hammond JL, Bhalla N, Rafiee SD, Estrela P. Localized surface plasmon resonance as a biosensing platform for developing countries. *Biosensors*. 2014 Jun;4(2):172-88.
- Hong W, Liang F, Schaak D, Loncar M, Quan Q. Nanoscale label-free bioprobes to detect intracellular proteins in single living cells. *Scientific reports*. 2014 Aug 26;4(1):1-5.
- Jain PK, Eustis S, El-Sayed MA. Plasmon coupling in nanorod assemblies: optical absorption, discrete dipole approximation simulation, and exciton-coupling model. *The Journal of Physical Chemistry B*. 2006 Sep 21;110(37):18243-53.
- Johnson PB, Christy RW. Optical constants of the noble metals. *Physical review B*. 1972 Dec 15;6(12):4370.
- Kelly, K. Lance, Eduardo Coronado, Lin Lin Zhao, and George C. Schatz. "The optical properties of metal nanoparticles: the influence of size, shape, and dielectric environment." (2003): 668-677.
- Kroto, H. W., Heath, J. R., O'Brien, S. C., Curl, R. F. & Smalley, R. E. C60: Buckminster fullerene. *Nature* (1985). doi:10.1038/318162a0
- Lee J, Hasan W, Odom TW. Tuning the thickness and orientation of single Au pyramids for improved refractive index sensitivities. *The Journal of Physical Chemistry C*. 2009 Feb 12;113(6):2205-7.
- Mahmood, H. Z., Farooq, S. & Lins, E. C. Optimizing the Plasmonic Sensing of Silica Coated Au/Ag Nanoshellse. *Int. J. Sci. Eng. Investig.* 87, 140–145 (2019).
- Mayer KM, Lee S, Liao H, Rostro BC, Fuentes A, Scully PT, Nehl CL, Hafner JH. A label-free immunoassay based upon localized surface plasmon resonance of gold nanorods. *ACS nano*. 2008 Apr 22;2(4):687-92.
- Pramod P, Thomas KG. Plasmon coupling in dimers of Au nanorods. *Advanced Materials*. 2008 Nov 18;20(22):4300-5.
- S.Underwood,P.Mulvaney,"Effect of the Solution Refractive on the Color of Gold Colloids," *Langmuir*, 10 , 3427–3430, 1994.
- Takemura K, Adegoke O, Takahashi N, Kato T, Li TC, Kitamoto N, Tanaka T, Suzuki T, Park EY. Versatility of a localized surface plasmon resonance-based gold nanoparticle-alloyed quantum dot nanobiosensor for immunofluorescence detection of viruses. *Biosensors and Bioelectronics*. 2017 Mar 15;89:998-1005.
- Zhang, B. Introduction. in *Physical Fundamentals of Nanomaterials* 1–18 (Elsevier, 2018). doi:10.1016/B978-0-12-410417-4.00001-0.
- Zalevsky, Z. & Abdulhalim, I. *Integrated Nanophotonic Devices*. *Integrated Nanophotonic Devices* (2010). doi:10.1016/C2009-0-62955-X.

CHAPTER 3

AB-INITIO STUDY OF ELECTRONIC AND MAGNETIC PROPERTIES OF ZnO NANOCRYSTALS CAPPED WITH ORGANIC MOLECULES

Data de submissão: 07/04/2021

Data de aceite: 29/04/2021

Aline L. Schoenhalz

Federal University of Santa Maria
Physics Department
Santa Maria – RS

<http://lattes.cnpq.br/2996035802901172>

Paulo Piquini

Federal University of Santa Maria
Physics Department
Santa Maria – RS

<http://lattes.cnpq.br/4496249071363237>

ABSTRACT: Unexpected ferromagnetic ordering in nonmagnetic metal oxide nanostructures, such as ZnO nanoparticles, has been attributed to several controversial origins. The experimental determination of the ZnO nanoparticle properties is difficult by the diminutive and the possible conformational, and chemical complexity of the systems. Systematic reliable theoretical studies using first principles density functional theory calculations have been applied to study the structural, electronic, energetic and magnetic properties of ZnO nanocrystals both pristine and bonded to thiol, amine and TOPO organic ligands. Our results show that the capping of ZnO nanocrystals by different organic

molecules induces electronic and structural transformations that directly affect their magnetic behavior. It is shown that structural distortions resulting from the interactions between the organic molecules and the surface layers is one of the main factors to reducing the total magnetic moment of the capped ZnO nanoparticles.

KEYWORDS: ZnO nanocrystals. DFT. Nanostructures surface.

1 INTRODUCTION

Nanostructures surface chemistry is a very rich and ample field of research, where semiconductor and metallic quantum dots have a prominent position. Most of these systems have their sizes reduced to few nanometers, i.e., the same order or smaller than the bulk exciton Bohr radius. At this scale, quantum confinement and surface effects are significant and the electronic and optical properties will deviate considerably from those of their bulk counterparts.

The surface of these nanomaterials presents, in general, many different structural patterns. The surface atoms are usually undercoordinated and chemically different from those at the core. These dangling bonds

can promote a structural disorder at nanostructures surface as well as originate trapping charge states within their energy bandgap (AZPIROZ et al., 2015; SINGLA et al., 2009; GUGLIERI et al., 2012) Possibilities to remediate this issue involve the incorporation of inorganic shells, such as CdSe, CdTe and ZnS (WANG et al., 2010; KIM et al., 2003; TALAPIN et al., 2001), or attaching organic molecules on the surface of the nanoparticle (HINES et al., 2014).

In fact, nanoparticle surfaces are, in general, very complex, presenting unbonded orbitals, reconstructions, intrinsic defects and impurities, and bonds to ligands (TSUI et al., 2016; VOZNY, 2011). Unpaired electrons at the nanoparticle surfaces lead to highly reactive and energetically unfavorable sites. The passivation with organic ligands (also referred to as surfactants or capping agents) is of particular interest since this is a common method used to stabilize nanoparticle's surface, control the growth of some of their facets and modulate their optical properties (SINGLA et al., 2009; CHEN et al., 2016; NOH et al., 2019; GAO et al., 2019). The control of size, structure, and composition of nanoparticle surfaces can, in this sense, be explored to tune the material properties in order to have specific functionalities. Therefore, a suitable choice of the organic capping agents is crucial.

In case of semiconductors quantum dots and nanocrystals, such as CdSe, ZnS, ZnO among others, surfactants from the families of thiol, amine or phosphine are often used. The physical properties of the resulting nanoparticle (nanocrystal+capping agent) will differ, depending on the choice of the adsorbed surfactant.

The magnetic response of organic-capped oxide-nanostructures is strongly dependent on the preparation conditions. For instance, capped ZnO nanoparticles are reported to have room temperature (RT) ferromagnetism in some experiments (GARCIA et al., 2007; GHOUL et al., 2020; BOUOUDINA, 2017; SAMANTA et al., 2018), while in others no ferromagnetism was detected (KITTLSTVED, et al., 2005). These controversial results show that even small structural/electronic variations can give rise to remarkable modifications in the magnetic properties of these materials.

The use of thiol molecules as capping agents is seen to enhance the optical properties of core-shell CdSe/ZnS QDs (ZHU et al., 2014). Further, the fluorescence quantum yields of CdSe and CdTe nanocrystals is observed to be greatly influenced by the capping of their surfaces with thiol molecules (WUISTER et al., 2004).

The TOPO molecule is known to weakly bind semiconductor surfaces like CdSe (KOPPING et al., 2008). This makes this capping agent very useful in processes where a previously QD+TOPO film is photobleached with UV irradiation under patterned masks, in order to obtain QD nets in a QD+TOPO film (PARK et al., 2011).

Actually, considerable advances have been made regarding quantum confinement effects in semiconducting nanostructures, but a precise description of phenomena taking place at these surface is still missing (HINES et al., 2014; YU et al., 2006; KUZNETSOV et al., 2014; SPERLING et al., 2010; KANGO et al., 2013). Despite the importance of surface morphology and chemistry to the electronic and optical properties, much has to be known about the atomistic description of the passivation of semiconducting nanoparticles.

One case to be highlighted is the pristine ZnO nanoparticles. When the surface of this nanoparticle is passivated with amine, thiol and TOPO, different intensities of the magnetic response are observed. It is suggested that the surface rearrangement and the different passivation are the main influences to the detected magnetic behavior. In this work we explore, via first-principles simulations, the effects of the organic ligands such as thiol, amine and TOPO groups in the physical properties of ZnO nanocrystals, specially the trends in the structural, electronic and magnetic properties. Our results show that thiol and amine ligands have similar bonding properties. The TOPO ligands, on the other hand, are weakly bond and promote greater structural disorder on the ZnO surface layers. It is shown that the total magnetization will be critically dependent on the amount of passivation of the reactive sites, and on the resulting structural distortions at the ZnO surface layers.

2 COMPUTATIONAL METHODS

All calculations are performed using Density Functional Theory (DFT) (HOHENBERG et al., 1964) as implemented in the Vienna Ab-initio Package (VASP) (KRESSE et al., 1996). The Bloch functions are represented through the projected augmented wave method (PAW) (BLOCHL, 1994), with a plane-wave cutoff of 400 eV. The Perdew-Burke-Ernzerhof (PBE) (PERDEW et al., 1997) version of the generalized gradient approximation (GGA) was used to describe the exchange-correlation interactions. The GGA/PBE approach to DFT has been shown to correctly describe the adsorption of adatoms and molecules in nanostructures' surfaces (TANG et al., 2015; YU et al., 2015; CHABAN et al., 2013; BHATTACHARYA et al., 2008). Before the evaluation of physical properties, all structures were geometrically relaxed until the force components converge below 25 meV/Å. An additional single-point total energy calculation was done using the optimized structures and the PBE0 (ADAMO et al., 1999) hybrid functional in order to improve the electronic description of the systems. Repeated structures are separated by vacuum layers of at least 7 Å to avoid interactions between neighboring images.

The ZnO nanoparticle consists of a spherical cut of a zinc blende ZnO bulk, with a diameter of ~ 0.9 nm, having a Zn atom at its center, as represented in Fig. 1(a). The

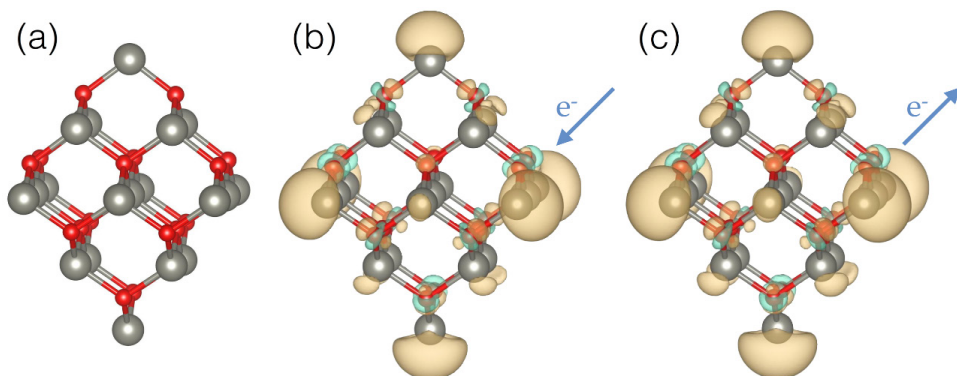
bulk-like local geometry is maintained after structural optimization, although some small changes in bond angles can occur. This system, like other nanostructured semiconducting oxides, presents a magnetization without magnetic impurities (OSORIO-GUILLEN et al., 2006; SCHOENHALZ et al., 2009; PODILA, et al., 2010). This “crude” model has many broken bonds and consequently, reactive sites at its surface.

3 RESULTS AND DISCUSSION

The modelling of organic ligands on nanoparticle surfaces is a complicated subject due to the structural complexity and the several possible binding sites and geometries. The most probable reactive sites for the attachment of organic ligands on the ZnO nanoparticle surface were found through the calculation of the electrophilic and nucleophilic Fukui functions associated with this system (PARR et al., 1989; ALLISON et al., 2013).

The electrophilic sites, which are prone to receive electrons, are identified by the charge density difference between the negatively charged and the neutral systems, i.e., $f_+ = \Delta\rho_+ = \rho_{q(+1e)} - \rho_{q(0)}$. The nucleophilic sites, which are prone to donate electrons, are obtained through the charge density difference between the neutral and the positively charged systems, i.e., $f_- = \Delta\rho_- = \rho_{q(0)} - \rho_{q(-1e)}$. In the calculation of the Fukui functions, f_+ and f_- , the charge densities of the charged systems are obtained using the equilibrium geometries of the respective neutral systems. The electrophilic and nucleophilic sites of the pristine ZnO nanoparticle are shown in Fig. 1(b), and Fig. 1(c), respectively. From the analysis of Fig. 1(b) and (c), it is possible to conclude that the surface has six expressive amphoteric symmetric sites, located on the Zn atoms at the six corners of the octahedral ZnO nanoparticle. Thus, these six amphoteric sites will be considered as the preferable ones for the adsorption of organic ligands.

Fig.1: (a) ZnO nanocrystal model with 0.9 nm of diameter. The gray and red spheres represent the zinc and oxygen atoms, respectively. (b) Isosurface identifying the electrophilic f_+ and (c) the nucleophilic f_- sites of the ZnO nanocrystal.

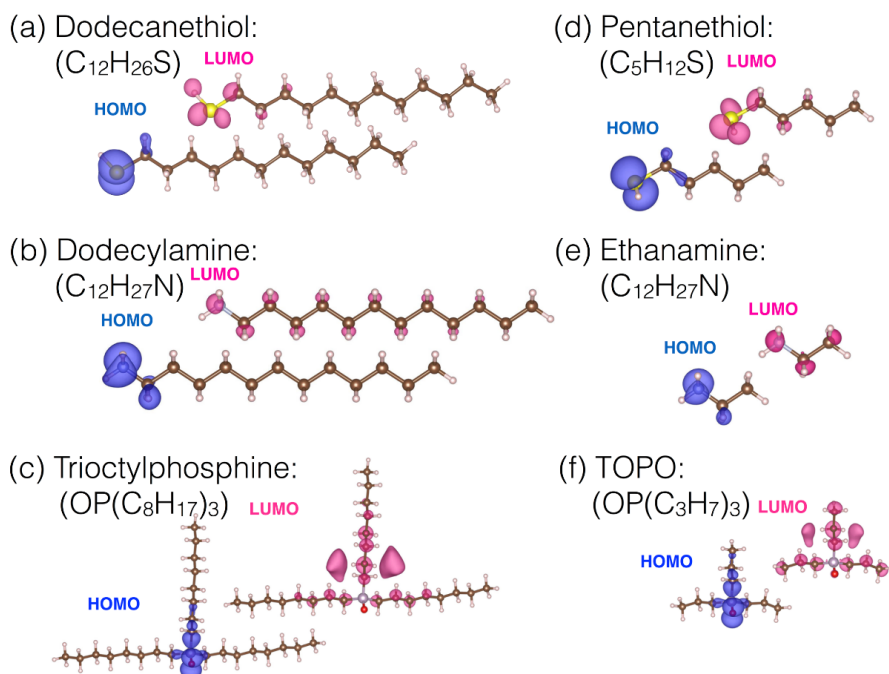


The thiol, amine, and phosphine groups are among the most common organic molecules used to cap semiconductor nanostructures, as ZnO nanocrystals (NCs) (GARCIA et al., 2007; VOZNY, 2011). Representative molecules of these groups are dodecanethiol ($C_{12}H_{26}S$), dodecylamine ($C_{12}H_{27}N$) and trioctylphosphine (TOPO ($OP(C_8H_{17})_3$)).

3.1 ORGANIC MOLECULES: THIOL, AMINE AND TOPO

In Fig. 2 (a), (b), and (c) the highest occupied (HOMO) and lowest unoccupied (LUMO) molecular orbitals are shown for each of these molecules. It can be observed that these frontier orbitals are located close to S, N and O atoms, respectively. These are the most probable regions to exchange electrons when these molecules act as functional agents. In order to reduce the computational efforts, the size of the hydrocarbon chains considered in the representative molecules has been reduced. The new representation of these molecules, now called simply as *thiol* (pentanethiol, $C_5H_{12}S$), *amine* (ethanamine, C_2H_7N), and *TOPO* ($OP(C_3H_7)_3$) as well as their respective frontier orbitals, are shown in Fig. 2(d), (e) and (f).

Fig.2: Structural model and the respective localization of HOMO and LUMO of representatives molecules of (a,d) thiol, (b,e) amine and (c,f) phosphine groups. The yellow, light blue, light purple, red, brown and light pink represents S, N, P, O, C and H atoms, respectively.



From Fig. 2 it is seen that, for the three considered molecules, the HOMO is more localized than the respective LUMO. Further, it is clear that the frontier orbitals are very similar to those for the molecules with longer hydrocarbon chains. This allows us to develop the investigation of ZnO NCs capped with thiol, amine and TOPO molecules while keeping the computational effort at a minimum.

3.2 STRUCTURAL PROPERTIES AND ENERGETICS

The results will be presented according to the number of ligands adsorbed on the ZnO NC. The studied models have one, two or six organic ligands, which will be connected to the reactive corners of the NC, as shown in Fig. 3. This allows to single-out the effects of the different number of ligands in the NC properties. Since all the reactive sites at the corners of the NC are symmetrically equivalent, the case of one adsorbed organic ligand implies in only one structural possibility. This is also true for the case of six adsorbed ligands, i.e., when there will be a ligand bonded to each reactive site in the NC. For two adsorbed ligands, there will be two non-equivalent structural possibilities: (i) when the ligands are bond to opposite sites, and (ii) when the ligands are at neighboring reactive sites in the NC. In this study, only the case (i) is considered.

Fig. 3: Representation of optimized ZnO NC capped with thiol, amine and TOPO molecules adsorbed in one, two or six amphoteric sites.

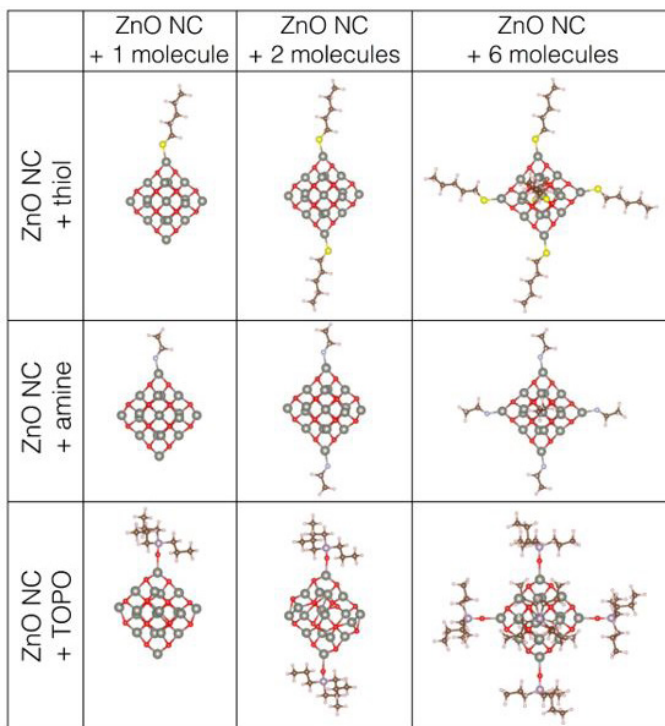
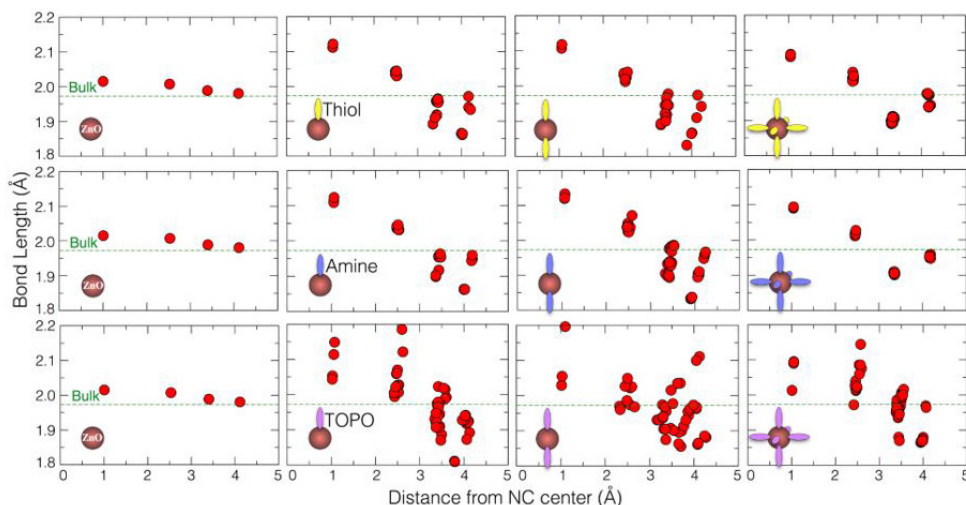


Fig. 4 presents the Zn-O bond length as a function of its distance from the center of ZnO NC. In the first column, it is possible to observe the behavior of the Zn-O bond length of the pristine NC with 35 atoms, i.e., without adsorbed molecules at its surface. It is clear from Fig. 4 that the NC has four crystalline Zn-O layers. Compared to the calculated zinc blende ZnO bulk (green dashed line), this NC has a small deviation ($\sim +0.05 \text{ \AA}$) of its degenerated bond lengths at the two inner layers, while the bond lengths at the surface (the two outer layers) are very similar to those of the bulk (1.97 \AA , PBE).

Fig. 4: Zn-O bond length as a function of the distance from the center of ZnO nanocrystal. The inset schemes represent ZnO NC (pale red sphere) with the different number of adsorbed thiol, amine and TOPO molecules (yellow, blue and violet rods, respectively).



The first, second, and third rows represent the cases for thiol, amine and TOPO ligands, respectively. As expected, ZnO nanocrystal presents structural changes when molecules are adsorbed at its surface. The bond length variation within a layer reveals structural disorder and a break of the NC symmetry. The higher the variation the greater the distortion in the NC crystallinity induced by the adsorbed molecule. A common observation of the bond lengths is that, for all cases, greater values are observed in inner layers of the nanocrystal and shorter ones at the surface, regardless the adsorbed molecule or the number of capped sites. The Zn-O bond lengths suffer higher deviations ($\sim -0.17 \text{ \AA}$ to $\sim +0.23 \text{ \AA}$), as compared to the pristine ZnO NC. The Zn atom bonded to the organic molecule is pulled outward, compared to the pristine case, reaching distances circa 4.5 \AA . This can also be identified through the angle O-Zn-O of this specific Zn atom. In the pristine case this angle is 130.1° , decreasing to 102.0° , 100.9° , and 124.5° when single molecules of thiol, amine and TOPO are adsorbed, respectively.

The second column in Fig. 4 represents the case of just one adsorbed molecule, and clearly shows that there is a more pronounced perturbation in the case of the TOPO molecule, where a Zn-O bond length variation is observed for all NC layers. For the cases where one thiol or one amine molecule is adsorbed, this perturbation is restricted to the external (or surface) layers, while the bond lengths in the internal layers remain degenerate.

In case of two TOPO adsorbed molecules, it is possible to observe a large structural deformation of the external layers, since it is not possible to clearly identify the crystalline pattern (layers of bonds), as shown in Fig. 3 and Fig. 4. When two thiol or amine molecules are adsorbed at NC, well defined layers can still be observed, although the dispersion in the bond lengths is greater than in the case of one adsorbed molecule. This loss of degeneracy is more pronounced in the external bonds, distant 2.5 Å or more from the NC center, reflecting the fact that the adsorbed molecules will perturb largely the atoms at the NC surface than those at the core.

When six molecules of thiol or amine are adsorbed to NC surface, i.e., when all the amphoteric sites are passivated, the symmetry of the system is partially recovered, presenting a less disturbed set of bond lengths in the surface. Furthermore, there are well defined layers of bonds, indicating a crystalline-like distribution, what can also be perceived in the structures of Fig. 3. In these cases, the external layer has bond lengths close to the bulk. For the case of the adsorption of six TOPO molecules, the crystalline symmetry is only partially recovered, having clearly defined layers, but presenting a variation of Zn-O bond lengths within each layer.

The distinct behavior of systems NC+TOPO is related to the different structural arrangement of this molecule: the thiol and amine molecules have a linear radical chain, while the TOPO presents a ramification in three linear radical chains. Since these chains have an umbrella-like conformation around the nanoparticle, their interaction with the NC will produce larger structural changes than thiol or amine molecules.

The adsorption energies (E_{ads}) presented in Table I are obtained for the charge-neutral nanostructured systems with one, two and six molecules adsorbed at the amphoteric sites. The E_{ads} are defined as:

$$E_{ads} = E_{ZnO+nX} - E_{ZnO} - E_{nX}$$

where E_{ZnO+nX} is the total energy of the ZnO NC with n adsorbed molecules, E_{ZnO} is the total energy of pristine ZnO NC, and E_{nX} is the total energy of nX molecules (X = thiol, amine or TOPO).

Table I: Adsorption energy (E_{ads}), charge transfer (C_T) and bond length average (d) for the ZnO+nX systems (X= thiol, amine or TOPO molecules). A positive C_T value indicates an electron transfer from the adsorbed molecules to ZnO NC.

System	% of capped sites	E_{ads} /molecule (eV)	C_T (e)	d (Å)
ZnO + 1 thiol	16	-3.20	-0.475	2.17
ZnO + 2 thiol	33	-3.22	-0.934	2.17
ZnO + 6 thiol	100	-3.16	-2.678	2.17
ZnO + 1 amine	16	-2.30	-0.555	1.86
ZnO + 2 amine	33	-2.29	-1.094	1.86
ZnO + 6 amine	100	-2.23	-3.175	1.86
ZnO + 1 TOPO	16	-1.97	0.125	1.97
ZnO + 2 TOPO	33	-1.63	0.298	1.99
ZnO + 6 TOPO	100	-0.93	0.183	2.04

The charge transfer C_T was calculated as the difference between the total charge of the nanoparticle with and without adsorbed molecules. The charge associated with each atom was obtained through the Bader charge analysis (HENKELMAN et al., 2006). Although the calculated charge transfer values can not to be directly compared with the experimental findings, they can give valuable information about the interactions between the NC and the thiol, amine, and TOPO molecules, as a function of the type and number of adsorbed molecules.

For one adsorbed thiol molecule (16% coverage of the amphoteric sites) the as-formed S-Zn bond length is 2.17 Å, which is lower than in the ZnS bulk (2.34 Å) (MADELUNG et al, 1982). For this case, the adsorption energy is -3.20 eV and the charge transfer from the ZnO nanoparticle to the thiol is 0.475 e (Table I). It is observed that, although being the ligand with the highest binding energy, the thiol molecule itself does not present severe structural changes. However, its adsorption can induce structural deformations at the surface and the inner structure of the nanoparticle. The same analysis is valid for the amine, with a N-Zn bond length of 1.86 Å. The adsorption energy of a single amine molecule is -2.30 eV, with a charge transfer of 0.555 e from the ZnO NP to the molecule. Although the larger bond length of S-Zn, as compared to N-Zn, the adsorption energies reveals a stronger interaction between the thiol molecule and the ZnO NC. The O-Zn bond distance is 1.97 Å, and the adsorption energy is -1.97 eV, with the TOPO being the weakly bonded molecule among those studied here. This is in agreement with previous results that showed that thiol has the strongest bond to semiconductor nanoparticles, with amine having intermediate values, and TOPO the weakest one (SPERLING et al.,

2010). This behavior is also valid for the charge transfer amount, being smaller for TOPO as compared to thiol and amine. It is observed from Table I that while thiol and amine act as electron acceptors, the TOPO molecule behaves as an electron donor. Previous studies suggest that, for low concentrations of TOPO in toluene, these molecules could behave as a Lewis base toward the semiconductor surface (LORENZ et al., 1998) which would explain the positive C_7 values in Table I. When the number of adsorbed molecules at the surface increases, the adsorption energy per molecule decreases.

Considering the thiol, amine, and TOPO molecules interacting with the ZnO NC, it can be seen that the number of dangling bonds is one at the S atom, two at the N atom, and none at O. For each bond formed between the S or the N atoms and the ZnO NC, approximately half an electron will be transferred from the NC to thiol and amine molecules, respectively. These transferred charges will participate in (partially ionic) S-Zn and N-Zn bonds. This S-Zn chemical bond will saturate the S dangling bond. However, the N atom at the amine will remain with an unbounded electron. It will result in a net magnetic moment at the N atom. The O atom at the TOPO molecule, on the other hand, has no electrons to be shared, and the TOPO molecule is seen to donate electrons to ZnO NC, in agreement with the experimentally observed behavior (LORENZ et al., 1998).

3.3 ELECTRONIC PROPERTIES AND MAGNETIC PROPERTIES

The density of states (DOS) for the pristine nanocrystal is exhibited in Fig. 5, and can be considered as a reference for the cases where the interaction with external molecules is taken into account.

Fig. 5: Density of states (DOS, black line) of a pristine ZnO NC, obtained by a Gaussian convolution of $\sigma = 0.01$ eV of the individual energy levels (gray lines). The inset presents the structure with the correspondent plot of the spin density ($\Delta\rho = \rho_{\uparrow} - \rho_{\downarrow}$) isosurface in orange.

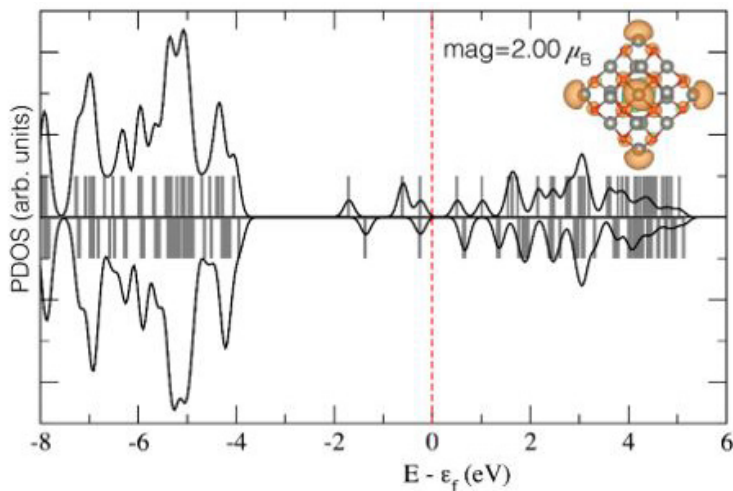


Fig. 6 and Fig. 7 show that the capping of the NC with any number of thiol and amine molecules results in energy levels close to the chemical potential, with contributions coming from both NC surface and adsorbed molecules. When the NC is capped with thiol molecules, the unpaired spin polarized electrons come from the NC, with no contribution from the molecule levels. On the other hand, for amine capped NCs, the spin polarized levels have contributions from both NC surface and the amine molecules.

Fig. 6: Density of states (DOS, black line) of ZnO NC, obtained by a Gaussian convolution of $\sigma = 0.01$ eV of the individual energy levels (gray lines), with (a) one, (b) two, and (c) six amphoteric sites functionalized by thiol molecules. The yellow lines are the PDOS on the thiol molecule(s). The right panels present structures with the correspondent plot of the spin density ($\Delta\rho$) isosurface in orange.

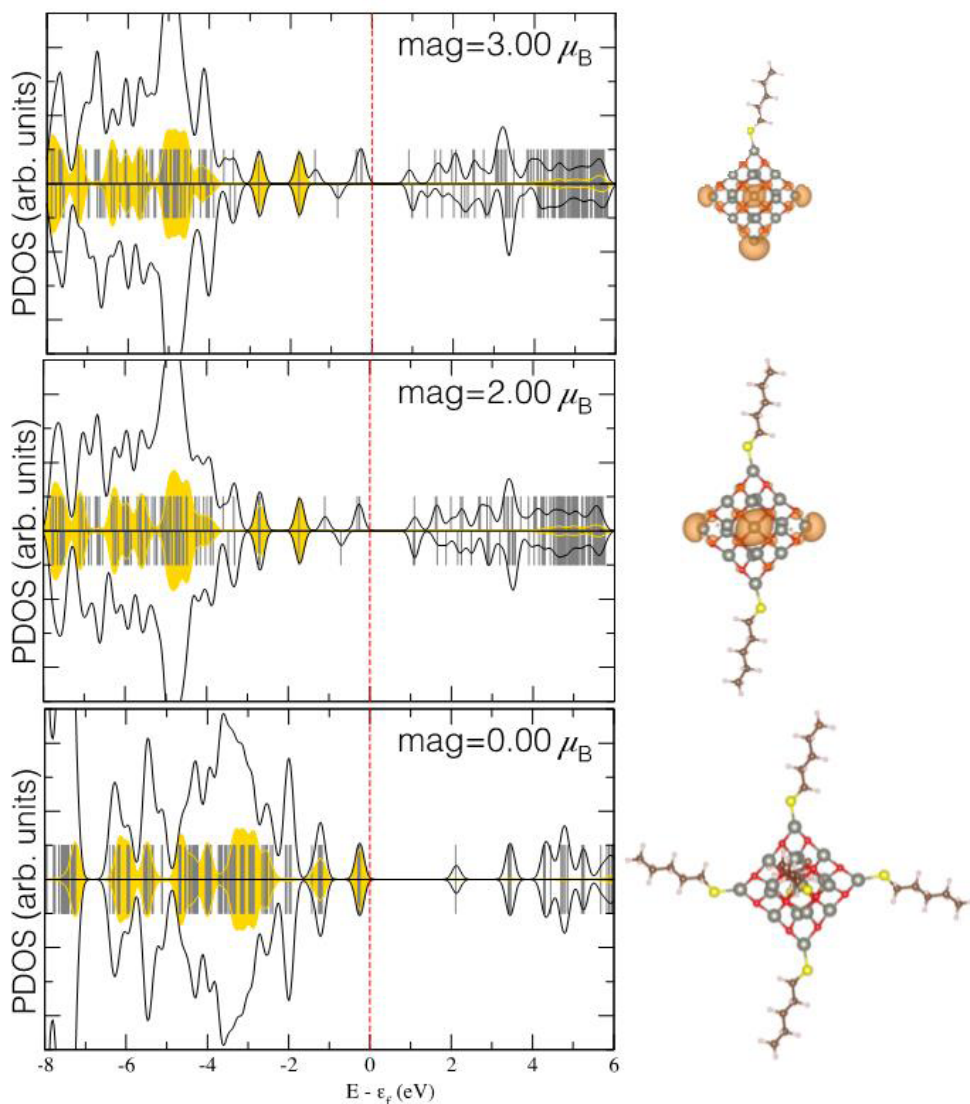
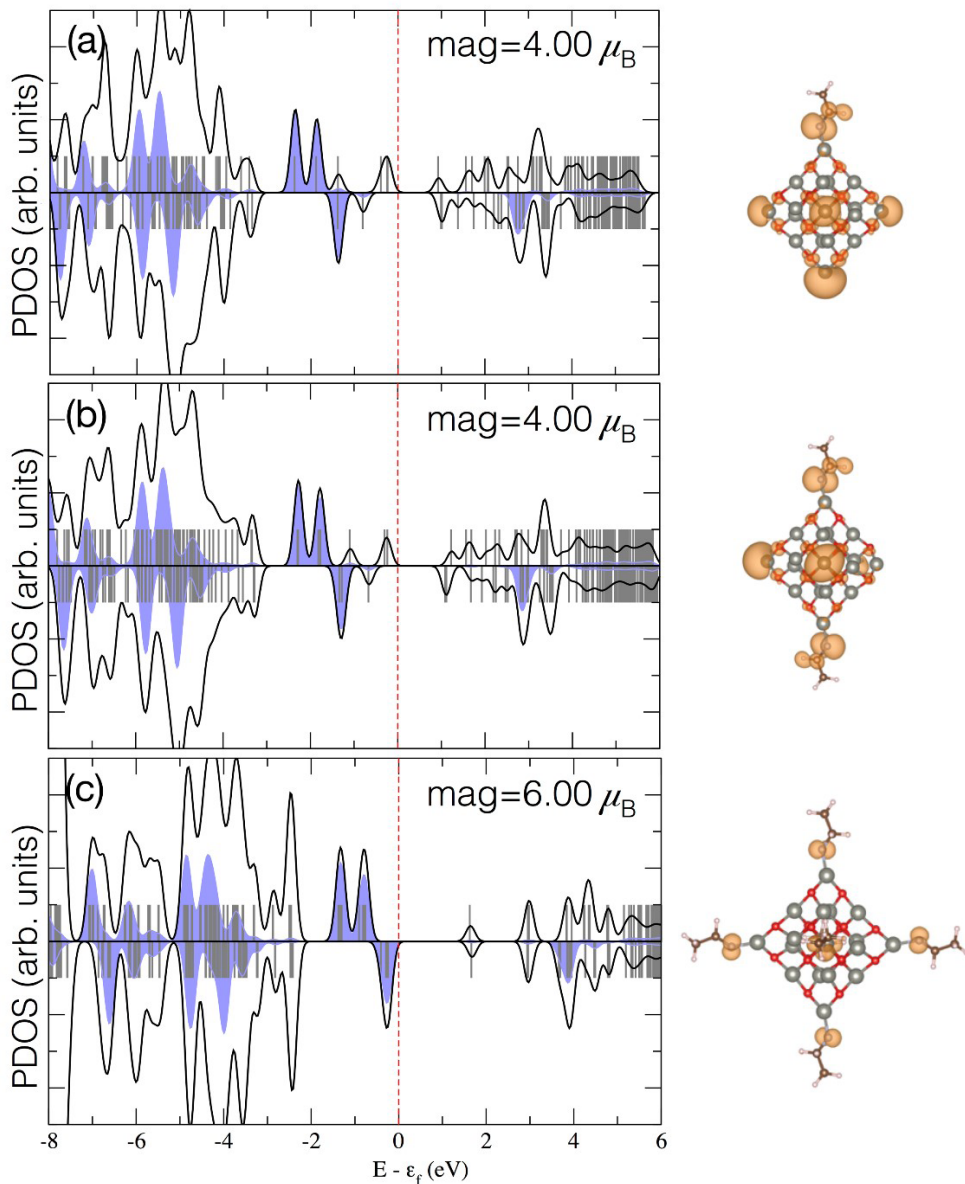


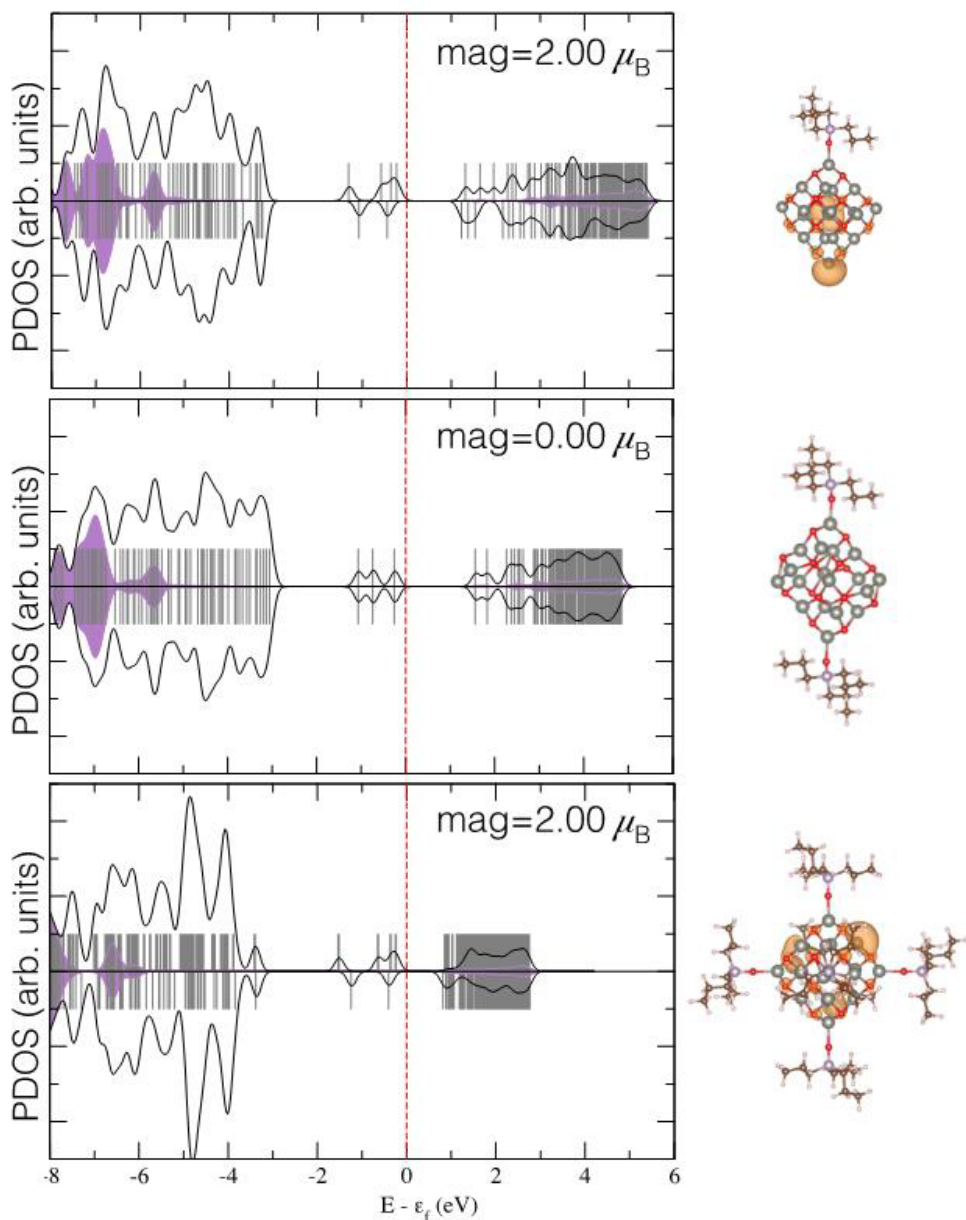
Fig. 7: Density of states (DOS, black line) of ZnO NC, obtained by a Gaussian convolution of $\sigma = 0.01$ eV of the individual energy levels (gray lines), with (a) one, (b) two, and (c) six amphoteric sites functionalized by amine molecules. The pale blue lines are the PDOS on the amine molecule(s). The right panels present structures with the correspondent plot of the spin density ($\Delta\rho$) isosurface in orange.



The PDOS at Fig. 8 shows that, contrarily to thiol and amine cases, the capping with TOPO molecules leads to levels close the chemical potential coming only from the NC, with the TOPO energy levels appearing deeper in energy. These results are in agreement with those reported by Garcia et al. (2007), who concludes that TOPO capped ZnO nanoparticles have an electronic configuration that is similar to the ZnO bulk.

The surface states at the corners of the pristine NC have a net magnetic moment. Five corners contribute with $+0.5 \mu_B$ and one with $-0.5 \mu_B$, leading to a total magnetization of $2.0 \mu_B$. Similar results have been experimentally and theoretically reported for several nanostructured oxide semiconductors (PODILA, et al., 2010).

Fig. 8: Density of states (DOS, black line) of ZnO NC, obtained by a Gaussian convolution of $\sigma = 0.01$ eV of the individual energy levels (gray lines), with (a) one, (b) two, and (c) six amphoteric sites functionalized by TOPO molecules. The violet lines are the PDOS on the TOPO molecule(s). The right panels present structures with the correspondent plot of the spin density ($\Delta\rho$) isosurface in orange.



The partial passivation of the amphoteric sites from the pristine NC with thiol, amine, and TOPO functional groups results in highest occupied electronic levels (HOMO) that are singly-occupied and located at the NC surface. The spin polarization of the HOMO states can explain the magnetization of the capped ZnO NC. An exception to this behavior is observed for the case of the NC capped with two TOPO molecules. For this specific case, a large structural deformation of the two outermost layers is clearly seen in Fig. 4, leading to the vanishing of the localized surface magnetic moments.

It is interesting to observe that the total magnetization of the ZnO NC increases from $2.00 \mu_B$ to $3.00 \mu_B$ when one thiol molecule is adsorbed on its surface. It occurs due to a charge (spin) localization when the symmetry of the system is reduced, as a consequence of the interaction with one thiol molecule. Taking the corner where the thiol molecule is adsorbed as a reference, it is seen that the four first-neighbor corners have magnetic moments of $0.5 \mu_B$, while the opposite corner has $1.0 \mu_B$. When two thiol molecules are adsorbed at opposite sites of the NC, the total magnetization will be reduced from $3.00 \mu_B$ to $2.00 \mu_B$. In the case of six thiol adsorbed molecules, the original ZnO NC symmetry is partially recovered, and the total magnetization is zero because all the reactive sites at the corners of NC are saturated.

Comparing Fig. 6 and Fig. 7, (a) and (b), it is observed that the magnetization of the NCs capped with one and two thiol and amine molecules differ by $1.00 \mu_B$ and $2.00 \mu_B$, respectively. It is due to the resulting magnetic moments at the N atoms of the adsorbed amine molecules. The evidence of a localized magnetic moment of $1.00 \mu_B$ at N atoms is made clearer when considering the NC capped with six thiols and six amine molecules. The total magnetization of the NC+6X systems is equal to $0.0 \mu_B$ or $X = \text{thiol}$, and $6.0 \mu_B$ for $X = \text{amine}$. Differently from the partial passivation with two thiol molecules, the magnetic moments for the case where two amine molecules are adsorbed will not be equally distributed among the remaining (four) unsaturated amphoteric sites. This happens because the interaction with two amine molecules induces greater structural changes at two of the unsaturated reactive sites, with a resulting spin concentration ($1.0 \mu_B$) at the two structurally less perturbed sites, as can be seen in Fig. 7(b). It is important to point out that, in the case of amine, one electron will remain unpaired at the N atom, even after the N-Zn bonding is formed. This unpaired electron leads to net magnetic moments at the N atoms. Hence, if this dangling bond is saturated by, e.g., one H atom, the magnetic moments at the N atoms will vanish, which would probably lead to equal magnetizations for the ZnO NCs capped with the same number of thiol and amine molecules.

The interaction between the ZnO NC with TOPO molecules show a different behavior, as compared with those for thiol and amine cases. It has already been revealed

through the values of binding energies and charge transfers. The radical chains in the TOPO molecule are closer to the NC surface than those present at the thiol and amine molecules. This structural proximity will promote greater distortions in the NC external layers, as is clearly seen at Fig. 4. As already discussed, structural distortions lead to less symmetric structures and, consequently, to lower values of total magnetization.

For the case of one adsorbed TOPO molecule, three of the unsaturated corners will show greater deviations for the crystalline pattern, while two remaining corners showing structures that are more similar to those at the pristine NC. This leads to a concentration of the spin density on these two less disturbed corners, each one with a magnetic moment of $1.0 \mu_B$. The adsorption of two TOPO molecules induces structural distortions of the two outer layers of the NC, as shown in Fig. 4. This leads to a total magnetization equal to zero. It shows that the maintenance of the crystalline structural pattern is important for the spin density concentration and a resulting magnetization of the system. When six TOPO molecules are adsorbed by the NC, the structural ordering of the outer two layers of the NC is partially recovered (see Fig. 4). As a consequence, a net magnetization of $2.0 \mu_B$ is obtained. However, the spin density on the NC surface has no defined pattern, showing a random distribution.

This direct relationship between the surface structural distortion of the capped NCs and its resulting magnetization is in agreement with experimental findings of Garcia et al., which measured the magnetic responses of pristine ZnO NCs capped with thiol, amine and TOPO molecules. The authors show that the magnetization magnitudes of the capped NCs show the following order: thiol capped NC > amine capped NC > TOPO capped NC. As has been pointed out, the thiol capped ZnO NCs have the lowest structural distortions, and the TOPO capped NCs the largest. The amine capped NC exhibiting intermediate surface structural distortions.

4 CONCLUSIONS

In conclusion, first principles DFT calculations have been used to systematically investigate the structural, electronic, energetic and magnetic properties of nX -capped ZnO nanocrystals (n is the number of molecules, X = thiol, amine or TOPO). When capped with thiol and amine molecules, a charge transfer from the ZnO NC to the adsorbed molecules is determined, and strong (partially ionic) chemical bonds are formed. On the other hand, a relatively weak bond is observed between the TOPO molecule and the NC, with electrons being transferred from TOPO to the NC. The valence states close to the chemical potential show contributions from both the NC and the organic molecules for the NC+thiol and

NC+amine systems. However, only the NC contributes to the levels close to the chemical potential for the NC+TOPO compound. The structural distortions appearing at the surface layers of the NC, due to the interactions with the organic molecules, are larger for TOPO than for amine, while are lower for thiol molecules. The resulting magnetization of these NC+molecules systems is seen to be related to the level of structural distortions of the NC surface layers as well as the saturation of the active adsorption sites at the NC surface, with greater magnetic moments for thiol and amine than for TOPO. These results provide atomistic explanations for the puzzling experimental findings, relating the structural and the magnetic properties of these oxides with their resulting magnetic moments.

5 ACKNOWLEDGMENTS

This study was financed by the Coordenação de Aperfeiçoamento de Pessoal de Nível Superior – Brasil (CAPES) – Finance Code 001. P. C. P. is thankful to the Conselho Nacional de Desenvolvimento Científico e Tecnológico - CNPq - Grant n° 312388/2018-7. The Calculations were performed using the Brazilian computational facilities of CENAPAD/Campinas, and CPAD/UFSM.

REFERENCES

- ADAMO, C.; BARONE, V. **Toward reliable density functional methods without adjustable parameters: The PBE0 model.** J. Chem. Phys., 1999, v. 110, p. 6158.
- ALLISON, T. C.; TONG, Y. J. **Application of the condensed Fukui function to predict reactivity in core-shell transition metal nanoparticles.** Electrochimica Acta, 2013, v. 101, p. 334.
- AZPIROZ, Jon M.; DE ANGELIS, Filippo. **Ligand Induced Spectral Changes in CdSe Quantum Dots.** ACS Appl. Mater. Interfaces, 2015, v. 7, p. 19736.
- BHATTACHARYA, S. Kr.; KSHIRSAGAR A. **First principle study of free and surface terminated CdTe nanoparticles.** Eur. Phys. J. D., 2008, v. 48, p. 355.
- BLOCHL, P. E. **Projector Augmented-Wave Method.** Phys. Rev. B, 1994, v. 50, p. 17953.
- BOUOUDINA, M. et al. **Structural and magnetic properties and DFT analysis of ZnO:(Al,Er) nanoparticles.** RSC Adv., 2017, v. 7, p. 32931.
- CHABAN, V. V.; PREZHDO, V. V.; PREZHDO, O. V. **Covalent Linking Greatly Enhances Photoinduced Electron Transfer in Fullerene-Quantum Dot Nanocomposites: Time-Domain Ab Initio Study.** J. Phys. Chem. Lett., 2013, v. 4, p. 1.
- CHEN, J. et al. **Ultrafast Photoinduced Interfacial Proton Coupled Electron Transfer from CdSe Quantum Dots to 4,4-Bipyridine.** J. Am. Chem. Soc., 2016, v. 138, p. 884.
- GAO, S. et al. **Creation of passivated Nb/N p-n co-doped ZnO nanoparticles and their enhanced photocatalytic performance under visible light illumination.** J. Mater. Sci. Technol., 2019, v. 35, p. 610.

- GARCIA, M. A. et al. **Magnetic Properties of ZnO Nanoparticles.** Nano Letters, 2007, v. 7, p. 1489.
- GHOUL, J. EI; AL HARBI, F. F. **Synthesis, structural, optical and magnetic properties of Gd co-doped ZnO:V nanoparticles.** Solid State Commun., 2020, v. 314, p. 113916.
- GUGLIERI, C. et al. **XMCD Proof of Ferromagnetic Behavior in ZnO Nanoparticles.** J. Phys. Chem. C, 2012, v. 116, p. 6608.
- HENKELMAN G.; ARNALDSSON, A.; JONSSON, H. **A fast and robust algorithm for Bader decomposition of charge density.** Comput. Mater. Sci., 2006, v. 36, p. 254.
- HINES, Douglas A.; KAMAT, Prashant V. **Recent Advances in Quantum Dot Surface Chemistry.** ACS Appl. Mater. Interfaces, 2014, v.6, p. 3041.
- HOHENBERG, P.; KOHN, W. **Inhomogeneous Electron Gas.** Phys. Rev., 1964, v. 136, p. B864.
- KANGOVA, S. et al. **Surface modification of inorganic nanoparticles for development of organic-inorganic nanocomposites: A review.** Progress in Polymer Science, 2013, v. 38, p. 1232.
- KIM, S. et al. **Type-II Quantum Dots: CdTe/CdSe(Core/Shell) and CdSe/ZnTe (Core/Shell) Heterostructures.** J. Am. Chem. Soc., 2003, v. 125, p. 11466.
- KITTILSTVED, K. R.; GAMELIN, D. R. **Activation of High-TC Ferromagnetism in Mn²⁺-Doped ZnO using Amines.** J. Am. Chem. Soc., 2005, v. 127, p. 5292.
- KOPPING, J. T.; PATTEN, T. E. **Identification of Acidic Phosphorus-Containing Ligands Involved in the Surface Chemistry of CdSe Nanoparticles Prepared in Tri-N-octylphosphine Oxide Solvents.** J. Am. Chem. Soc., 2008, v. 130, p. 5689.
- KRESSE, G.; FURTHMULLER, J. Efficient iterative schemes for ab initio total-energy calculations using a plane-wave basis set. Phys. Rev. B, 1996, v. 54, p. 11169.
- KUZNETSOV, Aleksey E.; BERATAN, David N. Structural and Electronic Properties of Bare and Capped Cd₃₃Se₃₃ and Cd₃₃Te₃₃ Quantum Dots. J. Phys. Chem. C, 2014, v. 118, p. 7094.
- LORENZ, J. K.; ELLIS, A. B. **Surfactant-Semiconductor Interfaces: Perturbation of the Photoluminescence of Bulk Cadmium Selenide by Adsorption of Tri-n-octylphosphine Oxide as a Probe of Solution Aggregation with Relevance to Nanocrystal Stabilization.** J. Am. Chem. Soc., 1998, v. 120, p. 10970.
- MADELUNG, O.; SCHULZ, M.; WEISS, H. **Semiconductors, Physics of Group IV Elements and III-V Compounds.** New Series, Group III. New York: Springer-Verlag, 1982, v. 17.
- NOH, K. et al. **Effect of ethanolamine passivation of ZnO nanoparticles in quantum dot light emitting diode structure.** Curr. Appl. Phys., 2019, v. 19, p. 998.
- OSORIO-GUILLEN, J. et al. **Magnetism without Magnetic Ions: Percolation, Exchange, and Formation Energies of Magnetism-Promoting Intrinsic Defects in CaO.** Phys. Rev. Lett., 2006, v. 96, p. 107203.
- PARK, Y.; FELIPE, M. J.; ADVINCULA, R. C. **Facile Patterning of Hybrid CdSe Nanoparticle Films by Photoinduced Surface Defects.** ACS Appl. Mater. INTERFACES, 2011, v. 3, p. 4363.
- PARR, Robert G.; YANG, Weitao. **Density-Functional Theory of Atoms and Molecules.** Oxford: Oxford University Press, 1989.

- PERDEW, J. P.; BURKE, K.; ERNZERHOF, M. **Generalized Gradient Approximation Made Simple.** Phys. Rev. Lett., 1997, v. 77, p. 3865.
- PODILA, R. et al. **Origin of FM Ordering in Pristine Micro- and Nanostructured ZnO.** Nano Letters, 2010, v. 10, p. 1383.
- SAMANTA, A.; GOSWAMI, M. N.; MAHAPATRA, P. K. **Magnetic and electric properties of Ni-doped ZnO nanoparticles exhibit diluted magnetic semiconductor in nature.** J. Alloy Compd., 2018, v. 730, p. 399.
- SCHOENHALZ, A. L. et al. **Surface magnetization in non-doped ZnO nanostructures.** Appl. Phys. Lett., 2009, v. 94, p. 162503.
- SINGLA, M. L.; SHAFEEQ M., M.; KUMAR, M. **Optical characterization of ZnO nanoparticles capped with various surfactants.** Journal of Luminescence, 2009, v. 129, p. 434.
- SPERLING, R. A.; PARAK, W. J. **Surface modification, functionalization and bioconjugation of colloidal inorganic nanoparticles.** Phil. Trans. R. Soc. A, 2010, v. 368, p. 1333.
- TALAPIN, D. V. et al. **Highly Luminescent Monodisperse CdSe and CdSe/ZnS Nanocrystals Synthesized in a Hexadecylamine-Trioctylphosphine Oxide-Trioctylphosphine Mixture.** Nano Letters, 2001, v. 1, p. 207.
- TANG, Y. et al. **Geometric stability, electronic structure, and intercalation mechanism of Co adatom anchors on graphene sheets.** J. Phys.: Condens. Matter, 2015, v. 27, p. 255009.
- TSUI, E. Y.; HARTSTEIN, K. H.; GAMELIN, D. R. **Selenium Redox Reactivity on Colloidal CdSe Quantum Dot Surfaces.** J. Am. Chem. Soc., 2016, v. 138, p. 11105.
- VOZNYI, Oleksandr. **Mobile Surface Traps in CdSe Nanocrystals with Carboxylic Acid Ligands.** J. Phys. Chem. C, 2011, v. 115, p. 15927.
- WANG, Jing; HAN, Heyou. **Hydrothermal synthesis of high-quality type-II CdTe/CdSe quantum dots with near-infrared fluorescence.** Journal of Colloid and Interface Science, 2010, v. 351, p. 83.
- WUISTER, S. F.; DONEGA, C. M.; MEIJERINK, A. **Influence of Thiol Capping on the Exciton Luminescence and Decay Kinetics of CdTe and CdSe Quantum Dots.** J. Phys. Chem. B, 2004, v. 108, p. 17393.
- YU, M. et al. **First principles study of CdSe quantum dots: Stability, surface saturations, and experimental validation.** Appl. Phys. Lett., 2006, v. 88, p. 231910.
- YU, X.-f. et al. **Monolayer Ti₂CO₂: A Promising Candidate for NH₃ Sensor or Capturer with High Sensitivity and Selectivity.** ACS Appl. Mater. Interfaces, 2015, v. 7, p. 13707.
- ZHU, H. et al. **Synthesis and Optical Properties of Thiol Functionalized CdSe/ZnS (Core/Shell) Quantum Dots by Ligand Exchange.** J. Nanomater., 2014, v. 2014, p. 324972.

CHAPTER 4

CONFINED WATER CHEMISTRY: THE CASE OF NANOCHANNELS GOLD OXIDATION

Data de submissão: 10/05/2021

Data de aceite: 28/05/2021

André Mourão Batista

Universidade Federal do ABC
Programa de Pós-Graduação em
Nanociências e Materiais Avançados
Santo André/SP.

<http://lattes.cnpq.br/6371655865302362>

Herculano da Silva Martinho

Universidade Federal do ABC
Departamento de Física - Santo André/SP.
<http://lattes.cnpq.br/6880602655569729>

ABSTRACT: Confined and interstitial water have a key role in several chemical, physical and biological processes. It is remarkable that many aspects of water behavior in this regime (e.g., chemical reactivity) remain obscure and unaddressed. In particular for gold surfaces, results from simulations indicated that the first wetting layer would present hydrophilic behavior in contrast to the overall hydrophobic character of the bulk water on this surface. In the present work we investigate the properties of confined water on Au <111> nanochannels. Our findings, based on a large set of morphological, structural, and spectroscopical experimental data and ab-initio computer simulations strongly supports the hypothesis of

hydrophilicity of the first wetting layer of Au <111> surface. A unique oxidation process was also observed in the nanochannels driven by confined water. Our findings indicated that the oxidation product is Au (OH)₃. Therefore, the Au surface reactivity against confined water needs to be considered for nanoscopic applications as, e.g., catalysis in fine chemicals, pharmaceuticals, and the food industry green processes.

KEYWORDS: Nanolithography. Confined water. Oxidation.

1 INTRODUCTION

1.1 CONFINED WATER

It is well-known that the distinction between gas and liquid disappears above its critical point. (Ferreira et al., 2015) At pressure and temperature above this point, the system becomes a supercritical fluid (McMillan; Stanley, 2010). Supercritical fluids are recognized as possessing unique solvation properties that make them important technological materials (McMillan; Stanley, 2010). Of particular interest is the behavior of water in confined spaces. For example, it plays a key role in protein hydration since nanoscale fluctuations associated with the so-called Widom line can influence biological processes (Chu et al., 2009; Frenkel, 2002).

In fact, confined and interfacial water is very important in chemical, physical, and biological processes. However, many of its properties in confinement remain unanswered. For this reason, it is relevant to probe how geometric confinements and surface interactions affect the properties of bulk water as well as the substrates containing it. (Brovchenko; Oleinikova, 2008; Swenson, 2004) In general, water is not in its bulk form, it is often bound to some substrates, or filling small cavities. Like, for example, water in porous media, as if it were in rocky interstices, and also water as biological material inside cells or bound to the surface of macromolecules and membranes. This is what is defined as confined waters. (Castrillón et al., 2009) Understanding the behavior of confined water at the nanoscale is also relevant to the very important problem of protein stability, transport in ion channels, nano-fluid devices and the thermodynamics of colloidal assemblies (Coudert et al., 2009). This fact highlights the relevance of advancing the understanding of the chemical reactivity of water in contact with these metals, a fact that goes far beyond direct applications in corrosion processes in industry and in transformation processes.

Therefore, several studies have been carried out to investigate the structure and dynamics of water in diverse systems such as biological environments, (Berntsen et al., 2005) nanoporous silica matrices, (Liu et al., 2005; Faraone et al., 2004) vermiculites, (Bergman; Swenson, 2000) molecular sieves, (Swenson et al., 2005) and organic coatings (Philippe et al., 2004).

Proteins, in particular, have many of their properties governed by interactions with water (Raschke, 2006). This, for example, establishes and shapes the panorama of free energy that governs the activity, structure, stability and tertiary and quaternary structures of proteins (Halle, 2004). In fact, a certain amount of water is necessary for the biological activity of all proteins. Even apparently dry enzymes in the presence of gaseous substrates do not show activity in the absence of water (Lind et al., 2004). This intriguing evidence depends on how the water molecules arrange themselves on the molecular scale. Thus, the explicit inclusion of water is essential in solving many biochemical problems. In addition, water, between molecular surfaces, induces different behaviors than those observed in bulk water (Steitz et al., 2003; Jensen et al., 2003; Schwendel et al., 2003), although there is no consensus in this aspect (Yaminsky; Ohnishi, 2003).

1.2 NANOLITHOGRAPHY

This type of manipulation is essential to work in orders of magnitude around 100 nm (Bitton; Frydman, 2006; Binnig et al., 1999). Currently, several studies related to nanolithography are being developed, including local oxidation of silicon and metal surfaces (Edwards et al., 2020; Kim et al., 2020; Chau et al., 2019). Nanolithography via

Atomic Force Microscopy (AFM) has the ability to move a probe over a specific sample surface in a controlled manner, by controlling this applied normal force (F_n) between the probe and the sample surface, thus forming silicon channels (Jirlèn et al., 2017), oxides (Melgarejo et al., 2020), polymers (Stoica; Barzic; Hulubei, 2017), magnetic materials and semiconductors (Celano, 2019).

For making the channels on a Si surface, an AFM tip with high wear resistance is required. Thus, Ogino et al. (Ogino; Nishimura; Shirakashi, 2008) studied a material capable of better resisting the effects of wear, reaching the conclusion of the use of the diamond, despite being expensive. In this way they developed a film of DLC (Diamond-Like Carbon), to coat the tip that is used conventionally of Si_3N_4 . The DLC film is an amorphous film with high hardness, high modulus of elasticity, low coefficient of friction and wear, and good tribological properties, being cheaper than a solid diamond tip. (Huang; Jeng; Liu, 2007) In nanolithography, the AFM tip acts as a cutting tool to remove nanoscale materials from the sample to create different types of grooves or trenches. The groove geometry is normally controlled by the normal applied force (F_n) of the applied tip through deflection of the AFM cantilever. To form desired scratched profiles, the grooves can be overlapped by repeated stripes, forming two- and three-dimensional structures, by different repetition and overlapping techniques.

1.3 METALS AND OXIDATION

Metals and metal ions are important inorganic cofactors for biological activity (Berg, 1994). In addition, it is estimated that approximately half of all known proteins contain a metal and that half of that amount only performs its function due to its presence Thomson; Gray, 1998; Waldron; Robinson, 2009). These are called metalloproteinases, which perform several functions in cells, such as storage and transport of proteins, enzymes and signal transducer proteins as well as the important role in infectious diseases (Carver, 2013). As examples we can mention the role of $\text{Fe}^{+2} / \text{Fe}^{+3}$ ions in the transport of oxygen via hemoglobin (Hsia, 1998) and $\text{Cu}^{+2} / \text{Cu}^{+3}$ ions in the superoxide dismutase enzyme (Kitajima et al., 1992). The action of these metal ions always occurs in an aqueous medium, where in general the water is in a confined regime.

In particular, some works addressed the issue of corrosion processes and metal reactivity under the action of confined water. Azmat et al. (Azmat et al., 2011) investigated the corrosion of Zn surfaces due to acidified droplets (diameter $\sim 0.1 - 5 \mu\text{m}$). They concluded that the process is dependent on the initial volume of aerosols, oxygen diffusion, surface area to volume ratio and likely the micro-structural features of the underlying metal. Xia et al. (Xia et al., 2006) investigated the corrosion characteristics of micro and nano-particles

of Cu in distilled water by measuring the absorbance and structure of corrosion products using X-Ray Diffraction (XRD) and Scanning Electron Microscopy (SEM). They concluded that corrosion products of micro-particles increase slowly with increasing immersion time. However, for Cu nano-particles its products increase rapidly with increasing immersion time. Liu et al. (Liu, 2013) investigated the de-hydrogenation on the oxygen-covered surface for Au <100>. They found that the energy barrier of decomposing water strongly reduces the surface of atomic Au covered with oxygen and the O atom can promote dehydration of the H₂O molecule.

These studies have important technological implications. In fact, Au/oxide catalysts are widely used in important processes, such as partial oxidation of hydrocarbons, hydrogenation of unsaturated hydrocarbons and CO oxidation. (Hussain; Shah, 2014; Takei et al., 2010) Investigations have shown that Au provides catalytically active systems, whereas selectivity and re-usability are advantages over non-catalyzed organic transformations. (Shahzad et al., 2017) Schryer et al. (Schryer et al., 1989) reported that these Au catalysts show increasing activity in the presence of water, unlike other traditional metal oxide catalysts.

In fact, the water: Au surface reactivity at nanoscale is a challenging issue. In the present paper we investigated the oxidation of Au by confined water at nanochannels of variable dimensions produced by nanolithography. The physical-chemical process occurring in the channels were analyzed by high resolution morphological (atomic force microscopy and scanning electron microscopy), structural (X-Ray diffraction, nuclear magnetic resonance), molecular spectroscopy (Fourier-Transform infrared absorption, Raman), and elemental analysis (X-Ray photoelectron spectroscopy) techniques. *Ab-initio* density functional calculations were also performed aiming to furnish possible molecular scenarios to interpret the experimental data.

2 MATERIAL AND METHODS

2.1 AU METALLIC THIN FILMS

High purity Au (99.99%) was sputtered and deposited on Si substrate (275 μm thick, <100> orientation, N/P type, from UniversityWafer, Inc.). The Si substrates were cleaned before Au deposition following a three steps sonication washing in:

- (i) 50/50 solution of Extran detergent and isopropyl alcohol;
- (ii) isopropyl alcohol;
- (iii) deionized water.

The washing time in each step was 30 minutes. The deposition was performed on a Leica EM ACE600 sputter coater equipped with quartz crystal for determination of

the thin film layer thickness. The thicknesses of produced films were 10, 50, 100, 302 and 600 nm.

2.2 SPUTTERING

Physical Vapor Deposition (PVD) consists of a group of deposition techniques, which have in common the fact that they allow material transport in the solid state between the target material and the substrate to be coated. The process takes place in a rarefied chamber. Among the main PVD techniques, evaporation and sputtering can be highlighted. Sputtering is a process very similar to thermal evaporation because it takes material from one place to another, but here there is the presence of an inert gas plasma (usually ionized argon) that ejects material from a metallic target by bombarding particles with high energy. The difference consists in a non-heating of the source (Ohring, 2001).

The advantages of this type of deposition in relation to evaporation is the uniformity of the film obtained, more precise control of thickness, control of the properties of the film such as grain structure and step covering, and also the deposition of multi layers with the use of targets. However, the disadvantages are: high cost of the equipment, deposition rate for some materials can be very low, some materials may suffer degradation due to high energy bombardment, and as the process is carried out at higher pressures than evaporation, an incorporation may occur impurities to the deposited film.

Basic Principles

The sputtering process begins with the chamber, already in a vacuum, being filled with inert gas at a low pressure (Petty, 2008). A high voltage electric field is created between the fixture of the part to be covered and a negative electrode (the metal target that serves as an atom donor), the positively charged gas ions are attracted by the negative metal electrode and are accelerated in their direction, transferring their kinetic energy to the metal atoms upon reaching the target, allowing the metal atoms to be ejected and then the substrate to be covered is bombarded by the ejected atoms and is coated with a thin metallic layer (Venables, 2000).

2.3 ATOMIC FORCE MICROSCOPY (AFM)

Atomic Force microscopy has proven to be a very versatile and multifunctional tool with regard to science and technology, since its creation in the 1980s. Many advances in instrument technology have been achieved, even though they still have their side of limitations, such as relatively slow speeds and restricted area (Shinato; Huang; Jin, 2020; Gómez-Varela et al., 2020; Dufrêne et al., 2021).

When considering its advantages and in relation to other related technologies, we have its ultra high capacity for spatial resolution and ultra low forces exerted on the surface (ranging from 10^{-6} to 10^{-11} N) and other unique features, including the cost of equipment, relatively easy operation and control. AFM has emerged as one of the essential technologies in the observation and fabrication of nanometric structures (Tseng; Notargiacomo; Chen, 2005). The AFM along with their techniques derived, as the Kelvin probe microscope and others, became the most important scanning probe microscope. Allowing topographic (3D) imaging of conductive and insulating surfaces with atomic resolution.

Basic Principles

Its principle is based on a scan made by a tip, which is mounted on a system that attaches the cantilever to a spring of the scanner itself. Throughout the scan, the force between the tip and the sample surface is measured by monitoring the deflection of the cantilever. Thus, a topographic image of the sample is obtained by drawing the deflection of the cantilever in relation to its position in the sample. The final topographic image is then reconstructed using the information from the scanned lines. Each measurement point has a well-defined position. The lines superimposed on the topographic image of AFM correspond to the movements of coming and going (called trace and retrace).

However, other relationships between the tip and the sample can be used to ascertain the properties of the sample, the tip or the intermediate medium, these measures are commonly known as “force measures”. In this type of measurement, the sample is moved up and down applying a tension to the piezoelectric translator, on which the sample is mounted, while measuring the deflection obtained in the cantilever. In some AFMs, the tip to which the cantilever is attached is moved by the piezoelectric translator instead of the sample (Butt; Cappella; Kappl, 2005). Tortonese et al. (Tortonese et al., 1991) developed the piezoresistive PET cantilever as an integrated sensor used to monitor the deflection of the cantilever. Since the initial development, the piezoresistive cantilever has been manufactured by other groups and is now available as a commercial product.

The problem of sample roughness is greatly reduced in AFM compared to other surface strength techniques, since the sample only needs to be smooth on a scale comparable to the radius of curvature at the end of the tip. Various materials, such as mica, a silicon or graphite wafer (HOPG) are available with sufficient smoothness over the required areas (Butt; Cappella; Kappl, 2005).

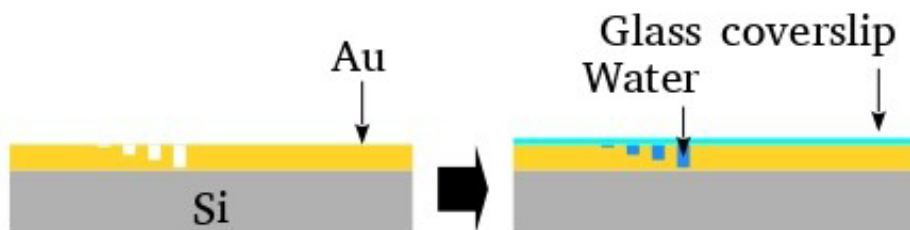
The essence of AFM force measurements today is to study intrinsic surface forces. The interaction between two surfaces in a medium is one of the fundamental issues in colloid and surface science (Suárez et al., 2012).

2.3.1. Nanolithography

In this work the nanolithography and topological characterization was performed on the Agilent AFM / SPM Series 5500 Atomic Force Microscope. Nanolithography was performed under ambient conditions using the vector scanning method. It was employed a DLC-coated Si tip (model 190DLC from BudgetSensors Innovative Solutions Bulgaria Ltd.) for static plowing. (Xie et al., 2006) The patterns were recorded on a $5 \mu\text{m}^2$ area. The nanochannels topography was imaged using a conventional Si_3N_4 tip (in contact mode) that has a low spring constant (about 0.02 N / m), in order to avoid local damage.

Next, the surface was covered by glass cover-slip and water confined between the cover-slip and nanochannels. After that the cover-slip was removed and samples preserved on vacuum. Figure 1 summarizes these steps.

Fig. 1 – Schematic representation of the nanolithography on the Au film deposited on $275 \mu\text{m}$ thick N/P Si substrate and water confinement in the channels by spreading a droplet on the surface. After preparation, the Au surface was covered with glass coverslip.



2.4 FOURIER-TRANSFORM INFRARED SPECTROSCOPY (FTIR)

This technique measures the absorption or emission of a given sample, be it solid, liquid or gaseous, in a high spectral resolution simultaneously. Protruding from a dispersive spectrometer, which measures the intensity over a narrow wavelength range separately. The term FT comes from a mathematical process called the Fourier Transform, which converts the raw data into a real spectrum, contributing to an improvement in the signal / noise ratio.

In short, FTIR spectroscopy is a measure of the wavelength and intensity of absorption of IR radiation by a sample, and is widely used in chemical analysis. (Zhang et al., 1995).

Basic Principles

The progression of this spectroscopy, in view of a quantitative analysis, occurs mainly due to the Fourier transform and the new geometries of the spectrometers with the use of Michelson's interferometer, thus making them faster and more effective (Durig; Sullivan, 2016; Eikrem, 1990).

An interferometer mainly consists of a set of mirrors and a beam splitter, transmitting half of the incident radiation from the source to the moving mirror and reflecting the

other half to the fixed mirror. These mirrors reflect the two beams to the divider, where they combine. Therefore, their resulting amplitudes can be constructive or destructive, depending on the divider. In infrared radiation, the sum of all interactions (constructive or destructive) for each component, results in a complex signal called an interferogram.

The Fourier transform spectrophotometer exposes the sample to a single pulse of radiation and response measures. The resulting signal, called biphasic induction, is a direct measure of the temporal coherence of light and contains a rapid decay composed of all possible frequencies. Since the signal measured on the interferometer cannot be interpreted, a mathematical technique called Fourier Transformation is required. This transformation is performed by the computer (software algorithms), presenting the user with the desired information for the spectral analysis (Morgano et al., 2005). The qualitative and quantitative analyzes using spectroscopy in the infrared region have expanded since the data generated by an FTIR spectrophotometer could be digitized, enabling statistical methods to solve chemical analysis problems.

In this work the FTIR spectra was collected using the FTIR spectrometer 640-IR FT-IR coupled to the 610-IR microspectrometer (Varian Inc.) with N₂-cooled Ge detector covering the 600 – 6000 cm⁻¹ spectral window. The detection area was 10 × 10 μm².

2.5 RAMAN SPECTROSCOPY

Chandrasenkhar Venkata Raman, an Indian scientist who in 1928 studied a phenomenon that was later called Raman scattering, started using this technique. He used sunlight as a source of electromagnetic radiation, a telescope with a collector, and the detector was just his own eyes. Later, more technological sources of excitation were created, such as lasers, which are widely used today (Ferraro; Nakamoto; Brown, 2002). The monochromaticity of radiation from lasers makes it possible to measure with relatively small Raman displacements, considering that the signal obtained in this type of displacement is very low.

The main purpose of this technique is to study the vibrational behavior of the molecules, observing the incident radiation. The Raman spectrum has its intensity in accordance with the Raman displacement. This displacement is due to the difference, in number of waves, between incident radiation and scattered radiation, being called the fingerprint region of a material. And this region has characteristic bands, which give structural and compositional information of the sample (Jenkins; Larsen; Williams, 2005).

Basic Principles

In a succinct description, it can be said that in the inelastic scattering of light, electromagnetic radiation interacts with matter through its electric field (Faria; Santos;

Gonçalves, 1997). Considering that in the Raman effect the transfer of energy depends on the existence of vibrational levels, in this spreading process the interaction of radiation with the network vibrations, initiates the change of the wave vector and the energy of the spread beam in relation to the beam incident (Dove; Dove, 2003).

Scattering can be classified into 3 types of different mechanisms, it is called Rayleigh scattering (or elastic scattering), when energy is preserved between the incident photon and the scattered photon when interacting with the molecule. Therefore, there is no change in the levels of rotational, vibrational or electronic energy in the molecule. As for the non-elastic collision between the photon and the molecule, the photon can be spread with less energy than the incident (Stokes), or with more energy than the incident (anti-Stokes).

In addition to the energy difference in absolute values, the spectrum resulting from non-elastic collisions has significant differences in intensity, since in the anti-Stokes region the intensity of a band is directly proportional to the population of the corresponding vibrational level, which in turn is inversely proportional to the energy needed to populate that level (Faria; Santos; Gonçalves, 1997).

In this work the T64000 Horiba Jobin-Yvon triple Raman spectrometer was used in the subtractive configuration with 1024x256 - OPEN-3LD / R CCD detector for Raman scattering measurements. The excitation laser was the Verdi G5 Laser (Coherent Inc.) operating at 532 nm (green) with a power of 1mW on a 100× objective (laser spot diameter of 1 µm).

2.6 NUCLEAR MAGNETIC RESONANCE (NMR)

Very briefly, Nuclear Magnetic Resonance, like all forms of spectroscopy, is based on the interaction of electromagnetic radiation with matter. However, NMR differs from optical spectroscopy in several fundamental aspects, such as:

- i- the separation between energy levels is a result of the interaction of the magnetic moment of an atomic nucleus with an applied magnetic field;
- ii- the interaction is with the magnetic component of electromagnetic radiation instead of the electrical component.

In NMR spectroscopy, it is possible to control electromagnetic radiation in the radio frequency (RF) range and describe the interaction of this radiation with the nuclear spins of the system. Thus contributing in part to the evolution of the large number of techniques used in NMR. Almost all chemical elements have at least one isotope with an atomic nucleus that has a magnetic moment, and when it is placed in an external magnetic field, and an excitation is applied with a frequency equal to its precession frequency, that nucleus is removed of your state of balance (Bathista, 2005).

In this work, the NMR experiments were performed with the sample placed inside a 4 mm Zirconia rotor. The control experiments where performed on a silicone greased

Si substrate with the empty rotor as well (i.e., inspecting probe and rotor background). ^1H spectra and spin-spin relaxation times (T_2) were measured using the spin-echo pulse sequence ($\pi/2 - \tau - \pi - \tau - \text{acquisition}$) conducted in a Varian VNMRS 500 MHz spectrometer operating at the resonance frequencies of 499.8 MHz, with temperature at 25°C. The inter-pulse delay (τ) of the spin-echo pulse sequence was varied from 67 to 4288 μs and 2048 transients were collected. T_2 was calculated from the single exponential decay fit of the intensity of the deconvoluted and background-subtracted peaks as a function of 2τ . The acquisition parameters were $\pi/2$ pulse length of 2.5 μs and relaxation delay of 5 s. Chemical shifts are reported relative to tetramethylsilane at 0 ppm. The signal was deconvoluted as sum of Lorentz/Gaussian line-shapes.

2.7 SCANNING ELECTRON MICROSCOPY (SEM)

With the technological evolution in the field of sciences as a whole, it requires the researcher to analyze and explain phenomena that occur in nanometric scales. The SEM has excellent resources that allow the observation and characterization of several inorganic and organic materials on this scale (Gomes, 2006). The scanning electron microscope is the most used equipment among the analysis instruments employing electron beams. It has different forms of image acquisition, it has an excellent special resolution, it is easy to prepare samples, it is easy to interpret the images obtained, and it is possible to perform elementary analyzes simultaneously (Zhou et al., 2006).

Basic Principles

The construction of the image takes place through an electron beam that draws the sample, with a point-to-point scanning in two dimensions. The processed signals from the interaction of electrons with the sample are used to amplify a second beam that produces the image on a screen. These signals are originated by the variation in the number of electrons released by the sample in the passage of the beam, which arrive at the detector. The enlargement of the image obtained is achieved by varying the sample size during scanning, reaching up to 1 million times (in current microscopes) (Zhou et al., 2006).

In this work, for morphological characterization was employed the high-resolution field emission scanning electron microscopy model FESEM JSM-6701F (JEOL) in secondary electron image mode and low-vacuum scanning electron microscopy SEM (JSM-6010LA, Jeol).

2.8 X-RAY DIFFRACTION

X-ray diffraction is a physical technique that can be used in several ways, one of which is to identify phases, either for natural or synthetic samples. XRD is well known in the research media, because with it it is possible to identify from peak patterns and their

positions and intensities, by which compounds a determined solid is formed. As these standards are practically unique, a signature for each material can be observed.

Basic Principles

X-rays are a form of electromagnetic radiation that has high energies and short wavelengths – 10 nm to 0.1 nm (Callister; Rethwisch, 2011). It is the main radiation applied in the study of material structures at the level of interatomic distances, that is, of the same order of magnitude as the interplanar spacings of the crystals, so that interference can occur (Padilha, 1997).

One of the main phenomena in wave physics is interference and diffraction. The interference is the result of the coherent superposition of two or more waves from different sources. The interference can be constructive, occurs at points where the displacement difference is equal to an integer number of wavelengths, or destructive, when the path difference is not equal to an integer number of wavelengths.

Diffraction is the phenomenon that occurs when a wave encounters an obstacle or opening of dimensions comparable to the wavelength it spreads and suffers interference. Diffraction is best explained from the Huygens principle, which states that all points on a wavefront can be considered sources of secondary waves that spread in all directions with a speed equal to the wave's propagation speed (Young et al., 2009).

In this work, the crystallographic phase was checked performing the X-ray diffraction experiments at room temperature on a Bruker D-8 Focuss diffractometer (Lynseye 1D detector) with Ni-filtered CuK α 1 radiation in range from 30 to 60 (0.02 increment) in θ - 2θ configuration.

2.9 DENSITY FUNCTIONAL CALCULATIONS (DFT)

2.9.1 Molecular dynamics

All the Ab-Initio molecular dynamics (MD) simulations were performed with the CP2K package. (Hohenberg; Kohn, 1964; Hutter et al., 2014) The Gaussian basis set by VandeVondele and Hutter (VandeVondele; Hutter, 2007) derived for use with the analytical dual-space pseudo-potentials proposed by Goedecker, Teter, and Hutter (GTH) (Goedecker; Teter; Hutter, 1996) was used (cutoff of 250 Ry). These pseudo-potentials were used in conjunction with the Gaussian and plane wave (GPW) scheme (Lippert; Parrinello; Michele, 1997) as implemented in the CP2K/QUICKSTEP program. All calculations were performed using the BLYP functional. (Lee; Yang; Parr, 1988) The crystallographic structure for Au obtained from refinement of XRD diffraction as reported by Suh et al. (Suh; Ohta; Waseda, 1988) was used as starting point of calculations. A super-cell of Au crystal was hydrated at

one side (see Results and Discussion section) and then 310 K (Nosé-Hoover thermostat) microcanonical NVE ensemble MD ran up to 100 fs.

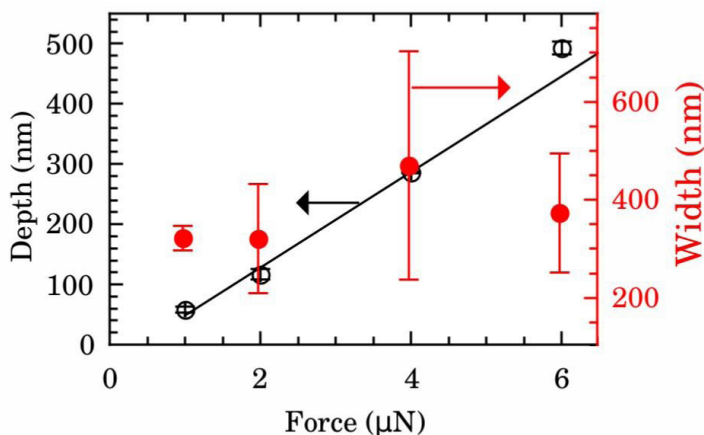
2.9.2 Vibrational calculations

DFT (Hohenberg; Kohn, 1964) was used in order to obtain equilibrium geometries and harmonic frequencies. Calculations were implemented in the CPMD program using the BLYP functional (Lee; Yang; Parr, 1988) augmented with dispersion corrections for the proper description of van der Waals interactions. (Lee; Yang; Parr, 1988; Lilienfeld et al., 2005) For all simulations, the cutoff energy was considered up to 100 Ry. The linear response for the values of polarization and polar tensors of each atom in the system was calculated to evaluate the eigenvectors of each vibrational mode.

3 RESULTS AND DISCUSSION

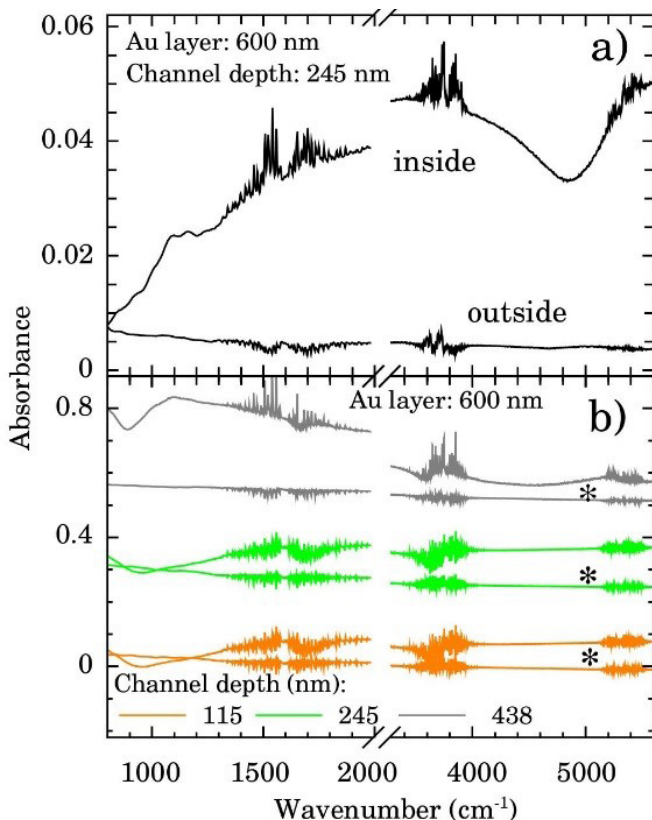
The width and depth produced by nanolithography on the surface of silicon coated with gold, as a function of the applied force of the AFM tip are shown in Figure 2 for films with 600 nm of Au layer. Up to 6 μN , the dependence of depth is almost linear (right scale, black symbols). The best fit of data to linear model (black line) furnished intercept of $-31(6)$ nm and slope of $80(2)$ nm/ μN . Controlling the applied force between 1 – 6 μN we obtained channels with depth of 50 – 500 nm. Otherwise, the values of width of nanochannels present a large dispersion (left scale, red symbols) being almost independent of the tip applied force. On average the width was $388(156)$ nm. Typical 2D AFM microscopy images before and after patterning for the 600 nm Au layer sample are presented on Supplementary Material section. We also checked the DLC-coated cantilever profile by SEM and we notice that the DLC film remained intact after the patterning process. Otherwise, the homogeneity of channels would be compromised.

Fig. 2 - Depth (left scale, black) and width (right scale, red) of nanochannels as function of AFM tip applied force for films with 600 nm of Au. The black line is the best fit to linear model (intercept of $-31(6)$ nm and slope of $80(2)$ nm/ μN).



FTIR spectra were taken inside and outside the nanochannels region in order to confirm the presence of water. The spectrum inside the nanochannels region (top of Fig. 3a) presents the typical characteristics water vibrational bands. (Vasylieva et al., 2018) We notice that all these bands presented negligible intensities outside the channels (bottom on Fig. 3a). The broad band from 1300 to 1900 cm^{-1} refers to the bending vibration of the H_2O molecule. (Ludvigsson; Lindgren; Tegenfeldt, 2000; Lucassen; Caspers; Puppels, 200) The band from 3450 to 3950 cm^{-1} refers to the symmetrical and asymmetrical stretch vibration of the O-H bond (WAB), (Ping et al., 2001; Lucassen; Caspers; Puppels, 2000) and the last band from 5150 to 5500 cm^{-1} refers to the inter-molecular hydrogen bonding vibration (WCB). (Kagi et al., 2000; Dickens; Dickens, 1999).

Fig. 3 - a) FTIR spectra showing the presence of water within nanochannels of depth of 245 nm. b) FTIR spectra showing the presence of water even after one week (*) for nanochannels of depth of 115, 245, and 438 nm on a 600 nm Au layer.



To certify the stability of the containment process, we observed the FTIR signal of the samples after 1 week of vacuum conditioning of the sample. Representative results are displayed on Fig.3b) for samples with nanochannels of depth of 115 nm (orange), 245 nm (green), and 438 nm (gray). The water bands are clearly detectable indicating that it is still present in the confinement region.

The Fig.4 shows the integrated intensities of the OH, WAB and WCB flexion bands after one week in relation to those for fresh samples as a function of the depth of the nanochannels. The relative intensities (and consequently water content) for shallowest samples of depth of 115 nm is almost constant up 1 week. Those of intermediate values of depth (245 nm) presented a intensity decrease of $\sim 50\%$ while for the deepest samples (438 nm) water bands intensities after 1 week were $\sim 10\%$ of the fresh ones. This finding indicates that confined water is almost bind to the Au surface at shallow samples and these presented higher hydrophilicity compared to the others. It represents an important experimental evidence concerning the hydrophilicity of the first layers of wetting for Au.

Fig. 4 - Relative integrated intensity (1 week/fresh samples intensities) of OH bending (solid black circle), symmetrical and asymmetrical stretch vibration of the O-H bond (WAB, solid red square), and inter-molecular hydrogen bonding (WCB, solid green diamond) bands.

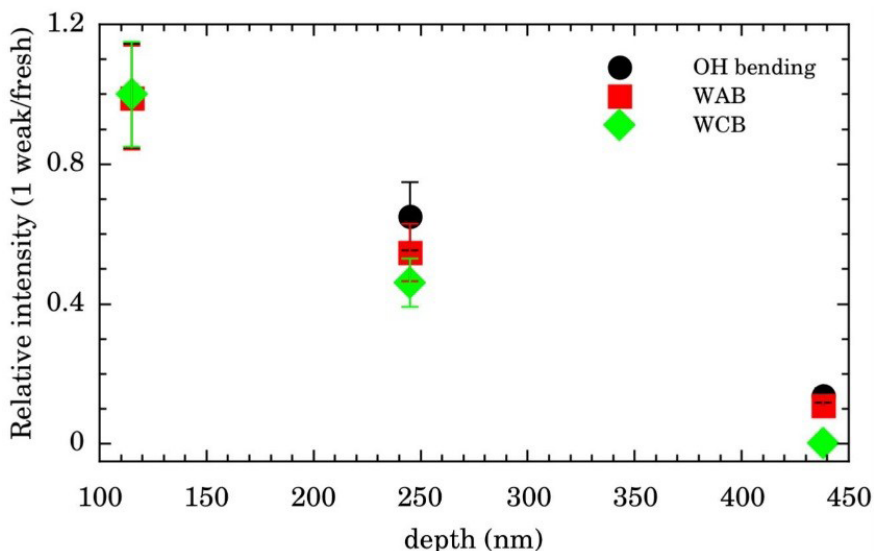
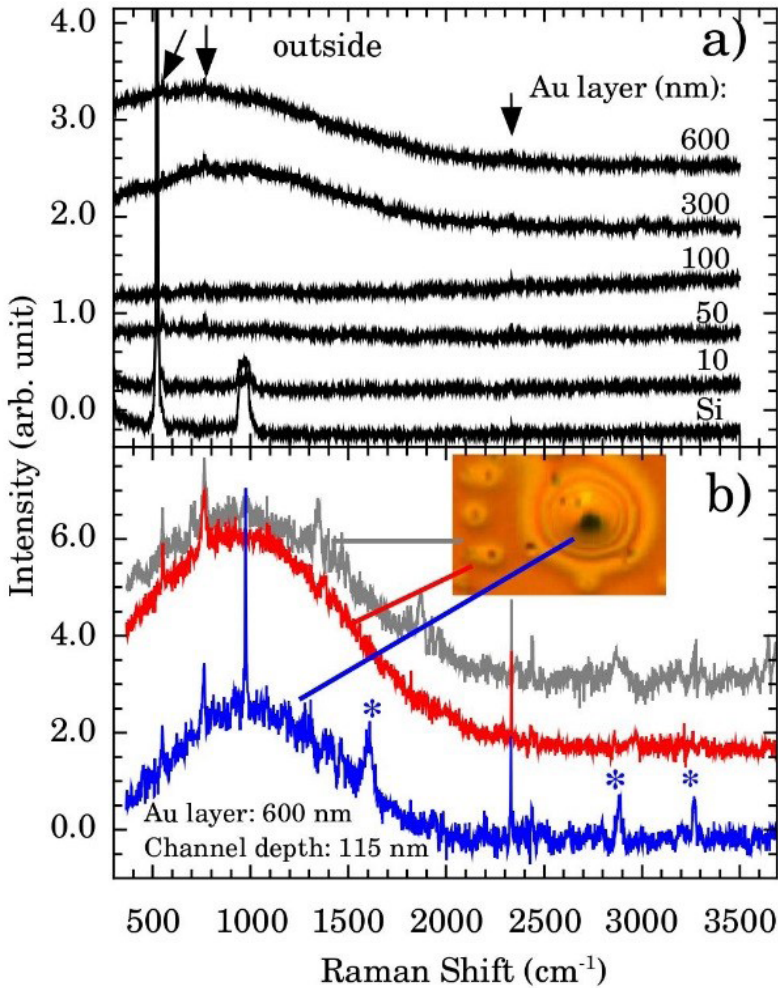


Figure 5a) presents the Raman spectra outside the nanochannels region for samples with Au thickness of 10, 50, 100, 300, and 600 nm. The Si band at $\sim 521 \text{ cm}^{-1}$ and the 2 th order scattering at $\sim 1000 \text{ cm}^{-1}$ are observed in all samples. However, it is also observed a strong and broad diffusive electronic Raman scattering for 300 and 600 nm samples. Additional tiny bands appear at 551, 765, and 2334 cm^{-1} (indicated by vertical arrows). These bands are associated to Au-OH stretching mode (Murphy; LaGrange, 1998), $e-(\text{H}_2\text{O})$ (Tauber; Mathies, 2002), and OH stretching (Kozlovskaya et al., 2018), respectively. The presence of these bands indicates that some water molecules are adsorbed on the Au surface. This represents another evidence concerning the Au <111> first water wetting layer hydrophilicity.

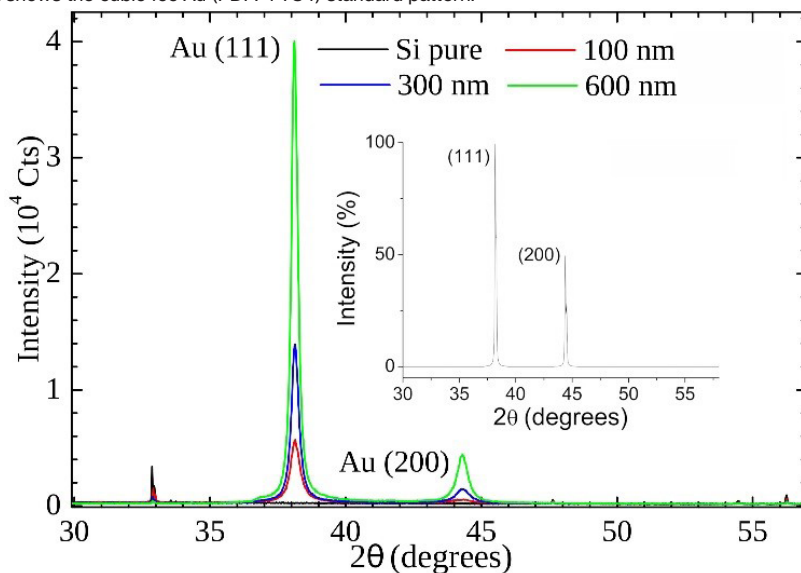
Fig. 5 - a) Raman spectra of Au thin films (thickness of 600, 300, 100, 50, and 10 nm) deposited over n/p Si and the Si substrate. All spectra were taken outside the nanochannels. Vertical arrows indicate additional Raman bands compared to Si spectrum. b) Representative Raman spectra taken outside (gray), around (red), and inside (blue) the observed oxidation in nanochannels of depth of 115 nm. The inset shows the optical image (100 X objective) in the oxidation region. Asterisks (*) indicates the characteristics oxidation bands at ~ 1602 , 2890 , and 3260 cm^{-1} .



A considerable oxidation process was observed around the nanochannel region (see inset of Fig. 5b). The holes observed in Figure 5b) resembles the “pitting” aspect of corrosion. It is reported that for Au $\langle 111 \rangle$ the surface oxidation occurs preferentially by pitting. (Chen; Vesecky; Gewirth, 1992; McCarley; Bard, 1992) We notice that the oxidation corrosion is almost Au-film thickness independent, being observed for 100, 302, and 600 nm films. Figure 5b) shows the Raman spectrum inside, around, and outside of the oxidized region. Bands ~ 2890 and $\sim 3260 \text{ cm}^{-1}$ are very distinctive in the oxidized region. To the best of our knowledge their assignment are not described in the literature.

Our XRD results (see Fig.6) indicate that the (111) is the preferential orientation on our samples. Reflections from (200) crystal planes are also present but at lower intensities ($\sim 5\%$). For comparison, in the fcc Au standard (see inset of Fig.6) the (200) to (111) intensity ratio is $\sim 50\%$. It was performed a symmetrical XRD measurement ($\theta - 2\theta$ configuration) the relative greater intensity of (111) reflection indicates that crystallites faces with this orientation predominates on the samples.

Fig. 6 - X-Ray powder diffraction patterns of gold thin films (thickness of 100 nm, 300, and 600 nm) on Si substrate. The inset shows the cubic fcc Au (PDF: 4-784) standard pattern.

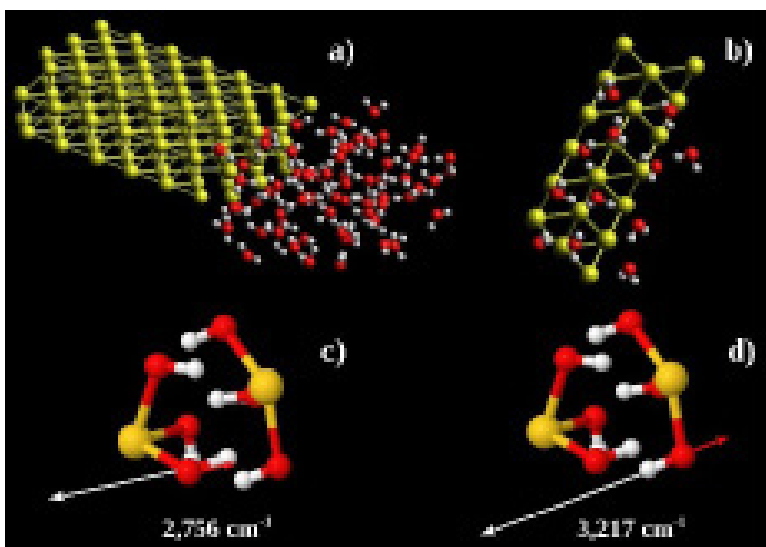


There is still no consensus and much is still being discussed about the coupling of water and gold (Michaelides et al., 2003). Recent experimental studies have shown that the surface of Au $\langle 111 \rangle$ at room temperature is hydrophilic and more stable than other orientations. (Chai; Klein, 2007) Cicero et al. (Cicero et al., 2011) studied the interaction of water layers on the $\langle 111 \rangle$ Au surface and the issue of hydrophobicity from ab initio MD simulations. Their results shown that the water/Au interface is hydrophilic due to the charge transfer from oxygen to Au which favours a dynamic attractive coupling between the metal and the first adsorbed water layer. They argue that while oxygen species preferentially reside at the Au $\langle 111 \rangle$ sites, hydrogen atoms are evenly distributed around them. Due to the formation of “pitting”, the deposited Au film is unleavened and the potential for local nucleation occurs at the edge of the unevenness. Thus the water at these steps binds more firmly to the Au surface, with a binding energy of 105 meV of the water monomer and the surface of Au $\langle 111 \rangle$ (Ibach, 2010). Considering that each water molecule in the bilayer structure is bonded by a half Au - O bond, this means that on Au surfaces the Au - O bond contributes 12 % of the total binding energy per molecule (Ibach, 2010).

Qiang Li et al. (Li et al., 2015) confirmed this theory of the unevenness nucleation point through simulations and previous AFM studies. They concluded that surface and edge defects determine better water adsorption on the Au substrate $\langle 111 \rangle$. They argued that the water clusters had initially been adsorbed to the edges of the Au steps under environmental conditions.

With this information, we started from a hypothesis related to the formation of some type of Au-OH complex performing MD calculations in Au $\langle 111 \rangle$ $3 \times 3 \times 2$ supercell with one face exposed to 67 water molecules. The simulation box had $30 \times 35 \times 12$ nm³. The water molecules were confined to $12 \times 16 \times 8$ nm³ (see Fig.7 a). The system found equilibration after 3 fs. Figure 7 b) shows a snapshot of a region close to Au $\langle 111 \rangle$ surface. On average there are 6 water molecules bound to the each Au $\langle 111 \rangle$ honeycomb (Fig.7 b). Thus the observed Au:O ratio is 1: 3 . Computing the energy of formation of 3 possible structures (Au(OH)_{3/2}, (Au(H₂O)₃)₂, and H₃Au₃(H₂O)₆ we found - 302.8 , - 236.2 and - 227.9 eV/atom, respectively. It is possible to conclude that the more stable one is (Au (OH)₃)₂ which corresponds to Au(OH)₃ unit formula. We also performed vibrational calculations on (Au (OH)₃)₂. From these calculations we were able to assign the 2890 (calculated 2756) and 3260 (calculated 3217) cm⁻¹ bands to out-of-phase (Fig. 7c) and in-phase (Fig. 7d) O-H stretching vibrations, respectively. These results enable us to argue the oxidation product observed in the Au nanochannels under confined water presence is the Au (OH)₃ complex. This species is usually observed on supported Au-catalytic (see, e.g., ref. (Park; Lee, 1999) and ref. (Takei et al., 2010)).

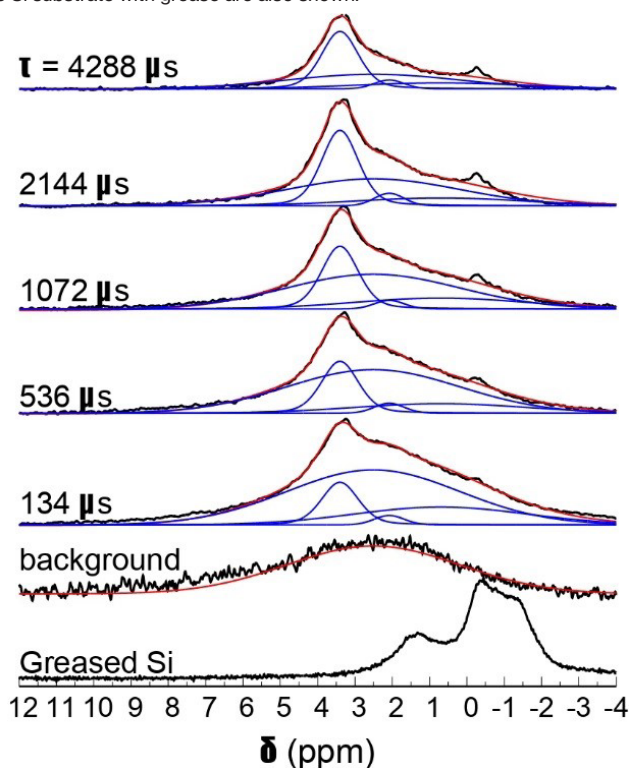
Fig. 7 - a) Au $\langle 111 \rangle$ $3 \times 3 \times 2$ supercell including 67 water molecules at one side. The simulation box had $30 \times 35 \times 12$ nm³. b) Snapshot of MD showing the adsorbed water molecules around Au $\langle 111 \rangle$ honeycomb face. c) and d) Eigenvectors of 2,756 cm⁻¹ and 3,217 cm⁻¹ vibrations, respectively. Yellow, red, and white spheres represent the Au, O, and H, atoms, respectively.



We then performed ^1H NMR spin-echo experiments to record the static spectra at different evolution times and to quantify the spin-spin relaxation time, aiming to describe chemical environments and the proton dynamics. However, NMR experiments in films are rarely reported since fast magic angle spinning (MAS) is difficult to implement in this geometry. Static ^1H NMR experiments in solid state suffer from strong dipolar coupling and chemical shift anisotropy broadening which results in poorly resolved spectra, unless the species inspected are considerably mobile. As noted below, the spectra obtained are reasonably resolved and the results can be interpreted based on the extensive literature on NMR of Au nanoparticles.

Figure 8 shows the normalized ^1H spin-echo spectra of the Au film (600 nm thick) and control experiments as a function of τ . The ^1H spin-echo spectra of the sample shows a broad peak around 3.4 ppm. The signal of the sample is more evidenced as the evolution time of the spin-echo is set longer ($\tau > 1000 \mu\text{s}$), as expected, since for longer evolution times the sample inside the rotor is efficiently excited while the probe-background is suppressed.

Fig. 8 - ^1H NMR spin-echo spectra of the SiAu sample (600 nm thick) as function of τ . The spectra of the background (empty rotor) and the Si substrate with grease are also shown.



The observed spectra resembles those of amorphous solids with inhomogeneous broadening due to multiple sites and conformations. Each spectrum was carefully

deconvoluted in three peaks and the background, as illustrated in the Figure 8 (see also Supplementary Materials). The most intense peak is at 3.4 ppm (with T₂ of 16 ms), there is a second peak at 2.1 ppm (T₂ of 7.9 ms), and a broad peak at 0.7 ppm (T₂ of 3.6 ms).

The line broadening in this case can be caused by: i) multiple sites and conformations (distribution of chemical shift), ii) chemical shift anisotropy, iii) dipolar coupling, iv) hyperfine coupling of nuclear spins to conduction electrons in the metal (Knight shift), and v) field inhomogeneities caused by variable magnetic susceptibilities around the protons. (Vanderhart; Earl; Garroway, 1981; Alla; Lippmaa, 1982; Sharma et al., 2009; Marbella; Millstone, 2015) The resonance shifts come from some of these features, as the chemical shift, Knight shift and the bulk magnetic susceptibility, which influences the effective local magnetic field. (Vanderhart; Earl; Garroway, 1981; Alla; Lippmaa, 1982; Sharma et al., 2009; Marbella; Millstone, 2015).

We noted that the measurements of the greased Si substrate and the Au covered sample show the silicone grease in the same chemical shift. This illustrates that the Au nanolayer does not contribute significantly to the overall magnetic susceptibility. (Pigliapochi et al., 2019) Possibly, bulk magnetic susceptibility is of secondary relevance in the spectral line broadening and resonance shifts. Furthermore, the importance of the Knight shift in the overall resonance shift and line broadening in ligand grafted Au nanoparticles is long debated. (Badia et al., 1997; Kohlmann et al., 2001) It should be dependent, e.g., on the size and shape of the Au nanolayer or the nanoparticle. More relevant, resonance shifts of the protons in the second or higher coordination to the Au on Au nanoparticles are not remarkably influenced by Knight shifts. For instance, Sharma et al. observed that the ¹H NMR of Triphenylphosphine (PPh₃) is observed at 7.3 ppm as free ligand, at 7.5 ppm as.

Au(PPh₃)₃ Cl complex, and at 7.1 ppm as PPh₃-capped gold 1.8 nm nanoparticle. (Sharma et al., 2009) For Tiopronin-capped Au 0.9 nm NPs, Kohlmann et al. found that the methine proton shifts from 3.6 ppm to 4.3-4.7 ppm when Tiopronin is attached to the Au nanoparticles. (Kohlmann et al., 2001) For a series of thiol-terminated-capped Au 1.7 - 4.2 nm NPs, (Hasan; Bethell; Brust, 2002; Schuetze et al., 2016) the ¹H downfield shifts of the grafted ligands can be as much as 1 ppm in comparison to the non-grafted ones. Thus, we can restrict our discussion considering that chemical shifts and dipolar interactions are the most important mechanisms influencing the spectral features and relaxation processes.

The first issue to be determined is to confirm the restricted motion of observed protons on the Au surface. Typically, the spin-spin relaxation rates in non-metallic solids are markedly influenced by ¹H-¹H homonuclear dipolar coupling and dipolar coupling to paramagnetic impurities. (Abragam, 1961; Levitt, 2015) Short T₂ imply in strong dipolar coupling that was not averaged out by molecular motion. For instance, ¹H T₂ of water

decreases from ~ 1 s to 80-240 ms when confined in 50-300 μm microporous glasses. (Taylor; Peterson, 2010; Chencarek et al., 2019) More closely related to our system, for Triphenylphosphine capped Au nanoparticles, T2 of the protons decreases from 5.2 s in the diluted ligand to 40 ms when grafted to the 1.8 nm nanoparticle. (Sharma et al., 2009) T2 of methine protons in tiopronin-capped Au 0.9-1.6 nm NPs has been reported by to be around 156-55 ms. (Kohlmann et al., 2001) These measurements were performed in liquid state, and unfortunately ^1H T2 of capped Au nanoparticles in solid state has not been reported (to the best of our knowledge). However, the shortening of T2 in solid state is expected. Thus, we can state that protons in our case are in restricted mobility, and not adsorbed molecules on the surface.

The candidates for the signal around 3.4 ppm are confined water or stable Au-OH complexes, since adsorbed molecules do not contribute to the observed signal. In fact, the ^1H NMR shift of adsorbed water is around 4.7-6.0 ppm, (Mogilevsky et al., 2011; Marbella et al., 2014; Osman et al., 2015) which is outside of the observed range. Confined water as monomer or dimer could be observed upfield shifted with respect to bulk water, (Grünberg et al., 2004; Kar; Scheiner, 2004; Osman et al., 2015) around 0.5 - 1.5 ppm, and cannot be ruled out as units contributing to the NMR spectra in that shift range. Another contribution could come from Au-OH complexes, that would be observed around 4.7 ppm, taking into consideration that water as monomer is ~ 3.8 ppm upfield shifted with respect to bulk water (Kar; Scheiner, 2004) while the Au \cdots H hydrogen bond would contribute to a 3.5 - 4.1 ppm downfield shift (which is, obviously, a very rough additive estimation taken from quantum chemical calculations). (Kryachko; Remacle, 2005) In summary, it is possible that water monomers or dimers and Au-OH₃ complexes could be existing species but they could only be responsible for small portions of the spectral sidebands (≈ 0.5 - 1.5 ppm and 4-6 ppm).

In order to assign the most characteristic band, centered at 3.4 ppm, we recall that for Au-OH complexes there should be electron donation from the Au to the chemisorbed molecules, (Abraham et al., 2010) similarly to Si-O bonds (to some extent). Remarkable, silanol groups in distinct configurations can be observed as a broad line from 1.8 to 4.5 ppm, the range of the shifts observed here. (Grünberg et al., 2004; Trébosc et al., 2005; Hartmeyer et al., 2007) Furthermore, the static ^1H NMR spectrum of MCM-41, with high concentration of surface silanol groups, is very similar to the one observed in our study. (Trébosc et al., 2005) Analogously, hydroxyl of Zr(OH)₄ is also observed in this range. (Mogilevsky et al., 2011) Thus, it is likely that the main observed peak around 3.4 ppm is due to protons on Au-OH complexes, in agreement with the proposed structures from quantum chemical calculations.

4 CONCLUSIONS

Bearing in mind that water is very important in several chemical, physical and biological processes and that many of its properties in confinement remain unanswered, a fact addressed in the introduction, it is of fundamental importance to understand in more depth how it behaves at the nanoscale, which is where its behavior differs in several aspects from the bulk form (Knight et al., 2019). Its understanding is still much discussed, as there is still no consensus on its reactivity at the nanoscale.

In this work, strong evidence was observed about the hydrophilicity of Au <111> through the relative intensities of the water bands probed by FTIR as a function of the depth of the nanochannels (Fig. 4) and the allocation of small Raman bands (Fig.5). Thus, a unique corrosion process of Au nanochannels exposed to confined water was also observed. Our experimental data pointed out by computer simulations indicated that the oxidation product is Au (OH)₃ also supporting the hydrophilicity of the first layer of water wettability over Au. Furthermore, our results indicate an important surface oxidation route that needs to be considered in Au nanosurface applications. An important example is the use of Au in catalysis, since a large amount of organic transformation into fine chemicals, pharmaceuticals and the green processes of the food industry depend on the catalytic activity of Au (see, e.g., ref. (Shahzad et al., 2017)).

REFERENCES

- Abragam, A. Thermal relaxation and dynamic polarization in solids. In: The principles of nuclear magnetism.: Clarendon Press, 1961. p. 354–423.
- Abraham, A.; Mihaliuk, E.; Kumar, B.; Legleiter, J.; Gullion, T. Solid-state nmr study of cysteine on gold nanoparticles. *J. Phys. Chem. C*, v. 114, n. 42, p. 18109–18114, 2010. Available on: <<https://doi.org/10.1021/jp107112b>>.
- Alla, M.; Lippmaa, E. Resolution limits in magic-angle rotation nmr spectra of polycrystalline solids. *Chem. Phys. Lett.*, v. 87, n. 1, p. 30 – 33, 1982. ISSN 0009-2614. Available on: <<http://www.sciencedirect.com/science/article/pii/0009261482835471>>.
- Azmat, N.; Ralston, K.; Muddle, B.; Cole, I. Corrosion of zn under fine size aerosols and droplets using inkjet printer deposition and optical profilometry quantification. *Corr. sci.*, Elsevier, v. 53, n. 11, p. 3534–3541, 2011.
- Badia, A. et al. Gold-sulfur interactions in alkylthiol self-assembled monolayers formed on gold nanoparticles studied by solid-state nmr. *J. Am. Chem. Soc.*, v. 119, n. 45, p. 11104–11105, 1997. Available on: <<https://doi.org/10.1021/ja9726163>>.
- Bathista, A. Princípios básicos de ressonância magnética nuclear do estado sólido. São Carlos, Brasil, 2005.
- Batista, A. M. et al. Gold nanochannels oxidation by confined water. *RSC Advances*, Royal Society of Chemistry, v. 10, n. 61, p. 36980–36987, 2020.

- Berg, J. M. Principles of bioinorganic chemistry.: University Science Books, 1994.
- Bergman, R.; Swenson, J. Dynamics of supercooled water in confined geometry. *Nature*, Nature Publishing Group, v. 403, n. 6767, p. 283–286, 2000.
- Berntsen, P.; Bergman, R.; Jansson, H.; Weik, M.; Swenson, J. Dielectric and calorimetric studies of hydrated purple membrane. *Biophys. J.*, Elsevier, v. 89, n. 5, p. 3120–3128, 2005.
- Binnig, G. et al. Ultrahigh-density atomic force microscopy data storage with erase capability. *Applied Physics Letters*, American Institute of Physics, v. 74, n. 9, p. 1329–1331, 1999.
- Bitton, L.; Frydman, A. Controllable room-temperature metallic quantum dot. *Appl. Phys. Lett.*, American Institute of Physics, v. 88, n. 11, p. 113113, 2006.
- Brovchenko, I.; Oleinikova, A. *Interfacial and confined water*.: Elsevier, 2008.
- Butt, H.-J.; Cappella, B.; Kappl, M. Force measurements with the atomic force microscope: Technique, interpretation and applications. *Surface science reports*, Elsevier, v. 59, n. 1-6, p. 1–152, 2005.
- Callister, W. D.; Rethwisch, D. G. *Materials science and engineering*.: John wiley & sons NY, 2011. v. 5.
- Carver, P. L. Metal ions and infectious diseases. an overview from the clinic. *Interrelations between Essential Metal Ions and Human Diseases*, Springer, p. 1–28, 2013.
- Castrillón, S. R.-V.; Giovambattista, N.; Aksay, I. A.; Debenedetti, P. G. Evolution from surface-influenced to bulk-like dynamics in nanoscopically confined water. *J. Phys. Chem.B*, ACS Publications, v. 113, n. 23, p. 7973–7976, 2009.
- Celano, U. *Electrical atomic force microscopy for nanoelectronics*.: Springer, 2019.
- Chai, L.; Klein, J. Large area, molecularly smooth (0.2 nm rms) gold films for surface forces and other studies. *Langmuir*, ACS Publications, v. 23, n. 14, p. 7777–7783, 2007.
- Chau, Y.-F. C. et al. Fabrication and characterization of a metallic–dielectric nanorod array by nanosphere lithography for plasmonic sensing application. *Nanomaterials*, Multidisciplinary Digital Publishing Institute, v. 9, n. 12, p. 1691, 2019.
- Chen, C. H.; Vesecky, S. M.; Gewirth, A. A. In situ atomic force microscopy of underpotential deposition of silver on gold (111). *J. Am. Chem. Soc.*, ACS Publications, v. 114, n. 2, p. 451–458, 1992.
- Chencarek, B. et al. Multi-exponential analysis of water nmr spin–spin relaxation in porosity/permeability-controlled sintered glass. *Appl. Magn. Reson.*, v. 50, n. 1, p. 211–225, Mar 2019. ISSN 1613-7507. Available on: <<https://doi.org/10.1007/s00723-018-1050-x>>.
- Chu, X.-q. et al. Proteins remain soft at lower temperatures under pressure. *J. Phys. Chem. B*, ACS Publications, v. 113, n. 15, p. 5001–5006, 2009.
- Cicero, G.; Calzolari, A.; Corni, S.; Catellani, A. Anomalous wetting layer at the au (111) surface. *J. Phys. Chem.*, ACS Publications, v. 2, n. 20, p. 2582–2586, 2011.
- Coudert, F.-X.; Cailliez, F.; Vuilleumier, R.; Fuchs, A. H.; Boutin, A. Water nanodroplets confined in zeolite pores. *Faraday Discuss*, Royal Society of Chemistry, v. 141, p. 377–398, 2009.
- CPMD <http://www.cpmc.org/> Copyright IBM Corp 1990–2008 Copyright MPI für Festkörperforschung Stuttgart 1997–2019.

Dickens, B.; Dickens, S. H. Estimation of concentration and bonding environment of water dissolved in common solvents using near infrared absorptivity. *J. Res. Natl. Inst. Stan., National Institute of Standards and Technology*, v. 104, n. 2, p. 173, 1999.

Dove, M. T.; Dove, M. T. *Structure and dynamics: an atomic view of materials.*: Oxford University Press, 2003. v. 1.

Dufrêne, Y. F.; Viljoen, A.; Mignolet, J.; Mathelié-Guinlet, M. *Afm in cellular and molecular microbiology. Cellular Microbiology*, John Wiley & Sons, Inc. Chichester, UK, p. e13324–e13324, 2021.

Durig, J.; Sullivan, J. *Vibrational spectroscopy, fourier transforms and analytical chemistry. TRAC: Trends in Analytical Chemistry: Volume 9*, Elsevier, v. 9, n. 4, p. 104, 2016.

Edwards, C. M.; Ulapane, S. B.; Kamathewatta, N. J.; Ashberry, H. M.; Berrie, C. L. Fabrication and growth control of metal nanostructures through exploration of atomic force microscopy-based patterning and electroless deposition conditions. *The Journal of Physical Chemistry C, ACS Publications*, v. 124, n. 46, p. 25588–25601, 2020.

Eikrem, L. *Process fourier transform infrared spectroscopy. TrAC Trends in Analytical Chemistry*, Elsevier, v. 9, n. 4, p. 107–109, 1990.

Faraone, A.; Liu, L.; Mou, C.-Y.; Yen, C.-W.; Chen, S.-H. Fragile-to-strong liquid transition in deeply supercooled confined water. *J. Chem. Phys., American Institute of Physics*, v. 121, n. 22, p. 10843–10846, 2004.

Faria, D. d.; Santos, L.; Gonçalves, N. Uma demonstraç o sobre o espalhamento inel stico de luz: repetindo o experimento de raman. *Quim. Nova, SciELO Brasil*, p. 319–323, 1997.

Ferraro, J.; Nakamoto, K.; Brown, C. *Introductory raman spectroscopy (new york: Academic)*. 2002.

Ferreira, P.; Ishikawa, M.; Kogikoski, S.; Alves, W.; Martinho, H. Relaxation dynamics of deeply supercooled confined water in l, l-diphenylalanine micro/nanotubes. *Physical Chemistry Chemical Physics, Royal Society of Chemistry*, v. 17, n. 48, p. 32126–32131, 2015.

Frenkel, D. *Soft condensed matter. Physica A, Elsevier*, v. 313, n. 1, p. 1–31, 2002.

Goedecker, S.; Teter, M.; Hutter, J. Separable dual-space gaussian pseudopotentials. *Phys. Rev. B, APS*, v. 54, n. 3, p. 1703, 1996.

Gomes, K. K. P. S ntese e caracteriza o do carbeto de molibd nio nanoestruturado para fins catal ticos na rea o de oxida o parcial do metano. *Disserta o (Mestrado) – Universidade Federal do Rio Grande do Norte*, 2006.

G mez-Varela, A. I. et al. Simultaneous co-localized super-resolution fluorescence microscopy and atomic force microscopy: combined sim and afm platform for the life sciences. *Scientific reports, Nature Publishing Group*, v. 10, n. 1, p. 1–10, 2020.

Gr nberg, B. et al. Hydrogen bonding of water confined in mesoporous silica mcm-41 and sba-15 studied by 1h solid-state nmr. *Chem. Eur. J.*, v. 10, n. 22, p. 5689–5696, 2004. Available on: <<https://chemistry-europe.onlinelibrary.wiley.com/doi/abs/10.1002/chem.200400351>>.

Halle, B. Protein hydration dynamics in solution: a critical survey. *Philosophical Transactions of the Royal Society of London. Series B: Biological Sciences, The Royal Society*, v. 359, n. 1448, p. 1207–1224, 2004.

Hartmeyer, G. et al. Speciation of silanol groups in precipitated silica nanoparticles by ^1H MAS NMR spectroscopy. *J. Phys. Chem. C*, v. 111, n. 26, p. 9066–9071, 2007. Available on: <<https://doi.org/10.1021/jp071490l>>.

Hasan, M.; Bethell, D.; Brust, M. The fate of sulfur-bound hydrogen on formation of self-assembled thiol monolayers on gold: ^1H NMR spectroscopic evidence from solutions of gold clusters. *J. Am. Chem. Soc.*, v. 124, n. 7, p. 1132–1133, 2002. PMID: 11841257. Available on: <<https://doi.org/10.1021/ja0120577>>.

Hohenberg, P.; Kohn, W. Inhomogeneous electron gas. *Phys. Rev.*, APS, v. 136, n. 3B, p. B864, 1964.

Hsia, C. C. Respiratory function of hemoglobin. *New England Journal of Medicine*, Mass Medical Soc, v. 338, n. 4, p. 239–248, 1998.

Huang, S.-J.; Jeng, Y.-R.; Liu, K.-F. Sliding wear characteristics of the diamond-like carbon films on alloy substrates. *Wear*, Elsevier, v. 263, n. 7-12, p. 1266–1273, 2007.

Hussain, A.; Shah, S. M. Computational study of complete methanol dehydrogenation on Au(100) and Au(310) surfaces: Dominant role of atomic oxygen. *Surf. Sci.*, Elsevier, v. 620, p. 30–37, 2014.

Hutter, J.; Iannuzzi, M.; Schiffmann, F.; VandeVondele, J. CP2K: atomistic simulations of condensed matter systems. *Wiley Interdiscip. Rev. Comput. Mol. Sci.*, Wiley Online Library, v. 4, n. 1, p. 15–25, 2014.

Ibach, H. Vibration spectroscopy of water on stepped gold surfaces. *Surf. Sci.*, Elsevier, v. 604, n. 3-4, p. 377–385, 2010.

Jenkins, A. L.; Larsen, R. A.; Williams, T. B. Characterization of amino acids using Raman spectroscopy. *Spectrochimica Acta Part A: Molecular and Biomolecular Spectroscopy*, Elsevier, v. 61, n. 7, p. 1585–1594, 2005.

Jensen, T. R. et al. Water in contact with extended hydrophobic surfaces: direct evidence of weak dewetting. *Physical Review Letters*, APS, v. 90, n. 8, p. 086101, 2003.

Jirlèn, J.; Concina, I.; Lundström, I.; Almqvist, N. Towards nanolithography with starch and α -amylase: Invited lecture. In: *European Advanced Materials Congress (EAMC-17)*, Stockholm, Sweden, 22-24 August 2017. 2017.

Kagi, H. et al. Evidence for ice VI as an inclusion in cuboid diamonds from high pressure near infrared spectroscopy. *Mineral. Mag.*, Cambridge University Press, v. 64, n. 6, p. 1089–1097, 2000.

Kar, T.; Scheiner, S. Comparison of cooperativity in $\text{C-H}\cdots\text{O}$ and $\text{O-H}\cdots\text{O}$ hydrogen bonds. *J. Phys. Chem. A*, v. 108, n. 42, p. 9161–9168, 2004. Available on: <<https://doi.org/10.1021/jp048546l>>.

Kim, U. S.; Baek, S.-Y.; Kim, T.-W.; Park, J. W. Cold tribo-nanolithography on metallic thin-film surfaces. *Journal of Nanoscience and Nanotechnology*, American Scientific Publishers, v. 20, n. 7, p. 4318–4321, 2020.

Kitajima, N. et al. A new model for dioxygen binding in hemocyanin. Synthesis, characterization, and molecular structure of the μ_2 - η^2 - η^2 -peroxo dinuclear copper(II) complexes, $[\text{Cu}(\text{hb}(3,5\text{-r}2\text{pz})_3)_2(\text{o}2)(\text{r}=\text{isopropyl and ph})]$. *Journal of the American Chemical Society*, ACS Publications, v. 114, n. 4, p. 1277–1291, 1992.

Knight, A. W.; Kalugin, N. G.; Coker, E.; Ilgen, A. G. Water properties under nano-scale confinement. *Scientific Reports*, Nature Publishing Group, v. 9, n. 1, p. 1–12, 2019.

Kohlmann, O. et al. Nmr diffusion, relaxation, and spectroscopic studies of water soluble, monolayer-protected gold nanoclusters. *J. Phys. Chem. B*, v. 105, n. 37, p. 8801–8809, 2001. Available on: <<https://doi.org/10.1021/jp011123o>>.

Kozlovskaya, E. et al. Raman spectroscopic and theoretical study of liquid and solid water within the spectral region 1600–2300 cm⁻¹. *Spectrochim. ACTA A*, Elsevier, v. 196, p. 406–412, 2018.

Kryachko, E.; Remacle, F. Three-gold clusters form nonconventional hydrogen bonds o–h au and n–h au with formamide and formic acid. *Chem. Phys. Lett.*, Elsevier, v. 404, n. 1-3, p. 142–149, 2005.

Lee, C.; Yang, W.; Parr, R. G. Development of the colle-salvetti correlation-energy formula into a functional of the electron density. *Phys. Rev. B*, APS, v. 37, n. 2, p. 785, 1988.

Levitt, M. H. Relaxation. In: *Spin dynamics: basics of nuclear magnetic resonance*. 2. ed.: Wiley, 2015. p. 571–594.

Li, Q.; Song, J.; Besenbacher, F.; Dong, M. Two-dimensional material confined water. *Acc. Chem. Res.*, ACS Publications, v. 48, n. 1, p. 119–127, 2015.

Lilienfeld, O. A. von; Tavernelli, I.; Rothlisberger, U.; Sebastiani, D. Performance of optimized atom-centered potentials for weakly bonded systems using density functional theory. *Phys. Rev. B*, APS, v. 71, n. 19, p. 195119, 2005.

Lind, P. A.; Daniel, R. M.; Monk, C.; Dunn, R. V. Esterase catalysis of substrate vapour: *Biochimica et Biophysica Acta (BBA)-Proteins and Proteomics*, Elsevier, v. 1702, n. 1, p. 103–110, 2004.

Lippert, B. G.; Parrinello, J. H.; Michele. A hybrid gaussian and plane wave density functional scheme. *Mol. Phys.*, Taylor & Francis, v. 92, n. 3, p. 477–488, 1997.

Liu, L.; Chen, S.-H.; Faraone, A.; Yen, C.-W.; Mou, C.-Y. Pressure dependence of fragile-to-strong transition and a possible second critical point in supercooled confined water. *Phys. Rev. Lett.*, APS, v. 95, n. 11, p. 117802, 2005.

Liu, R. Adsorption and dissociation of h₂o on au (1 1 1) surface: A dft study. *Comput. Theor. Chem.*, Elsevier, v. 1019, p. 141–145, 2013.

Lucassen, G. W.; Caspers, P. J.; Puppels, G. J. Water content and water profiles in skin measured by ftir and raman spectroscopy. In: *International Society for Optics and Photonics. Controlling Tissue Optical Properties: Applications in Clinical Study*. 2000. v. 4162, p. 39–45.

Ludvigsson, M.; Lindgren, J.; Tegenfeldt, J. Ftir study of water in cast nafion films. *Electrochim. Acta*, Elsevier, v. 45, n. 14, p. 2267–2271, 2000.

Marbella, L. E. et al. Gold-cobalt nanoparticle alloys exhibiting tunable compositions, near-infrared emission, and high t₂ relaxivity. *Adv. Funct. Mater.*, v. 24, n. 41, p. 6532–6539, 2014. Available on: <<https://onlinelibrary.wiley.com/doi/abs/10.1002/adfm.201400988>>.

Marbella, L. E.; Millstone, J. E. Nmr techniques for noble metal nanoparticles. *Chem. Mater.*, v. 27, n. 8, p. 2721–2739, 2015. Available on: <<https://doi.org/10.1021/cm504809c>>.

McCarley, R. L.; Bard, A. J. Surface reactions of gold (111) with aqueous cyanide studied by scanning tunneling microscopy. *J. Phys. Chem.*, ACS Publications, v. 96, n. 18, p. 7410–7416, 1992.

McMillan, P. F.; Stanley, H. E. Fluid phases: Going supercritical. *Nature Physics*, Nature Publishing Group, v. 6, n. 7, p. 479–480, 2010.

- Melgarejo, A.; Schoenek, B.; Zhang, J.; Kim, B. Contact afm nanolithography based on anodic oxidation. *Microscopy Today*, Cambridge University Press, v. 28, n. 6, p. 12–13, 2020.
- Michaelides, A.; Ranea, V.; Andres, P. D.; King, D. General model for water monomer adsorption on close-packed transition and noble metal surfaces. *Phys. Rev. Lett.*, APS, v. 90, n. 21, p. 216102, 2003.
- Mogilevsky, G.; Karwacki, C. J.; Peterson, G. W.; Wagner, G. W. Surface hydroxyl concentration on $\text{Zr}(\text{OH})_4$ quantified by ^1H mas nmr. *Chem. Phys. Lett.*, v. 511, n. 4, p. 384 – 388, 2011. ISSN 0009-2614. Available on: <<http://www.sciencedirect.com/science/article/pii/S0009261411007822>>.
- Morgano, M. A.; Faria, C. G.; Ferrão, M. F.; Bragagnolo, N.; Ferreira, M. Determinação de proteína em café cru por espectroscopia NIR e regressão PLS. *Food Science and Technology, SciELO Brasil*, v. 25, n. 1, p. 25–31, 2005.
- Murphy, P.; LaGrange, M. Raman spectroscopy of gold chloro-hydroxy speciation in fluids at ambient temperature and pressure: a re-evaluation of the effects of pH and chloride concentration. *Geochim. Cosmochim. Acta*, Elsevier, v. 62, n. 21-22, p. 3515–3526, 1998.
- Ogino, T.; Nishimura, S.; Shirakashi, J.-i. Scratch nanolithography on Si surface using scanning probe microscopy: influence of scanning parameters on groove size. *Japanese Journal of Applied Physics*, IOP Publishing, v. 47, n. 1S, p. 712, 2008.
- Ohring, M. *Materials science of thin films.*: Elsevier, 2001.
- Osman, M. B. et al. Discrimination of surface and bulk structure of crystalline hydroxyapatite nanoparticles by nmr. *J. Phys. Chem. C*, v. 119, n. 40, p. 23008–23020, 2015. Available on: <<https://doi.org/10.1021/acs.jpcc.5b08732>>.
- Padilha, A. F. *Microestrutura e propriedades*. São Paulo: Hemus, 1997.
- Park, E. D.; Lee, J. S. Effects of pretreatment conditions on CO oxidation over supported Au catalysts. *J. Cat.*, Elsevier, v. 186, n. 1, p. 1–11, 1999.
- Petty, M. C. *Molecular electronics: from principles to practice.*: John Wiley & Sons, 2008.
- Philippe, L.; Sammon, C.; Lyon, S. B.; Yarwood, J. An FTIR/ATR in situ study of sorption and transport in corrosion protective organic coatings: 1. water sorption and the role of inhibitor anions. *Prog. Org.*, Elsevier, v. 49, n. 4, p. 302–314, 2004.
- Pigliapochi, R. et al. When do anisotropic magnetic susceptibilities lead to large NMR shifts? Exploring particle shape effects in the battery electrode material LiFePO₄. *J. Am. Chem. Soc.*, v. 141, n. 33, p. 13089–13100, 2019. PMID: 31271033. Available on: <<https://doi.org/10.1021/jacs.9b04674>>.
- Ping, Z.; Nguyen, Q.; Chen, S.; Zhou, J.; Ding, Y. States of water in different hydrophilic polymers – DSC and FTIR studies. *Polymer*, Elsevier, v. 42, n. 20, p. 8461–8467, 2001.
- Raschke, T. M. Water structure and interactions with protein surfaces. *Current Opinion in Structural Biology*, Elsevier, v. 16, n. 2, p. 152–159, 2006.
- Schryer, D. R.; Vannorman, J. D.; Brown, K. G.; Schryer, J. The effects of pretreatment conditions on a Pt/SnO₂ catalyst for the oxidation of CO in CO₂ lasers. *NASA-™*, v. 103487, p. 19900016993, 1989.
- Schuetze, B. et al. Conjugation of thiol-terminated molecules to ultrasmall 2 nm-gold nanoparticles leads to remarkably complex ^1H -NMR spectra. *J. Mater. Chem. B*, The Royal Society of Chemistry, v. 4, p. 2179–2189, 2016. Available on: <<http://dx.doi.org/10.1039/C5TB02443A>>.

Schwendel, D. et al. Interaction of water with self-assembled monolayers: neutron reflectivity measurements of the water density in the interface region. *Langmuir*, ACS Publications, v. 19, n. 6, p. 2284–2293, 2003.

Shahzad, S. A.; Sajid, M. A.; Khan, Z. A.; Canseco-Gonzalez, D. Gold catalysis in organic transformations: A review. *Synth. Commun.*, Taylor & Francis, v. 47, n. 8, p. 735–755, 2017.

Sharma, R. et al. Nmr characterization of ligand binding and exchange dynamics in triphenylphosphine-capped gold nanoparticles. *J. Phys. Chem. C*, v. 113, n. 37, p. 16387–16393, 2009. Available on: <<https://doi.org/10.1021/jp905141h>>.

Shinato, K. W.; Huang, F.; Jin, Y. Principle and application of atomic force microscopy (afm) for nanoscale investigation of metal corrosion. *Corrosion Reviews*, De Gruyter, v. 38, n. 5, p. 423–432, 2020.

Steitz, R. et al. Nanobubbles and their precursor layer at the interface of water against a hydrophobic substrate. *Langmuir*, ACS Publications, v. 19, n. 6, p. 2409–2418, 2003.

Stoica, I.; Barzic, A. I.; Hulubei, C. Fabrication of nanochannels on polyimide films using dynamic plowing lithography. *Applied Surface Science*, Elsevier, v. 426, p. 307–314, 2017.

Suárez, V. I. T. et al. Sistema de microscopia com multi-pontas: força atômica e campo próximo. Universidade Federal de Alagoas, 2012.

Suh, I.-K.; Ohta, H.; Waseda, Y. High-temperature thermal expansion of six metallic elements measured by dilatation method and x-ray diffraction. *J. Mater. Sci.*, Springer, v. 23, n. 2, p. 757–760, 1988.

Swenson, J. The glass transition and fragility of supercooled confined water. *J. Condens. Matter Phys.*, IOP Publishing, v. 16, n. 45, p. S5317, 2004.

Swenson, J.; Jansson, H.; Howells, W.; Longeville, S. Dynamics of water in a molecular sieve by quasielastic neutron scattering. *J. Chem. Phys.*, American Institute of Physics, v. 122, n. 8, p. 084505, 2005.

Takei, T.; Okuda, I.; Bando, K. K.; Akita, T.; Haruta, M. Gold clusters supported on Ia (oh) 3 for co oxidation at 193 k. *Chem. Phys. Lett.*, Elsevier, v. 493, n. 4-6, p. 207–211, 2010.

Tauber, M. J.; Mathies, R. A. Resonance raman spectra and vibronic analysis of the aqueous solvated electron. *Chem. Phys. Lett.*, Elsevier, v. 354, n. 5-6, p. 518–526, 2002.

Taylor, R.; Peterson, R. D. Comparison of spin–lattice relaxation measurements made in the presence of strong radiation damping. *J. Mol. Struct.*, v. 970, n. 1, p. 155 – 159, 2010. ISSN 0022-2860. Available on: <<http://www.sciencedirect.com/science/article/pii/S0022286010002140>>.

Thomson, A. J.; Gray, H. B. Bio-inorganic chemistry. *Current opinion in chemical biology*, v. 2, n. 2, p. 155–158, 1998.

Tortonesi, M.; Yamada, H.; Barrett, R.; Quate, C. Atomic force microscopy using a piezoresistive cantilever. In: IEEE. TRANSDUCERS'91: 1991 International Conference on Solid-State Sensors and Actuators. Digest of Technical Papers. 1991. p. 448–451.

Trébosc, J.; Wiench, J. W.; Huh, S.; Lin, V. S.-Y.; Pruski, M. Solid-state nmr study of mcm-41-type mesoporous silica nanoparticles. *J. Am. Chem. Soc.*, v. 127, n. 9, p. 3057–3068, 2005. PMID: 15740145. Available on: <<https://doi.org/10.1021/ja043567e>>.

Tseng, A. A.; Notargiacomo, A.; Chen, T. Nanofabrication by scanning probe microscope lithography: A review. *Journal of Vacuum Science & Technology B: Microelectronics and*

Nanometer Structures Processing, Measurement, and Phenomena, American Vacuum Society, v. 23, n. 3, p. 877–894, 2005.

Vanderhart, D.; Earl, W. L.; Garroway, A. Resolution in ^{13}C nmr of organic solids using high-power proton decoupling and magic-angle sample spinning. *J. Magn. Reson.*, v. 44, n. 2, p. 361 – 401, 1981. ISSN 0022-2364. Available on: <<http://www.sciencedirect.com/science/article/pii/0022236481901785>>.

VandeVondele, J.; Hutter, J. Gaussian basis sets for accurate calculations on molecular systems in gas and condensed phases. *J. Chem. Phys.*, American Institute of Physics, v. 127, n. 11, p. 114105, 2007.

Vasylieva, A.; Doroshenko, I.; Vaskivskiy, Y.; Chernolevska, Y.; Pogorelov, V. Ftir study of condensed water structure. *J. Mol. Struct.*, Elsevier, v. 1167, p. 232–238, 2018.

Venables, J. Introduction to surface and thin film processes.: Cambridge University Press, 2000.

Waldron, K. J.; Robinson, N. J. How do bacterial cells ensure that metalloproteins get the correct metal? *Nature Reviews Microbiology*, Nature Publishing Group, v. 7, n. 1, p. 25–35, 2009.

Xia, X.; Xie, C.; Cai, S.; Yang, Z.; Yang, X. Corrosion characteristics of copper microparticles and copper nanoparticles in distilled water. *Corros. Sci.*, Elsevier, v. 48, n. 12, p. 3924–3932, 2006.

Xie, X. N.; Chung, H.; Sow, C.; Wee, A. Nanoscale materials patterning and engineering by atomic force microscopy nanolithography. *Mater. Sci. Eng. R Rep.*, Elsevier, v. 54, n. 1-2, p. 1–48, 2006.

Yaminsky, V.; Ohnishi, S. Physics of hydrophobic cavities. *Langmuir*, ACS Publications, v. 19, n. 6, p. 1970–1976, 2003.

Young, C.-C.; Wu, C. H.; Liu, W.-C.; Kuo, J.-T. A higher-order non-hydrostatic σ model for simulating non-linear refraction–diffraction of water waves. *Coastal Engineering*, Elsevier, v. 56, n. 9, p. 919–930, 2009.

Zhang, Y.-P.; Lewis, R. N.; Hodges, R. S.; McElhaney, R. N. Peptide models of helical hydrophobic transmembrane segments of membrane proteins. 2. differential scanning calorimetric and ftir spectroscopic studies of the interaction of ac-k2-(Ia) 12-k2-amide with phosphatidylcholine bilayers. *Biochemistry*, ACS Publications, v. 34, n. 7, p. 2362–2371, 1995.

Zhou, W.; Apkarian, R.; Wang, Z. L.; Joy, D. Fundamentals of scanning electron microscopy (sem). In: *Scanning microscopy for nanotechnology.*: Springer, 2006. p. 1–40.

CHAPTER 5

PLASMONIC RESPONSE OF GOLD- SILICA AND SILVER- SILICA METAL CORE NANOSHELLS BY OPTIMIZING THE FIGURE OF MERIT

Data de submissão: 05/04/2021

Data de aceite: 28/04/2021

Hafiz Zeeshan Mahmood

PhD Electrical Engineering
University of Central Punjab
Faisalabad Campus, Pakistan
<https://www.researchgate.net/profile/H-Zeeshan-Mahmood>

Zainab Shahid

University of Central Punjab
Faisalabad Campus, Pakistan

Alina Talat

University of Central Punjab
Faisalabad Campus, Pakistan

Imama Irfan

University of Central Punjab
Faisalabad Campus, Pakistan

Bushra Arif

University of Central Punjab
Faisalabad Campus, Pakistan

Sana Habib

University of Central Punjab
Faisalabad Campus, Pakistan

Saba Munawar

University of Central Punjab
Faisalabad Campus, Pakistan

Yasir Javed

Assistant Professor, PhD
University of Agriculture Faisalabad, Pakistan
Department of Physics
<https://www.researchgate.net/profile/Yasir-Javed-6>

Shaukat Ali Shahid

Professor and Head of Physics Department
PhD Physics
Higher Education Department
Government Graduate College of Science
Faisalabad, Pakistan
<https://www.researchgate.net/profile/Shaukat-Shahid>

Sajid Farooq

Doctor of Philosophy
Universidade de Pernambuco, UPE
50950-050, Recife, Brazil
Institute of Innovation and Technology
Escola Politécnic de Pernambuco - POLI
<https://www.researchgate.net/profile/Sajid-Farooq>

ABSTRACT: Plasmonic nanoaggregates have great potential for sensing applications, due to their spectral sensitivity response to the surrounding environment of the nanostructure and efficient extinction efficiency. A novel refractive index (RI) based SPR nano scale sensor which composed of metallic (Au/Ag) core and silica shell has been analysed theoretically. To simulate the

proposed geometry in radio frequency module, 3-D finite element method (FEM), an efficient tool to investigate the electromagnetic properties and electric field distribution surrounding the nanoparticle surface, based on commercially available software COMSOL Multiphysics were utilized. In FEM simulation, to determine the scattered field distribution and extinction cross section the nanostructure surface was divided into extremely small mesh elements which lead to finer size. The background field amplitude was fixed 1 Vm^{-1} and to restrain the simulation from any reflection, a perfectly matched layer was created around the nanostructure. We found dielectric metal nanoshells to be more absorbing with gold core compared to silver core, leading to high figure of merit (FoM) for Ag nanoshell 3.0, having the same silica shell thickness 5 nm. This result points out that our proposed multilayer geometry can be extended to other systems, enabling the plasmonic sensors have a high FoM over wide spectral ranges with phenomenal accuracy).

KEYWORDS: RI. FEM. COMSOL. FoM.

1 INTRODUCTION

The plasmonic metallic nanostructures have been extensively investigated substantial subject which stimulated the interest of the researchers due to their fascinating optical characteristics, conspicuous features linked with geometric tunability (M. Alejandro-Arellano et al., 2000), as well as advancements in particle synthesis which makes them valuable in the fields of controlled drug delivery, imaging, nonlinear optics and various biosensing modalities (Yang, X et al., 2015). An interesting phenomenon provokes when light interacts with noble metals nanostructures (Au/Ag) known as Localized Surface Plasmon Resonance (LSPR), i.e., the collective oscillations of the conduction electrons (Non- Propagating) prompted by electromagnetic radiation having a pertinent wavelength. In nanoscale regime, the resonances for Au/Ag exhibits within the visible region i.e., 400-700 nm (A. Maier, 2007).

It has been studied that Refractive index (RI) based sensitivity and figure of merit, (defined as the ratio of sensitivity to the linewidth) (Jéssica et al 2021), depends on the geometry of the Au nanoparticles (Klantsataya. E et al., 2015; Z Yang et al., 2008). For single particle LSPR sensor, the fundamental principle utilizes the fact that LSPR spectrum position varies as a function of dielectric host medium (A.D. McFarland et al., 2003; Klantsataya et al., 2015) revealed the fact narrow full width at half maximum (FWHM) will result in the enhancement of LSPR sensing behavior.

In this study, we evaluate the Au/Ag nanoshell based on gold/silver core encapsulated by silica shell having nano scale varying thickness likewise their tune ability linked with surface plasmon resonance were also theoretically investigated. The simulations were carried out by Finite Element Method (FEM) based on partial differential equations commercially available software COMSOL Multiphysics 5.2, which is an

efficient tool to explore the electromagnetic properties as well as electric field distribution on the surface of nanostructures having various shapes to predict the unprecedented dependence of the plasmonic properties of core-shell nano scale structure (Du, C, M et al., 2014). The background field amplitude was fixed 1 Vm⁻¹ and to restrain the simulation from any reflection, a perfectly matched layer was created around the nanostructure.

2 LSPR MATERIAL DEPENDENCE

The fundamental optical characteristics of metal nanoparticles may be predicted calculating their size-dependent dielectric function. The dielectric function value of a metal is influenced by its structure. As the metallic nanoparticle becomes smaller, electron scattering on the NP surface becomes more pronounced, therefore affecting the dielectric function value of the material. The complex dielectric function $\epsilon(\omega)$ can be described by Drude model, which also accounts for the conduction electrons scattered by the nanoparticle surface. Therefore, dielectric function can be written as [1]:

$$\epsilon(\omega) = \epsilon_{inter}(\omega) + \frac{\omega_p^2}{\omega(\omega + i\gamma)} \quad (1)$$

Where $\epsilon_{inter}(\omega)$ depicts interband transitions, ω_p represents plasmon frequency and γ is a phenomenological scattering parameter. The plasma frequency can be expressed for bulk metal by:

$$\omega_p = \left(\frac{Ne^2}{\epsilon_0 m_e} \right)^{1/2} \quad (2)$$

Where m_e is the effective mass of an electron, N is the number density of free electrons, e is the charge of an electron and ϵ_0 dielectric function of free space (vacuum). For nanoparticles, the scattering parameter has inherent contributions of the intrinsic properties of the material as well as from interface scattering and therefore, it can be described as $\gamma = \gamma_{bulk} + \gamma_{scat}$.

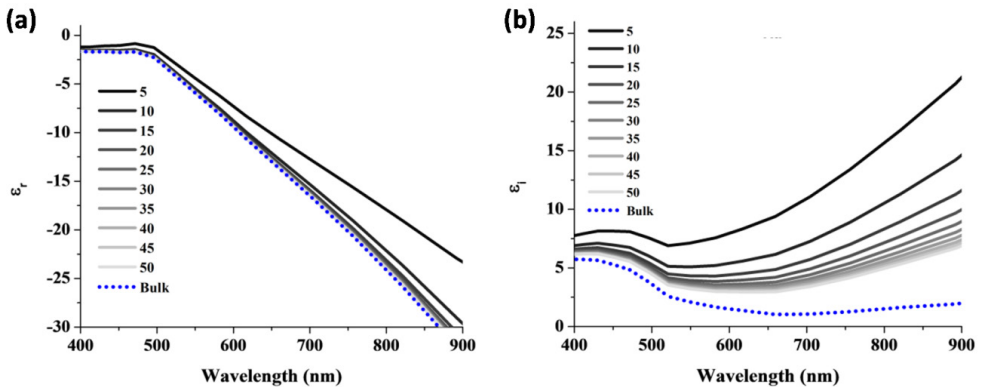
Interface scattering becomes significant when the effective electron path length L_{eff} is larger than to the nanoparticle itself (L.J. Mendoza et al 2014). The effective path length for convex shapes particles, for instance sphere, rods, cubes etc., is expressed as $L_{eff} = 4V/S$ where V is the volume and S is the surface area (Ross et al. 2015). Thus, the scattering parameter is given by $\gamma_{scat} = AV/L_{eff}$ where A is scattering efficiency (L.J. Mendoza et al 2014). For gold, $\gamma_{bulk} = 1.07 \times 10^{14} \text{ s}^{-1}$, $V_f = 1.40 \times 10^6 \text{ ms}^{-1}$, while for silver $\gamma_{bulk} = 3.22 \pm 1.22 \times 10^{13} \text{ s}^{-1}$, and $V_f = 1.39 \times 10^6 \text{ ms}^{-1}$ (P.B Johnson 1973). Table 1 depicts the radii of spheres and effective electron path lengths with respect to their sizes.

TABLE 1: NANOSPHERES RADII AND THEIR CORRESPONDING EFFECTIVE ELECTRON PATH LENGTHS (L_{eff}).

Sphere Radius (nm)	L_{eff}
5.0	6.67 nm
10.0	13.34 nm
15.0	20.00 nm
20.0	26.67 nm
25.0	33.34 nm
30.0	40.00 nm
35.0	46.67 nm
40.0	53.34 nm
45.0	60.00 nm
50.0	66.67 nm

The figure 1 depicts the dielectric functions of Au materials, considering size correction, showing that decreasing the nanoparticle radius (effective path length) both real (ϵ_r) and imaginary parts (ϵ_i) of metallic dielectric changes. The real part of dielectric function depicts the pattern of electron polarization in the medium as a consequence of incident field and determines LSPR peak position.

Figure 1. Complex dielectric function based on surface scattering of real (a) and imaginary part (b) of gold materials with different radii (5, 10, 15, 20, 25, 30, 35, 40, 45, 50 nm).



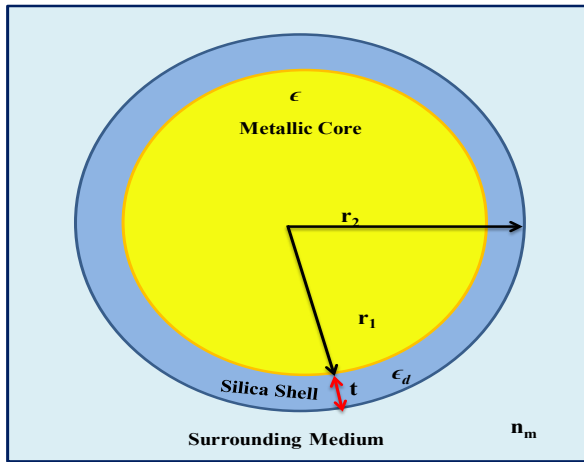
However, imaginary part ϵ_i describes energy dissipation or loss in the materials. Decreasing of the nanoparticle size leads to a lower polarizability of the metal, while increases the magnitude of ϵ_i Figure.1 (b). Therefore, higher loss is expected for metallic particle with 5nm radius than to 50 nm radius nanostructures due to surface scattering. One can notice that on decreasing effective path length (particle radius), both real and imaginary parts of $\epsilon(\omega)$ are affected. Real part of $\epsilon(\omega)$ Figure. 1(a) becomes less negative, showing that metals are less polarizable, while increase in magnitude of imaginary part

Figure.1 (b) of $\epsilon(\omega)$ causing increase in overall losses in the NP. In particular, these effects yield overall poor plasmonic metal.

3 MODELLING AND CALCULATIONS

Figure 2 illustrates the schematic geometry of Au/Ag silica coated nanoshell being investigated in this work. The inner most region is attributed as core having radius and dielectric function r_1 and ϵ respectively. The second portion represents the shell with radius r_2 and dielectric function ϵ_d , where shell thickness is given by $t = r_2 - r_1$.

Figure. 2. Schematic model of the gold/silver silica coated nanoshell.



The interaction between core-shell based metallic nanostructures and electromagnetic radiation in this study was ascribed by Mie theory which elucidated well the solution of Maxwell's equation with appropriate boundary conditions. The general solution for the potion in each region ($i= 1, 2, 3$) is expressed as in Eq. 3, (Erickson, T. A. and J. W. Tunnel, 2009):

$$V_i = \left[L_i r + \left(\frac{M_i}{r^2} \right) \right] \cos(\theta) \quad (3)$$

Where radius r , angle θ and coefficients L_i, M_i can be calculated by satisfying the boundary conditions (Averitt, R. D et al., 1999). When the dielectric function is geometrically tunable, the effect of electron scattering can be interpreted by practicing the modified bulk collision frequency as expressed in Eq. 4:

$$\Gamma = \Gamma_{bulk} + \frac{Av_f}{m_f} \quad (4)$$

Where Γ_{bulk} , m_f and v_f are collision bulk frequency, electron mean free path and Fermi velocity respectively. In case of single refractive scattering and for simple Drude model $A = 1$ (Averitt, R. D et al., 1999). For nanoshells, the bulk dielectric function can be modified to analyse the free electrons scattering, which is given by Eq. 5:

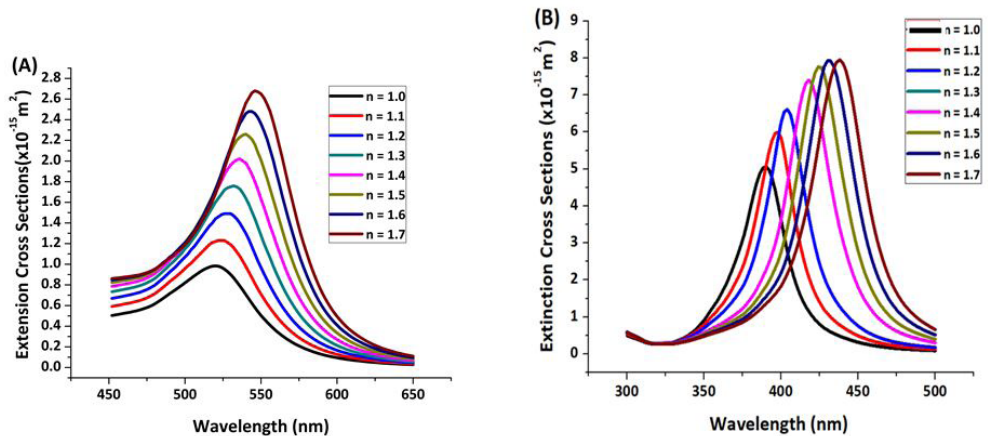
$$\epsilon(m_f, \omega) = \left(1 - \frac{\omega_{bp}^2}{\omega^2 + i\omega\Gamma}\right) + \epsilon(\omega)_{int} \quad (5)$$

Here, the second term represents the Interband transitions, ω_{bp} bulk plasma frequency and $\epsilon(m_f, \omega)$ is dielectric function (size dependent).

4 RESULTS AND DISCUSSION

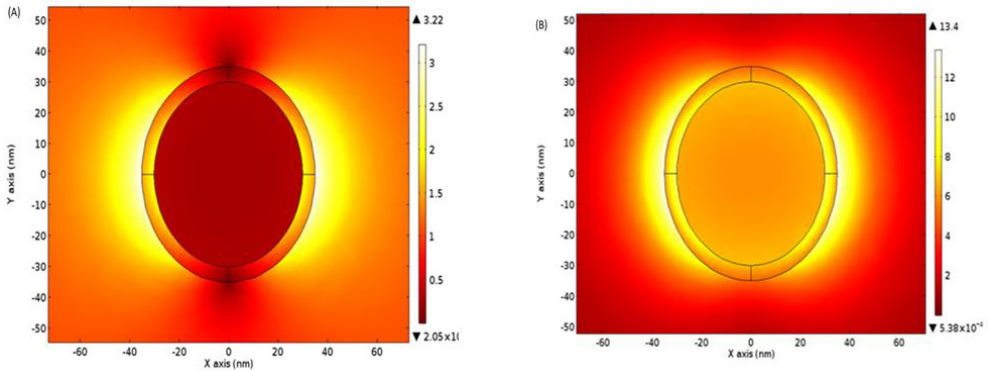
In this probed model, our focus is on the optimization of the figure of merit by varying the refractive index of the surrounding medium. Despite their simplest core-shell based structure, these metallic nanostructures can still display refractive index tunability based on their LSPR effect. Fig. 3 (A & B) depicts the response of the λ_{LSPR} and extinction spectra of Au/Ag@SiO₂ nanoshells to the refractive index of the neighbouring medium respectively. For both nanoparticles, by varying the RI the extinction varied significantly in the visible regime and exhibits red shifts which obviously results increase in the intensity of the extinction peak. In case of Au@SiO₂ shell, the extinction spectra continued to red shift in the visible region and the peak wavelength approaches 540 nm. On contrary, the extinction peak of Ag@SiO₂ shell initially blue shifted near UV regime and eventually the peak wavelength was recognizable around 430 nm in the visible region.

Figure. 3. The LSPR extinction for gold (A) and silver (B) nanoshells



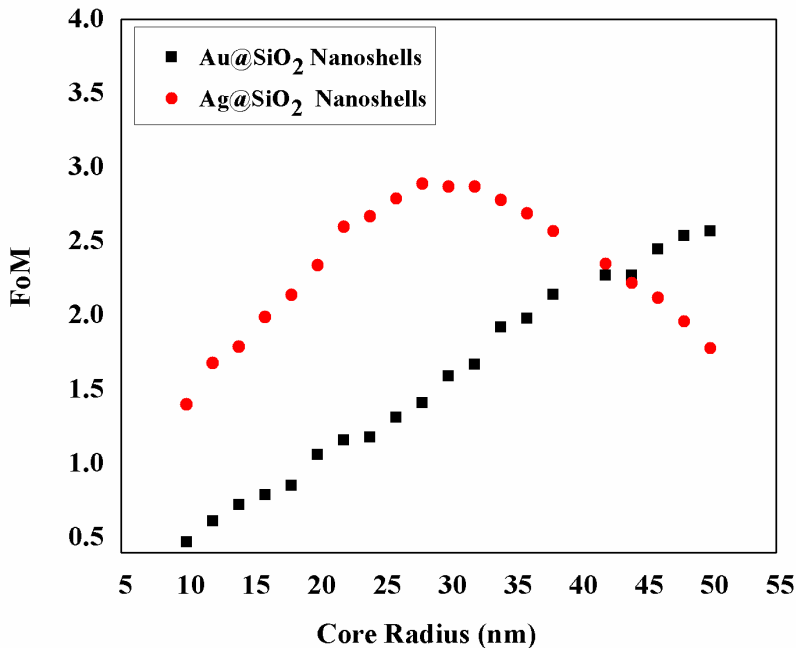
The E-field profile around the nanoshells for the dipole mode (gold and silver) can be observed in Figures 4 (A) and 4 (B) respectively. The changes in normalized electric field of nanoshells were compared at the LSPR wavelengths.

Figure. 4: Electric field profile for gold (A) and silver nanoshells (B).



For linear polarization, the electric field distribution is expressed by the two lobes which ensure the influence of plasmon dipole. LSPR peak position can be determined not only by the real part of nanostructure dielectric function, but also by the RI of the surrounding medium. In refractive index based LSPR sensors, bulk sensitivity reflects how LSPR peak position varies by changes in the RI of the local medium.

Figure. 5. Figure of merit for gold and silver nano shells



The effects of NP core radius on the FoM determining nanoparticle sensing efficiency with varying radii from 10 - 50 nm were theoretically analysed as depicted in figure 5. As the Ag nanosphere radius increases, the FWHM increase due to radiation damping factor (Hu, H., Novo et al., 2008). Therefore, FoM of Ag nanoshells decrease as the particle size grows, as shown in Figure 5. Albeit, the ϵ_i value of Ag dielectric function is less than that of Au across visible region, therefore less damping occurs, resulting narrow FWHM (Figure 2(A) and Figure 2(B) and high values of FoM for silver particles. The calculated value of FoM (3.0) of silver nanoshells ($r = 30$ nm) is higher than the reported values of more complex shapes, such as single Au nanorod (1.3) (Mayer, K.M et al., 2008), Au nanostar (1.9) (Nehl, C.L et al., 2006), Au pyramid (2.2) (Nehl, C.L et al., 2006) Ag nanocube (1.6) (Sherry, L.J et al., 2005).

5 CONCLUSION

The theoretical results indicated a nonlinear behavior of the bulk and refractive indexed based sensitivity as function of the varying shell thickness. Moreover, LSPR peak shift is also determined by changing surrounding medium and the shell thickness. Our results possess high figure of merit for silver nanoshell (3.0) as compared to gold nanoshell (2.50) having silica shell thickness 5 nm for each nanostructure. The proposed approached can be extended to engineer the efficiently use of different nanostructures on molecular biosensing.

6 ACKNOWLEDGEMENT

This work was supported by the Brazilian Agencies: Coordination for the Improvement of Higher Education Personnel (CAPES), the Brazilian National Council for Scientific and Technological Development (CNPQ), the Polytechnic School of Pernambuco, and the authors are thankful to the University of Central Punjab, Faisalabad Campus, Pakistan for their support.

REFERENCE

- A.D. McFarland, R.P. Van Duyne, Single silver nanoparticles as real-time optical sensors with zeptomole sensitivity, *Nano Lett.* 3 (2003) 1057-1062.
- Averitt, R. D., S.L. Westcott and N.J. Halas. Linear optical properties of gold nanoshells. *J optical society of America B.* 16(1999), 1824-1832.
- C. Huanjun, X. Kou, Z Yang, W. Ni, J. Wang: Shape and size dependent Refractive index sensitivity of Gold Nanoparticles, *Langmuir.* 24 (2008), 5233-5237.

- Du, C, M. Huang, T. Chen, F. Sun, B. Wang, C. He and D. Shi. Linear or quadratic plasmon peak sensitivities for individual Au/Ag nanosphere sensors, *Sens. Actuators B Chem.* 203 (2014), 812–816.
- Erickson, T. A. and J. W. Tunnel. Gold Nanoshells in biomedical Applications. *Nanomaterial for the life sciences*, WILEY-VCH. 3(2009), 1-44.
- Hu, H., Novo, C., Funston, A., Wang, H., Staleva, H., Zou, S., Mulvaney, V., Xia, Y. and Hartland, G.V. Dark-Field Microscopy Studies of Single Metal Nanoparticles: Understanding the Factors That Influence the Line Width of the Localized Surface Plasmon Resonance. *Journal of Materials Chemistry*, 18 (2008), 1949-1960.
- Jéssica E.S. Fonsaca, Mateus P. Moreira, Sajid Farooq, Renato E. de Araujo, Christiano J.S. de Matos, Daniel Grasseschi, Surface Plasmon Resonance Platforms for Chemical and Bio Sensing, Reference Module in Biomedical Sciences, Elsevier, 2021, ISBN 9780128012383, <https://doi.org/10.1016/B978-0-12-822548-6.00036-4>.
- Klantsataya, E, A. François, H. Ebendorff-Heidepriem, P. Hoffmann and T. M. Monro, Surface Plasmon Scattering in Exposed Core Optical Fiber for Enhanced Resolution Refractive Index Sensing, *Sensors*. 15(2015), 25090-25102.
- Lee, J., Hasan, W. and Odom, T.W. Tuning the Thickness and Orientation of Single Au Pyramids for Improved Refractive Index Sensitivities. *The Journal of Physical Chemistry C*, 113 (2009), 2205-2207.
- L.J. Mendoza Herrera, D.M. Arboleda, D.C. Schinca, L.B. Scaffardi, Determination of plasma frequency, damping constant, and size distribution from the complex dielectric function of noble metal nanoparticles, *J. Appl. Phys.* 116 (2014). doi:10.1063/1.4904349.
- M. Alejandro-Arellano, T. Ung, Á. Blanco, P. Mulvaney, and L. M. Liz-Marzán: Silica-coated metals and semiconductors, Stabilization and nanostructuring. *Pure Appl. Chem.* 72(2000), 257–267.
- Maier, *Plasmonics: Fundamentals and applications*, Springer, 2007.
- Mayer, K.M., Lee, S., Liao, H., Rostro, B.C., Fuentes, A., Scully, P.T., Nehl, C.L. and Hafner, J.H. A Label-Free Immunoassay Based upon Localized Surface Plasmon Resonance of Gold Nanorods. *ACS Nano*, 2(2008), 687-692.
- M.B. Ross, G.C. Schatz, Radiative effects in plasmonic aluminum and silver nanospheres and nanorods, *J. Phys. D: Appl. Phys.* 48 (2015) 184004. doi:10.1088/0022 3727/48/18/184004.
- Nehl, C.L., Liao, H. and Hafner, J.H. Optical Properties of Star-Shaped Gold Nanoparticles. *Nano Letters*, 6(2006), 683-688.
- P.B Johnson, R. W. Christy, Optical Constants of the Noble Metals, *Phys. Rev. B.* 6 (1972) 4370–4379. doi:<https://doi.org/10.1103/PhysRevB.6.4370>.
- Sherry, L.J., Chang, S.H., Schatz, G.C., Van Duyne, R.P., Wiley, B.J. and Xia, Y. Localized Surface Plasmon Resonance Spectroscopy of Single Silver Nanocubes. *Nano Letters*, 5(2005), 2034-2038.
- Yang, X., Yang, M., Pang, B., Vara, M. & Xia, Y. Gold Nanomaterials at Work in Biomedicine. *Chem. Rev.* 115(2015), 10410–10488.

CHAPTER 6

AMORPHOUS MICRO AND NANO SILICA EXTRACTED FROM RICE HUSKS AND OBTAINED BY ACIDIC PREHYDROLYSIS AND CALCINATION: PREPARATION ROUTE AND CHARACTERIZATION

Data de submissão: 20/01/2021

Data de aceite: 12/02/2021

Eduardo Roque Budenberg

Faculdade de Ciências e Tecnologia
Universidade Estadual Paulista – FCT/UNESP
Departamento de Física
Presidente Prudente/SP, Brazil.
<http://lattes.cnpq.br/5528617902631667>

Elton Aparecido Prado dos Reis

Faculdade de Ciências e Tecnologia
Universidade Estadual Paulista – FCT/UNESP
Departamento de Física, Presidente
Prudente/SP, Brazil.
<http://lattes.cnpq.br/4431600198656955>

Deuber Lincon da Silva Agostini

Faculdade de Ciências e Tecnologia
Universidade Estadual Paulista – FCT/UNESP
Departamento de Física
Presidente Prudente/SP, Brazil.
<http://lattes.cnpq.br/8933884950667644>

Renivaldo José dos Santos

Campus Experimental Rosana
Universidade Estadual Paulista
Rosana/SP, Brazil
<http://lattes.cnpq.br/0254580245173848>

Felipe Silva Bellucci

Ministério da Ciência
Tecnologia e Inovações (MCTI)
Brasília, Distrito Federal (DF), Brasil.
<http://lattes.cnpq.br/5606324184113459>

Aldo Eloizo Job¹

Faculdade de Ciências e Tecnologia
Universidade Estadual Paulista – FCT/UNESP
Departamento de Física
Presidente Prudente/SP, Brazil.
<http://lattes.cnpq.br/6475585105456744>

Daltro Garcia Pinatti

Escola de Engenharia de Lorena da
Universidade de São Paulo – EE-USP
Lorena/SP, Brazil.
<http://lattes.cnpq.br/3941372311975209>

Rosa Ana Conte

Escola de Engenharia de Lorena da
Universidade de São Paulo – EE-USP
Lorena/SP, Brazil.
<http://lattes.cnpq.br/3830856273943834>

ABSTRACT: This chapter presents the characterization of three kinds of silicas produced by three different routes of preparation (PH, C and B) in order to replace traditional Commercial Silica (Z), widely used in the Industry of Elastomer. The PH Silica was obtained by acidic prehydrolysis of rice husks. The C and B Silicas are typical ashes of rice husks commercialized as amorphous silica of rice husks and Z Silica was obtained from quartz sand. The morphological assays identified morphologically different products due to the different routes of preparation. C and B Silicas presented well-defined and

¹ Corresponding author: aldo.job@unesp.br

irregular grains, while PH and Z Silicas presented an agglomerate formation of micro and nano particles, as well as high area and surface porosity. From the analyzed material, the Z and PH Silicas were the ones, which provided higher potential for processing and dispersion because their surface area was smaller than 200 m²/g and DOP absorption higher than 235 mL/100g. Thus, the results point to a satisfactory potential for the use of PH Silica as an option to replace commercial Z silica, in addition to the possibility of adding value and allowing an environmentally acceptable disposal of the abundant waste produced by the industry of rice processing.

KEYWORDS: Rice husk Silica. Micro and Nano Silica. Silica Morphology. Comparison among Silica and reuse of waste.

MICRO E NANO SÍLICA AMORFA EXTRAÍDA DA CASCA DE ARROZ E OBTIDA POR PRÉ-HIDRÓLISE ÁCIDA E CALCINAÇÃO: ROTA DE PREPARAÇÃO E CARACTERIZAÇÃO

RESUMO: O presente capítulo apresenta a caracterização de três tipos de sílicas produzidas por rotas de preparação diferentes (PH, C e B) com o objetivo de substituir a Sílica Comercial (Z) amplamente utilizada na indústria de elastômeros. A Sílica PH foi obtida por pré-hidrólise ácida da casca do arroz, as Sílicas C e B são típicas cinzas de casca de arroz comercializadas como sílicas amorfas da casca do arroz e a Sílica-Z é obtida da areia quartzítica. Os ensaios morfológicos evidenciaram produtos finais morfológicamente distintos devidos às diferentes rotas de preparação. Para as sílicas C e B foram gerados apresentaram grãos bem definidos e irregulares enquanto que nas sílicas PH e Z houve a formação de aglomerados de micro e nano partículas como alta área e porosidade superficiais, que proporcionaram melhor potencial de processabilidade e dispersão, por apresentarem a área superficial menor que 200 m²/g e absorção de DOP maior que 235 mL/100g. Desta forma, os resultados apontam para um satisfatório potencial de utilização da Silica-PH como opção para substituição da sílica comercial Z, bem como para a possibilidade de agregar valor e permitir um descarte ambientalmente aceitável para os resíduos produzidos em abundância pela indústria de beneficiamento de arroz.

PALAVRAS-CHAVE: Sílica da casca do arroz. Micro e nano sílica. Morfologia da sílica. Comparação entre sílicas e reaproveitamento de resíduos.

MICRO Y NANO SÍLICE AMORFA EXTRAÍDA DE LA PIEL DE ARROZ Y OBTENIDA POR PREHIDROLISIS ÁCIDA Y CALCINACIÓN: RUTA DE PREPARACIÓN Y CARACTERIZACIÓN

RESUMEN: Este capítulo presenta la caracterización de tres tipos de sílices producidas por tres rutas diferentes de preparación (PH, C y B) para reemplazar la sílice comercial tradicional (Z), ampliamente utilizada en la industria del elastómero. La sílice PH se obtuvo por prehidrólisis ácida de cáscaras de arroz. Las sílices C y B son cenizas típicas de cáscaras de arroz comercializadas como sílice amorfa de cáscaras de arroz y la sílice Z se obtuvo de arena de cuarzo. Los ensayos morfológicos identificaron productos morfológicamente diferentes debido a las diferentes rutas de preparación. La sílice C y B presentó granos bien definidos e irregulares, mientras que las sílices PH y Z presentaron una formación de micro y nano partículas aglomeradas, así como una

alta porosidad de área y superficie. Del material analizado, las sílices Z y PH fueron las que proporcionaron un mayor potencial para el procesamiento y la dispersión porque su área de superficie era menor que 200 m²/g y la absorción DOP mayor que 235 ml/100g. Por lo tanto, los resultados apuntan para un potencial satisfactorio para el uso de sílice PH como una opción para reemplazar la sílice Z comercial, además de la posibilidad de agregar valor y permitir una eliminación ambientalmente aceptable de los abundantes desechos producidos por la industria del procesamiento del arroz.

PALABRAS CLAVE: Sílice de la piel de arroz. Micro y nano sílice. Morfología de sílice. Comparación entre sílice y reutilización de residuos.

1 INTRODUCTION

The growth of developing countries has tremendously increased the consumption of energy, material and food. The maintenance of the environment requires the reuse of all kinds of waste [solid, liquids, emissions, greenhouse gas (CO₂), nuclear]. The solution to these issues depends on interaction in the fields of energy, materials, food and environment; such interaction will be one of the main characteristics of the third millennium. Modern society must make a great effort to promote the rational reuse of the tailings created by industrial and agricultural processing, as well as the reuse of urban solid wastes, by transforming them into economically competitive energy together with other forms of energy. These materials must have optimized properties, always bearing in mind the environment in order to produce minimum pollution during the transformation processes [1,2].

In this context of environmental assets reuse which can be transformed into high added value material silica from rice husks (RHS) can be added as a pozzolanic material to cement to produce high performance concrete (HPC), with resistance from 90 to 120 MPa. The world RHS production has the potential to reach more than 29 million tons/year [3], which can be amplified 3.5 times if rice straw silica is exploited in a better way (10% silica and a collection rate equal to rice production). Taking into consideration that cement production is 3,300 million tons/year [4] and that the adding of 10% silica to high performance concrete (HPC 90 MPa) triplicates the resistance of simple concrete (SC 30 MPa), it can be concluded that rice straw and husk silica is enough to cater for all the demand of the civil construction market².

The production of micro and nano silica from the rice husk by the calcination process of the *in natura* husk has the following main process variables - temperature, time and combustion atmosphere. The treatment of inorganic contaminant removal is also evaluated [5]. Regarding temperature and the atmosphere of carbonization, a homogeneous distribution of nano-scale particles of silica can be obtained from the rice husk when it is burned at temperatures between 873 and 1073 K, in a pure oxygen

² [(29 x 10⁶ t of RHS/yr.d)/0.1] x 3.5 times x 3 times higher resistance = 3.1 x 10⁶ T of RHS/a

atmosphere [6]. Alternatively, micro and nano silica with a high surface area, which is essentially amorphous, can be obtained from rice husks burning at 973 K in air, since silica undergoes thermic treatment for 6 hours [7] or when burning is over, in fluidized bed boilers at temperatures lower than 800°C [8].

Amorphous Silica with a purity of 95% and an average size of 60 nm is obtained after the controlled burning of the rice husk in an atmosphere of highly purified oxygen [9,10]. In studies performed about the kinetic modeling of the pyrolysis and the effect of the treatment on rice husks with different acids (hydrochloric, sulfuric, phosphoric) concerning the purity of the silica which was obtained, it was observed that hydrochloric acid is the most effective when removing metals which are considered impurities [11]. Amorphous micro and nano silica with a purity of 99.66% was obtained using treatment with HCl 3% solution in v/v before and after carbonization for two hours in an argon atmosphere, followed by 1 hour in an oxygen atmosphere [12]. Even though the thermic route required to obtain the silica consists of simple technology, the product presents a great variety of properties due to the difficulties found when controlling the parameters of the process. In this context, the search for efficient routes of processing which are capable of modulating the final properties of the silica is worthy of note.

In this study, PH, C and B micro and nano silicas were proposed as preparation routes to be compared with commercial Z Silica obtained from quartz sand. The PH silica was obtained from the rice husk acidic prehydrolysis while C and B Silicas are typical rice husk ashes, commercialized as amorphous micro and nano silica of rice husks for the rubber and cement industry. Such materials are aimed at adding technological value and at providing a way of disposing of industrial waste. The silicas were characterized morphologically, structurally, physically and chemically and the results showed that the studied Silicas present potential to replace Commercial Z Silica, depending on the requirement needed.

2 EXPERIMENTAL SECTION

2.1 PREPARATION OF THE SILICAS

In this work three silicas (PH, C and B) were prepared for comparison with Commercial Z-Silica. Z-Silica is widely used as a reinforcement filler in the Rubber Industry and it has a large consumer market. The description of the Silica preparation is presented as follows:

PH-Silica: Amorphous silica obtained by acidic prehydrolysis of rice husks with sulfuric acid in a solution of 2% m/m at approximately 170°C. After this treatment, the material is calcined at 800°C;

C-Silica: Silica from Corradini Farm (Rio Grande do Sul State), commercially called CCA-PLUS, obtained by calcination of raw rice husks at 500°C for approximately 1 hour,

later it is ground and sifted. This process is widely used in Africa and Asia and there are many different suppliers;

B-Silica: Brazil Silica (Rio Grande do Sul State), commercially called Microsilica 500, obtained by calcination of raw rice husks at 900°C for approximately 1 hour, later it is ground and sifted; and

Z-Silica: Zeosil-125 Silica (RHODIA), commercial silica obtained by a reaction of quartz sand with sodium hydroxide in water and a precipitation with diluted sulfuric acid, later it is ground and sifted.

The high cost of chemical processes is the biggest limiting factor for a large scale application of this silica in elastomers, refractory materials and cement.

2.2 CHARACTERIZATION OF THE SILICAS

In order to evaluate the potentiality of the C, B and PH Silicas which were studied in this work as alternatives to Commercial Z Silica, a series of assays was proposed, the parameters of which are presented as follows:

Scanning Electron microscopy (SEM)

The images of Scanning electron microscopy of silica particles were obtained by using a JEOL JSM-820 microscopy, Quanta 200 model with a field emission gun (FEG). The images were taken on the sample surface.

Raman scattering spectroscopy (Raman)

The investigation of the molecular structure of the particles was carried out using a Raman scattering spectroscopy in a micro-Raman spectrophotometer, Renishaw, In-Via model in the observation region between 1800 and 1200 cm^{-1} . The exposure time of the sample to the laser was 10s, 1 accumulation, laser with wavelength equals to 785 nm and used at 100% of its power.

Oil Absorption Number

The assay of oil absorption is used to measure the porosity of the product and consists of the incorporation of the Dioctyl Phthalate Oil (DOP) (Specification: analytic purity, minimum title of 99% in ester) to the silica sample, until a well-defined absorption point is reached. DOP is added progressively in order to obtain a small cylinder of silica and DOP. As for the silica particles, the DOP index was estimated according to DOP equation ($\text{mL}/100\text{g}$) = $\{[\text{used DOP volume (mL)}]/\text{sample mass (g)}\} \times 100$.

Specific Surface (BET)

The measuring of the surface area of silica particles was carried out using a Nova 10000 model quantachrome instrument, and by the Brunauer-Emmer-Teller method (BET) founded in adsorption of N_2 by the sample surface.

Particle size distribution Analysis

For particle size analysis, Cilas equipment, model 1180L, was utilized to measure the average size of the particles and granulometric distribution by laser diffraction. For this assay, 1.00 g of sample was used.

Chemical Silica Analysis

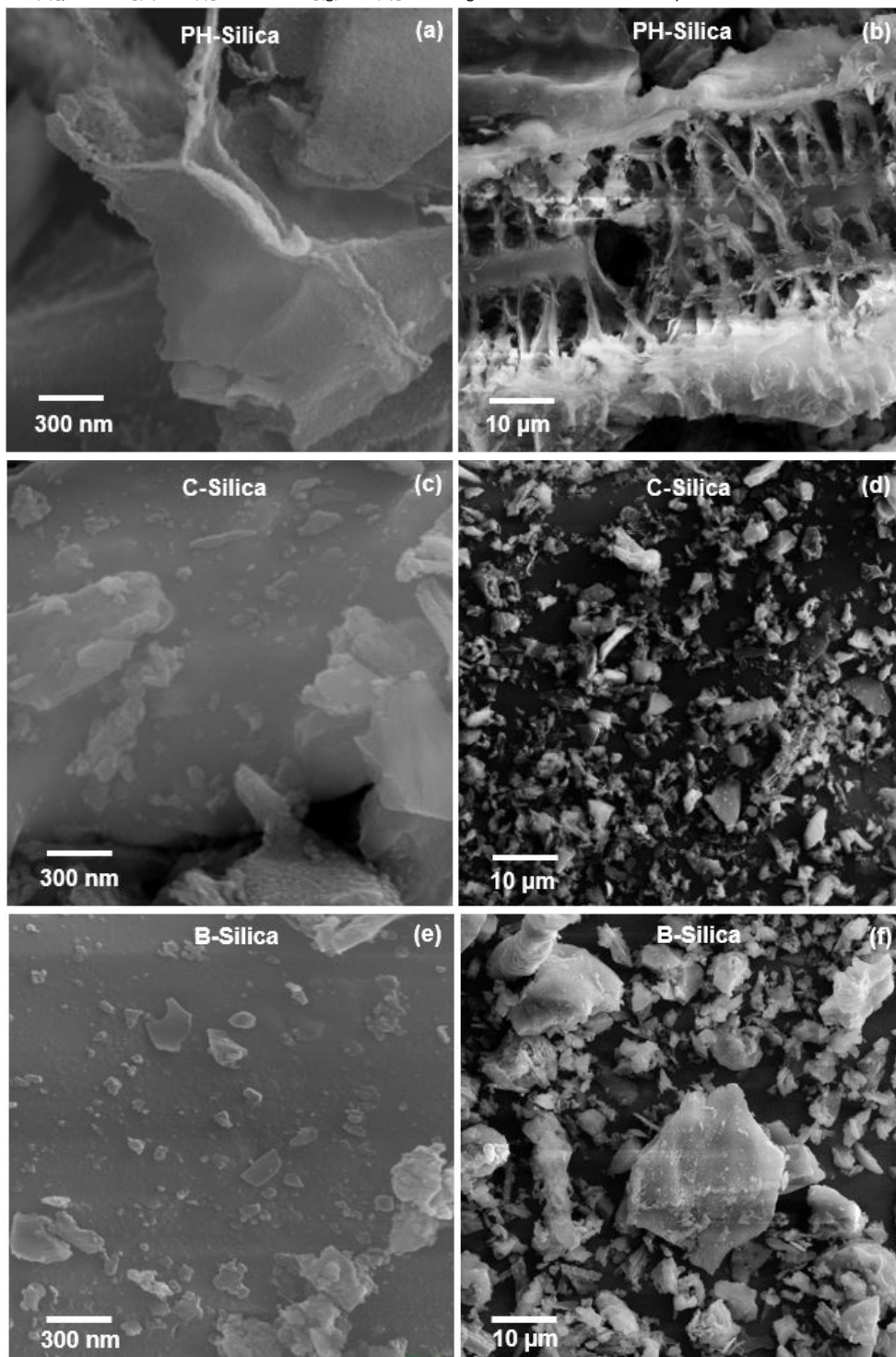
The chemical analysis of the silica was made by x-ray fluorescence spectrometry, in a Shimadzu spectrometer, model XRF1800, Rh tube. The samples used in the assay were weighted, 1.00g and patched using 50% in mass of boric-acid.

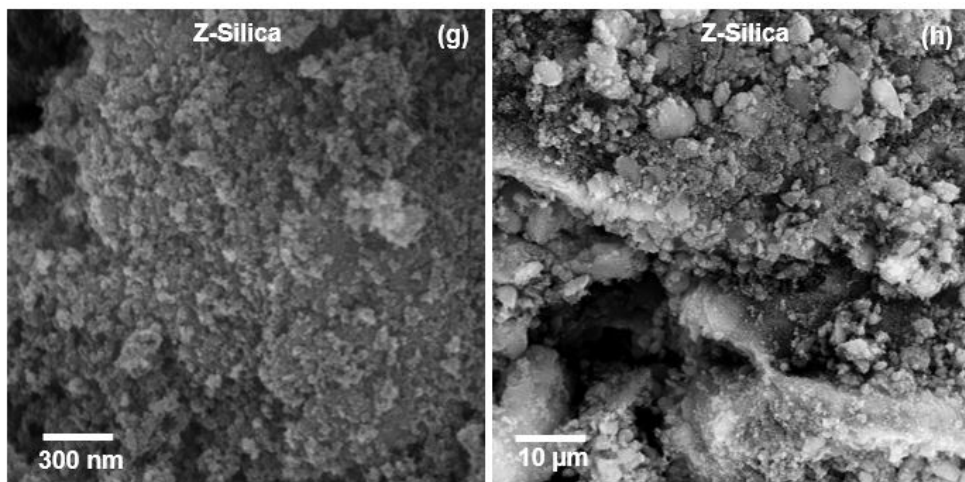
3 RESULTS AND DISCUSSIONS

3.1 MORPHOLOGICAL ASSAY FOR THE SILICAS

Electronic Microscopy techniques are typically used to evaluate the surface structure of samples due to the excellent relation resolution/preparation of the sample. Figure 1 shows SEM images of the surface of the micro and nano particles of PH-Silica [(a) and (b)], C-Silica [(c) and (d)], B-Silica [(e) and (f)] e Z-Silica [(g) e (h)]. The amplification used was equal to 25,000 and 1,000 times. As can be observed in Fig. 1, in all four types of primary particles, the geometry is approximately non spherical due to the growing mechanism of the particle (nucleation) predominant in ceramic materials and to the principle of surface energy minimization. Therefore, if the thermal energy source were maintained, an increasing in the grain size via the coalescence phenomenon would be expected, together with a reduction in the numbers of grains, a reduction in the grain boundary area and, therefore, the surface energy would decrease. The use of different routes for the silica preparation generated some final micro and nano materials, which were morphologically different. In the case of C and B silicas, very-well defined grains were observed, although somewhat irregular, with low surface porosity. In the case of PH and Z silicas, the formation of an agglomerating of particles was identified, which is typical of a chemical route synthesis, as well as high area and surface porosity. Different morphological characteristics provide different surface properties, such as surface energy, zeta potential, interaction with radiation, different coefficients of thermal diffusion and different capability of chemical absorption, besides the capability of significantly altering the mechanical properties of polymeric matrices, such as synthetic and natural rubber [13]. For both observed structures, their dimensions are in the micrometer and nanometer scales and they are coherent with the diameter of particles previously reported in scientific literature [14,15].

Figure 1. Scanning electron microscopy images from the surface of the particles of PH-Silica [(a) and (b)], C-Silica [(c) and (d)], B-Silica [(e) and (f)] and Z-Silica [(g) and (h)]. The magnifications utilized were equal to 25.000 and 1.000 times.

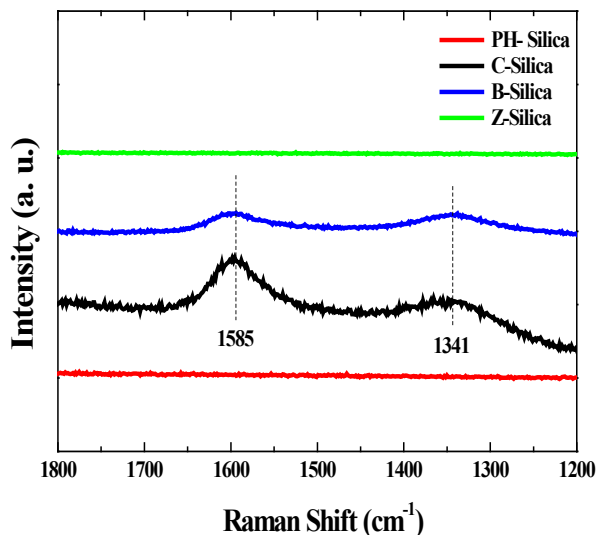




3.2 STRUCTURAL CHARACTERIZATION OF THE SILICAS

Low cost of the equipment, high accuracy results, low necessity of sample preparation, wide range of usage and easy handling. The Raman spectra with a wavelength between 1800 and 1200 cm^{-1} for PH-Silica, C-Silica, B-Silica and Z-Silica particles are shown in Figure 2. The Raman spectrum for silica particles presents a typical profile of amorphous material due to the non-resolution of the peaks in the region of low wavenumber. The nonresolution of peaks is also related to the fluorescence phenomenon, due to the presence of organic matter, originated from chemical synthesis processing, especially carbonic groups, such as those identified through chemical analysis shown in Table 3. For B and C silica samples, two low resolution and intensity bands were identified, characterizing the formation of a short-range ordering state. Such observation corroborates the microscopy images in Fig 1, in which the difference between the PH and Z silica morphology is clear, with agglomerates of particles, and C and B Silicas, with well-defined micro and nano grains. Both bands or superposition of bands with maxima in 1341 and 1585 cm^{-1} , are associated to vibrations of carbon-carbon bond and carbon-silica, as studied by T. Narushima *et al* [16]. From a morphological point of view, Fig 1, and structure, Fig. 2, The PH Silica resembles commercial Z Silica, reflecting the potential for the use of the silicas proposed in this work.

Figure 2. Raman spectra with wavelength between 1800 and 1200 cm^{-1} at room temperature for PH-Silica, C-Silica, B-Silica and Z-Silica micro and nano particles. Utilized laser: $\lambda = 514 \text{ nm}$ and 10s of sample exposition.



3.3 PHYSICAL AND CHEMICAL PROPERTIES

The physical and chemical properties of the materials reflect the characteristic behavior of the material when submitted to physical stimuli or when in contact with other substances. Such properties determine the range of technological uses of the material and can be modulated to improve the relation property/application. Table 1 lists the physical and chemical parameters pH, specific surface area and oil adsorption (DOP) of the PH-Silica, CSilica, B-Silica and Z-Silica. According to the data listed in Tab. 1, as expected and desired, the PH, C and Z silicas presented a neutral character, around 7, while B-Silica presented a basic character, $\text{pH} = 10.4$. It is suggested that the basic character of the B-Silica sample is a result of excess organic matter which originated from thermochemical processing, mostly in the case of magnesia (MgO), which is well known for its basic pH. From the perspective of material processing and the use of micro and nano silica as a burden in polymeric matrices, it is desirable to have pH values close to 7, neutral in character, in order to avoid interference in the curing process or in the matrix polymer chain. As for the surface area, estimated in this work via BET, values higher than $100 \text{ m}^2/\text{g}$ are currently considered satisfactory for a good dispersion in the polymer matrix, besides assuring an adequate surface activity to interact with other materials. Out of the materials which were prepared, only the B-Silica samples presented low values of surface area, which were possibly associated to micrometric scale and, predominantly, to the smallest amorphous character of the material as identified by SEM images. Once

the oil absorption (DOP) assays had reflected the combination between the surface area parameters, surface porosity and particle size variation, the B-Silica sample presented the lowest value of oil absorption (DOP), due to its low area and porosity surface, see Fig. 1 (f), while the Z-Silica sample presented the highest value of the same parameter, resulting mainly from high area and porosity surface, see Fig. 1 (h). According to A. Blume *et al* [17], a good estimative of the silica processability and dispersion in polymer matrix results from the combination of the surface area and the oil absorption (DOP). According to this correlation, silicas with good processability or dispersion are the ones which present a surface area which is smaller than 200 m²/g and oil absorption (DOP) which is higher than 235 mL/100g. It is worth emphasizing that it would be possible to adjust the processing parameters of the PH-Silica by introducing grinding and micronizing stages in order to adjust its surface characteristics to those of Z-Silica.

Table 1. List of physical and chemical parameters pH, BET and DOP absorption for PH-Silica, C-Silica, B-Silica and Z-Silica particles.

Samples	Physical and Chemical Properties		
	pH	Specific Surface Area (m ² /g)	DOP Absorption (mL/100g)
PH-Silica	6.9	94.2	112
C-Silica	7.5	112.0	84
B-Silica	10.4	25.1	66
Z-Silica	7.0	120.4	250

The grain size analysis of the particulate materials reports the distribution and the percentage frequency of dimensional occurrence of the grains or agglomerates. Thus, it is possible to estimate the interaction profile of the particles and particle/matrix, reactivity and average size of the particulate material. Table 2 lists the grain size distribution (size of particles and aggregates) whereas Figure 3 shows the evolution of the granulometry to the PH-Silica, C-Silica, B-Silica and Z-Silica particles. In Fig. 3 the average particle size of each of the samples studied are listed. Once Z-Silica had become the commercial material with the desired set of properties, it was used as reference and comparison material. It was observed that the PH-Silica presents an average particle diameter which is bigger than Z-Silica, see Tab. 2 and Fig. 3. This fact indicates that, if this kind of burden were inserted into a polymer matrix, such as SBR 1502 rubber, inferior mechanical properties would be expected when compared with composites of Z-Silica. This is partly due to

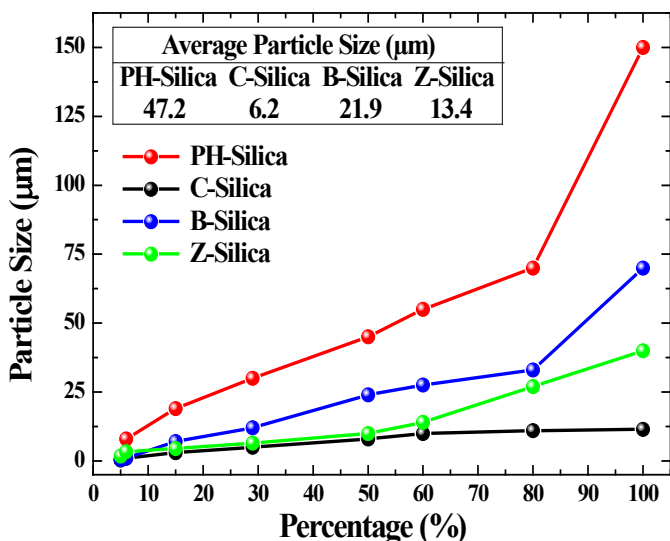
the lesser availability of the silanol groups to interact with the polymer matrix. When comparing the size of the particles, it is seen that the PH-Silica particle is 3.5 times bigger than the Z-Silica particle, demonstrating that in order to become similar to the PH-Silica properties, it would be necessary to insert micronizing stages in the preparation process of the PH-Silica. As for value adding, it is considered that the insertion of micronizing stages presents a favorable benefit-cost ratio, once it is possible to convert rice husk waste into particulate burden in a well-defined consumer market.

Table 2. Grain size distribution (particle and aggregate size) for PH-Silica, C-Silica, B-Silica and Z-Silica particles.

	%	Samples			
		PH-Silica	C-Silica	B-Silica	Z-Silica
Particle Size Distribution: Particle size (µm) for each percentage value (%)*	0.5	0.5	0.4	0.5	1.8
	6	8.0	1.0	1.0	3.4
	15	19.0	3.0	7.0	4.5
	29	30.0	5.0	12.0	6.5
	50	45.0	8.0	24.0	10.0
	60	55.0	10.0	27.5	14.0
	80	70.0	11.0	33.0	27.0
	100	150.0	11.5	70.0	40.0

* Example: 50% of the PH-Silica sample has particle size up to 45.0 µm.
80% of the Z-Silica sample has particle size up to 27.0 µm.

Figure 3. Evaluation of grain size for PH-Silica, C-Silica, B-Silica e Z-Silica particles.



The chemical analysis of the materials allows the chemical species present in the samples to be identified, besides establishing the relative quantity of each species. Table 3

shows the chemical composition of the PH-Silica, C-Silica, B-Silica and Z-Silica. Regarding the components from a quantitative point of view, it is possible to observe that the silicas display very different compositions, mainly due to the level of SiO₂. PH and Z silicas present high levels of SiO₂, which indicate the similarity between them, while the amorphous silica B and C display a 20% lower quantity of SiO₂. Besides, they are rich in different metals, which, when in oxide form interact, with SiO₂ and reduce the level of silanol. The fact that the B and C Silicas present considerable levels of carbon is also noteworthy, 18.55%w/w and 16.27%w/w, respectively, probably because of incomplete combustion of the rice husks organic fraction, but which can also bring functionality to these materials regarding their electrical and thermal conductivity. When comparing PH and Z Silicas, it is observed that the PH-Silica presents low levels of trace elements (Ca, Fe, Al, S, P and K), while Z-Silica is 100% SiO₂. It is expected that the presence of trace elements in particulate burdens will provide a poorer mechanical performance of the composite when facing the properties of composites which are prepared with pure burdens.

Table 3. Chemical composition of PH-Silica, C-Silica, B-Silica and Z-Silica particles.

Compounds present in samples of Silica	Concentration (%w/w)			
	PH-Silica	C-Silica	B-Silica	Z-Silica
SiO ₂	99.1	80	80	100
CaO	0.3	0.5	0.5	ND
MgO	0	0.8	0.28	ND
Fe ₂ O ₃	0.06	ND	0.1	ND
Al ₂ O ₃	0.18	0.15	0.65	ND
Na ₂ O	ND*	ND	ND	ND
K ₂ O	0.06	ND	0.88	ND
TiO ₂	ND	ND	0.02	ND
MnO	ND	ND	0.2	ND
SO ₃	0.22	ND	0.3	ND
P ₂ O ₅	0.08	ND	0.8	ND
Carbon	ND	18.55	16.27	ND
Total	100	100	100	100
Water insoluble salts	ND	ND	1.03	1.2
Humidity	2.0	1.0	2.3	5.0

* ND = Not Detected.

3.4 SPECIFIC DENSITY OF SILANOL GROUPS

Silanol groups are derived from silanes in which a hydroxyl group replaces a hydrogen, Si_nH_(2n+1)OH, where n is the number of atoms of Si. Silanol groups can be

of isolated, vicinal and germinal types. The germinal type presents the most reactive surface of the three [18]. According to L. T. Zhuravlev [19] and C. Airoidi *et al* [20], the physical constant which relates the quantity of hydroxyl groups per molecule area can be considered equal to 5.0 OH/nm² in all kinds of silica. Taking this into account, a good estimative for the density of silanol groups in mol.OH/g can be obtained using the surface area of the silica in m²/g and the constant to the above cited silicas (5.0 OH/nm² x 10¹⁸ nm²/m² = 5.0x10¹⁸ OH/m²), as listed in Table 4. When analyzing the data of Tab. 4, it is verified that, in the second column (nr. of mol OH/g *with* carbon) for B and C Silicas, the number of OH/g moles has been calculated considering the surface of “silica + carbon”, once B and C silicas contain about 17-18% of carbon weight, see Tab. 3. However, the silanol groups are only found on the silica surface. For this reason, the number of OH/g moles without carbon (last column) was estimated. Probably the K₂O, Na₂O, CaO, and MgO impurities decreased the quantity of silanol and the other impurities were considered inert.

Table 4. Specific density of silanol groups for PH-Silica, C-Silica, B-Silica and Z-Silica particles.

Silicas	Specific Surface Area (m ² /g)	no. mol OH/g com carbono	no. mol OH/g sem carbono
PH-Silica	94.2	7.82x10 ⁻⁴	7.82x 10 ⁻⁴
C-Silica	112.0	9.29x10 ⁻⁴	7.44x10 ⁻⁴
B-Silica	25.1	2.08x10 ⁻⁴	1.67x10 ⁻⁴
Z-Silica	120.4	9.99x10 ⁻⁴	9.99x10 ⁻⁴

3.5 POTENTIAL APPLICATION TO THE PH-SILICA

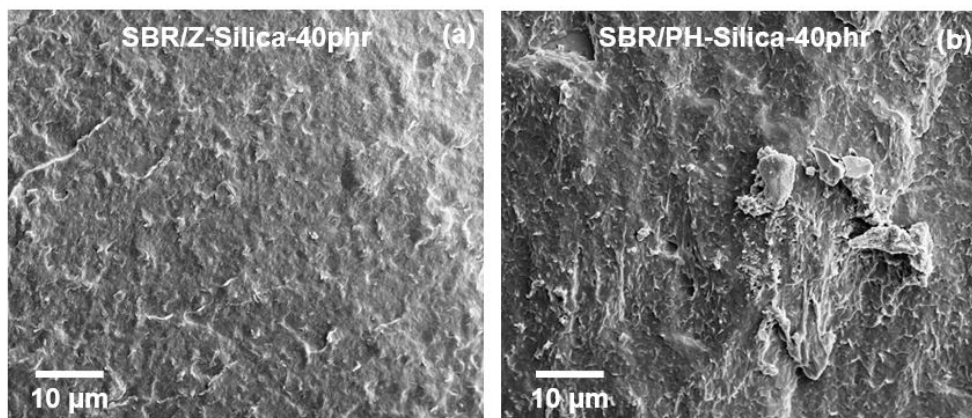
Aiming to evaluate the potential utilization of PH-Silica as a possible replacement for commercial silica, Z-Silica, in styrene-butadiene rubber (SBR) formulation, exploratory tests utilizing composites based on SBR rubber loaded with 40 phr (parts per hundred rubber) of Z-Silica (SBR/Z-Silica-40phr) or of PH-Silica (SBR/PH-Silica-40phr) were carried out. Figure 4 and Table 5 respectively, show images of scanning electronic microscopy (SEM) of micro and nano composites and some main mechanical parameters for both samples. As can be seen in the SEM images, a satisfactory dispersion could be observed for both composites, as well as, a good coupling between particles and polymeric matrix with a low quantity of remnant silica particles with a diameter size of 3 μm, almost 5 times lower than the initial diameter size of silica (13.4 μm), indicating a deagglomeration dispensation due to the mechanical processing of the composites [21]. From a mechanical point of view, differences of more than 20% were not obtained, with

the exception of the tensile strength at break and elongation at break. However, it should be noted that the materials are not strained to breaking point in normal applications and the lowering of breaking stress does not undermine the material in comparison to its enhancement in elastic properties. Thus, from the mechanical and morphological points of view, the PH-Silica particles exhibit a potential to replace Z-Silica (commercial) particles in the SBR rubber industry. A more detailed study concerning the mechanical and morphological properties will be presented in a future publication.

Table 5. Exploratory testing to evaluate the potential of replacement of commercial silica to PH-Silica in samples of styrene-butadiene rubber (SBR). List of mechanical parameters comparing samples of SBR rubber loaded with 40 phr of Z-Silica and PH-Silica.

Parameter	Mechanical Properties	
	SBR/Z-Silica-40phr	SBR/PH-Silica-40phr
Hardness Shore A	61	53
Permanent Deformation (% for 22h/100 °C)	21.8±3.2	29.7±1.5
Abrasion Index (mm ³ /40m)	66.4±10.5	101.4±15.5
Mooney Viscosity (ML 1+4) 100°C	112.8	95.2
Tensile Strength (MPa) at 100%	2.0±0.3	2.1±0.1
Tensile Strength (MPa) at 300%	7.8±0.7	5.3±0.1
Tensile Strength at break (MPa)	15.1±0.1	3.1±0.1
Elongation at break (%)	870.9±10.5	497.7±41.5

Figure 4. Exploratory testing to evaluate the potential of replacement of commercial silica to PH-Silica in samples of styrene-butadiene rubber (SBR). (a) Images of SEM for SBR rubber loaded with 40 phr of Z-Silica (SBR/Z-Silica-40phr) and (b) images of SEM for SBR rubber loaded with 40 phr of PH-Silica (SBR/PH-Silica-40phr).



4 CONCLUSIONS

The thermochemical route (acidic prehydrolysis followed by calcination at 800°C) for production of rice husk micro and nano silica showed that it is possible to obtain material with morphological, physical and chemical characteristics which are capable of replacing commercial silica for application in elastomers. The results of the characterizations obtained indicate micronizing as a mandatory stage in order for the PH Silica to have a similar performance to Z-Silica. The initial objective of transforming a highly pollutant environment liability into an additive in the rubber industry was achieved, making large scale supply possible in a competitive cost in comparison with the quartz sand silica. In addition to obtaining PH-Silica, it is possible to obtain an amorphous silica for a cement application and also generates electric energy in an integrated industrial plant using rice husks as a raw material.

5 ACKNOWLEDGEMENTS

The authors acknowledge the Brazilian research agencies: FAPESP, CAPES, CNPq and FEPISA for their financial support.

REFERENCES

- [1] OZORIO, M. S.; REIS, E. A. P.; TEIXEIRA, S. R.; BELLUCCI, F. S.; JOB, A. E. Sugarcane bagasse ash as a reinforcing filler in thermoplastic elastomers: Structural and mechanical characterizations. **J. Appl. Polym. Sci.**, 132, 41466, (2015).
- [2] ALMEIDA, F. C. L.; BRENNAN, M. J.; PASCHOALINI, A. T.; SANTOS, V. M.; BELLUCCI, F. S.; JOB, A. E. An analytical investigation into the use of magneto-rheological elastomers to suppress flexural waves in beams. **Procedia Engineering**, v. 199, p. 1338-1343, 2017.
- [3] AGRICULTURA RURAL. Produção mundial de arroz. 2012. <<http://agricultura.ruralbr.com.br/noticia2012/06/producao-mundial-de-arroz-deve-ser-maior-na-safra-2012-2013-3791504.html>>. Accessed on: 03 Mar. 2013.
- [4] CIMENTO. Produção mundial de cimento. São Paulo, 2013. <<http://www.cimento.org/site/cimentomundo.html>>. Accessed on: 20 Mar. 2013.
- [5] CHAVES, M. R. M. Preparação da sílica organofuncionalizada a partir de casca de arroz com capacidade adsorvente de íons metálicos. 2008, 118 f. Tese (Doutorado em Engenharia Química) - Escola Politécnica, Universidade de São Paulo, São Paulo, 2008.
- [6] REAL, C.; ALCALÁ, M. D.; CRIADO, J. M. Preparation of silica from rice husk. **J. Am. Soc.**, 79, 2012-2016, 1996.
- [7] DELLA, V. P.; KÜLN, I.; HOTZA, D. Rice husk ash as an alternative source for active silica production. **Mater. Lett.**, 57, 818-821, 2002.
- [8] PINATTI, D. G.; Marton, L. F. M.; Pilecco, O. Processo de produção de sílica de casca de arroz fluidizada e respectivo produto resultante, **PI 1101915-8 A2**, setembro 2012, 35 p.

- [9] LIOU, T-H. Evolution of chemistry and morphology during the carbonization and combustion of rice rusk. **Carbon**, 42, 785-794, 2004a.
- [10] LIOU, T-H. Preparation and characterization of nano-structured silica from rice rusk. **Mater. Sci. Eng. A.**, 364, 313-323, 2004b.
- [11] LIOU, T-H.; CHANG, F.W.; LO, J-J. Pyrolysis kinetics of acid-leached rice rusk. **Ind. Eng. Chem. Res.**, 36, 568-573, 1997.
- [12] YALÇIN, N.; SEVINÇ, V. Studies on silica obtained from rice husk. **Ceram. Int.**, 27, 219-224, 2001.
- [13] BELLUCCI, F. S.; BUDEMBERG, E. R.; NOBRE, M. A. L.; DE SAJA, J. A.; AROCA, R. F.; RODRÍGUEZ-PÉREZ, M. A.; JOB, A. E. Mechanical Properties of Vulcanized Natural Rubber Nanocomposites Containing Functional Ceramic Nanoparticles. **Sci. Adv. Mater.**, 5, 6, 637-646, 2013.
- [14] REAL, C.; ALCALÁ, M. D.; CRIADO, J. M. Preparation of Silica from Rice Husks. **J. Amer. Ceram. Soc.**, 79, 8, 2012-2016, 1996.
- [15] BELLUCCI, F. S. Caracterização dielétrica de partículas nanométricas e nanoestruturadas de óxido de niobato da família tetragonal tungstênio bronze com estequiometria $\text{KSr}_2\text{Nb}_5\text{O}_{15}$. 185p. Dissertation (Master in Science and Technology), UNESP, Presidente Prudente, 2009.
- [16] NARUSHIMA, T.; GOTO, T.; MARUYAMA, M.; ARASHI, H.; IGUCHI, Y. Oxidation of Boron Carbide–Silicon Carbide Composite at 1073 to 1773 K. **Mater. Trans.**, 44, 3, 401-406, 2003.
- [17] BLUME, A. A key for understanding silica reinforcement. **Applied Technology Advanced Fillers**. Zuerich: Evonik Degussa International AG. 1999, p.1-7.
- [18] ILER, R. K. The chemistry of Silica, **John Wiley & Sons, New York**, 1979.
- [19] ZHURAVLEV, L. T. The surface chemistry of amorphous silica. Zhuravlev model. **Colloids and Surfaces A: Physicochemical and Engineering Aspects**, 173, 1-3, 1–38, 2000.
- [20] AIROLDI, C.; FARIAS, R. F. O uso de sílica gel organofuncionalizada como agente sequestrante para metais. **Química Nova**, 23, 4, 496-503, 2000.
- [21] BELLUCCI, F. S.; ALMEIDA, F. C. L.; AGOSTINI, D. L. S.; NOBRE, M. A. L.; PASCHOALINI, A. T.; JOB, A. E. Evolution of thermal properties of natural rubber nanocomposites functionalized by nickel-zinc ferrite and potassium strontium niobate nanopowders. **J. Therm. Anal.**, 126, 1397-1406, 2016.

CHAPTER 7

FORMATION OF METAL NANOPARTICLES BY SPUTTER DEPOSITION ON UNCD FILMS BY NPIII INSIDE CONDUCTIVE TUBES

Data de submissão: 29/03/2021

Data de aceite: 16/04/2021

Nazir Monteiro dos Santos

National Institute for Space Research
Associated Laboratory of Plasma
São José dos Campos, SP, Brazil
nazirmonteiro@gmail.com
<https://orcid.org/0000-0002-1518-9403>

Divani Carvalho Barbosa

Faculty of Technology of Taubaté
State Center for Technological Education
Paula Souza
Taubaté, SP, Brazil
divanibarbosa@gmail.com
<https://orcid.org/0000-0003-4938-4095>

Evaldo José Corat

National Institute for Space Research
Associated Laboratory of
Materials and Sensors
São José dos Campos, SP, Brazil
evaldo.corat@inpe.br
<https://orcid.org/0000-0003-3011-5522>

Mario Ueda

National Institute for Space Research
Associated Laboratory of Plasma
São José dos Campos, SP, Brazil
mario.ueda@inpe.br
<http://lattes.cnpq.br/9226460532838417>

ABSTRACT: Surface modification of ultrananocrystalline diamond (UNCD) films by Nitrogen Plasma Immersion Ion Implantation (NPIII) using conductive tubes was studied. UNCD films were deposited on titanium substrates by CVD process using a hot filament reactor. The UNCD films were treated by NPIII inside stainless steel metallic tubes. The tubes, with 150 mm of length and different diameters, containing the UNCD films were placed in the interior of vacuum chamber of 600 liters. Field Emission Gun Scanning Electron Microscopy (FEG-SEM) with Energy Dispersive Spectroscopy (EDS) auxiliary, X-Ray Diffraction (XRD), Raman Scattering Spectroscopy (RSS), and X-ray Photoelectron Spectroscopy (XPS) were used to investigate the effect of NPIII treatment on UNCD films. The results showed that the NPIII treatment changed the surface morphology of UNCD films, increased the degree of disorder and the structural defects, and the formation of metallic nanoparticles by sputter deposition of the materials from the conductive tubes. Surface analysis have also demonstrated substantial dependence of NPIII with the conductive tubes diameter. For the UNCD film treatment by NPIII inside tube with diameter of 110 mm (T110), there was formation of metal oxide and nitride layers on the surface. For the treatment carried out inside the tube with a diameter of 40 mm (T40), there was implantation of metallic particles, indicating that the surface of the UNCD films was completely covered by iron (Fe^o).

KEYWORDS: Plasma Immersion Ion Implantation. Surface Modification. Ultrananocrystalline Diamond Films. Conductive tubes.

1 INTRODUCTION

Plasma immersion ion implantation (PIII) is a well-known technique used for the three-dimensional surface modification of materials by ion implantation [1]. Recently, new developments in PIII using conductive tubes have been attained [2]. Both moderate (< 450 °C) and high temperature (> 700 °C), PIII inside tubes are now possible. Tube temperature is dependent on the diameter when hollow cathode plasma is produced inside it for PIII treatments of the tube walls, components or samples. Hollow cathodes are also providing plasmas for materials surface modifications [3], in particular, using PIII method in tubular or concave geometry samples or workpieces [4]. UNCD films have been the subject of large interest in the scientific community, motivated by their exceptional properties for tribological [5], mechanical [6, 7], biomedical [8] and electronic [9] applications. This interest is especially due to their high smoothness, electron field emissivity [10], as well as their unique capability to incorporate n-type dopants [11, 12]. Nitrogen atoms, adsorbed in diamond, upon equilibration at elevated temperatures tend to enrich at the surface and at grain boundaries. Adsorbed nitrogen atoms on UNCD surfaces strongly affect their physico-chemical properties and phenomena as surface energy, morphology, equilibrium shape, surface diffusion and sintering, adhesion and wear, surface reactivity and corrosion, metal-gas reactions and catalytic reactions [13]. In addition, adsorption at grain boundaries strongly influences materials properties, and the adsorbed nitrogen atoms are of special interest as effective semiconductor. Nitrogen incorporation in the UNCD structure is recognized to affect most of the film properties, including changes in the tribological behavior, molecular structure and chemical bonds. Nitrogen incorporation results in the enhanced adhesion strength of UNCD films by increasing sp^2 bonds and subsequently relaxing residual stress in the films [14]. In addition, the tribological performance of UNCD films can be improved by nitrogen incorporation because promotes the graphitization of the films and could be used in protective and coating technologies.

In this study, we have been exploring NPIII treatment using different size stainless steel (SS)304 tubes with diameters of 110 mm (T110) and 40 mm (T40) with length of 150 mm for the surface modification of UNCD film. PIII is a powerful tool for adding impurities to a host material. We attempt to elucidate the effects of NPIII treatment on the structural, morphological, and chemical properties of UNCD films. The results shows that the structure of UNCD film surface was modified by NPIII treatments and metallic nanoparticles were implanted by sputter deposition. This treatment can certainly include

other species that would give UNCD films with other properties and applications including enhanced magnetic UNCD.

2 EXPERIMENTAL

2.1 SUBSTRATE PRETREATMENT

To improve the adhesion of the diamond film on the titanium substrate and the nucleation density during growth of the films, we performed a pre-treatment on the surface of substrates, which consists of a mechanical incision by blasting with glass beads, whose main objective is to increase roughness [15]. After this, the substrates (15 mm x 15 mm x 1 mm) were cleaned with acetone in an ultrasonic bath in order to remove grease or any other contaminants. Soon after, the substrates were prepared for growth by plating with nanometric diamond powder in ultrasonic hexane bath during 60 minutes to enhance diamond nucleation.

2.2 UNCD FILMS PRODUCTION

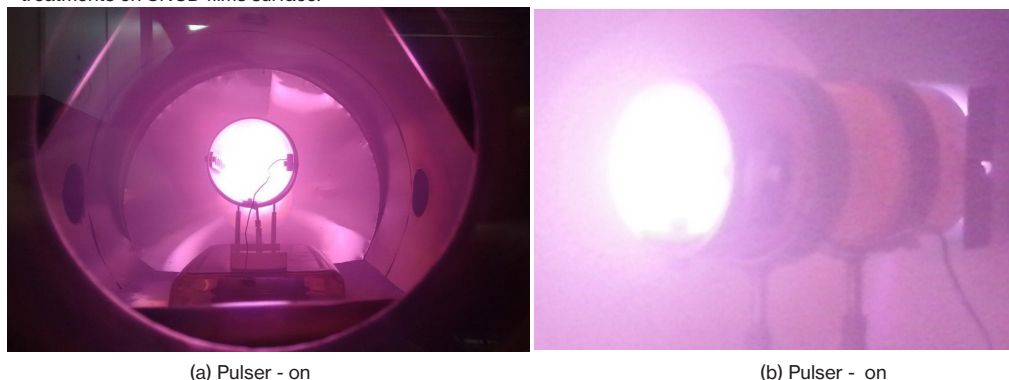
Ultrananocrystalline diamond (UNCD) films were produced on titanium substrate using Hot Filament Chemical Vapor Deposition (HFCVD) technique. The films were carried out using an experimental system from the Associated Laboratory of Sensors and Materials/Group of Diamond and Related Materials at National Institute for Space Research. The experimental setup is composed of the reactor made of a stainless steel cylindrical shape chamber with Pyrex windows and copper coil through which cooling water circulates. The internal layout of the reactor consists of five filament of tungsten with diameter of 125 μm supported by two brackets of molybdenum and a gas inlet tube located just above the region of the filaments. The distance between the filaments and the substrate was 5 mm and the deposition time was 7 h. The chemical process included treatments in $\text{CH}_4/\text{H}_2/\text{Ar}$ gases with 9 vol.% hydrogen, 1 vol.% methane and 90 vol.% argon at a total flow of 200 sccm (standard centimeter cubic per second). The temperature and the pressure inside the reactor were maintained at 750 °C and 30 Torr, respectively. Details of deposition set-up and procedure have been described earlier [16]

2.3 UNCD FILMS TREATMENT BY NPIII INSIDE CONDUCTIVE TUBES

UNCD films were treated during 120 min by nitrogen plasma immersion ion implantation (NPIII) inside conductive tubes, with 150 mm in length and different diameters. The NPIII treatments employed here was carried out using an experimental system from

the Associated Laboratory of Plasma at National Institute for Space Research. It consists of a cylindrical vacuum chamber of 600 liters with a vacuum system composed of a mechanical, a root and a diffusion pumps. Its detailed description is found in some recent published paper of our research group [17], with a difference that the SS pipes were connected directly to the high voltage pulser and no additional plasma source was used. Stainless steel (SS) tubes were placed in the interior of cylindrical vacuum chamber and were isolated from the ground by a set of dielectric insulators (corrugated alumina tubes, then a glass plate, and a Makor support and alumina tubings), as can be seen in Fig.1 (a) and 1(b). In this set-up, samples of UNCD films fixed to the inside wall of the tube were bombarded with accelerated nitrogen ions. The temperature distribution at the end of the treatment was measured with an infrared pyrometer (Mikron, model MK-90Q), looking at the middle positions of the tubes. The NPIII treatment conditions are shown in Table 1.

Fig. 1. Stainless steel tubes with diameters of (a) 110 mm (T110) and (b) 40 mm (T40) that were used to perform NPIII treatments on UNCD films surface.



As can be seen from Table I, the nitrogen pressure used in T110 was about 3.0 Pa. The pulser was operated at pulse length of 30 μ s and at a frequency of 1 kHz. Using peak voltages of 3 kV and peak currents of 3 A, the implantation condition led to the tube temperature in the order of 380 $^{\circ}$ C, in this case of SS304 tube with 110 mm \varnothing and both sides of the tube open (Fig. 1(a)).

Table I. Conditions of NPIII treatments on UNCD films surface inside T110 and T40 size conductive tubes.

NPIII	Tube Diameter Size (mm)	Peak Pulse Current (A)	Peak Pulse Voltage (kV)	Frequency (kHz)	Final Temperature ($^{\circ}$ C)	Argon Time (min)	Pulse Length (μ s)	Pressure of Nitrogen (Pa)
T110	110	3.0	3.0	1.0	380	10	30	3.0
T40	40	2.0	2.7	3.0	780	10	30	3.0

In case T40, a 40 mm Ø SS304 tube was closed in one end, using a thin sheet of SS304, as can be seen in Fig.1 (b). This resulted supposedly in much higher density plasma inside the tube. The operation condition was now: nitrogen pressure of 3.0 Pa, pulse length of 30 μ s, at a frequency of 3 kHz, reaching peak voltage of 2.7 kV and peak pulse current of 2.0 A. The resultant plasma showed much higher light emission and soon after turning on the pulser, the tube started glowing due to the very high temperatures reached there.

2.4 SURFACE CHARACTERIZATION SYSTEMS

The analysis of crystallinity was performed by X-Ray Diffraction (XRD) in a Philips 3410 diffractometer in the Seeman-Bolin 2θ scanning mode using Cu K α radiation ($\lambda=0.154056$ nm). The evaluations of the morphology and the content of various elements in the UNCD films were investigated before and after the NPIII treatment, using Field Emission Gun Scanning Electron Microscopy (FEG-SEM) – Hitachi microscope model SU-70 (Tescan MIRA3) with auxiliary Energy Dispersive Spectroscopy (EDS) at an operating voltage of 25 kV. The quality of UNCD films and the existence of carbon layer was evaluated by Raman Scattering Spectroscopy (RSS) – Labram HR evolution – Horiba Scientific with a 514 nm excitation light source by argon ion laser. The chemical bonding states of the UNCD films before and after NPIII treatment were analyzed using X-ray Photoelectron Spectroscopy (XPS) - Thermo Scientific K-Alpha with monochromatic Al-K α radiation (1486.6 eV). The binding energies in the spectra were calibrated with carbon (C1s 284.8 eV) peak. Instrument base pressure was about 10^{-10} Torr and high-resolution spectra were collected with 40 eV pass energy. The surface samples were sputter cleaned prior to analysis using a 4 kV argon ion beam by 1200 seconds. Spectra were analyzed using casaXPS software (version 2.3.15). Gaussian (30%)-Lorentzian (70%), defined in CasaXPS as GL (30), profiles were used for each component and a standard Shirley background are used for all reference samples spectra.

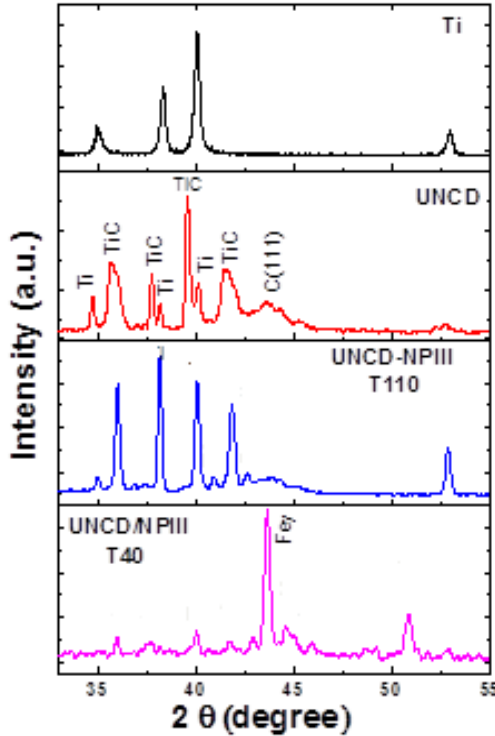
3 RESULTS AND DISCUSSION

3.1 STRUCTURAL SAMPLES CHARACTERIZATION

X-ray diffraction (XRD) analysis was carried out to investigate the structural properties of titanium substrate, and UNCD films, before and after NPIII treatments, in T110 and T40 tubes, and the results are shown in Fig. 2. It can be observed that the Ti substrate have α -phase – hexagonal close-packed (hcp) crystalline structure. The 35° ,

38°, 40.1°, and 52.8°, diffraction peaks can be observed relative to the titanium diffraction planes (100), (002), (101), (102), respectively (JCPDS 89-5009) [18].

Fig. 2. XRD pattern of Ti substrate, UNCD film before and after NP/III treatment in T110 and T40.



From Fig. 2, it can also be found that for the UNCD films before NP/III treatment, the typical carbon (111) diffraction plane relative to the peak at 44° appears little evidence of low diamond crystallinity. The line broadening of the diamond peak suggests a ballaslike morphology. In addition, apart from the carbon peaks, the most usual TiC formation is clear, related to (111), (200), (220), and (311) planes. The XRD of UNCD films after NP/III treatment in T110 tube contains peaks that correspond to α -Fe (110), (200), and (211) planes (JCPDS No. 06-0696) as resulted from the metal nanoparticles by sputter deposition. It can be seen then that the TiC peaks have disappeared and new peaks have emerged as nitride phase. One can verify the presence of the peaks (111), (200), (220) and (311) for thin TiN film of NaCl-like structure (cubic face centered), with the N atoms replacing the carbon atoms. The XRD pattern of the UNCD film after NP/III in T40 tube contains peaks that correspond to α -Fe and γ -Fe that are relatively strong due to intense sputter deposition from the SS304 tube. UNCD film with metal nanoparticles implantation was obtained, which

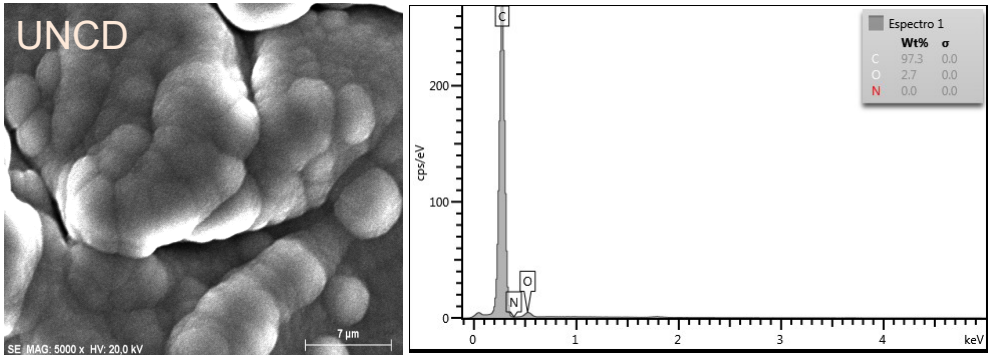
gives it new prospective applications. However, no diffraction peaks relative to diamond is present anymore in this sample. Therefore, it suggests the presence of high defect density induced by the NPIII, in the case of small diameter tube, providing higher intensity sputter deposition of the metal nanoparticles and higher temperature (780°C).

3.2 FIELD EMISSION GUN SCANNING ELECTRON MICROSCOPY (FEG-SEM) WITH AUXILIARY ENERGY DISPERSIVE SPECTROSCOPY (EDS)

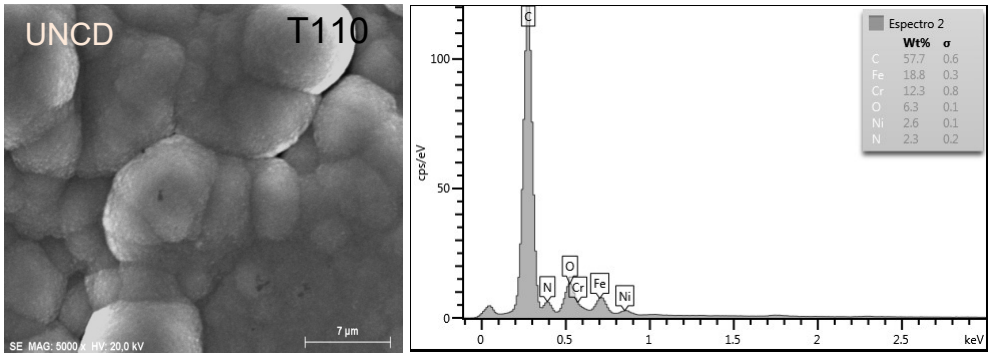
Surface morphologies and EDS analysis of the UNCD film before and after NPIII treatments in T110 and T40 tubes, analyzed by FEG-SEM, are shown in Fig. 3. It can be seen from images, that whilst the UNCD film shows evidence of low crystallinity at this length scale. From the top-view SEM images of the UNCD film before and after NPIII treatment in T110 tube, it can be observed that the structures are similar, as shown in Fig. 3(a) and 3(b). The films presented extremely fine-grained coalescent crystallites, uniformly distributed on the surface of the Ti substrate and abrupt grain boundaries, presenting non-columnar growth structure of a ballaslike morphology. The grains tend to form agglomerates that become more pronounced than those formed after NPIII treatment in T110 tube. These agglomerate sizes are in the range of 42 and 48 nm of diameter, showing grains with an undefined texture for this image magnification. Yang et al. observed the cauliflower or ball-shaped diamond formation, the so-called CVD balls diamond, for argon concentrations above 30%v [19]. They discussed that balls diamond is nearly a pure diamond with strongly twinned microstructure that grows at the transition from faceted diamond to graphite depositions. This morphology is clearly observed in these images. In Fig. 3(b), the UNCD film after NPIII treatment in T110 tube present an appreciable decrease in the carbon concentration and the simultaneous implantation of the nitrogen, oxygen and deposition of metallic nanoparticles such as Fe, Cr and Ni derivation of the stainless steel tube. In Fig. 3(c), the UNCD film after NPIII treatment in T40 tube shows that one-dimensional wire structures are uniformly distributed on the surface of the sample and no diamond structure is seen on the surface. It was estimated that the Fe content in the UNCD is around 73.0 wt% by EDS. It was because of the presence of these Fe atoms, that the UNCD film became magnetic. These results are a consequence of the high temperature (780°C) in smaller diameter tubes used during the NPIII treatment that significantly affect the properties of the UNCD films and it is very important in the transformation process from UNCD film to diamond/metals composite.

Fig. 3. FEG-SEM images and EDS analysis of (a) UNCD films deposited on titanium substrate, (b) UNCD films treated by NPIII in T110 and (c) UNCD films treated by NPIII in T40.

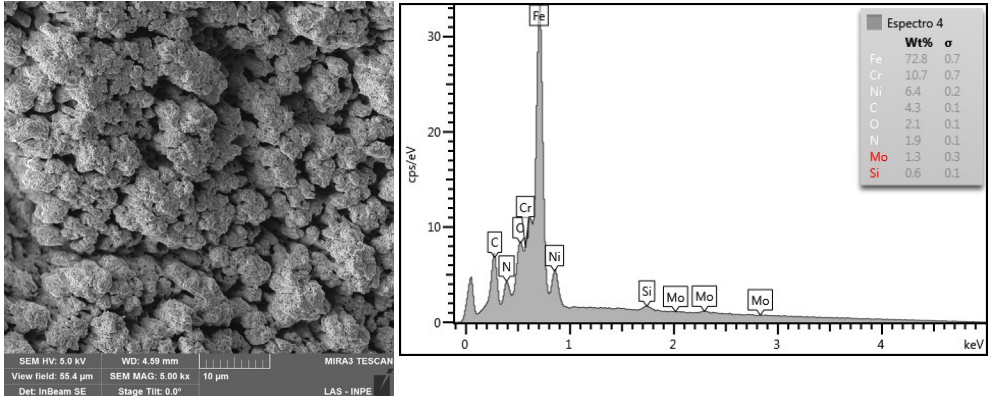
(a)



(b)



(c)



Other elements (Si and Mo) shown in Fig. 3(c) are probably from surface contamination. Based on these results, it is evident that both types of NPIII treatments of the UNCD film result in a very intense surface enrichment of high purity metal

nanoparticles in the surface layer by sputter deposition of these metallic species of the stainless steel coming from the conductive tube. The metal nanoparticles in both cases are characterized by a transfer of electron charge from metallic tube used for the NPIII treatment, which is more pronounced in the case of the T40 tube.

3.3 RAMAN SCATTERING SPECTROSCOPY (RSS)

Raman spectroscopy was used to examine the property of UNCD films before and after NPIII treatments in conductive tubes. Figure 4 shows the measured Raman spectra of the UNCD film before and after NPIII treatment in T110 tube, exhibiting broad bands (D and G) located at approximately 1358 cm^{-1} and 1570 cm^{-1} , which is probably due to surface graphitic structure. G band presence is relative to crystalline graphite impurities and D band represents the presence of disordered graphite. The peak at $\sim 1150\text{ cm}^{-1}$ which is observed in our visible Raman spectra, is attributed as transpolyacetylene segments at the grain boundaries [22] and commonly assigned as to the vibrations of C sp^3 atoms for the UNCD film. Recent works argue that the 1150 cm^{-1} band is due to a deformation mode of the CH_x bonds present in the diamond nanoparticles, which showed that an increase of C–H bonds was associated with decreasing in the C–C bonds in the morphology transition from faceted to ballaslike diamond. This conclusion also agrees with theoretical diamond studies proposing that CH_x species have a more important role in the growth environment of ballaslike UNCD compared to faceted diamond films [20].

In the second-order Raman spectra, it is possible to observe the band at 2500 to 3500 cm^{-1} attributed to transpolyacetylene (TPA). The TPA (poly-CH_x) is as alternate chain of sp^2 carbon atoms, with a single hydrogen bonded to each carbon atom. It is interesting to note that the intensity of this band decreases in the UNCD film after NPIII treatment in T110. The decrease in the intensity of these bands is accompanied by a frequency shift, as can be seen in Table II. This table shows the results of the positions, area, width (FWHM- full width at half-maximum), height and integrated intensity ratio of the D and G bands (I_D/I_G). I_D/I_G is proportional to the presence of 'disordered' carbon and inversely proportional to graphite crystal size. This is because both the electron and energy transfer mechanisms could result in the reduction of the absorption intensity of the UNCD film after NPIII treatment in T110 tube. The morphologic changes observed by SEM/EDS analysis are also reflected on the Raman spectra features. The evidence of nitrogen and metal nanoparticles incorporations was taken due to great decrease in the intensity of the peaks D and G, besides a pronounced enlargement accompanied with a shift to lower wavenumbers. The intensity of the UNCD film peaks after NPIII treatment in T110 tube

greatly decreased, accompanied with a much wider peak. Due to the fact that metallic ions are heavier in mass, when the implanted Fe ions sit in the diamond lattice (whether the one replace the carbon atom or relax in interstitial sites in diamond lattice), it will introduce strain in the UNCD films. Hence, the strain in the UNCD film after NPIII treatment and the decreasing of the intensity indicate clearly that the structure was changed.

Fig. 4. Raman spectra of UNCD film before and after NPIII treatment in T110 and T40 tubes. The figures inset demonstrate the fitting Raman spectra of the samples.

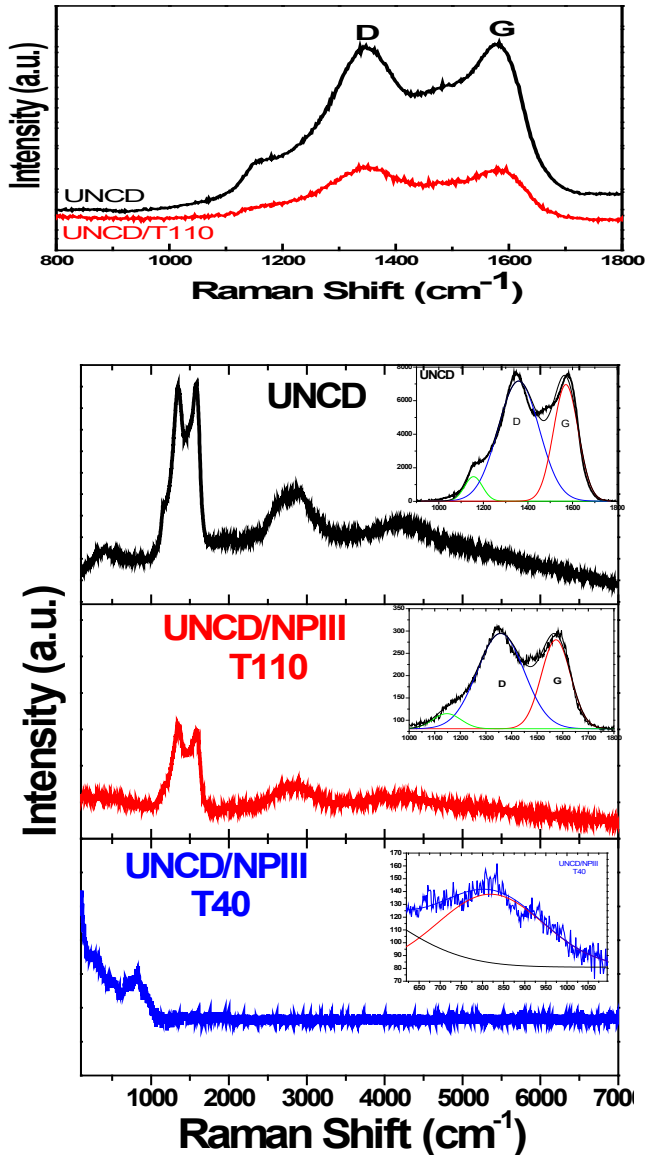


Table II. Position, area, width, height and ID/IG ratio of UNCD film and UNCD film treated by NPIII in T110 and T40 tubes.

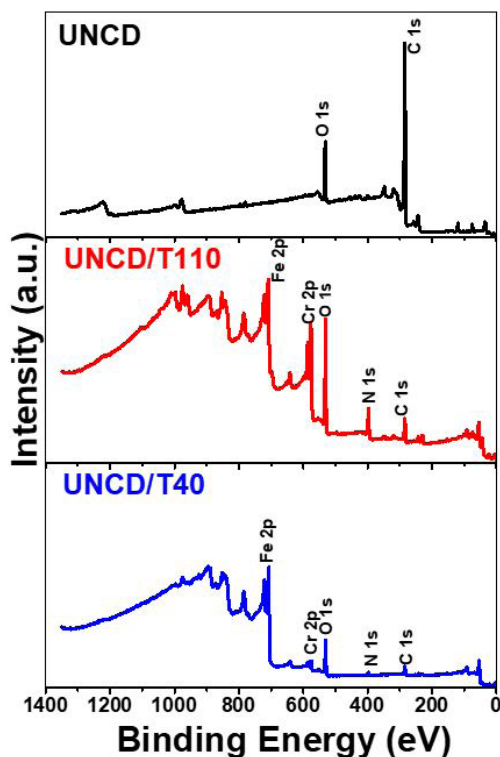
514 nm		Position (cm ⁻¹)	Area (x10 ³)	Width (cm ⁻¹)	Height	ID/IG
UNCD		1155.8	146.3	80.0	1458.5	1.03
	D	1358.0	165.4	184.5	7153.5	
	G	1570.1	967.7	111.2	6946.6	
NPIII T110		1147.4	4.65	109.7	33.8	1.07
	D	1357.5	49.1	183.4	213.7	
	G	1573.5	28.5	114.28	199.3	
NPIII T40		818.6	17.8	249.4	56.9	

For UNCD film after NPIII treatment in T40 tube, the structure D and G spectral line is not observed in the Raman shift, suggesting that there is formation of film without carbon phase, which evidently covered the entire surface of the sample. NPIII changed significantly the surface morphologies and characteristics of the Raman peaks. It is a consequence of high concentration of nitrogen implanted into the sample, due to an increase of temperature and to the high ion flux bombardment on the surface, which resulted from an increase of plasma density. One Raman-active broader and asymmetric band at the lower frequency side was observed at about 820 cm⁻¹. It was attributed to the stretching mode vibrations of heavy ions. Metal oxides do not always occur in a crystalline form. When in an amorphous state, the Raman bands are quite broad. The assumption is that in the amorphous form, there is a distortion of interatomic bond angles. Long-range order is lost, but nearest neighbor interactions are affected to shift a particular vibrational frequency. This happens because there is a population of such distortions, and the observed band was broad (width ~250 cm⁻¹), as can be seen in table II. There is often an interest in engineering materials of particular dimensions, especially in nanotechnology. When the dimensions of crystals get small enough, the phonons experience “quantum confinement”. UNCD films can be composed with additional metals, especially chromium, which has the benefit of “passivating” the surface. The Raman bands of the amorphous, supported surface oxide species sharpen and simultaneously shift in frequency at elevated temperatures due to the high ion flux bombardment of nitrogen. High amount of heavy ions sputter deposited from conductive tubes during NPIII treatment of the films. Thus, ion irradiation may be able to alter the surfaces of UNCD films. Several works have been developed in the study of Raman spectroscopy conducted on different UNCD materials with nitrogen in the gas during the synthesis, including studies by Vlasov, Arenal, Ikeda et al [21-23], but the present work is pioneer in the treatment of UNCD films in conductive tubes by NPIII with metal nanoparticle sputter deposition. Thus, the amount or size of the metal nanoparticles supported on the substrates could be appropriately controlled by NPIII parameters.

3.4 X-RAY PHOTOELECTRON SPECTROSCOPY (XPS) ANALYSIS

Until here, we have shown and discussed the morphology and structure of the film and their modifications performed by NPIII. However, there are other important points related to NPIII to take into account, as the atomic configuration and quantification of the nitrogen atoms and metal nanoparticle in the surface. Several groups measured for instance the sp^2 and sp^3 ratio in UNCD films for the investigation of the C_xN_x phases, and in order to elucidate the nitrogen bonding environments, have employed XPS technique [24, 25]. Fig. 5 show the XPS wide-large spectra of the UNCD films before and after NPIII treatment in T110 and T40 tubes, and atomic concentration of their components, after 45 minutes etching time. XPS analysis revealed the presence of C (70.63 at%) and O (28.8 at%) in UNCD film as produced.

Fig. 5. XPS wide-scan spectra of the UNCD film before and after NPIII treatment in T110 and T40 tubes.



The spectra for UNCD films, after NPIII treatment in T110 and T40 tubes, showed similar characteristic confirming the nitrogen incorporation and metal nanoparticle sputter deposition. However, elemental composition was been significantly changed. UNCD films treated in T110 tube presented high atomic concentration of Fe 2p (49.17 at%) and Cr 2p (34.92at%). These metal elements are typically involved in the formation of a chromium-

rich passive layer on the top surface. UNCD film after NPIII treatment in T40 tube had more of the iron-rich metallic layer relative to Fe 2p (86.10 at%) region.

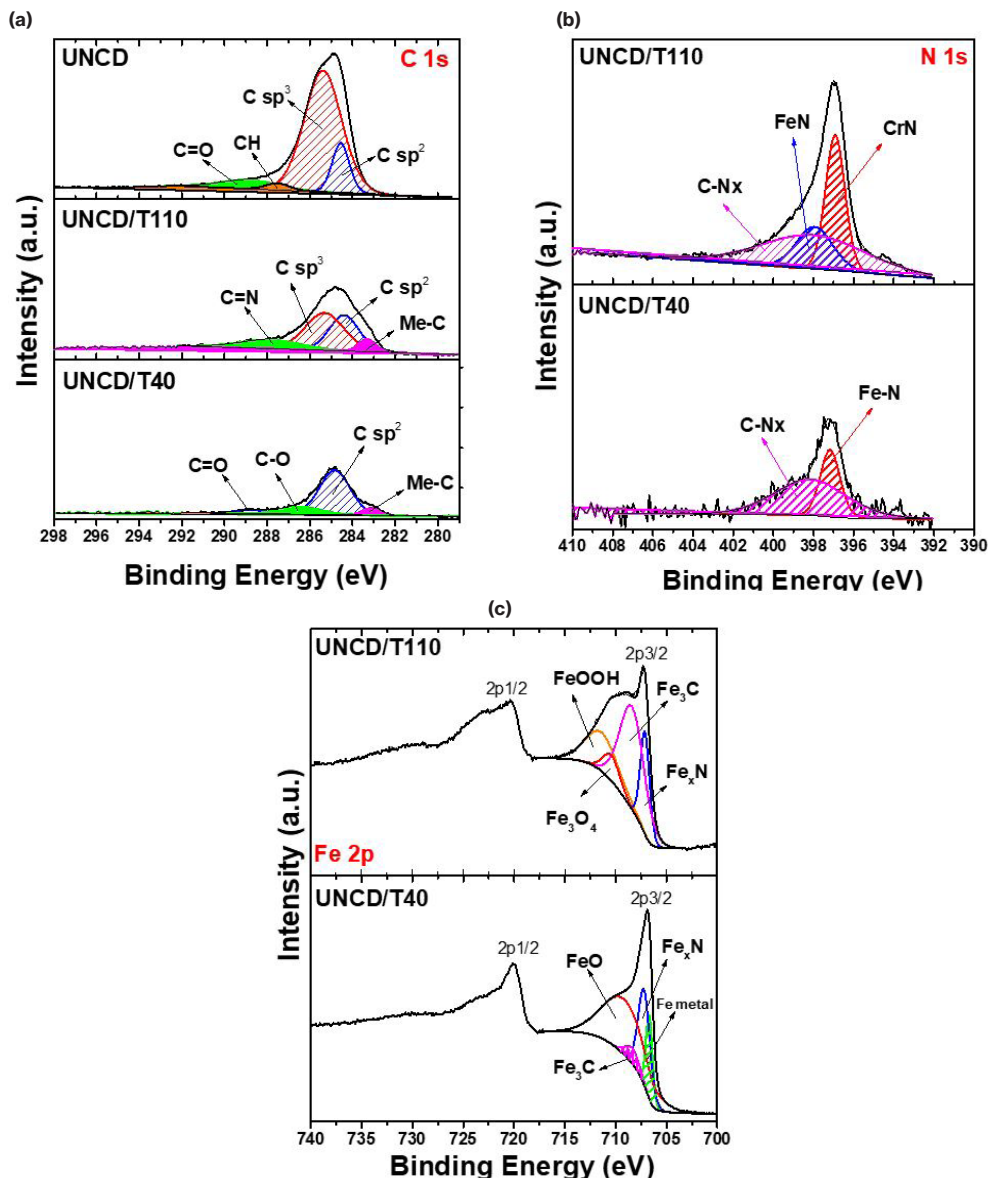
Fig. 6 shows the high-resolution XPS spectra of UNCD films before and after NPIII treatment in conductive tubes. In Fig. 6(a), the XPS C 1s spectrum of UNCD film before NPIII treatment was deconvoluted to four components with the binding energies of 284.5 eV, 285.3 eV, 287.5 eV, and 288.8 eV. The first component is assigned to the unoccupied π^* bond, which is characteristic of the sp^2 C=C bond (14.12 at%). The second component is due to σ^* bond, which is characteristic of the C-C bond for carbon tetrahedral sp^3 (74.67 at%). The components with higher binding energy, observed between the π^* and σ^* bonds, are characteristic of C-H bond (2.73 at%), and carboxyl group C=O (8.49 at%), respectively. These bonds originate from the absorption of hydrocarbon to the dangling bonds at grain boundaries and oxygen residual gas during the film deposition process [26, 27]. For UNCD film after NPIII treatment in T110 tube (UNCD/T110), one can see that, the component with higher binding energy (288.1 eV) is characteristic of C=N (16.80 at%), and the peak with smaller binding energy (283.3 eV) can be assigned to Fe-C and/or Cr-C bonds (6.42 at%). These peaks are features mainly originating from the nitrogen incorporation and metal nanoparticle sputter deposition from T110. The other two peaks indicate the increase of the amount of sp^2 C=C bond (32.42 at%) and the decrease of C-C bond for carbon tetrahedral sp^3 (44.35 at%). The presence of lower intensity C1s peak implies the increasing of the formation and disorderness of sp^2 -bonded carbon phase as a result of the incorporation of nitrogen into UNCD film that have also been-illustrated in Raman spectra (Fig. 4). Another important aspect is the reduction of crystallinity and the increasing of graphitization of the UNCD/T110.

For UNCD film treated in T40 tube, the amounts of sp^2 C=C bond (65.28 at%) and C-metal (12.83 at%) are increased as compared to the UNCD film treated in T110 tube, as can be seen in Fig. 6 (a). The peaks at 288.6 eV and 286.3 eV indicates the amount of the C=O (7.38 at%) and C-O (14.51 at%) bonding in the surface.

In Fig 6 (b), the corresponding N1S band shows asymmetry and involves at least three peaks near 396.9 eV, 397.8 eV, and 398.0 eV for the UNCD film treated in T110 tube. They indicate CrN (34.13 at%), FeN (19.89 at%), and C-Nx (45.98) bonds, respectively. However, in the UNCD films treated in T40 tube, two peaks near 397.1 eV and 398.1eV are present for N 1s band, that correspond to FeN (33.94at%) and C-Nx (66.06 at%) bonds, respectively. The Fe 2p_{3/2} peak included four components, whose peaks were centered at 707.1 eV, 708.3 eV, 710.4 eV, and 711.3 eV, as shown in Fig. 6(c). In line with the existing literature [28], we can associate these components with FexN, Fe₃C, Fe₃O₄ and FeOOH phases, respectively. NPIII favored the attainment of an interface type layer consisting of oxide, nitride, metals, sp^2 phases and the diffusion zone characterized by a decreasing C content.

For the UNCD film treated in T40 tube, the peak-to-peak separation (spin-orbital splitting) between these peaks is 13.2 eV, which corresponds to iron metal, as shown in Fig. 6(c). No peak shift was observed in the Fe 2p spectrum but only a decrease in peak intensity due to the sputter deposition layer. Another effect of NPIII in T40 tube that can be emphasized here is the disappearance of the diamond carbon at about 285.3 eV (Fig. 6(a)), which indicates that most of the constituents on the surface are formed by metal nanoparticles sputter deposition from the conductive tube.

Fig. 6. High resolution XPS spectra of (a) C 1s, (b) N 1s, (c) Fe 2p for the UNCD films after NPIII treatment in T110 and T40 tubes.



The incorporation of metallic atoms in these UNCD films is capable of creating surface changes and leaving the chemical inertia. This represents a viable path for a number of new applications. The special properties of the diamond for its hardness, thermal conductivity, optical transparency over a wide range of wavelength and chemical stability can be allied to these new features.

4 CONCLUSIONS

The surface modification of UNCD films by NPIII treatments changed the surface morphologies, increased the degree of disorder and the structural defects. In UNCD films after NPIII treatments in T40 tube, diamond and other carbon phases are extinguished on the surface. Analysis of the treated surfaces have demonstrated a substantial dependence of NPIII performance with the tube diameter. Characteristic peaks of metal nanoparticles were found to coexist in the UNCD film after NPIII treatment in T110 tube and it is predominant in samples after NPIII treatment T40 tube case. Raman spectra from the treated samples presented a decrease of the G and D peaks intensities attributed to increase of disorder induced by NPIII/T110 on sp^2 phase (C=N) in the treated UNCD films. EDS results revealed the presence of nitrogen adsorbed in samples and new elements such as metal nanoparticles (Fe, Cr and Ni) by sputter deposition from conductive tube walls. This is a consequence of high concentration of nitrogen implanted into samples, proving the efficiency of the PIII process inside conductive tubes. The results indicate a significant difference of PIII performance when diameter of the tube is reduced from 110 mm to 40 mm. In the case of T40 tube, changes caused by the increase of temperature due to the high ion flux bombarding on the surface, favored larger metal sputter deposition. A strong magnetic field attracted the samples of UNCD films after NPIII treatments in T40 tube. This was an indirect diagnostic feature, which has been used to confirm the magnetic properties of the new film. This was due to the presence of the Fe atoms that can create magnetic carbon structures that could be very useful for protective-coating technology and other nano-electronic device applications. Here we have summarized the key experimental results and the understanding of UNCD films treated in conductive tubes. We have presented an overview of the changes in the properties upon nitrogen incorporation in these films. Applications for these types of new structures have been pointed out.

5 ACKNOWLEDGEMENTS

This research program was supported by Brazilian agencies MCTI and CNPq (Proc. 30008/2015-7/PCI-DA). The authors thank National Nanotechnology Laboratory of Brazil, CNPEN/LNNano/MCTI under proposal XPS-20577.

REFERENCES

- [1] Maitz, M. F.; Shevchenko, N. Plasma immersion ion implanted nitinol surface with depressed nickel concentration for implants in blond. *Journal of Biomedical Materials Research*, v. 76 A, p. 356-365, 2005.
- [2] S.F.M. Mariano, M. Ueda, R.M. Oliveira, E.J.D.M. Pillaca, N.M. Santos, Magnetic-field enhanced plasma immersion ion implantation and deposition (PIII&D) of diamond-like carbon films inside tubes, *Surface and Coatings Technology* 312 (25) (2017) 47-54.
- [3] S. Muhl, A. Pérez, *Thin Solid Films* 579 (2015) 174.
- [4] A. Anders, *Handbook of Plasma Immersion Ion Implantation & Deposition*, John Wiley&Sons, New York, 2000.
- [5] N. Kumar, K. Panda, S. Dash, J.P. Reithmaier, B.K. Panigrahi, A.K. Tyagi and B. Raj, "Tribological properties of nanocrystalline diamond films deposited by hot filament chemical vapor deposition" *AIP Adv.*, vol. 2, pp. 032164-032156, 2012.
- [6] Mello, C. B.; Ueda, M.; Silva, M. M.; Reuther, H.; Pichon, L.; Lepienski, C. M. Tribological effects of plasma immersion ion implantation heating treatments on Ti-6Al-4V alloy. *Wear*, v. 267, p. 867-873, 2009.
- [7] S. Srinivasan, J. Hiller, B. kabius, O. Auciello, *Appl. Phys. Lett.* 90 (2007) 134, 101.
- [8] A. V. Sumant, A. R. Kraus, D.M. Gruen, O. Auciello, A. Erdemir, M. Williams, A.F. Artilles, W. Adams, *Tribol. Trans.* 48 (2005) 24.
- [9] P. Bajaj, D. Akin, A. Gupta, D. Sherman, B. Shi, O. Auciello, R. Bashir, *Biomed. Microdevices* 9 (2007) 787.
- [10] O.A. Williams, *Semicond. Sci. Technol.* 21 (2006) R49.
- [11] A.R. krauss, O. Audello, M.Q.Ding, D.M. Gruen, Y. Huang, V.V. Zhirnov, E.I. Givazirzov, A. Breskin, R. Chechen, E. Shefer, V. Konov, S. Pimenov, A. Karabutov, A. Rakhimov, N. Suetin, *J. Appl. Phys.* 89 (2001) 2958.
- [12] S. Bhattacharyya, O. Audello, j. Birrel, J.A. Carlisle, I.A. Curtiss, A.N. Goyette, D.M. Gruen, A.R. Krauss, J. Schlueter, A. Sumant, p. Zapol, *Appl. Phys. Lett.* 79 (2001) 1441.
- [13] O.A. Williams, S. curat, J.E. gerbi, D.M.Gruen, R.B. Jackman, *Appl. Phys. Lett.* 85 (2004) 1680.
- [14] J.M. Blakely, *Introduction to the Properties of Crystal Surfaces* (Pergamon, Oxford, 1973).
- [15] G. Tauber and H.J. Grabke, *Ber. Bunsenges. Phys. Chem.* 82 (1978) 198.
- [16] H. Erhart and H.J. Grabke, *Scripta Met.* 15 (1981) 531.
- [17] J. Robertson, *Diamond-like amorphous carbon*, *materials Science and Engineering* R37 (2002) 129-281.
- [18] N.M. SANTOS, M. R. V. LANZA, N.G. FERREIRA, M. R. BALDAN, Boron-doped diamond electrodes for carbofuran electrochemical degradation. *Bras. Apl. Vác.* 35 (2016) 17-24. doi: 10.17563/rbav.v35i1.1002

- [19] D.C. Barbosa, M.R. Baldan, V.J. Trava-Airoldi, E.J. Corat, Activation energies for the growth of diamond films and the renucleation of diamond grains during film growth, *J. Vac.Sci. Technol.*B32 (2014) 3. <http://dx.doi.org/10.1116/1.4874308>
- [20] M. Ueda, A.R. Silva, E.J.D.M. Pillaca, S.F.M. Mariano, R.M. Oliveira, J.O. Rossi, C.M. Lepienski, L. Pichon, New method of plasma immersion ion implantation and also deposition of industrial components using tubular fixture and plasma generated inside the tube by high voltage pulses, *Review of Scientific Instruments* 87 (2016) 013902. doi: 10.1063/1.4939013
- [21] Joint Committee on Powder Diffraction Standards (JCPDS)-International Center for Diffraction Data, Joint Committee on Powder Diffraction Standards Card, 89-5009 (2002).
- [22] R. Pfeiffer, H. Kuzmany, p. Knoll, s. Blkova, N. Salk, B. Gunther, evidence for trans-polyacetylene in nano-crystalline diamond films, *Diamond relat. Mater.* 12 (2003) 268.
- [23] Vlasov I. I., Ralchenko V. G., Goovaerts E., Saveliev A. V. & Kanzyuba M. V. Bulk and surface-enhanced Raman spectroscopy of nitrogen-doped ultrananocrystalline diamond films. *Phys Stat Sol (a)* 203, 3028–35 (2006).
- [24] R. Arenal, P. Bruno, D. J. Miller, M. Bleuel, J. Lai and D. M. Gruen, *Phys. Rev. B: Condens. Matter Mater. Phys.* 2007,75, 195431
- [25] Ikeda, K. Teii, C. Casiraghi, J. Robertson and A. C. Ferrari, *J. Appl. Phys.*, 2008,104, 073720.
- [26] K.L. Ma, J.X. tang, Y.S. Zou, Q.Ye, W.J. Zhang, S.T. Lee. Photoemission spectroscopic study of nitrogen incorporated nanocrystalline diamond films, *Appl. Physic. Lett.* 90 (2007) 092105.
- [27] C.C. Teng, S.M. Song, C.M. Sung, C.T. Lin, Structural transformation upon nitrogen doping of ultrananocrystalline diamond films by microwave plasma CVD, *J. Nanomater.* 621208, 7 (2009).
- [28] L. Ponsonnet, C. Donnet, K. Varlot, J. M. Martin, A. Grill, and V. Patel, *Thin Solid Films* 319, 97 (1998).
- [29] D. S. Grierson, A. V. Sumant, A. R. Konicek, M. Abrecht, J. Birrell, O. Auciello, J. A. Carlisle, T. W. Scharf, M. T. Dugger, P. U. P. A. Gilbert, and R. W. Carpick, *J. Vac. Sci. Technol. B* 25, 1700 (2007).
- [30] J.F. Moulder, W.F. Stickle, P.E. Sobol, K.D. Bomben, *Handbook of X-ray Photoelectron Spectroscopy*, Perkin-Elmer Corporation, Physical Electronics Division, Eden Prairie (1992).
- [31] O.A. Shenderova, D.M. Gruen, *Ultrananocrystalline Diamond: Syntheses, Properties, and Applications*, William Andrew, chapter 4, p. 125 (2012).

CHAPTER 8

X-RAY PHOTOELECTRON SPECTROSCOPY (XPS) STUDY OF CONDUCTIVE TUBE AFTER NITROGEN PIII

Data de submissão: 29/03/2021

Data de aceite: 22/04/2021

Pericles Lopes Sant'Ana

São Paulo State University (UNESP)

Technological Plasmas Laboratory

Sorocaba, SP, Brazil

drsantanapl@gmail.com

<http://lattes.cnpq.br/3752107640196845>

Nazir Monteiro dos Santos

National Institute for Space Research

Associated Laboratory of Plasma

São José dos Campos, SP, Brazil

nazirmonteiro@gmail.com

<https://orcid.org/0000-0002-1518-9403>

Elver Juan de Dios Mitma Pillaca

National Institute for Space Research

Associated Laboratory of Plasma

São José dos Campos, SP, Brazil

elver.mitma@inpe.br

<https://orcid.org/0000-0003-4893-8893>

Mario Ueda

National Institute for Space Research

Associated Laboratory of Plasma

São José dos Campos, SP, Brazil

mario.ueda@inpe.br

<http://lattes.cnpq.br/9226460532838417>

Steven Frederick Durrant

São Paulo State University (UNESP)

Technological Plasmas Laboratory

Sorocaba, SP, Brazil

steven.durrant@unesp.br

<https://orcid.org/0000-0002-4511-3768>

ABSTRACT: This work reports an X-ray photoelectron spectroscopy (XPS) study of inner surface modification of stainless steel (SS) conducting tubes after nitrogen plasma immersion ion implantation (PIII) within a non-uniform magnetic field. Nitrogen PIII was carried out in tubes of length 150 mm and diameters (D) of 110 mm, 40 mm and 15 mm, for two arrangements: (a) a tube with an auxiliary electrode (AE) and (b) a tube without an AE. Metal nitrides (CrN, Cr₂N and FeN) and oxide states were observed by XPS in all cases. In the presence of an AE, however, a significant reduction in oxidation and an increase in Cr₂N for the tube with D = 40 mm were detected. Consequently, the wear rate decreased by about a factor of ten compared with the case without an AE.

KEYWORDS: Chemical composition of SS surface. Plasma immersion ion implantation. X-ray photoelectron spectroscopy. PIII in magnetic field.

1 INTRODUCTION

Plasma immersion ion implantation (PIII) is a widely used technique for the

surface modification of materials, employed mainly to improve mechanical, chemical, and tribological properties of complex-shaped three-dimensional objects [1]. To alter a material's surface properties, however, the treatment must achieve a high dose and conformal coverage [2]. These issues were discussed in several investigations, where it was suggested that the dose obtained could be influenced by the target geometries [3] [4]. Effective implantation is difficult in workpieces with concave, rather than flat or convex, geometry [5]. An example where PIII is ineffective is within metallic tubes, which are extensively used in the industry. According to Sheridan [4][6], this problem is caused by low ion energy during PIII. Possibly, this is caused by the reduction of the electric potential inside the tube, which is related to the aspect ratios: (a) the ratio between the tube radius and their length (R/L) [5] [7]; (b) ratio between the tube radius and the overload radius (R/D) [6] [8]. This approach is important because depending on the radius, the dose can be maximized producing a large number of ions with high impact energy bombarding the tube inner surface. Electron cyclotron resonance (ECR) and microwave discharges have been proposed in recent decades to produce greater doses, especially in small diameter tubes [9, 10].

Recently, PIII has been extensively used to improve some properties of austenitic stainless steel tubes. Stainless steel offers high corrosion resistance, low wear resistance and reduced hardness. These properties can be improved if implantation of nitrogen with a high retained dose is performed. To satisfy this condition requires a minimum temperature (of 350 to 400 °C) in the tube to activate the diffusion process. Nitrogen diffusion caused by the increased temperature during implantation could cause great changes in surface properties owing to the formation of new phases (γ_N) and structures (chromium and iron nitrides). Thus, stainless steel tubes with this new surface layer could enhance significantly their properties. If, however, the temperature exceeds 450 °C, the available chromium for chromium oxide can be reduced and there will be a decrease in the corrosion resistance [11].

Recently, interest has arisen in the possibility of using a magnetic field to enhance the PIII process for the treatment of tubes made of stainless steel [12, 13]. The principal advantage of this approach is related to promoting an electric discharge at low gas pressure [14]. This is possible owing to the presence of a magnetic field transversal to the electric field. In this configuration, a region with high plasma density is created via the intense background gas ionization caused by the trapped electrons where the **E** and **B** fields cross [11, 15]. Additionally, if an earthed electrode is introduced along the axis of the tube, the discharge occurs preferentially within Successful PIII depends on such conditions since higher pressures would cause undesirable arcing [16].

Thus, the major objective of this work is to study the effects of nitrogen implantation on the changes in chemical composition of the inner surfaces of SS 304 tubes, using X-ray photoelectron spectroscopy (XPS), after performing PIII in a non-uniform magnetic field. Special attention is given to the analysis of the Fe 2p, Cr 2p and N 1s regions of the spectra. The analyses are completed with studies employing atomic force microscopy (AFM), scanning electron microscopy (SEM) and wear rate measurements to characterize the inner surfaces of the tubes. Tubes of D = 110 mm, 40 mm and 15 mm were studied in two arrangements: (a) tube with an auxiliary electrode and (b) tube without an auxiliary electrode.

2 EXPERIMENTAL

In this work, tubes made of AISI type 304 Stainless Steel (SS), whose chemical composition is given in **Table I**, were used to perform nitrogen PIII on their inner surfaces.

Table I: Chemical composition (%) of type 304 Stainless Steel (SS) tubes

Iron	Carbon	Chrome	Manganese	Silicon	Phosphorus	Sulfur	Nickel	Nitrogen
67 to 72	0.07	18.00	2.00	1.00	0.045	0.015	8.00	0.10

This stainless steel was chosen since it has received considerable attention from the scientific and industrial community, owing to its excellent resistance to corrosion, low cost and extensive use in the manufacturing industry. Nitrogen ion implantation was carried out in a vacuum chamber of 20 liters with a system of two magnetic coils mounted on it to produce a non-uniform magnetic field configuration (magnetic bottle). This system is described in detail elsewhere [14]. Inside the chamber, metallic tubes of length 150 mm and diameters of 110 mm, 40 mm and 15 mm were placed on the axis to coincide with the region where the magnetic field has its minimum value. A SS grounding rod, 2 mm in diameter, was placed inside each tube to work as an auxiliary electrode (AE). For characterization of the inner surface of the tubes, specimens made of SS 304 (3 mm thickness and 7.5 mm radius) were prepared. Five SS sample equidistantly distributed along the 150 mm length were used in each tube. The tubes were polished and subsequently cleaned in an ultrasound bath just before their insertion into the tubes with diameters of 110 mm and 40 mm. For the tube of smallest diameter (15 mm), five holes (diameter of 8 mm) were perforated equidistantly along the surface, to expose them to the internal plasma. A system of mechanical and diffusion pumps was used to reduce the pressure to about 2.0×10^{-2} Pa. Later, nitrogen gas was admitted into the system, reaching a working pressure of 3 Pa. The PIII treatment conditions were kept constant throughout the experiment, with 20 μ s pulses of 6 kV at 500 Hz. The total current on the

target was measured with a Rogowski coil installed in the high voltage pulser. An infrared thermometer Micron model M90 with range between 250 - 2000 °C was used to monitor the temperature of the tubes. Measurements of total current density (j) and temperature (T) during the treatment of tubes for large, medium and small diameters are shown in **Table II**. Finally, the tubes were PIII treated for 60 min in a non-uniform magnetic field with an intensity between 60 G and 90G.

Table II: Current density (j) and temperature (T) for tubes with D = 110 mm, D = 40 mm and D = 15 mm after 60 min. of treatment with and without AE and in presence of magnetic field.

	D =110 mm		D = 40 mm		D = 15 mm
	Without AE	With AE	Without AE	With AE	Without AE
j (mA/cm ²)	7.33	7.72	10.6	15.9	28.3
T (°C)	< 250	< 250	340	475	440

After the treatment, samples placed on the inner surface of the tubes were characterized. Only the SS sample placed in the center part of each tube was used for all the characterization tests. Chemical composition was measured using XPS on a Kratos Axis Ultra^{DLD} electron spectrometer. The experimental resolution of the binding energy was less than 0.5 eV. Samples were excited with monochromatic Al κ_{α} radiation (1486.6 eV) in an ultra-high vacuum of pressure less than 10^{-7} Pa, an acceleration voltage of 15 kV and a current of 10 mA. After Shirley-type background correction [15], peak fitting was performed using the Casa XPS software (2.3.15 version) with mixed Gaussian/Lorentzian (70/30) functions and least-squares fitting [16]. The chemical state of the SS sample after treatment was tested by examining the spectra of the Fe 2p and Cr 2p and N 1s regions after argon ion sputtering for 600 s.

For XPS depth profiling of samples (tubes of D = 110 mm and 40 mm) treated by NPIII, the analysis area was $110 \mu\text{m} \times 110 \mu\text{m}$ (small spot mode) for 600 s, resulting in a sputter rate of 10 nm/min. In the untreated sample and the treated inner tube of D=15mm, the analysis were only superficial, the sputtering of an area of $700 \times 300 \mu\text{m}$ (large spot mode) for 600 s was performed with an Ar⁺ ion gun (4 keV), resulting in a sputter rate of 0.2 nm/min.

The assessment of the wear damage was performed with a microscope and a profilometer, following a pin-on-disk test in a CSM-Instruments tribometer. This was operated with a load of 1.0 N in air at a relative average humidity of about 47 %. An alumina ball of 3.0 mm diameter with fixed linear velocity of 5 cm/s was used. A NanoScope V microscope, operated in the tapping mode, was used to analyze surface topography and roughness (R_q)

over a scanning area of 15 μm x 15 μm . Wear width was observed by SEM using an electron beam of 20.0 keV at a magnification of 500x, and a scanning time of 100 s.

3 RESULTS AND DISCUSSIONS

3.1 ELEMENTAL COMPOSITION

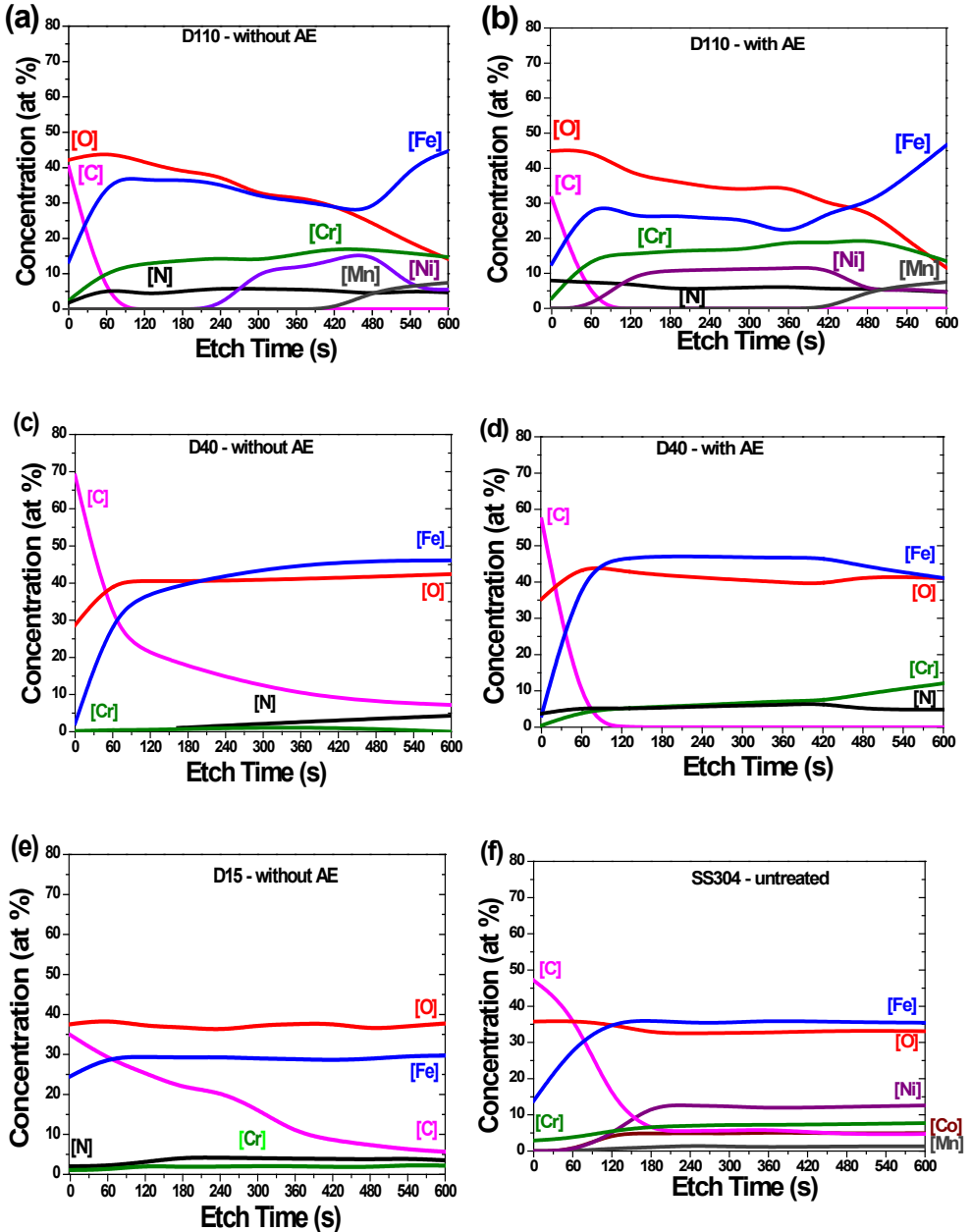
As XPS is a surface analysis technique, depth profiling of the samples was obtained by combining a sequence of ion gun etch cycles interleaved with XPS measurements. An ion gun was used to etch the material for 600 s before being turned off while XPS spectra were acquired. Each ion gun etch cycle exposed a new surface and the XPS spectra allowed determination of the composition of the exposed surfaces. Elemental concentrations were thus revealed as a function of etch-time.

Figure 1 shows XPS elemental concentrations seen after ion implantation for tubes with $D = 110$ mm: (a) without AE and (b) with AE; for tubes with $D = 40$ mm: (c) without AE and (d) with AE (e) D15 without AE (f) SS 304 untreated.

Fig. 1(a, b) shows XPS concentration profiles of O, Fe, C, Cr, Mn, Ni and N elements present for the tube with $D = 110$ mm. In the absence of an AE, [N] on the surface began at 2.5 at %, increasing to 5 at % and remaining constant thereafter. When an AE was introduced into the tube, [N] roughly doubled, then fell to about 5 at % at 180 s. The [Ni] was negligible until 420 s of etching (Fig. 1(a)). With an AE [Ni] initially rises, and reaches a plateau at ~150 s. Both with and without an AE, a significant [Mn] appears only at ~400 s.

For the tube with $D = 40$ mm without AE, as shown in Fig. 1(c), [N] was initially zero and increased monotonically, reaching 5 at % at the end of the test. Similarly, a low [Cr], close to zero, may be observed. The C composition shows high atomic concentration (70 at %) on the surface and then falls, to reach ~8 at.% after 600 s. As can be seen in Fig. 1(d), when an AE is introduced, [Cr] and [N] increase throughout the etching process. Furthermore, no Mn or Ni was detected while [C] is similar to that found in the tube with $D = 110$ mm with and without the use of an AE. Both [Fe] and [O] profiles show plateaus throughout the argon ion sputtering. These results are similar to that for the tube with $D = 15$ mm (figure not shown) where a low [N] and [Cr] of about 1.5 at % were detected. For both tubes ($D = 40$ mm and $D = 15$ mm) there were plateaus of high [Fe] and [O]. This suggests the formation of an oxide layer on the surface, even though the same conditions were used for all cases. These facts can be attributed to a rise in temperature caused by the reduction in tube diameter, as suggested by the temperature measurements shown in **Table II**.

Fig. 1: XPS elemental compositions seen after ion implantation for tubes with D = 110 mm: (a) without AE and (b) with AE; for tubes with D = 40 mm: (c) without AE and (d) with AE (e) D15 without AE (f) SS 304 untreated.



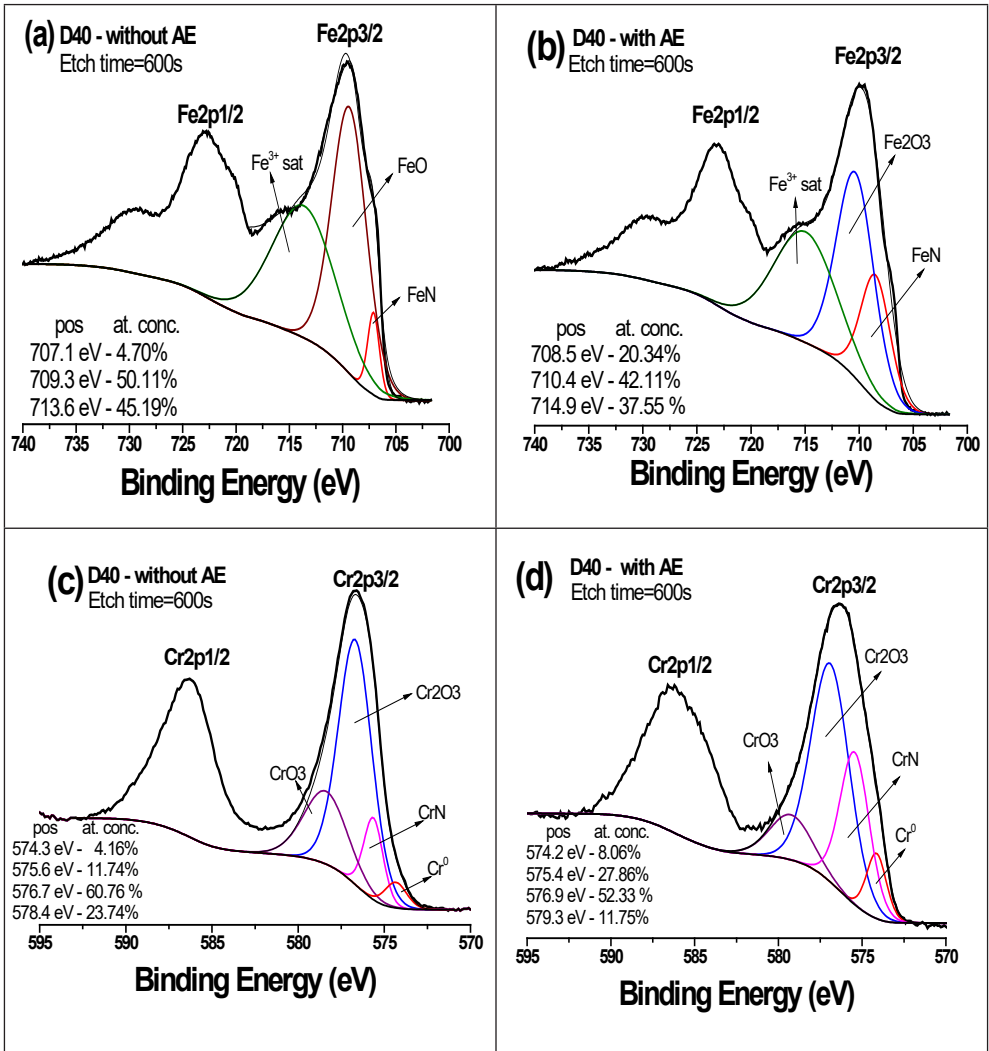
After the elemental concentration profile analysis, the chemical states formed after PIII in tubes with D = 110 mm, 40 mm and 15 mm were investigated. High resolution spectral lines of Fe 2p, Cr 2p, and N 1s regions were considered because they are responsible for the chemical modification of the SS surface. Only XPS spectra for the tube with D = 40

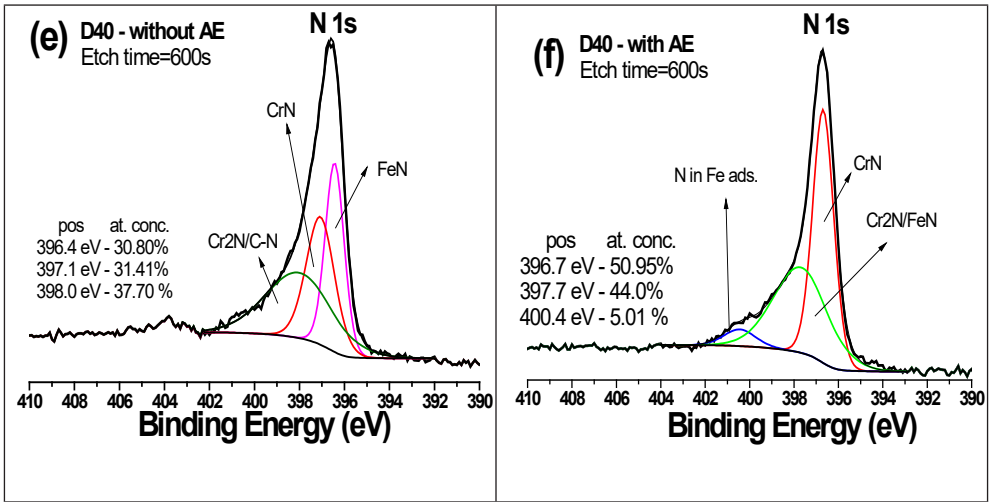
mm are shown in Fig. 2 owing to the high current measured for this case, as can be seen in **Table II**; these are displayed in panels for Cr 2p and N 1s regions. However, information concerning binding energy, chemical state, atomic concentration and author references for Fe 2p_{3/2}, Cr 2p_{3/2} and N 1s spectral lines in tubes with D = 110 mm and D = 15 mm are listed in **Table III**, for the SS304 untreated and treated samples [17-23].

3.2 CR 2P REGION

Fig. 2m (a, b, c, d, e, f) show deconvoluted XPS spectra of the Fe 2p, Cr 2p and N 1s regions for the tube with D = 40 mm, with and without AE.

Fig. 2: Spectra of Fe 2p, Cr 2p and N 1s regions for the tube of D = 40 mm. Without AE: (a), (c) and (e); With AE: (b), (d) and (f).





High intensity peaks of chromium-oxide (Cr_2O_3) after PIII are identified. Both CrN and CrO_3 were also found for the both cases. According to the results of **Table III**, there is a decrease in the $\text{Cr}_2\text{O}_3/\text{CrN}$ ratio from 5.2 to 1.9 when an AE is used. This indicates a greater [CrN] in the presence of an AE. For the tube with $D = 110$ mm, results presented in Table III indicate the presence of Cr_2N peaks with similar intensities when the treatments are performed with and without AE. However, the Cr_2N group was not detected when the diameter of tube was reduced from 110 mm to 40 mm. In the absence of AE, the $\text{Cr}_2\text{O}_3/\text{CrN}$ ratio was 5.2 whereas it decreased to 1.9 when the AE was introduced. This result indicates a greater presence of CrN than Cr_2O_3 which resulted in increased surface hardness [24].

For the tube with $D = 15$ mm without AE, chromium oxide (Cr_2O_3) and metallic chromium were identified on the treated surface. These results are similar to the untreated sample case. For this diameter of tube, no formation of CrN was detected, even though the temperature in the tube increased to 440 °C (see Table II). It is possible that the low ion energy inside the tube was insufficient to promote this kind of chemical bond or the CrN layer was sputtered away.

3.3 N 1S REGION

The N 1s high resolution fitted spectra for the tube with $D = 40$ mm treated without an AE is shown in Fig. 2(e) The chemical states in this sample presented FeN (396.4 eV), CrN (397.1 eV) and revealed Cr_2N (398.0 eV). Some authors [20, 21] assign such peak energies (398.0 eV) to C-N. This coincides with the results observed throughout the etching time profile shown in Fig. 1(e), where an appreciable amount of contaminant carbon

remains near the surface after argon ion sputtering. For the case with an AE, evidence of high intensity CrN and Cr₂N and/or FeN peaks was identified in Fig. 2(d). In addition, a weak peak observed at 400.4 eV indicates the possible presence of nitrogen adsorbed in the Fe lattice [23]. We assume in this work that [Cr₂N] is significantly greater than [FeN] owing to the high nitrogen ion current measured during the treatment (see Table II). On the other hand, for D = 110 mm, data of binding energies reported in **Table III** indicate the presence of CrN, Cr₂N and/or FeN and nitrogen adsorbed in iron for the cases with and without an AE. With exception of nitrogen adsorbed in iron, similar concentrations at% of Cr₂N and/or FeN and CrN were obtained for both cases.

When the tube diameter was reduced from 110 mm to 40 mm, the XPS results showed a decrease in the Cr₂N/CrN intensity ratio, from 1.8 to 1.2, for the case without an AE, whereas with an AE it decreased from 1.7 to 0.9. These results indicate the presence of greater [CrN] in the tube with D = 40 mm with an AE. Another characteristic is the partial reduction of nitrogen adsorbed in iron for the case with an AE, and its total absence without an AE.

For D = 15 mm, the results shown in Table III indicate the presence of a high intensity peak at 403.4 eV that is related to NO₂. Nitrogen adsorbed into iron was attributed to the peak at 400.1 eV, whereas the presence of FeN was identified at 396.4 eV. No Formation of CrN peak can be resulted to the increase of current density (j) and of the temperature of the PIII.

3.4 FE 2P REGION

Binding energies of the Fe 2p region for the tube with D = 40 mm, with and without AE are reported in Table III. After nitrogen PIII, FeN is detected for both arrangements as well as the satellite iron (Fe³⁺ sat), corresponding to SS304. The oxidation states were modified from FeO to Fe₂O₃, however, after introduction of the AE. However, the FeO/FeN to Fe₂O₃/FeN intensity ratio fell from 10.7 to 2.07. This indicates larger presence of FeN which was favored perhaps by higher temperatures during PIII.

On the other hand, information shown in **Table III** for the tube with D = 110 mm, without an AE, revealed bonding energies corresponding to FeN. Metallic iron (α-Fe) in the ground state, and Fe₂O₃ corresponding to iron oxide present in the bulk were also identified. After introduction of AE in PIII, similar chemical states were obtained, which indicate no significant changes with respect to these states.

Remarkable differences are observed when the tube diameter is reduced from 110 mm to 40 mm. For D = 40 mm, changes of oxidation states from Fe₂O₃ to FeO are

found for the tube without an AE. Perhaps, this is caused by the increase in temperature promoted by the high ion flux bombarding the surface (see current in Table II) which was favorable to oxidation. Another significant change detected is the variation of $\text{Fe}_2\text{O}_3/\text{FeN}$ ratio. The analysis for the case with AE indicated an increment from 1.9 to 2.07. As can be noticed from this result, this occurs only when an AE is introduced into the tube.

Results obtained for $D = 15$ mm without an AE are compared to those of the untreated sample because it was not possible to perform an experiment with an AE in this case (the tube diameter was too small). As can be seen from Table III, the atomic concentration of the Fe_2O_3 oxidation state increased and a new FeO oxidation stage appeared after PIII. Although a high current density was measured, no FeN was observed, as indicated by the data shown in Table II.

In summary, iron oxide was present in all the analyzed tubes. This is attributed to the high affinity between oxygen and iron, which is favored by higher temperatures. Looking at Table II, a dependence on temperature is seen as the tube diameter is reduced (110 mm to 15 mm). The temperature increase is caused by ion implantation. This is consistent with the results shown in Fig. 1(a), which suggests thicker oxygenated layers after 600 s etching. The cause of so much oxygen, however, is not yet clear. Possibly, the intense electric field created at the ends of the tubes, promotes greater ionization of the gas. Clearly, the specific distribution of the magnetic field is also a contributing factor. Implanted oxygen may also originate from residual and adsorbed gas and water vapor.

Table III: Results of the XPS analyses. Binding Energy, chemical state and atomic concentration of standard and samples treated by nitrogen PIII for tubes with $D = 110$ mm, $D = 40$ mm and $D = 15$ mm.

Samples	Fe 2p _{3/2}				Cr 2p _{3/2}				N 1s			
	BE (eV)	Chemical state	*at%	Ref	BE (eV)	Chemical state	*at%	Ref	BE (eV)	Chemical state	*at%	Ref
SS304 untreated	706.9	Fe ^o	1.8	[22]	574.1	Cr ^o	4.4	[22]				
	709.9	FeO	34.7	[23]	576.6	Cr ₂ O ₃	95.6	[22]				
	714.9	Fe ³⁺ sat	63.5	[25]								
D110 with AE	706.7	Fe ^o	21.9	[22]	573.9	Cr ^o	13.1	[22]	396.9	CrN	30.4	[22, 24]
	707.7	FeN	27.4	[26, 27]	574.6	CrN	24.6	[22]	397.7	Cr ₂ N/FeN	50.4	[22]
	710.4	Fe ₂ O ₃	50.7	[22]	576,4	Cr ₂ N	62.4	[22]	399.9	N ads	19.2	[27]

Samples	Fe 2p _{3/2}				Cr 2p _{3/2}				N 1s			
	BE (eV)	Chemical state	*at%	Ref	BE (eV)	Chemical state	*at%	Ref	BE (eV)	Chemical state	*at%	Ref
D110 without AE	706.7	Fe ^o	21.5	[22]	573.7	Cr ^o	13.7	[22]	396.9	CrN	25.7	[22, 24]
	707.6	FeN	27.0	[26, 27]	574.3	CrN	26.6		397.6	Cr ₂ N/FeN	47.1	[22]
	710.4	Fe ₂ O ₃	51.5	[22]	576.1	Cr ₂ N	59.8	[22]	399.2	N ads	27.2	[27]
D40 with AE	708.5	FeN	20.3	[26]	574.2	Cr ^o	8.1	[22, 23]	396.7	CrN	50.9	[22, 24]
	710.4	Fe ₂ O ₃	42.1	[22]	575.4	CrN	27.9	[22]	397.7	Cr ₂ N/FeN	44.0	[22]
	714.9	Fe ³⁺ sat	37.6	[25]	576.9	Cr ₂ O ₃	52.3	[22]	400.4	N ads	5.0	[27]
				579.3	CrO ₃	11.8	[22, 24]					
D40 without AE	707.1	FeN	4.7	[22]	574.3	Cr ^o	4.2	[22]	396.4	FeN	30.8	[26]
	709.3	FeO	50.1	[22, 24]	575.6	CrN	11.7	[22, 23]	397.1	CrN	31.4	[22]
	713.6	Fe ³⁺ sat	45.2	[25]	576.7	Cr ₂ O ₃	60.8	[22]	398.0	Cr ₂ N/C-N	37.7	[25, 26]
				578.4	CrO ₃	23.7	[25]					
D15 without AE	709.4	FeO	27.7	[22, 24]	573.9	Cr ^o	6.4	[22]	396.4	FeN	27.5	[26]
	711.4	Fe ₂ O ₃	48.3	[22, 24]	576.6	Cr ₂ O ₃	93.6	[22]	400.1	N ads	10.4	[27]
	717.8	Fe ³⁺ sat	23.9	[25]					403.4	NO ₂	62.2	

*atomic concentration (at%)

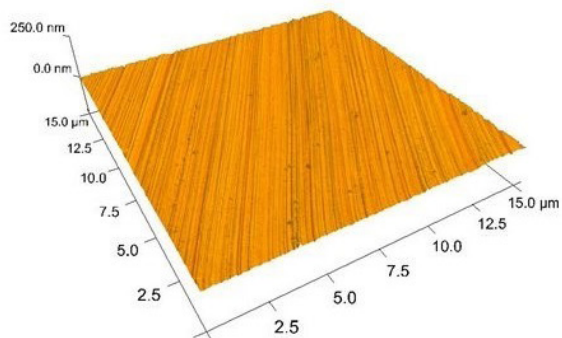
3.5 SURFACE MORPHOLOGY AND WEAR RATE

We also examined the topography of the inner surfaces of the tubes and their surface roughness (R_q) using AFM images. AFM images are shown in Fig. 3 and R_q data are reported in **Table IV**.

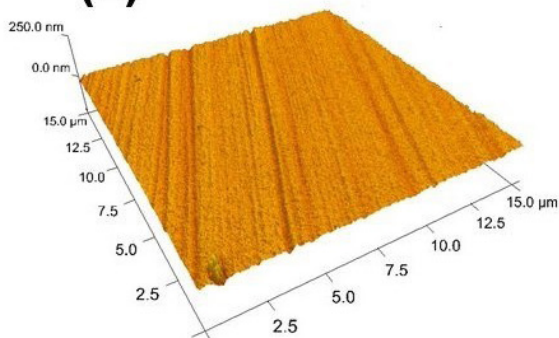
In Fig. 3(a) an AFM image of the untreated sample is show the scratches caused by the polishing are visible. Fig. 3 (b, c) shows AFM images of samples treated in the tube with D = 40 mm with and without an AE. In Fig. 3(b) for tube with D= 40 mm without an AE, the image is similar in morphology to the untreated one shown in Fig. 3(a). The morphology is similar to that observed in all of the implanted samples, except for the tube with D = 40 mm with an AE. It is possible to see a significant, change in surface morphology after the treatment was performed with the presence of an AE.

Fig. 3: AFM images of untreated tube (a), D = 40 mm without an AE (b), D = 110 mm with an AE (c).

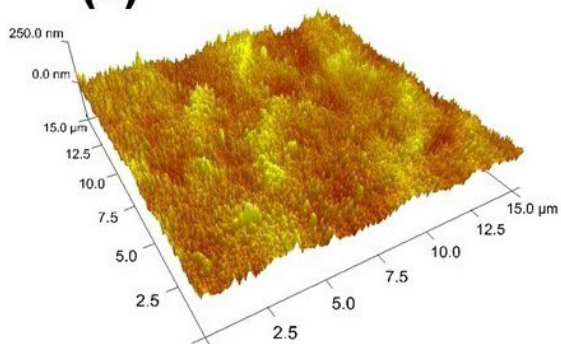
(a)



(b)



(c)



The selection of this AFM image as representative was based on the similar R_q values reported in Table IV which indicate a small increase from 3.6 nm (untreated tube) to 4.0 nm for tube with D= 40 mm, and 6.8 nm for tube with D = 15 mm of treatment without AE. When an AE was introduced into the tube with D = 40 mm, however, the AFM image in

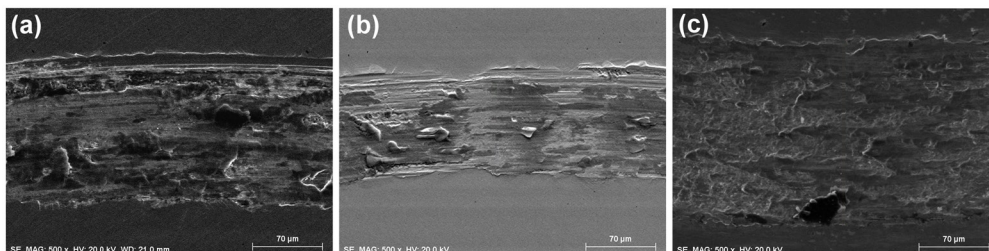
Fig 3(c) revealed strong erosion of the sample surface, producing an increase in R_{q_i} from 4.0 nm to 14 nm. This result can be attributed to a greater ion current (about 16 mA/cm²) and temperature (475 °C), how can be seen in the Table II, causing higher sputtering rate and higher ion flux hitting the tube inside wall.

Table IV: Roughness and wear rates for tubes with D = 110 mm, D = 40 mm and D = 15 mm after 60 min of treatment with and without AE.

	D =110 mm		D = 40 mm		D= 15 mm
	Without AE	With AE	Without AE	With AE	Without AE
Roughness (nm)	-	5.3	4.0	14.0	6.8
Wear ($\times 10^{-5}$ mm ³ /Nm)	19.0	4.0	6.0	0.6	3.0

Wear results reveal a significant reduction of 19×10^{-5} mm³/Nm to 4×10^{-5} mm³/Nm for samples treated in discharge with the presence of the AE, for D=40 mm tube. For D=110 mm tube when the AE was not used, the value of wear was from 6×10^{-5} mm³/Nm and reduced to 0.6×10^{-5} mm³/Nm with the presence of AE. This can be explained by the XPS results discussed in 3.2 section where the increase of bonded Cr₂N on the surface favored a decrease in wear. This did not happen for D = 110 mm without an AE, where a high wear rate was measured (19×10^{-5} mm³/Nm), however, as listed in Table IV. Typical widths of wear tracks caused by the ball of a pin-on-disk system are seen in the SEM images of Fig. 4. One possible explanation for this result may be deduced from the etch time profiles of Fig 1(a, b), where the surface Ni concentrations are different. Recent studies [25] have associated that result with surface oxidation rather than nitrogen implantation/diffusion. Another investigation showed the presence of residual oxygen gas, depending on the gas feeding system in PIII experiments, which contributes to the copious formation of oxides [26].

Fig. 4: Images of the wear caused by the ball of a pin-on-disk system seen by scanning electron micrography of untreated tube (a), D = 40 mm tube without an AE (b), D = 40 mm tube with an AE (c).



4 CONCLUSIONS

Effects of nitrogen ion implantation on the inner walls of tubes as a function of their diameters were studied by XPS, after performing PIII employing a magnetic field using two

arrangements: SS tubes with and without AE. The Fe 2p, Cr 2p and N1s regions of the XPS spectra were used to study the chemical state of SS specimens. A dependence of the nitrogen incorporation on the tube diameter was revealed. This was most evident in a tube with $D = 40$ mm and in the presence of an AE, where the ion bombardment of the surface was intense. A surface with CrN, Cr_2N and FeN of high roughness was detected. As a consequence, the resistance against wear was improved about five times compared to the one without an AE. In the other cases (tubes with $D = 110$ mm with an AE and $D = 15$ mm without AE), the wear rate and surface topography were similar to the untreated sample. Finally, the presence of a high concentration of oxide on the top surface, in all tubes, was detected by XS after PIII. The effect increased for the tube smaller diameters. We conclude that PIII treatments inside the tubes were enhanced by the presence of the magnetic field for all three size tubes. It was particularly favorable for the case with the introduction of an AE for medium diameter ($D = 40$ mm) one.

5 ACKNOWLEDGMENTS

This work was supported by the São Paulo State Research Foundation (FAPESP, 15/09781-0), the National Council for Scientific and Technological Development (CNPq), and the Ministry of Science Technology and Innovation (MSTI). This study was also financed in part by Coordination for the Improvement of Higher Education Personnel – Brazil (CAPES).

REFERENCE

- [1] A. Anders, Handbook of Plasma Immersion Ion Implantation and Deposition, Jhon Wiley & Sons, Inc, 2000.
- [2] D.J. Rej, R.J. Faehl, J.N. Matossian, Key issues in plasma-source ion implantation, Surf. Coatings Technol. 96 (1997) 45–51. doi:10.1016/S0257-8972(97)00095-9.
- [3] T.E. Sheridan, J.A. Goree, Analytic expression for the electric potential in the plasma sheath, IEEE Trans. Plasma Sci. 17 (1989) 884–888. doi:10.1109/27.41228.
- [4] T.E. Sheridan, Analytic theory of sheath expansion into a cylindrical bore, Phys. Plasmas. 3 (1996) 3507. doi:10.1063/1.871501.
- [5] B. Liu, G. Zhang, D. Cheng, C. Liu, R. He, S.-Z. Yang, Inner surface coating of TiN by the grid-enhanced plasma source ion implantation technique, J. Vac. Sci. Technol. A Vacuum, Surfaces, Film. 19 (2001) 2958. doi:10.1116/1.1415356.
- [6] E. J. D. M. Pillaca; M. Ueda; S. F. M. Mariano, R. O. Moraes. Reprint of Study of plasma immersion ion implantation inside a conducting tube using an $E \times B$ field configuration. Surface & Coatings Technology, 256 (2014) 73–77.

- [7] C.B. Mello, M. Ueda, C.M. Lepienski, H. Reuther, Tribological changes on SS304 stainless steel induced by nitrogen plasma immersion ion implantation with and without auxiliary heating, *Appl. Surf. Sci.* 256 (2009) 1461–1465. doi:10.1016/j.apsusc.2009.09.001.
- [8] X.B. Tian, Y.X. Leng, T.K. Kwok, L.P. Wang, B.Y. Tang, P.K. Chu, Hybrid elevated-temperature, low/high-voltage plasma immersion ion implantation of AISI304 stainless steel, *Surf. Coatings Technol.* 135 (2001) 178–183. doi:10.1016/S0257-8972(00)00996-8.
- [9] M. Samandi, B.A. Shedden, D.I. Smith, G.A. Collins, R. Hutchings, J. Tendys, Microstructure, corrosion and tribological behaviour of plasma immersion ion-implanted austenitic stainless steel, *Surf. Coatings Technol.* 59 (1993) 261–266. doi:10.1016/0257-8972(93)90094-5.
- [10] E.J.D.M. Pillaca, M. Ueda, H. Reuther, C.M. Lepienski, Study of the effects of plasma immersion ion implantation on austenitic stainless steel using E×B fields, *Surf. Coatings Technol.* 246 (2014) 1–5. doi:10.1016/j.surfcoat.2014.02.044.
- [11] E.J.D.M. Pillaca, M. Ueda, K.G. Kostov, Investigation of Plasma Immersion Ion Implantation Process in Magnetic Mirror Geometry, *IEEE Trans. Plasma Sci.* 39 (2011) 3049–3055. doi:10.1109/TPS.2011.2160209.
- [12] X. Wang, W.T. Zheng, H.W. Tian, S.S. Yu, W. Xu, S.H. Meng, et al., Growth, structural, and magnetic properties of iron nitride thin films deposited by dc magnetron sputtering, *Appl. Surf. Sci.* 220 (2003) 30–39. doi:10.1016/S0169-4332(03)00752-9.
- [13] L. C. Gontijo, R. Machado, E.J. Miola, L.C. Casteletti, P.A.P. Nascente, Characterization of plasma-nitrided iron by XRD, SEM and XPS, *Surf. Coatings Technol.* 183 (2004) 10–17. doi:10.1016/j.surfcoat.2003.06.026.
- [14] E.J.D.M. Pillaca, M. Ueda, S. de F.M. Mariano, R. de Moraes Oliveira, Study of plasma immersion ion implantation inside a conducting tube using an E×B field configuration, *Surf. Coatings Technol.* 249 (2014) 104–108. doi:10.1016/j.surfcoat.2014.03.042.
- [15] D.A. Shirley, High-Resolution X-ray Photoemission Spectrum of the Valance Bands of Gold, *Phys. Rev. B* 5 (1972) 4709–4714.
- [16] CasaXPS Manual 2.3.15 Rev 1.2. Introduction to XPS and AES. Neal Fairley. Casa Software Ltd. (2009).
- [17] J.F. Moulder, W.F. Stickle, P.E. Sobol, K.D. Bomben, *Handbook of X-ray Photoelectron Spectroscopy*, 1992. doi:10.1002/sia.740030412.
- [18] B. Vincent Crist, *Handbooks of Monochromatic XPS Spectra, Volume 2 -Commercially Pure Binary Oxides*, XPS International, LLC. 2 (2005) 1-172.
- [19] B. Vincent Crist, *Handbooks of Monochromatic XPS Spectra Volume 1 - The Elements and Native Oxides*, *Handb. Elem. Nativ. Oxides*. 1 (1999) 1–43.
- [20] P. Li, E.Y. Jiang, H.L. Bai, Fabrication of ultrathin epitaxial γ -Fe₂O₃ films by reactive sputtering, *J. Phys. D: Appl. Phys.* 44 (2011) 075003. doi:10.1088/0022-3727/44/7/075003.
- [21] S. Chakravarty, N. Kumar, K. Panda, T.R. Ravindran, B.K. Panigrahi, S. Dash, et al., The influence of nitrogen concentration on microstructure and ultra-low friction behaviour of Fe-N thin films, *Tribol. Int.* 74 (2014) 62–71. doi:10.1016/j.triboint.2014.01.022.
- [22] I. Bertóti, Characterization of nitride coatings by XPS, *Surf. Coatings Technol.* 151-152 (2002) 194–203. doi:10.1016/S0257-8972(01)01619-X.

- [23] D.C. Kothari, M.R. Nair, A.A. Rangwala, K.B. Lal, P.M. Raole, xps studies at various temperatures steel of nitrogen 304 stainless, 8 (1985) 235–241. doi:075003075007.
- [24] L. Shan, Y. Wang, J. Li, H. Li, X. Lu, J. Chen, Structure and mechanical properties of thick Cr/Cr₂N/CrN multilayer coating deposited by multi-arc ion plating, *Trans. Nonferrous Met. Soc. China*. 25 (2015) 1135–1143. doi:10.1016/S1003-6326(15)63708-6.
- [25] X. Tian, R.K.Y. Fu, L. Wang, P.K. Chu, Oxygen-induced nickel segregation in nitrogen plasma implanted AISI 304 stainless steel, *Mater. Sci. Eng. A*. 316 (2001) 200–204. doi:10.1016/S0921-5093(01)01245-X.
- [26] M. Ueda, A.R. Silva, C.B. Mello, G. Silva, H. Reuther, V.S. Oliveira, Influence of the residual oxygen in the plasma immersion ion implantation (PI³) processing of materials, *Nucl. Instruments Methods Phys. Res. Sect. B Beam Interact. with Mater. Atoms*. 269 (2011) 3246–3250. doi:10.1016/j.nimb.2011.04.095.

CHAPTER 9

APPLICATION OF CLAY-CARBOXIMETHYLCHITOSANE NANOCOMPOSITE-SILVER NANOPARTICLES IN FILTERS TO TREAT CONSUMPTION WATER IN RURAL AREAS OF CAMANA - AREQUIPA-PERU

Data de submissão: 05/04/2021

Data de aceite: 28/04/2021

Maria Elena Talavera Nuñez

Universidad Nacional
San Agustín De Arequipa
Arequipa, Perú

<https://orcid.org/0000-0002-6400-1227>

Irene Zea Apaza

Universidad Nacional
San Agustín De Arequipa
Arequipa, Perú

<https://orcid.org/0000-0002-6403-3245>

Corina Vera Gonzales

Universidad Nacional
San Agustín De Arequipa
Arequipa, Perú

<https://orcid.org/0000-0002-4639-8259>

Julia Zea Alvarez

Universidad Nacional
San Agustín De Arequipa
Arequipa, Perú
CV

Luis Rodrigo Benavente Talavera

Universidad Nacional
San Agustín De Arequipa
Arequipa, Perú
CV

ABSTRACT: A filter was formulated with a clay nanocomposite-carboxymethylchitosan-silver nanoparticles, which was used to eliminate bacteria and anions in water for human consumption. Silver nanoparticles were obtained by reduction of 1mM silver nitrate, with 0.01% carboxymethylchitosan and 2mM sodium borohydride as initiator of the reduction. Subsequently, the filters were obtained as containers with clay and wood sawdust as pore former, in the proportion of 2: 1; it was molded, dried and sintered at 800 ° C for 3 hours. The filters were then impregnated with the colloidal dispersion of carboxymethylchitosan-silver nanoparticles, by immersion for 12 hours. Four water sampling points were defined: Huacapuy, La Punta, Plaza de Quilca, Caleta de Quilca. When evaluating the filtering capacity of the filters, it was found that they are removed: conductivity 84.03% in La Plaza de Quilca, sulfates 85.48% in La Plaza de Quilca; Chlorides 93.93% in La Plaza de Quilca. On the other hand, fecal coliform and total coliform bacteria were 100% removed in La Punta and in the Plaza de Quilca. Coliform bacteria were not found in Huacapuy or in Caleta de Quilca. Therefore, it can be confirmed that the results have a significant removal percentage in the elimination of anions, in terms of total coliform bacteria and fecal coliforms they were completely removed.

KEYWORDS: Nanocomposite. Clay. Filter. Carboxymethylchitosan. Silver nanoparticles.

1 INTRODUCTION

Nanotechnology is the study, design, creation, synthesis, manipulation and application of materials, devices and functional systems through the control of matter at the nanoscale, and the exploitation of phenomena and properties of matter at the nanoscale, at this scale and molecules, show totally new phenomena and properties. Therefore, scientists use nanotechnology to design novel and inexpensive materials with unique properties [1].

These phenomena are governed under the laws of colloidal thermodynamics and their properties are between quantum mechanical phenomena and classical mechanics, these new properties are what scientists take advantage of to synthesize new materials (nanomaterials) or nanotechnological devices, in this way Nanotechnology promises solutions to multiple problems that humanity currently faces such as: environmental, energy, health (nano medicine), and many others, however these new technologies can lead to risks and dangers if they are misused [2].

Nanomaterials are a new class of materials, whether they are ceramics, metals, semiconductors, polymers or a combination of these or nanocomposites, in which at least one of its components has one of its dimensions between 1 and 100 nm; they represent a transition between molecules, atoms and a material with dimensions of volumetric solid. Due to its size reduced to nanometers, the physicochemical properties differ for the same material, molecules and atoms [3].

Treatment of drinking water is a viable option to improve and ensure water quality, mainly in places that do not have treatment systems, or existing systems operate poorly or there are drought conditions, in the comparative study of two filtration systems for drinking water at home[4], two systems were evaluated: a filter with 1 candle (1VC) and another with 2 ceramic candles (2VC) for 6 months. The efficiency of turbidity reduction and E. coli was evaluated. A synthetic substrate was used whose average turbidity value was 32.7 ± 2.81 NTU and 3.9×10^5 CFU / 100mL of E. coli. The results showed that both filtration systems were able to reduce turbidity to average values of 0.28 NTU (99% efficiency) and eliminate E. coli between 99.99 and 100%. No statistically significant differences were found in terms of the quality of water filtered by both systems.

A conventional method is applied to produce porous ceramics, by addition and pyrolysis of an organic material: starch, which acts as a pore former. The aqueous suspensions of (52-55 V%) of the zirconium mixture were stabilized with a commercial ammonium polyacrylate solution as dispersant and consolidated in plastic molds at 90 ° C for 30 minutes. Then they were sintered between 1000-1500 ° C for 2 h. The

characteristics of the product were evaluated by measurements of density, volumetric contraction, mercury intrusion and the evolution of the crystalline phases by X-ray diffraction (XRD) and scanning electron microscopy (SEM). It was found that the microstructural properties of the ceramic (pore volume, relationship between open and closed porosity, size distribution, pore morphology) depend on the amount of starch added and the sintering temperature [5]

2 EXPERIMENTAL PART

The experimental development was carried out in the Laboratories of the Academic Department of Chemistry of the San Agustín de Arequipa National University.

The clay samples, used as the matrix of the nanocomposite, were sampled in the Yarabamba district, which is located southwest of the city of Arequipa, whose coordinates are: Latitude: -16.5481, Longitude: -71.4775; 16 ° 32 ' 53 " South, 71 ° 28 ' 39 " West, were placed in hermetic plastic bags and were transported to the laboratory for characterization. Regarding the structure and composition of the clay, it was carried out by scanning electron microscopy techniques (SEM - EDX), in the physicochemical characterization the following parameters were determined: pH, soluble salts, exchangeable bases, cation exchange capacity (CEC) and absolute density [6].

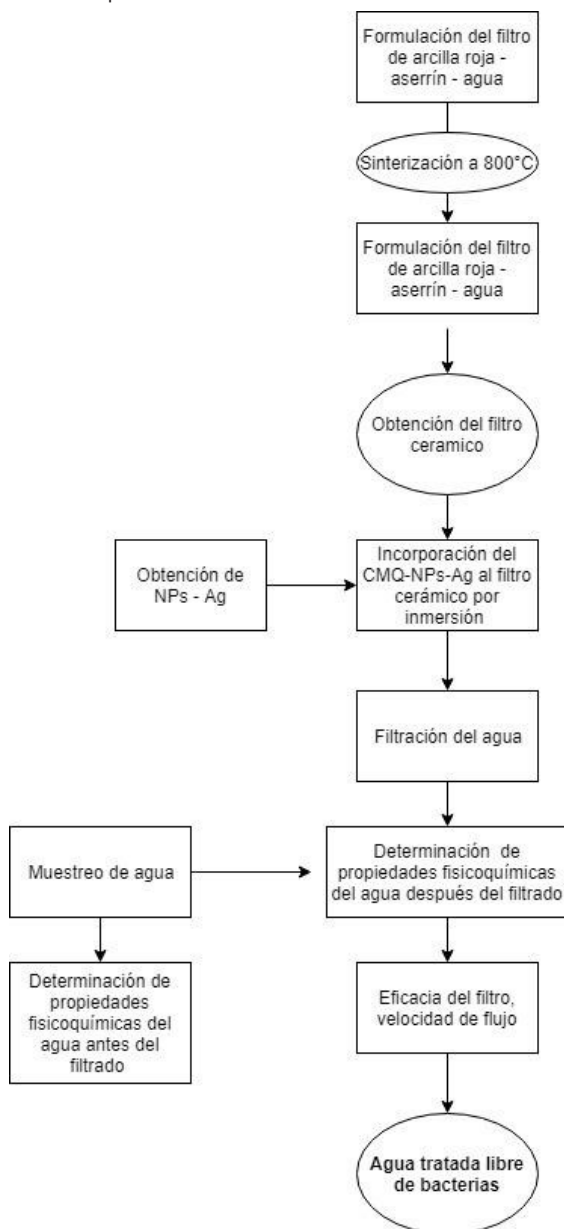
The obtaining of silver nanoparticles was by chemical reduction of silver nitrate with carboxymethylchitosan using 2mM sodium borohydride as initiator of the reduction; the evaluation of the plasmon of the silver nanoparticles was carried out by UV-visible spectroscopy and dynamic light scattering (DLS) [7].

Filters were obtained by making a mixture of clay-sawdust (as pore former, in the ratio 2: 1) and water to form a paste, molded, dried and sintered at 800 ° C for 3 hours. Subsequently, the filters were treated by the immersion method in the colloidal dispersion of silver-carboxymethyl chitosan nanoparticles for 12 hours, they were dried and with these filters the tests of the water under study were carried out [10].

In water for human consumption, the following variables were measured: pH, conductivity, turbidity, chlorides, sulfates, fluorides, nitrates, nitrites, phosphates and the count of microorganisms; numbering of total coliforms, numbering of fecal coliforms (NMP), by AWWA methods, before and after filtering [8] and in this way the efficiency of the filter was determined. The water sampling points were: Huacapuy, La Punta, Plaza de Quilca, Caleta de Quilca, located in Camaná located in the south western part of Arequipa, whose coordinates are: Latitude: -16.6238, Longitude: -72.7105; 16 ° 37 ' 26 " South, 72 ° 42 ' 38 " West. The tests were carried out with the water before filtering,

with the water passed through the filter impregnated with the colloidal dispersion of the nanocomposite: carboxymethylchitosan-silver nanoparticles. Figure N° 1 shows the block diagram of the process for obtaining and operating the filters with the nanocomposite clay-Carboxymethylchitosan-Silver Nanoparticles.

Figure N° 1: Block Diagram of the obtaining and operation of the filter with the clay nanocomposite-Carboxymethylchitosan-Silver Nanoparticles.

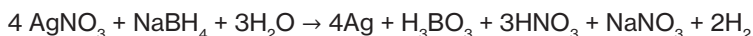


Source: self made

3 RESULTS AND DISCUSSION

3.1 SYNTHESIS OF SILVER NANOPARTICLES:

The synthesis was made by chemical reduction of 1mM [9] silver nitrate with carboxymethylchitosan and 2mM sodium borohydride as reaction precursor, according to the following equation:

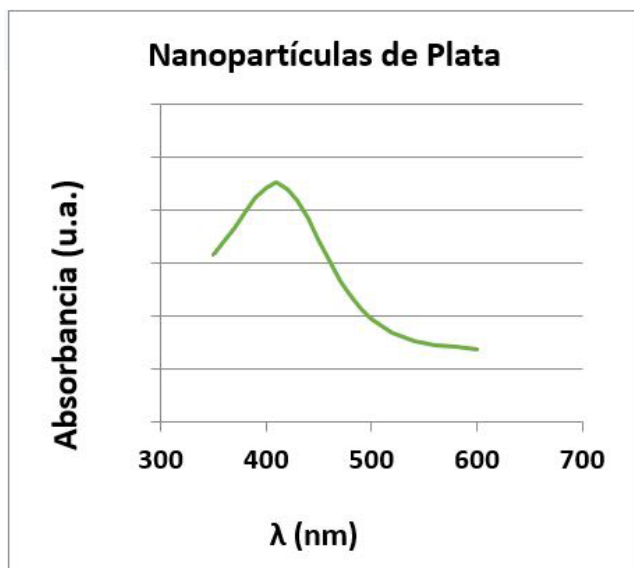


When performing the synthesis, a yellow solution was observed due to the resonance of the plasmon of the silver nanoparticles, which indicates its presence.

3.2 EVALUATION OF SILVER NANOPARTICLES BY UV-VISIBLE SPECTROSCOPY

When characterizing the nanoparticles by UV-visible, it was found that the maximum absorbance is between 410 nm and 420 nm, which is a characteristic of the presence of spherical silver nanoparticles. Metals such as silver, which have free electrons, show a resonance plasmon in the visible spectrum, giving rise to colors not observed in the same materials on a macro scale [11]. For example, silver nanoparticles show an intense SPR (surface plasmon resonance) mainly in the wavelength ranges of 410-420 nm, as seen in Figure N° 2:

Figure N° 2: UV-visible spectrum of silver nanoparticles



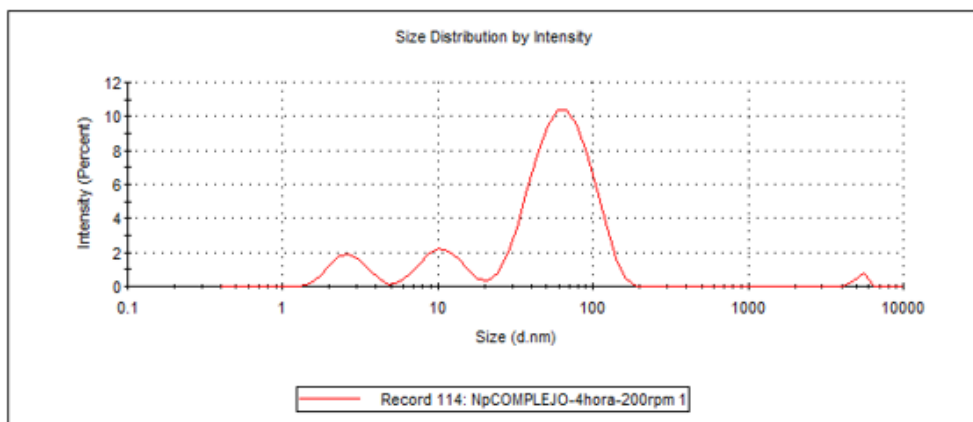
Source: self made

An absorbance maximum is observed between 410 nm and 420 nm, which is a characteristic of the presence of silver nanoparticles, due to the resonance of surface plasmons.

3.3 SIZE EVALUATION OF SILVER NANOPARTICLES BY DYNAMIC LIGHT SCATTERING (DLS)

In the evaluation by Dynamic Light Scattering (DLS), the hydrodynamic diameter of the silver nanoparticles was determined. In the distribution histograms, there are sizes of 2,716 nm, 11.05 and 67.63nm; what is observed in Figure N° 3:

Figure N° 3: Graph of the histogram of the hydrodynamic diameters of the silver Nanoparticles by Dynamic Light Scattering (DLS)



Source: self made

In the histogram of the hydrodynamic diameters of the silver nanoparticles, a polydisperse distribution is observed with sizes of hydrodynamic diameter reached 2,716 nm in 8.7%; 11.05nm by 11.8% and 67.63nm by 78.4%; size less than 100 nm, which confirms the presence of nanoparticles.

3.4 PHYSICOCHEMICAL CHARACTERIZATION OF THE CLAY

Below in Table N° 1 are the results of the physicochemical properties of the clay:

Table N° 1: Physicochemical Characterization of the clay

Sample	pH	Soluble salts g/%	Interchangeable bases %	C I C (Cation exchange capacity) meq/100g	Density g/cm ³	Humidity %	Carbo nates %
Clay	5,6	0,06	27,84	16,60	1,595	3,608	0,00

Source: self made

When characterizing the clay, it is found that it has a high value of exchangeable bases: 27.84%, as well as a high value of Ion Exchange Capacity (CEC) of 16.60 meq / 100g, so it would be easy for these bases to come out or cations, creating free spaces.

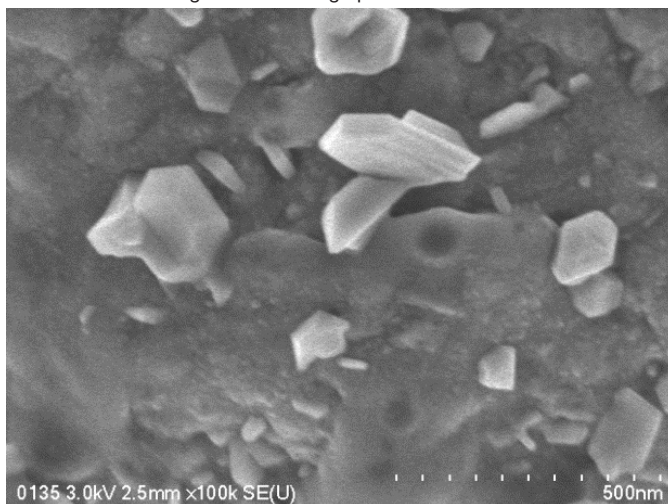
3.5 OBTAINING THE CLAY-SAWDUST FILTER

The clay-sawdust filters were obtained by mixing 100 mesh pulverized clay and 100 mesh pulverized wood sawdust, in a 2: 1 ratio with water, they were molded, dried and brought to a temperature of 800°C, obtaining a hard ceramic of russet. Porosity is an important property of a ceramic filter, since the water filtration flow depends on it, this porosity is obtained by the sawdust present in the mixture and occurs when the filter is subjected to temperatures above 800°C.

3.6 MORPHOLOGICAL CHARACTERIZATION BY SEM-EDX OF THE CERAMIC OBTAINED

The micrograph of the ceramic obtained is shown below, in Figure N° 4:

Figure N° 4: Micrograph of the ceramic

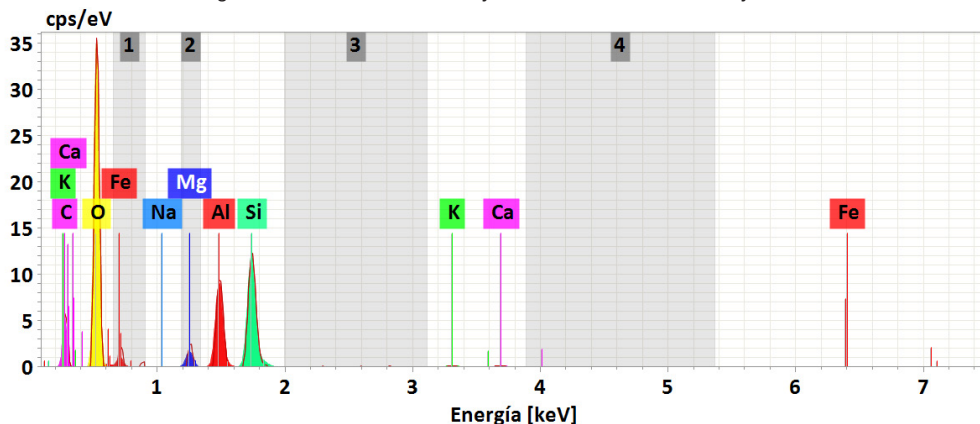


Source: self made

The micrography taken by SEM shows a magnification of the surfaces of 100 thousand times, the structure of the ceramic is observed, with crystallizations corresponding to the typical morphology of clay in sizes from 50 nm to 200 nm. Likewise, an inhomogeneous phase with small depressions is observed. The most dominant phase are homogeneous surfaces.

We can also observe the spectrum of the results of the elemental microanalysis of the ceramic obtained by EDX, in Figure N° 5:

Figure N° 5: Elemental microanalysis of the ceramic obtained by EDX



Source: self made

In this spectrum it can be observed, different signals that show a higher proportion of oxygen, silicon, followed by aluminum, carbon and iron and to a lesser extent as minorities: potassium, calcium, magnesium and sodium.

The general composition indicates that there is a high amount of silicon and oxygen (silicates), minor amounts of calcium carbonate (calcite), and probably small fractions of aluminum and magnesium silicates in the form of micas or feldspar and iron oxides.

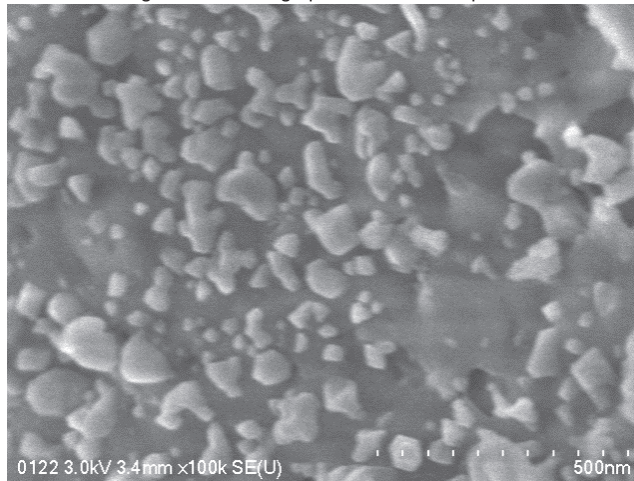
3.7 IMMERSION PROCESS OF THE FILTER IN THE COLLOIDAL DISPERSION OF CARBOXYMETHYLCHITOSAN-SILVER NANOPARTICLES

The nanoparticles were incorporated into the filter by the in situ immersion method, which consists of immersing the filter in the silver-carboxymethyl chitosan nanoparticle solution for 12 hours, they were dried at room temperature and the tests were carried out with these filters.

3.8 MORPHOLOGICAL CHARACTERIZATION BY SEM-EDX OF THE NANOCOMPOSITE: CERAMIC - CARBOXYMETHYLCHITOSAN - SILVER NANOPARTICLES

Below is a micrograph of the nanocomposite: carboxymethylchitosan ceramic-silver nanoparticles, in Figure N° 6:

Figure N° 6: Micrograph of the nanocomposite

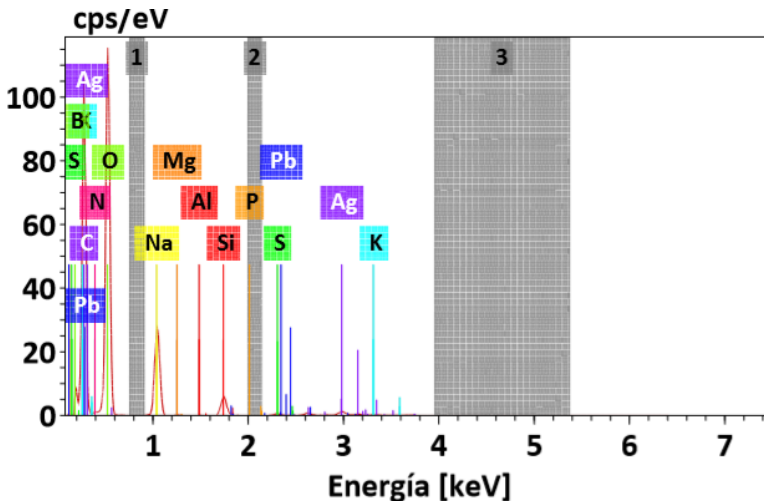


Source: self made

The micrograph taken by SEM shows a magnification of the surfaces of 100 thousand times, crystallizations corresponding to the typical morphology of clay are observed, with sizes between 20 nm and 100 nm and a layer that covers the crystallizations, which would correspond to carboxymethylchitosan with nanoparticles silver.

We can also observe the spectrum of the results of the elemental microanalysis of the ceramic obtained by EDX, in Figure N° 7:

Figure N° 7: EDX analysis of the ceramic obtained



Source: self made

In this spectrum it can be observed, different signals that show a higher proportion of oxygen, sodium, silicon, sulfur followed by carbon, boron, nitrogen, aluminum and to a lesser extent as minorities: potassium, magnesium and the presence of silver is notorious due to the silver nanoparticles.

3.9 PHYSICOCHEMICAL AND BACTERIOLOGICAL PROPERTIES OF THE WATERS UNDER STUDY BEFORE AND AFTER FILTERING.

To carry out this step, the waters under study were filtered with the ceramic filter obtained and the following physicochemical tests were carried out: pH, conductivity, turbidity, anions [12], as well as the bactericidal properties of the nanocomposite, determining the count of microorganisms: Numbering of Total Coliforms, Fecal Coliform Numbering, using AWWA [13] Standard Methods. The tests were carried out on the water samples before and after filtering. Table N° 2 is shown below with the results obtained.

TABLE N° 2: Water quality versus the physicochemical and bacteriological values before and after filtering.

Variables	Normatividad (SUNASS)	Huacapuy			La Punta			Plaza de Quilca			Caleta de Quilca		
		Ant Filt	D e s p Filt	% Remoc	Ant Filt	D e s p Filt	% Remoc	Ant Filt	D e s p Filt	% Remoc	Ant Filt	D e s p Filt	% Remoc
pH (0 a 14)	6,5 a 8,5	7,8	7,7	0,1	7,8	7,6	0,2	7,9	7,9	0	7,8	7,7	0,1
Conductiv (µS)	1500	1180	520	55,93	1590	570	64,15	5260	840	84,03	5050	872	82,73
Turbiedad (NTU)	5	0,72	0,43	40,28	0,7	0,36	48,87	0,8	0,29	63,65	0,64	0,3	53,12
Cl- mg/L	250	112	96,4	13,93	146,3	102,56	29,75	1344,6	81,57	93,93	1356,67	87,05	93,58
(SO ₄) ²⁻ (mg/L)	250	236,32	156,45	33,80	345,2	205,2	40,56	1611,6	234,9	85,42	1621,4	249,6	84,60
F- (mg/L)	1,0	0,43	0,41	4,65	0,46	0,44	4,35	0,48	0,47	2,08	0,48	0,46	4,17
(NO ₃) ⁻ (mg/L)	50	4,83	4,81	0,41	10,95	10,91	0,37	38,29	15,72	58,94	37,27	13,86	62,81
(NO ₂) ⁻ (mg/L)	0,2	< 0,002	< 0,002	-	< 0,002	< 0,002	-	< 0,002	< 0,002	-	< 0,002	< 0,002	-
(PO ₄) ³⁻ (mg/L)	0,4	0,21	0,19	9,52	0,16	0,13	18,75	0,07	< 0,002	100	0,17	< 0,002	100
C.F. (UFC/100ml)	0 (ausencia)	< 1,1	< 1,1	-	11	< 1,1	100	92	< 1,1	100	< 1,1	< 1,1	-
C.T. (UFC/100ml)	0 (ausencia)	< 1,1	< 1,1	-	1,6	< 1,1	100	2,2	< 1,1	100	< 1,1	< 1,1	-

Source: self made

To do the analysis of the results, Table N° 3 was made where the values before filtering are appreciated, which exceeded the values allowed by the National Superintendency of Sanitation Services (SUNASS) and that after filtering they decreased to normal values:

TABLE N° 3: Summary table of the physicochemical and bacteriological values that exceeded the established values before and after filtering.

Variables	Normativity (SUNASS)	Huacapuy		La Punta		Plaza de Quilca		Caleta de Quilca	
		Before Filter	After Filter	Before Filter	After Filter	Before Filter	After Filter	Before Filter	After Filter
Conductiv (µS)	1500	1180	520	1590	570	5260	840	5050	872
Cl- mg/L	250	112	96,4	146,3	102,56	1344,6	81,57	1356,67	87,05
(SO ₄) ²⁻ (mg/L)	250	236,32	156,45	345,2	205,2	1611,6	234,9	1621,4	246,6
C.F.(UFC/100ml)	0 (absence)	< 1,1	< 1,1	11	< 1,1	92	< 1,1	< 1,1	< 1,1
C.T.(UFC/100ml)	0 (absence)	< 1,1	< 1,1	1,6	< 1,1	2,2	< 1,1	< 1,1	< 1,1

Source: self made

In Table N° 3, it is observed that comparing the values established according to (SUNASS) with the values found in the different sampling points, it is found that: the waters after filtering by applying the nanocomposite, it was found that they remove the following in a greater proportion values: conductivity: 84.03% in La Plaza de Quilca, sulfates 85.42% in La Plaza de Quilca, chlorides 93.93% in La Plaza de Quilca. On the other hand, the Fecal Coliform and Total Coliform bacteria were 100% removed in La Punta and in the Plaza de Quilca. Coliform bacteria were not found in Huacapuy or in Caleta de Quilca. Therefore, it can be confirmed that the results have a significant removal percentage in the removal of anions and in terms of total coliform bacteria and fecal coliforms as a whole.

4 FILTER OPERATION

The procedure is based on microfiltration through a porous material, where the filter pores have a size between 0.6 and 0.3 µm, approximately determined by SEM. According to Van Der L.H. [15], if the pore size would be 0.1 µm, the filter would not need a disinfectant for the elimination of Escherichia coli, which has a size between 0.5 to 1 µm.

On the other hand, according to Ludeña J. [14], the presence of silver nanoparticles near a virus, fungus, bacterium or any other unicellular pathogenic microbe, incapacitates the oxygen metabolism enzyme and in a few minutes the pathogenic microbe suffocates, dies and it is eliminated from the body by the immune and lymphatic systems.

Vidal S.10 indicates that if silver binds to the cell membrane of bacteria, they increase their size and cytoplasmic content and present abnormalities that result in cell lysis and death.

According to the results obtained from Lantagne, the clay and sawdust-based filters form pores of 0.6 to 3 μm , which was determined by SEM, and microorganisms such as parasites are eliminated, including *Giardia* and *Cryptosporidium*, ranging from 5 - 7 μm and 5 μm , respectively. 99.99% but not 100% so it is necessary to impregnate the colloidal silver as it completely removes the bacteria.

5 CONCLUSIONS

When applying to the water samples under study, the filtering system based on the clay-carboxymethylchitosan nanocomposite - silver nanoparticles, the quality of the waters contaminated with bacteria and chemical substances was improved, producing water suitable for human consumption, therefore a low-cost filter system, simple technology, ecologically acceptable and economically accessible to low-income rural populations is being developed.

After filtering the waters using the nanocomposite, it was found that they remove the following values in a greater proportion: conductivity: 84.03% in La Plaza de Quilca, sulfates 85.42% in La Plaza de Quilca, chlorides 93.93% in Quilca Square. On the other hand, the Fecal Coliform and Total Coliform bacteria were 100% removed in La Punta and in the Plaza de Quilca. Coliform bacteria were not found in Huacapuy or in Caleta de Quilca. Therefore, it can be confirmed that the results have a significant removal percentage in the removal of anions and in terms of total coliform bacteria and fecal coliforms as a whole.

BIBLIOGRAPHY

1. Díaz del Castillo F. "Introduction to Nanomaterials". Mexico. 2012.
2. Almansi Florence. "Improving the provision of water, sanitation and hygiene services for low-income urban communities in Latin America: Guayaquil case." Water and Sanitation Program for Latin America - World Bank (WSP-BM). 2006.
3. Zhang, H. et al: "Facile preparation and characterization of highly anti-microbial colloid Ag or Au nanoparticles". United States. 2008.

4. Pérez Andrea, Díaz Jaime, González Ginna: "Comparative study of two home filtration systems for treating water for human consumption". Colombia. 2014.
5. Garrido L. and Albano M. "Processing of porous zirconia ceramics by direct consolidation with starch" Santiago-Chile.2008.
6. Weepiu Barrientos and Jhewerson Kevin: "Evaluation of Ceramic Filters to Improve the Quality of Water for Human Consumption in the San Mateo Sector, Moyobamba". Peru. 2015.
7. Balu Alina: "Nanoparticles supported on porous materials for the synthesis of high added value products". Cordova. 2012.
8. Juárez Henry, Juan Contreras, García Victor, Herrera Carlos. "Systematization of the water treatment filter process" Guatemala. 2011.
9. Monge Miguel: "Silver nanoparticles: dissolution synthesis methods and bactericidal properties". Spain 2009.
10. Vidal Sandra: "Evaluation of the effectiveness of the filter based on clay and colloidal silver in the purification of water, measured by physicochemical and microbiological tests". Colombia. 2010.
11. Tarazona Andrés "Study of the removal of coliforms in natural waters using a cartridge type filter packed with nanocomposites of fique fibers with silver nanoparticles". Bucaramanga. Colombia. 2011.
12. APHA-AWWA-WEF (2005) Standard Methods for the Examination of Water and Wastewater. 21th Edition. Washington DC, 2-1 to 2-3, method 2120 B.
13. Balcázar Cecilia. "Water and sanitation for the marginal urban Water and Sanitation Program areas of Latin America". Memory of the international workshop. Medellin Colombia. 2008.
14. Ludeña Julio and Tinoco Freddy: "Red Paste formulation for the elaboration of a water purifying ceramic filter and verification of its filtering effectiveness". Ecuador. 2010.
15. Van Der L. H., Van Halem D., Smeets P.W., Soppe A.I., Kroesbergen J., Wubbels F.G. : "Bacteria and virus removal effectiveness of ceramic pot filters with different silver applications in a long term experiment". Water Research. 2014.

CHAPTER 10

NANOGRAIN BOUNDARY PHENOMENON IN CERAMIC NANOMETRIC MICROSTRUCTURE¹

Data de aceite: 15/05/2021

Marcos Augusto Lima Nobre

São Paulo State University, School of
Technology and Sciences – FCT/UNESP
Department of Physics
Presidente Prudente – SP
<http://lattes.cnpq.br/7201928600704530>

Silvania Lanfredi

São Paulo State University School of
Technology and Sciences – FCT/UNESP
Department of Chemistry and Biochemistry
Presidente Prudente – SP
<http://lattes.cnpq.br/0239752189917951>

ABSTRACT: Nanograin boundary relaxation frequency phenomenon at cryogenic temperatures of $\text{KSr}_2\text{Nb}_5\text{O}_{15}$ ceramic with microstructure based on nanosized grains has been investigated. The presence of nanosized microstructure results in an increasing of “grain boundary” contribution dielectric response. A process to derive the nanograin relaxation frequency assigned to nanograins boundary from deconvolution of the Imaginary component of impedance is discussed.

¹ This chapter is the translation of the chapter published in the book: The great world of nanotechnology / Organizador Marcos Augusto Lima Nobre. – Curitiba, PR: Artemis, 2020, Cap. 6, p. 59.

KEYWORDS: Nanotechnology. Nanostructures. Nanograins. $\text{KSr}_2\text{Nb}_5\text{O}_{15}$ ceramic.

1 INTRODUCTION

Compounds based on niobium and alkali and alkaline earth metals have been considered one of the most promising ferroelectric materials. Among these compounds stands out the strontium potassium niobate, $\text{KSr}_2\text{Nb}_5\text{O}_{15}$, with tetragonal tungsten bronze, TTB-type structure. However, only in recent years that these materials have attracted attention. This fact suggests that there is a potential for the discovery of new ferroelectric materials. In addition, the development of new materials is not only relevant, well as the monitoring of the properties of these materials in nanometric scales is fundamental. This aspect is important to the design of properties and new technologies involving nanometric and/or nanostructured ceramics, multilayer capacitors, polymer-ceramic composites.

The scale effect can be considered a phenomenon that describes the appearance or disappearance of a material property due to the variation in the dimensional scale. A similar

effect, denominated particle size effect, is attributed to the intensification or reduction of a property of the material due to the dimensional variation, however this property exists regardless of the scale.

Nanoparticles, nanopowders and nanostructured materials have been used with great success to allow optical, calorimetric, mechanical, magnetic and electrical resistance properties, as a function of scale and size effects. In fact, in the nanometric scale, size effects are also relevant to structural properties.

The tetragonal tungsten bronze TTB-type structure belongs to an important class of ferroelectric materials, from a series of lead-free compounds. This TTB structure has the capacity to arrange cations of different ionic radius and different valences along their interstitial sites (Magneli, 1949).

The TTB-type structure consists of a complex matrix of octahedral distortions BO₆, in order to generate cavities and/or crystallographic sites denominated A, B and C, where these correspond to the pentagonal, tetragonal and trigonal sites, respectively (Abrahams et al., 1971; Tribotte et al., 1998; Lanfredi et al. 2004).

The TTB-niobate structure can be further described by the general formula $(A1)_2(A2)_4C_4(B1)_2(B2)_8O_{30}$. A1 and A2 occupy 12-fold coordinated and 15-fold coordinated tunnels, respectively. C sites are typically vacant. (B1) and (B2) sites are resulting from two types of octahedral distortions BO₆.

The TTB-type structure enables the substitution of a wide-variety of cations in the A1, A2 sites, in particular alkali and alkaline earth. Other substitutions based on the transition metal are viable in the (B1) and (B2) sites. The cations substitution in the different sites of the structure have a significant effect on its dielectric properties (Lanfredi et al., 2012).

Strontium potassium niobate has attracted particular interest for presenting several properties such as ferroelectric, dielectric, piezoelectric, high polarization (Shanming et al., 2008; Lanfredi et al. 2014), besides to have electro-optical, catalytic and photocatalytic properties (Matos et al., 2017) .

This work provides a comprehensive report on the structural thermal stability of the $KSr_2Nb_5O_{15}$ powder investigated by X-ray diffraction and the dielectric-permittivity properties at cryogenic temperatures of $KSr_2Nb_5O_{15}$ ceramic with microstructure based on nanosized grains. The correlations between thermal hysteresis of dielectric permittivity and non structural phase transitions are established.

2 SYNTHESIS OF THE NIOBATE POWDER BY THE MODIFIED POLYOL METHOD

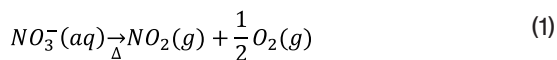
The Modified Polyol Method (Lanfredi et al., 2012) was used in this work for the chemical synthesis of strontium and potassium niobate powders with stoichiometry

$\text{KSr}_2\text{Nb}_5\text{O}_{15}$. This method allows the synthesis of powders in a reduced number of steps and the obtention of single-phase powders. The first step consists of the mixing of starting reagents followed by the pre-calcination, giving rise to the precursor powders. Then, the precursor was calcined in order to obtain single-phase and crystalline powders. The starting reagents for the powder synthesis via chemical route were nitric acid HNO_3 (99.5% Reagen), strontium carbonate SrCO_3 (99.0% Reagen), potassium carbonate K_2CO_3 (99.0% Reagen), ethylene glycol $\text{HOCH}_2\text{CH}_2\text{OH}$ (98.0 % Synth) and hydrated niobium oxide ($\text{Nb}_2\text{O}_5 \cdot 3.28\text{H}_2\text{O}$) (CBMM-Brazil).

In a beaker was added niobium oxide to which was dripped slowly nitric acid until its dissolution. Then, strontium and potassium carbonates were added gradually, and again, drops of concentrated nitric acid were added. After dissolving all the starting salts, 100 ml of ethylene glycol was added in the mixture, which was submitted to heating at 423K.

The gradual increase in temperature caused the release of a gas of brown color, due to the decomposition of the nitric acid, similar to the reaction developed in the synthesis by the Polymeric Precursor Method, or Pechini (Pechini, 1967; Lanfredi et al., 2004).

The gas formed was the NO_2 , resulting of the pyrolysis of the nitrate group in solution, according to the chemical reaction:



After this process, a gel polymeric is obtained. Then, the gel polymeric is maintained in the beaker undergoes a primary calcination in a furnace type box. The heating cycle was carried out using two steps.

In the first step, the temperature was increased using a heating rate equal to 10 K/min from room temperature up to 423 K. At this point, the temperature was kept constant during 1 hour for eliminating low molecular mass molecules, such as water vapor and some organic groups. In the second step, maintaining the same heating rate, the temperature was increased at 573 K, being maintained during 2 hours for the partial elimination of elements not belonging to the stoichiometry of solid solutions, such as CO , CO_2 and H_2O molecules. Both pre-calcination steps were performed under an N_2 (g) atmosphere with a flow rate of 300 mL/min. After the cycle, the furnace was cooling to the natural rate.

After pre-calcination, the precursor powder was obtained in the form of black porous charcoal, which was deagglomerate in an agate mortar and then in a sieve of 325 mesh with opening of 45 μm . Then, the precursor powder exhibited a dark gray color and a fine and homogeneous aspect. The precursor powder was calcined in a furnace type box at 1423 K for 10 hours, in oxygen atmosphere with flux of 300 mL/min, and then the furnace was cooling to the natural rate.

2.1 STRUCTURAL CHARACTERIZATION OF THE $\text{KSr}_2\text{Nb}_5\text{O}_{15}$ POWDER

Structural analysis of the $\text{NaSr}_2\text{Nb}_5\text{O}_{15}$ powder was carried out by X-ray diffraction (XRD), using a SHIMADZU (model XRD-6000) diffractometer with $\text{Cu-K}\alpha$ radiation ($\lambda = 1.54 \text{ \AA}$) and a graphite monochromator. Measurements were carried out at 40kV e 30mA over an angular range of $5^\circ \leq 2\theta \leq 80^\circ$ with a scanning step of 0.02° and a fixed counting time of 1.2s. Divergence, scattered and receiving radiation slits were 1° , 1° and 0.3 mm, respectively.

The $\text{KSr}_2\text{Nb}_5\text{O}_{15}$ structure was refined according to the Rietveld method using the Fullprof program FullProf (Carvajal, 2008). The parameters and variables adopted during the refinement process were the background coefficients, profile coefficients, lattice parameters, linear absorption coefficients, coordination parameters and structure factor.

The data obtained, from the structural parameters refinement, were used in the Diamond program to build the crystallographic structure of the $\text{KSr}_2\text{Nb}_5\text{O}_{15}$.

2.2 ELECTRICAL CHARACTERIZATION OF THE $\text{KSr}_2\text{Nb}_5\text{O}_{15}$ CERÂMIC

Prior to the sintering, the powder was uniaxially pressed into pellet form of 8x2 mm dimension. The green compact was sintered at 1553 K in air for 2 h at a heating rate of 2.0 K/min. Relative density equal to 97 % of the theoretical density was reached. Microstructure was characterized using scanning electron microscopy – SEM (Zeiss DSM 962).

Electric measurements were carried out by impedance spectroscopy over a complete thermal cycle. Electrodes were deposited on both faces of the sample with a platinum paste coating (TR-7905 –Tanaka). After complete solvent evaporation, the electrode/ceramic was dried at 1073 K for 30 min. Measurements were taken in the frequency range of 5 Hz to 13 MHz, with an applied potential of 500 mV using an Impedance Analyzer Alpha N High Resolution Dielectric from Novocontrol GmbH. The sample was placed in a sample holder with a two-electrode configuration. Measurements were taken from room temperature to 800 K in 50-K steps at a heating rate equal to 1.0 K/min in air. A 30-min interval was used prior to thermal stabilization before each measurement. The data were plotted using the complex plane formalism ortho-normalized, $Z'(\omega)$ versus $Z''(\omega)$ plot, and analyzed with Boukamp's EQUIVCRT software.

Dielectric spectroscopy characterization was performed in the frequency range of 1 kHz to 1 MHz and a temperature range of 15K to 800 K.

The complex permittivity function $\epsilon^*(\omega)$ was derived from the impedance function, $Z^*(\omega)$:

$$Z^*(\omega) = \sum_i^n Z_i^*(\omega) = Z_1^*(\omega) + Z_2^*(\omega) + \dots + Z_n^*(\omega) \quad (2)$$

$$Z^*(\omega) = \sum_i^n Z_i'(\omega) + j \sum_i^n Z_i''(\omega) = \sum_i^n \text{Re}_i(Z) + j \sum_i^n \text{Im}_i(Z) \quad (3)$$

where $Z^*(\omega)$ is an apparent response composed by the contribution of all electroactive components of the system and can be represented by Eq. (2) and (3), n is the number of electroactive component of the system. The most frequent response to $Z^*(\omega)$ is a semicircle which can be decentralized or not be. In a general way, this semicircle is an apparent response which represents a combination of two or more semicircles, as example grain and grain boundary (Lanfredi et al., 2012). Each semicircle can be fulfilled observed on the impedance diagram only if the relaxation frequency that ascribes each semicircle differ at least of two orders of magnitude.

Typically, for polycrystalline ceramic systems, the impedance can be described by two electroactives contributions assigned to the grain (G) and the grain boundaries (GB). From Eq. (2) determines the impedance of the system given by Eq. (4):

$$Z_{\text{CERAMIC}}^*(\omega) = Z_G^*(\omega) + Z_B^*(\omega) \quad (4)$$

From of the function transformation $\varepsilon_{\text{CERAMIC}}^*(\omega) = [j\omega\varepsilon_0\Lambda Z^*(\omega)]^{-1}$, these components of transformation relationships are given by the Eq. (5), as follows (Nobre e Lanfredi, 2000):

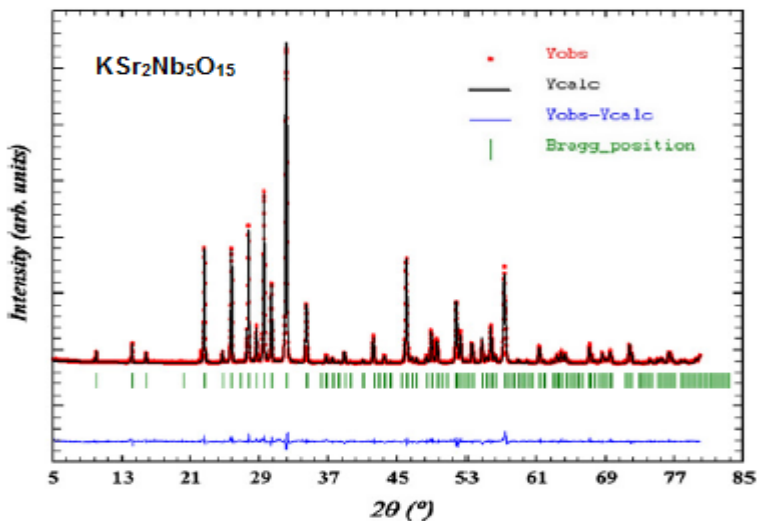
$$\varepsilon_{\text{CERAMIC}}^*(\omega) = \frac{1}{j\omega\varepsilon_0\Lambda Z^*(\omega)} = \begin{cases} \varepsilon'(\omega) = -\frac{1}{\Lambda\omega\varepsilon_0} \left(\frac{Z''(\omega)}{|Z^*(\omega)|^2} \right) \\ \varepsilon''(\omega) = \frac{1}{\Lambda\omega\varepsilon_0} \left(\frac{Z'(\omega)}{|Z^*(\omega)|^2} \right) \end{cases} \quad (5)$$

where Λ represents the geometric factor of the cell, ω represents the angular frequency ($\omega = 2\pi f$), ε_0 represents the vacuum permittivity constant (8.8542×10^{-12} F/m), and $|Z^*(\omega)|$ represents the module of the impedance; $\varepsilon'(\omega)$ and $\varepsilon''(\omega)$ represent both the real and imaginary component of the complex dielectric permittivity $\varepsilon^*(\omega)$, respectively.

3 STRUCTURAL ANALYSIS

The $\text{KSr}_2\text{Nb}_5\text{O}_{15}$ powder exhibited only a set of diffraction lines ascribed to the TTB-type structure. The structural parameters of $\text{KSr}_2\text{Nb}_5\text{O}_{15}$ were derived the Rietveld method. The Rietveld plot for the $\text{KSr}_2\text{Nb}_5\text{O}_{15}$ is shown in Figure 1.

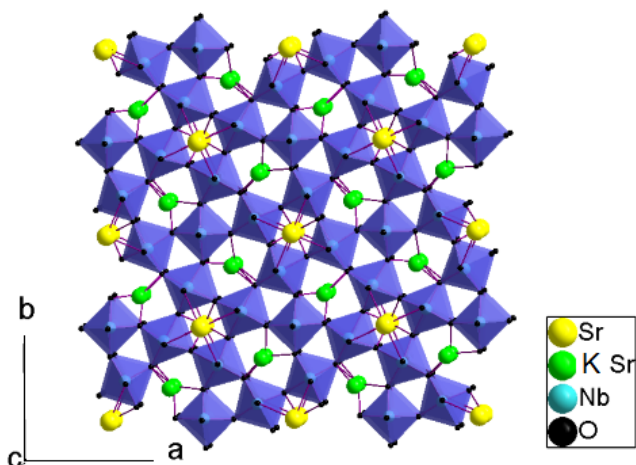
Figure 1: Rietveld plot for the $\text{KSr}_2\text{Nb}_5\text{O}_{15}$ powder obtained at 1423 K for 10h.



The best refinements were performed by taking into account the space groups $P4bm$ that are compatible with the rule of existence $[(0\ k\ l)\ k = 2n]$, where each tetragonal site was occupied by a Sr^{2+} ion and each pentagonal site was statistically occupied by equal quantities of K^+ and Sr^{2+} ions. The trigonal site was considered vacant. Two non-equivalent octahedral sites are occupied by Nb^{5+} cations called Nb (1) and Nb (2) (Lanfredi et al., 2004).

Figure 2 shows the graphic representation of the unit cell obtained for $\text{KSr}_2\text{Nb}_5\text{O}_{15}$ powder at 1423 K for 10h.

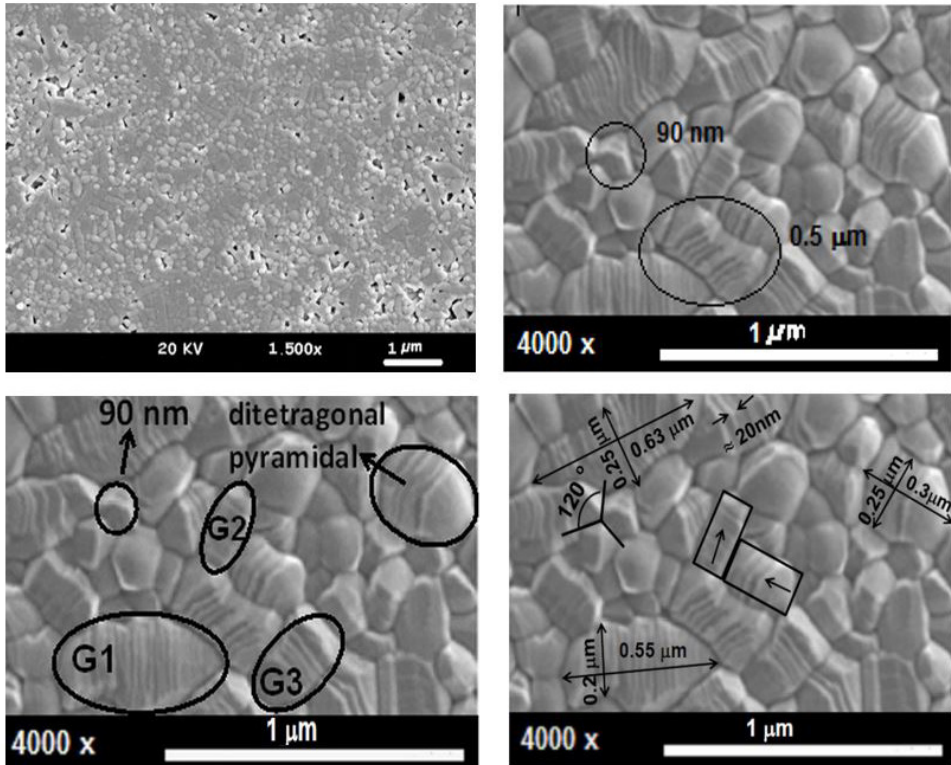
Figure 2: Tetragonal tungsten bronze structure of the $\text{KSr}_2\text{Nb}_5\text{O}_{15}$ powder obtained at 1423K for 10h.



4 MICROSTRUCTURAL ANALYSIS

Figure 3 shows the scanning electron microscopy (SEM) image of the $\text{KSr}_2\text{Nb}_5\text{O}_{15}$ ceramic sintered at 1553 K for 2 h.

Figure 3: Scanning electron microscopy image of the nanostructured ceramic.



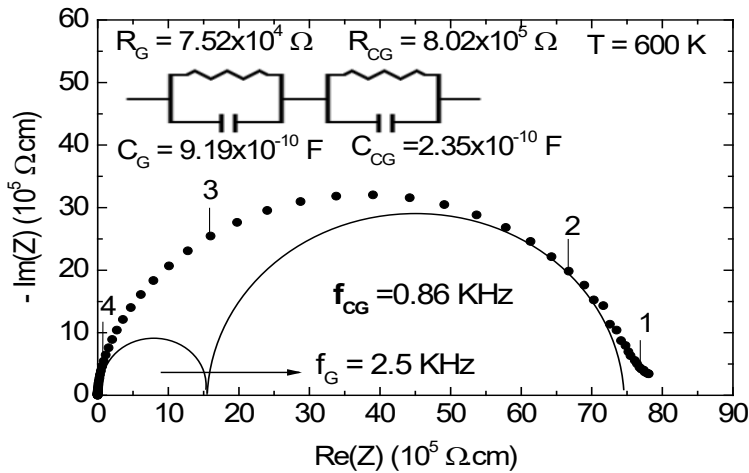
The microstructure shows few pores and nanosized grains. The inset shows an expanded region of Figure 3 that exhibits some grains with anisotropic growth because the growth rate in the *c*-axis direction [001] is faster than that in the *a*-axis direction, resulting in a growth and displacement of grains, as can be seen in G1, G2 and G3.

According to Figure 3, grains are formed by a substructure of ≈ 20 nm. The formation of these substructures are due the displacement of grains that can be observed along of grains of size of 0.3 μm, 0.55 μm and 0.63 μm of length and of 0.20 μm and 0.25 μm of wide. Such substructure seems be generated by perpendicular forces to *c*-axes, which leads to the cleavage phenomenon.

5 ANALYSIS OF ELECTRICAL PROPERTIES

Figure 4 shows the $\text{KSr}_2\text{Nb}_5\text{O}_{15}$ impedance diagram and theoretical adjustment attained at 600 K.

Figure 4: Impedance diagram ($Z'(\omega)$ vs $Z''(\omega)$) and theoretical adjustment obtained at 600 K.

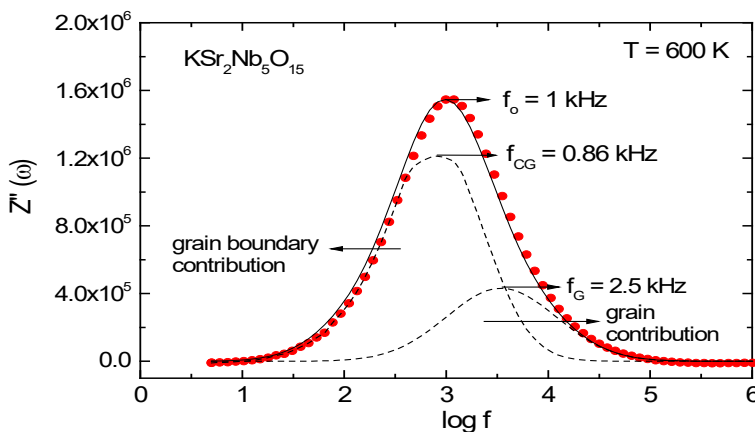


According to Figure 4, points on the plot represent the experimental data, while the continuous line represents the theoretical adjustment. The agreement between the experimental points and the theoretical curve is excellent.

The electric response is well represented by four equivalent parallel RC circuits in series, where R represents the resistance and C represents the capacitance.

The semicircle at low frequency ($<10^3$ Hz) represents the grain boundary contributions and the semicircle at high frequency ($> 10^3$ Hz) represents the contribution corresponding to the grain or bulk. The relaxation frequency of the grain is at around 2.5 KHz, while for the grain boundary is of 0.86 KHz. The same relaxation frequency values were obtained from adjustment of the imaginary part curve, $Z''(\omega)$, as a function of $\log f$, as shown in Figure 5. The adjustment was performed by two Gaussian functions.

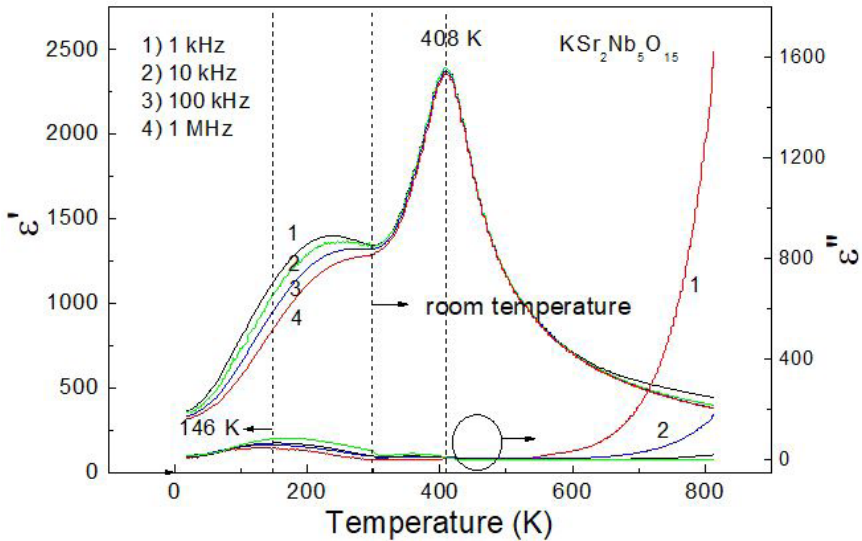
Figure 5: $Z''(\omega)$ as a function of $\log f$ adjusted by two Gaussian functions.



6 ANALYSIS OF DIELECTRIC PROPERTIES

Figure 6 shows the real part $\epsilon'(\omega)$ and the imaginary part $\epsilon''(\omega)$ of the complex dielectric permittivity $\epsilon^*(\omega)$ as a function of temperature at several frequencies.

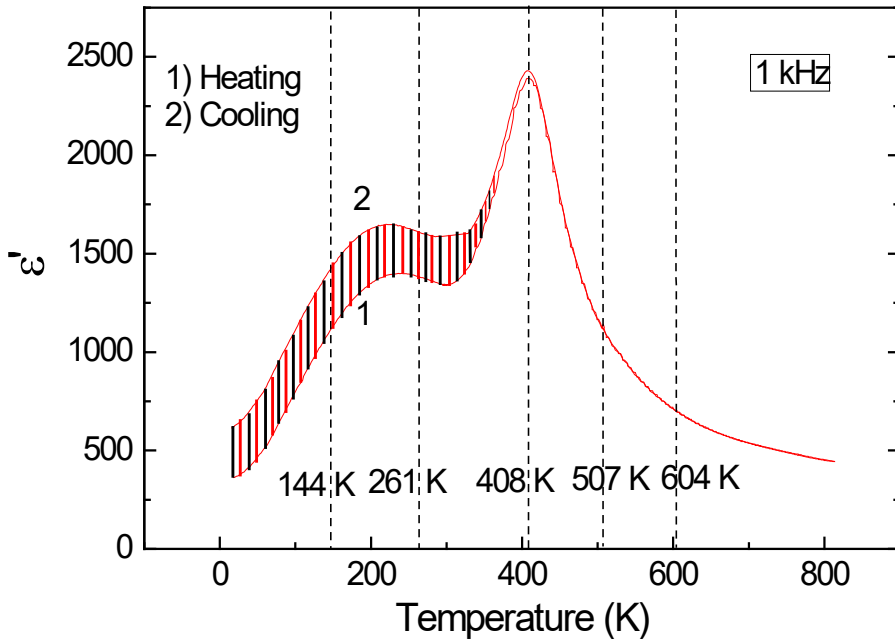
Figure 6: Evolution of the real (ϵ') part and imaginary (ϵ'') part of the complex dielectric permittivity of $\text{KSr}_2\text{Nb}_5\text{O}_{15}$ ceramic.



A visual inspection of curves shows two broad peaks or anomalies in both the $\epsilon'(\omega)$ and $\epsilon''(\omega)$ curves. Considering the peak-superposition phenomenon, an apparent peak in $\epsilon'(T)$ is closely centered at 255 K as a shoulder with a very broad peak, while a defined peak is positioned at 408 K. The apparent relative maximum of ϵ' at approximately 255 K also has been observed as function of the frequency of measurement. The dependence of a maximum value of permittivity with a frequency has been assigned to some degree of chemical and structural disorder. Therefore, the phenomenon observed at approximately 255 K as function of the frequency can be resulted of different domains in the structure. On the other hand, the peak centered at close to 408 K exhibits a sharp absolute-maximum ($\epsilon' = 2375$) in the $\epsilon'(\omega)$ versus T curve and has been assigned to the ferroelectric-paraelectric transition due the Curie's temperature (Belghiti al., 2002). A single peak in the $\epsilon''(\omega)$ versus T curve of small intensity, occurring as a broader peak at approximately 146 K, is attributed to the existence of dielectric loss by conduction (Lanfredi et al., 2002).

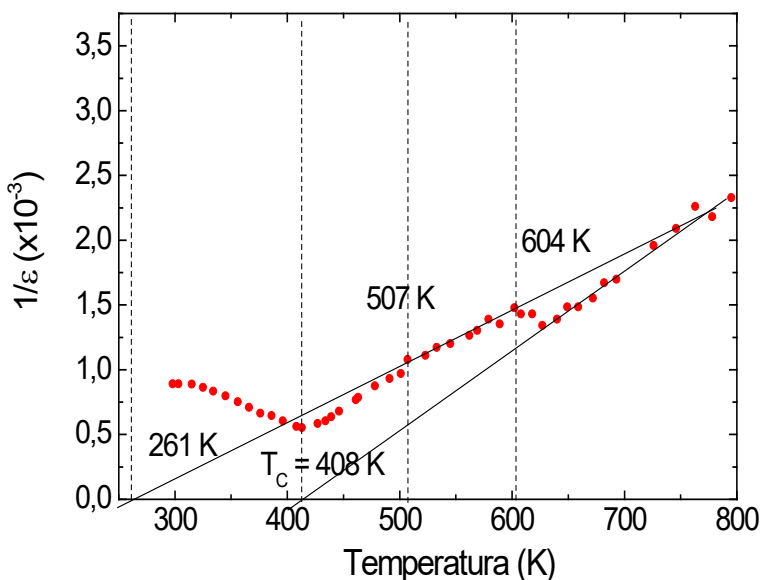
Figure 7 shows the evolution of the real permittivity, ϵ' , as a function of temperature, measured at 1 KHz during the heating cycle.

Figure 7: Permittivity curves as a function of temperature measured at 1 kHz.



The ϵ' parameter exhibits a well-behaved thermal-hysteresis at cryogenic temperatures domain, see the dashed area. Typically, mixture of phases of same stoichiometry but distinct symmetry structure gives the above mentioned hysteretical effect (Nobre e Lanfredi, 2001). A significant area of thermal hysteresis below 408 K strongly suggests that there are not a structural phase transition corroborated by the specific lattice parameter evolution and that non exhibits discontinuous or abrupt changing. Then, significant part of the phenomenon has only basis on the structural distortion. These phase transitions observed in the permittivity curves are confirmed in the permittivity inverse curve as a function of temperature, shown in Figure 8. The sequence of phase transitions can be related to the coexistence of same symmetry phases, but with a particular crystal lattice distortion. This concept is relevant, since the transitions can be structural or not. If a sufficient degree of distortion is generated, a new symmetry can emerge, otherwise the phase transition occurs, but the symmetry of the prototype is maintained, while only specific distortions are allowed, such as the distortion of the niobium off-center in the NbO_6 octahedral of the tetragonal tungsten bronze structure.

Figure 8: Permittivity inverse as a function of temperature.



7 CONCLUSION

In the cryogenic temperature domain of the permittivity curve, the large area of hysteresis below Curie's temperature of relative maximum was associated to the intrinsic structural distortion with major contributing of niobium that exhibits distinct degree of off-centering character. Electrical phenomena of interface polarization are reviewed from microstructural, electrical and specific crystalline features. Frequency values of the interfaces showed that the $\text{KSr}_2\text{Nb}_5\text{O}_{15}$ nanostructured ceramic can be used as electroactive components in the low frequencies domain.

REFERENCES

ABRAHAMS, S., C.; JAMIESON, P., B.; BERNSTEIN, J., L.; Ferroelectric tungsten bronze-type crystal structures III – potassium lithium niobate $\text{K}_{(6-x-y)}\text{Li}_{(4+x)}\text{Nb}_{(10+y)}\text{O}_{30}$, **Journal of Chemical Physics**, v. 54, p. 2355, 1971.

H. El A. Belghiti, A. Simon, P. Gravereau, A. Villesuzanne, M. Elaatmani and J. Ravez, *Sol. State Sci.*, 2002, **4**, 933.

CARVAJAL, J.R. An Introduction to the Program FullProff 2000, CEA/Saclay, France, 2008.

MATOS, J.; LANFREDI, S.; MONTAÑA, R.; NOBRE, M.A.L.; FERNÁNDEZ DE CÓRDOBA, M. C.; ANIA, C. O. Photochemical reactivity of apical oxygen in $\text{KSr}_2\text{Nb}_5\text{O}_{15}$ materials for environmental remediation under UV irradiation, **Journal of Colloid and Interface Science**, v. 496, p. 211–221, 2017.

LANFREDI, S.; DARIE, C.; BELLUCCI, F.S.; COLIN, C.V.; NOBRE, M.A.L. Phase transitions and interface phenomena in the cryogenic temperature domain of a niobate nanostructured ceramic, **Dalton Transactions**, v. 43, p. 10983, 2014.

LANFREDI, S.; PALACIO, G.; BELLUCCI, F. S.; COLIN, C. V.; NOBRE, M. A. L. Thermistor Behavior and Electric Conduction Analysis of Ni-Doped Niobate Ferroelectric: the Role of Multiples β Parameters, **Journal of Physics D: Applied Physics**, v. 45, p. 435302, 2012.

LANFREDI, S.; BRITO, I.A.O.; POLINI, C.; NOBRE, M.A.L. Deriving the magnitude of niobium off-center displacement in ferroelectric niobates from infrared spectroscopy **Journal of Applied Spectroscopy**, v.79, p. 254-260, 2012.

LANFREDI, S.; CARDOSO, C.X.; NOBRE, M. A. L. Crystallographic properties of $\text{KSr}_2\text{Nb}_5\text{O}_{15}$, **Materials Science and Engineering B-Solid State Materials for Advanced Technology**, v. 112, p. 139-143, 2004.

LANFREDI, S.; LENTE, M. H.; EIRAS, J. A. Phase transition at low temperature in NaNbO_3 ceramic, **Applied Physics Letter**, v. 80, p. 2731-2733, 2002.

MAGNELI, A.; The crystal structure of tetragonal potassium tungsten bronze, **Ark. Kemi**, v. 24, p. 213, 1949.

NOBRE, M. A. L.; LANFREDI, S. Phase transition in sodium lithium niobate polycrystal: an overview based on impedance spectroscopy, **Journal of Physics and Chemistry of Solids**, v. 62, p. 1999-2006, 2001.

NOBRE, M. A. L.; LANFREDI, S. Impedance Spectroscopy Analysis of High-Temperature Phase Transitions in Sodium Lithium Niobate Ceramics. **Journal of Physics: Condensed Matter**, v. 12, p.7833-7841, 2000.

PECHINI, M. P. "Method of Preparing Lead and Alkaline-Earth Titanates and Niobates and Coating Method Using the Same to Form a Capacitor," U.S. Pat. No. 3 330 697, July 11, 1967.

SHANMING, K. E.; HUIQING, F.; HUANG, H.; CHAN, H. L. W.; YU, S. Dielectric, ferroelectric properties, and grain growth of $\text{Ca}_x\text{Ba}_{1-x}\text{Nb}_2\text{O}_6$ ceramics with tungsten bronzes structure. **Journal of Applied Physics**, v. 104, p. 24101, 2008.

TRIBOTTE, B.; HERVIEU, M.; DESGARDIN, G.; Dielectric and structural properties of A-cation-deficient perovskites, tetragonal tungsten bronzes and their composites in the $\text{K}_2\text{Sr}_4(\text{Mg}_x\text{Nb}_{10-x})\text{Li}_{3x}\text{O}_{30}$ system, **Journal of Materials Science**, v. 33, p. 4609, 1998.

CHAPTER 11

ON SPIN HAMILTONIAN FITS TO MÖSSBAUER SPECTRA OF NIFE₂O₄ NANOPARTICLES SYNTHESIZED BY CO-PRECIPIATION¹

Data de submissão: 04/04/2021

Data de aceite: 28/04/2021

Jose Higinio Dias Filho

Universidade Estadual de Montes Claros
Programa de Pós-Graduação em Modelagem
Computacional e Sistemas
Montes Claros – MG
<https://orcid.org/0000-0003-1769-2907>

Jorge Luis Lopez

Centro de Ciências Biológicas e da Natureza
Universidade Federal do Acre
Rio Branco – AC
<https://orcid.org/0000-0003-0749-1351>

Adriana Silva de Albuquerque

Serviço de Nanomateriais do CDTN /CNEN
Belo Horizonte – MG
<https://orcid.org/0000-0003-4167-7678>

Renato Dourado Maia

Universidade Estadual de Montes Claros
Programa de Pós-Graduação em Modelagem
Computacional e Sistemas
Montes Claros – MG
<https://orcid.org/0000-0002-1969-2364>

Wesley de Oliveira Barbosa

Instituto Federal do Norte de Minas Gerais
Reitoria
Montes Claros – MG
<https://orcid.org/0000-0001-8737-5179>

Ernando Campos Ferreira

Escola Estadual Irmã Beata
Montes Claros – MG
<https://orcid.org/0000-0002-0731-0197>

Fellipe Silva Pereira

Escola Estadual Zinha Meira
Bocaiúva – MG
<https://orcid.org/0000-0001-5659-4934>

Kátia Guimarães Benfica

Escola Estadual Gilberto Caldeira Brant
Bocaiúva – MG
<https://orcid.org/0000-0001-5119-7382>

ABSTRACT: Nanocrystalline NiFe₂O₄ particles prepared by chemical co-precipitation method were studied using magnetic measurements, ⁵⁷Fe Mössbauer spectroscopy, X-ray diffraction, and transmission electron microscopy. Fits to Mössbauer spectra, in the range of 4.2 K – 300 K, were done using spin hamiltonians to describe both the electronic and nuclear interactions, a model of superparamagnetic relaxation of two levels (spin ½) and stochastic theory, a log-normal particle size distribution function as well as a dependency

¹ Published in: Revista Mundi Engenharia, Tecnologia e Gestão, vol. 5, n. 6 (2020), pp. 287-300. Online first version: <http://periodicos.ifpr.edu.br/index>

of the magnetic transition temperature and the anisotropy constant on particle diameter. We have used evolutionary strategies to fit the more complex Mössbauer spectra line shapes. The nanoparticles have an average size of 7 nm and exhibit superparamagnetism at room temperature. The saturation magnetization (M_s) at 4.2 K was determined from M vs. $1/H$ plots by extrapolating the value of magnetizations to infinite fields, to 24.21 emu/g and coercivity to 3.15 kOe. A magnetic anisotropy energy constant (K) $1.9 \cdot 10^5$ J/m³, at 4.2 K, were calculated from magnetization measurements. The synthesis, characterization, and functionalization of magnetic nanoparticles is a highly active area of current research located at the interface between materials science, biotechnology, and medicine. Superparamagnetic iron oxides nanoparticles have unique physical properties and have emerged as a new class of diagnostic probes for multimodal tracking and as contrast agents for magnetic resonance imaging (MRI). **KEYWORDS:** NiFe₂O₄ nanoparticles. Evolutionary strategies. Fits on Mössbauer spectra.

SOBRE AJUSTES POR HAMILTONIANO DE SPIN DE ESPECTROS MÖSSBAUER DE NANOPARTÍCULAS DE NIFE2O4 SINTETIZADAS POR CO-PRECIPITAÇÃO

RESUMO: Partículas nanocristalinas de NiFe₂O₄ preparadas pelo método de co-precipitação química foram estudadas usando-se medidas magnéticas, espectroscopia Mössbauer de ⁵⁷Fe, difração de raios-X e microscopia eletrônica de transmissão. Ajustes de espectro Mössbauer, na faixa de 4,2 K – 300 K, foram feitos utilizando-se hamiltonianos de spin para descrever as interações eletrônicas e nucleares, um modelo de relaxação superparamagnética de dois níveis (spin 1/2) e teoria estocástica, função distribuição de tamanho de partículas log-normal, bem como uma dependência da temperatura de transição magnética e da constante de anisotropia dependendo do diâmetro das partículas. Usamos estratégias evolutivas para ajustar as formas mais complexas das linhas de espectro Mössbauer. As nanopartículas têm um tamanho médio de 7 nm e exibem superparamagnetismo à temperatura ambiente. A magnetização de saturação (M_s) a 4,2 K foi determinada a partir de plotagens de M vs $1/H$, extrapolando o valor das magnetizações para campos infinitos, para 24,21 emu/g e coercividade para 3,15 kOe. Uma constante de energia de anisotropia magnética (K) $1,9 \cdot 10^5$ J/m³, a 4,2 K, foi calculada a partir de medidas de magnetização. A síntese, caracterização e funcionalização de nanopartículas magnéticas é uma área altamente ativa de pesquisa atual localizada na interface entre ciência dos materiais, biotecnologia e medicina. Nanopartículas de óxidos de ferro superparamagnéticos têm propriedades físicas únicas e emergiram como uma nova classe de sondas de diagnóstico para rastreamento multimodal e como agentes de contraste para ressonância magnética (RM).

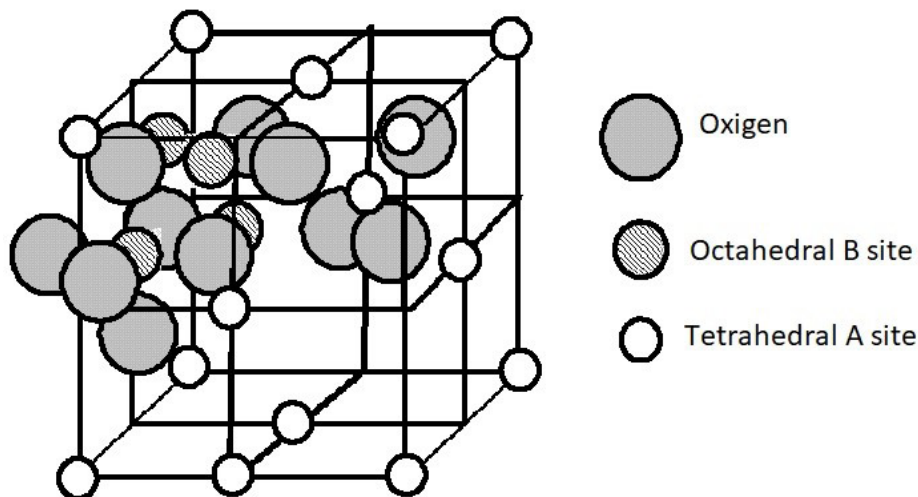
PALAVRAS-CHAVE: Nanopartículas de NiFe₂O₄. Estratégias Evolucionárias. Ajustes de espectros Mössbauer.

1 INTRODUCTION

Nickel ferrite nanoparticles, NiFe₂O₄ prepared in different ways, have attracted considerable attention due to both their unusual properties compared to those of the bulk materials and their potential applications (J. L. López, 2001). Like other iron oxides,

e.g., magnetite (Fe_3O_4), manganese ferrite (MnFe_2O_4), and cobalt ferrite (CoFe_2O_4), NiFe_2O_4 is a soft ferrite and presents easy magnetization and demagnetization. All of them have a *spinel* structure with octahedral and tetrahedral sites (Fig. 1). Sites A and B are antiferromagnetic and ferromagnetic regions, respectively. The synthesis, characterization, and functionalization of magnetic nanoparticles is a highly active area of current research located at the interface between materials science, biotechnology, and medicine.

Figure 1 – Spinel structure.



Source: Adapted from MARTINS (2008, p. 16).

For many years, it has been known that magnetic particles with a size smaller than few tens of nanometer can be considered as single domains and, hence, display properties markedly different from the bulk (MEDRANO et al., 2018). Another exciting feature of the nanoparticles is due to the surface spin disorder, which is induced by the broken exchange bonds at the surface. This is especially true for the case of ferrites where the (negative) superexchange interaction is mediated by an intervening oxygen ion, and it can be missing at the surface. As a result, the system should be considered a core-shell structure with ferromagnetically aligned core spins and a spin-glass like surface layer. With the reduction of the particle size at the nanoscale, the surface to volume ratio becomes very large, and surface effects may induce a spin-canted structure as well as an enhanced surface anisotropy (KODAMA, 1996).

Besides having unique physical properties, nanoparticles are a couple with size range commensurate with biomolecular and cellular systems. These properties make nanoparticles attractive for therapeutic and diagnostic applications (photothermal therapy, imaging, and delivery applications). However, application in biomedicine requires controlled

interactions with molecules, like non-cytotoxicity, cellular internalization ability, and carrier ability (SAHA, 2011). For the effective utilization of these materials in biomedicine, nanoparticles have been functionalized with a variety of ligands such as surfactants, small molecules, polymers, dendrimers, and biomolecules. Nanoparticles interacting with organic compounds show different effects that depend on how the functionalization is performed (LÓPEZ, 2001) (TOURINHO, 1999). Oleic acid has proved to be useful as a surfactant to magnetic nanoparticles. On the other hand, vegetable oils have in their composition different fatty acids, including oleic acid, palmitic, linolenic, and others.

NiFe₂O₄ nanoparticles studied in this work were prepared by chemical co-precipitation method using an aqueous solution of Ni(NO₃)₂·6H₂O and Fe(NO₃)₃·9H₂O and the NaOH solution as the precipitating agent. They were studied using magnetic measurements, ⁵⁷Fe Mössbauer spectroscopy, X-ray diffraction, and transmission electron microscopy.

Mössbauer spectroscopy (ME) allows displaying the hyperfine structure of an ion in a solid. Due to the interactions of the ion with its environment, the electronic, magnetic moment, and the charge distribution of the ion can fluctuate. The times which characterize these fluctuations depend on the intensity of the interactions. Through the hyperfine coupling, the nucleus feels these effects. By means of ME one can observe fluctuations whose characteristic times are in the interval 10⁻⁶-10⁻¹¹ s (CIANCHI, 1986).

The paper is organized as follows. In section 2, the basic informations of sample preparation are presented, the basic features of the theoretical model and of the Mössbauer spectroscopy are introduced, and the characteristics of evolutionary algorithms used in the model parameterization are discussed. In section 3, the obtained results are presented and discussed. In section 4, we made conclusions and proposals for future works.

2 MATERIALS AND METHODS

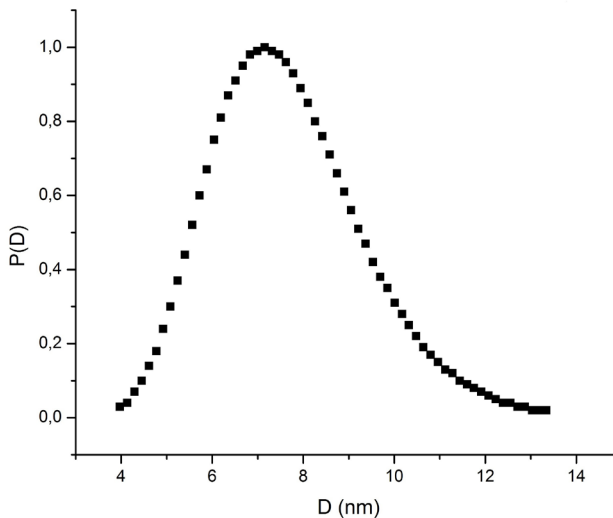
NiFe₂O₄ nanoparticles were prepared by the chemical co-precipitation method using an aqueous solution of Ni(NO₃)₂·6H₂O and Fe(NO₃)₃·9H₂O and the NaOH solution as the precipitating agent. The precipitate was calcined at 500 °C. (Albuquerque et al., 2001). They were studied using magnetic measurements, ⁵⁷Fe Mössbauer spectroscopy, X-ray diffraction, and transmission electron microscopy.

The nanoparticles have an average size of 7 nm (obtained from XRD pattern) and exhibit superparamagnetism at room temperature. The saturation magnetization (M_s) at 4.2 K was determined from M vs 1/H plots by extrapolating the value of magnetizations to infinite fields, to 24.21 emu/g and coercivity to 3.15 kOe. A magnetic anisotropy energy constant (K) 1.9x10⁵ J/m³, at 4.2 K, were calculated from magnetization measurements.

Fits to Mössbauer spectra, in the range of 4.2 K – 300 K, were done using spin hamiltonians to describe both the electronic and nuclear interactions, a model of superparamagnetic relaxation of two levels (spin $\frac{1}{2}$) and stochastic theory (CLAUSER, 1971) (JONES et al., 1989), a log-normal particle size distribution function $P(D)$ (Eq. 1) (Fig. 2).

To fits on more complexes Mössbauer spectra lineshapes, it's necessary to consider a hyperfine magnetic field distribution (which is a purely statistical approach) or, as is done in the Pfannes-Higino model (PFANNES et al., 1998; PFANNES et al., 2001; FILHO, 2001), a dependency of the magnetic transition temperature and the anisotropy constant on particle diameter (Eqs. 2 and 3) (Fig. 3). The magnetic transition temperature dependency on particle diameter leads to a Brillouin function (Eq. 4), a relation between the reduced hyperfine internal field and the reduced temperature (Fig. 4).

Figure 2 – Log-Normal size distribution, $P(D)$.



Source: The authors.

$$P(D) = \frac{1}{\sqrt{2\pi}\sigma D} e^{\left[\frac{\ln(D/D_0)^2}{2\sigma^2} \right]} \quad (1)$$

where D is the particle diameter, σ is the standard deviation, D_0 is the average size.

$$T_N(D) = -A_1 \times e^{(-D/A_2)} + T_{bulk} \quad (2)$$

where T_{bulk} is the bulk magnetic transition temperature of the sample, and A_1 and A_2 are parameters to be found.

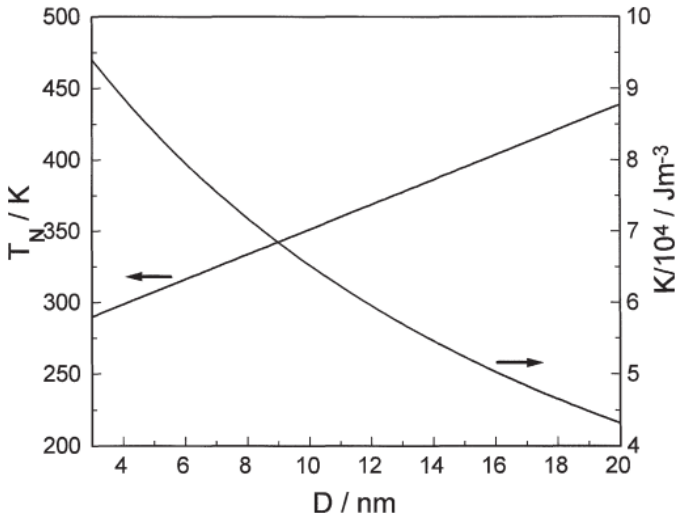
$$K(D) = AN01 + \frac{AN02}{(D \times AN03)} \quad (3)$$

where AN01, AN02 e AN03 are parameters to be found.

$$BR1(T/T_N) = BR11 \times [1.0 - BR12 \times (T/T_N)^{BR13}] \quad (4)$$

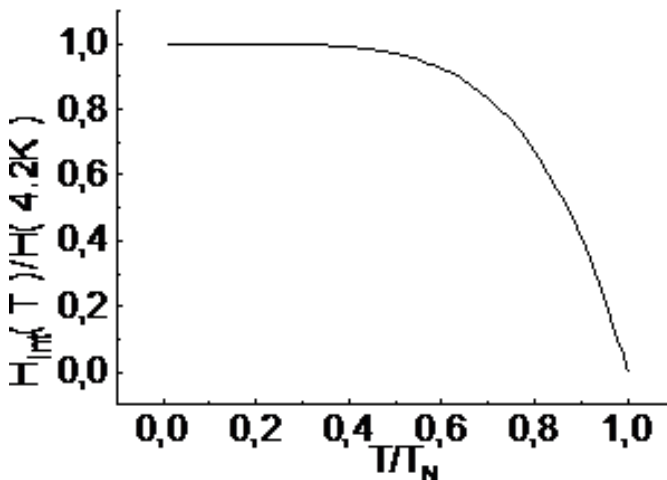
Where BR11, BR12 e BR13 are parameters to be found.

Figure 3 – Transition temperature T_N and anisotropy constant K vs. diameter.



Source: (PFANNES et al, 1998).

Figure 4 – Reduced Internal Field [$H_{int}/H(4.2K)$] vs. reduced temperature (T/T_N).



Source: (PFANNES et al., 1998).

We have used evolutionary strategies and non-linear to fit the more complex Mössbauer spectra line shapes (BARBOSA, 2017; RECHENBERG, 1965; SCHWEFEL, 1975). The CHI2 parameter is a way of measure the differences between experimental and theoretical spectra, calculated by the theoretical model. CHI2 values in the range [1,6] indicate that experimental and theoretical spectra are in good agreement.

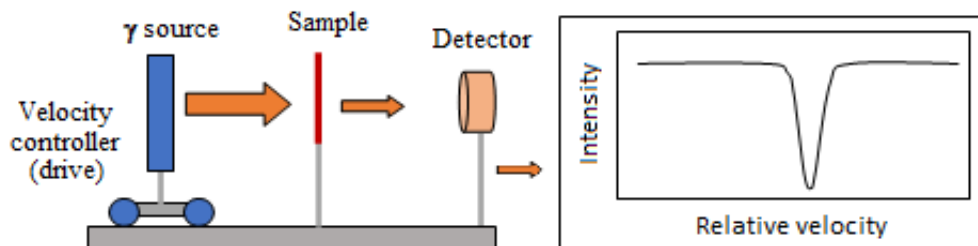
The evolutionary algorithms have been implemented using Python programming language. The parameterization problem is treated as a problem of minimizing the measure of the Root Mean Square Error, RMSE, of the points of the theoretical spectrum obtained by the model, compared to the experimental spectrum.

2.1 MÖSSBAUER SPECTROSCOPY

The Mössbauer effect is the nuclear recoil free emission and absorption of gamma photons (nuclear resonance fluorescence). This effect only occurs when the nucleus is embedded in a solid matrix (GOLDANSKII, 1968; YOSHIDA, 2013). The Mössbauer effect was discovered in 1958 by Rudolf L. Mössbauer, who, in order to correctly interpret and explain the effect, developed an experimental technique called Mössbauer spectroscopy (Fig. 5), which is applied in several areas of knowledge, such as the study of magnetism and magnetic materials (GÜTLICH et al., 2011). Mössbauer spectroscopy has high energy resolution that allows the study of electrical and magnetic hyperfine interactions arising from the interaction between electrical and magnetic moments of the nucleus and the fields created by the core electrons. It is widely used, for example, in the characterization of organometallic iron compounds (CHEN, 2007). Zeeman nuclear splitting for the fundamental and first excited states of the ^{57}Fe and the respective Mössbauer spectra are shown in Figure 6 (allowed transitions between nuclear levels are labeled with the magnetic, m , and nuclear spin, I , quantum numbers).

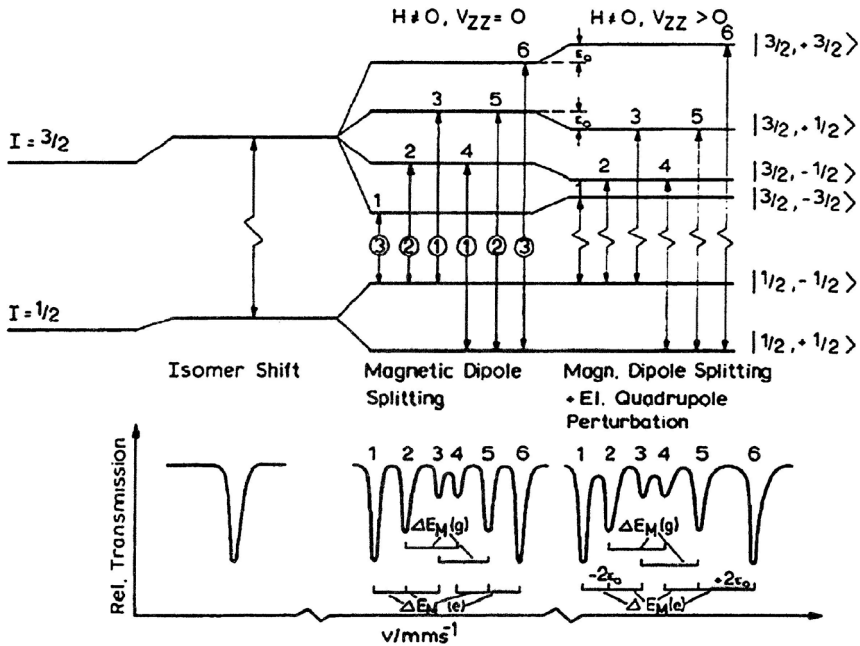
The Mössbauer theoretical lineshape used in the model is a complicated expression that calculates the Laplace transform of the correlation function for the nuclear transition operator. A detailed deduction of this expression can be found in (CIANCHI, 1986).

Figure 5 – Typical experimental arrangement for Mössbauer spectroscopy (scheme) and an outline of a transmission spectrum.



Source: Adapted from PIRES (2014, p. 11).

Figure 6 – Scheme of nuclear energy levels (^{57}Fe) for electric monopole interaction (causing isomer shift, left), pure magnetic dipole interaction (causing magnetic splitting, middle), and combined electric quadrupole and magnetic dipole interactions.



Source: (YOSHIDA, 2013).

3 RESULTS AND DISCUSSION

With the aim to evaluate the algorithm's parameterization performance, we applied the Differential Evolution (DE) and Evolution Strategies (ES) algorithms (BARBOSA, 2017) in the fitting procedure of nickel ferrite powder Mössbauer spectra in several temperatures. All experiments involved in this work were carried out in the Physics Department, Federal University of Minas Gerais.

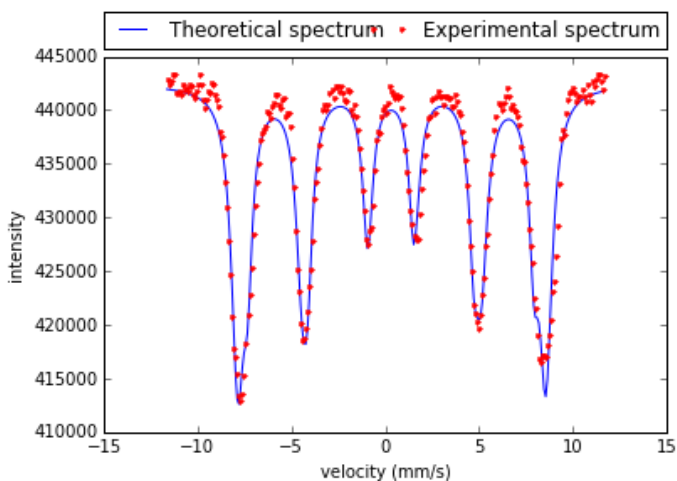
Experimental and theoretical Mössbauer spectra of the powder sample at temperatures in the range of 4.2 K – 300 K are shown in figures 7 to 10. The spectra collapse rapidly in the range of 140 K – 300 K without showing a pronounced central peak (characteristic of superparamagnetic relaxation) initially. There should be another cause of internal field reduction besides increasing relaxation frequency. We adopted a dependence of T_N and the anisotropy on the particle diameter (cf. figure 3). For each diameter D , we obtain T_N , and from this and the actual temperature T , we get an internal magnetic field value corresponding to the variation of the internal field dependence shown in figure 4. A lot of parameters must be found during the fit process. Tables 1 and 2 show these parameters founded for the spectrum at 140 K. For comparison, the two algorithms obey the termination criterion of 6,000 evaluations of the objective function. Each algorithm has been executed 30 times.

Table 1 – Parameters founded during the fit on the spectrum at 140 K.

Parameters	Values found
AN01	4641.009
AN02	279736378.496
AN03	20.000
BR12	4.500
BR13	5.600
BR21	-0.200
BR22	5.499
BR23	2.224

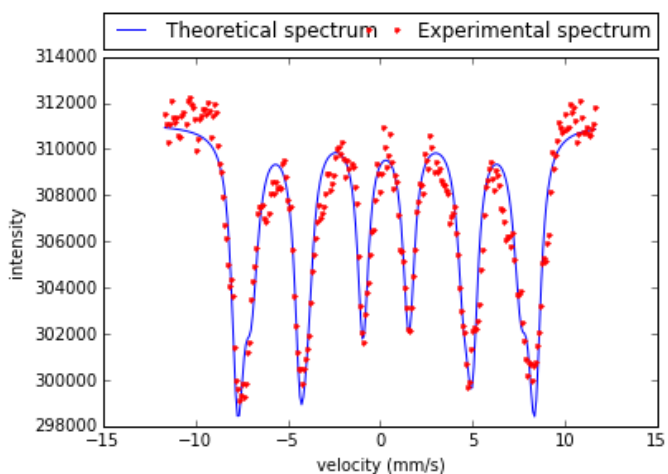
Source: The authors.

Figure 7 – Nickel ferrite Mössbauer spectrum at 4 K (CHI2 = 5.77).



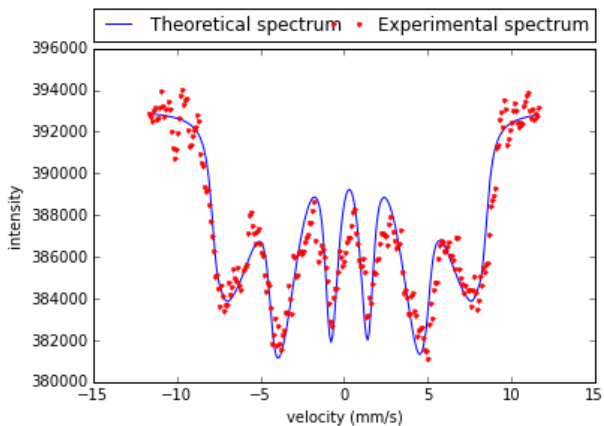
Source: The authors.

Figure 8 – Nickel ferrite Mössbauer spectrum at 100 K (CHI2 = 3.32).



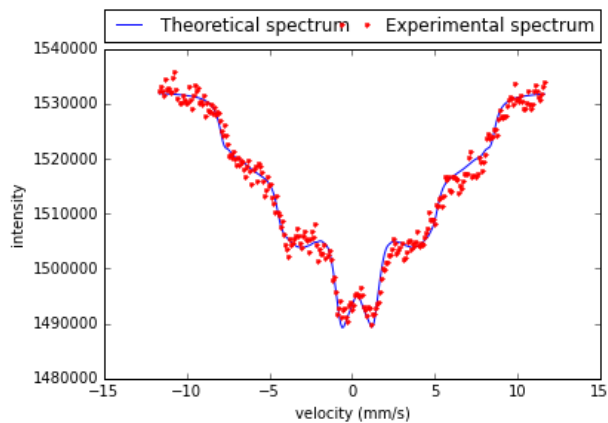
Source: The authors.

Figure 9 – Nickel ferrite Mössbauer spectrum at 140 K (CHI2 = 2.98).



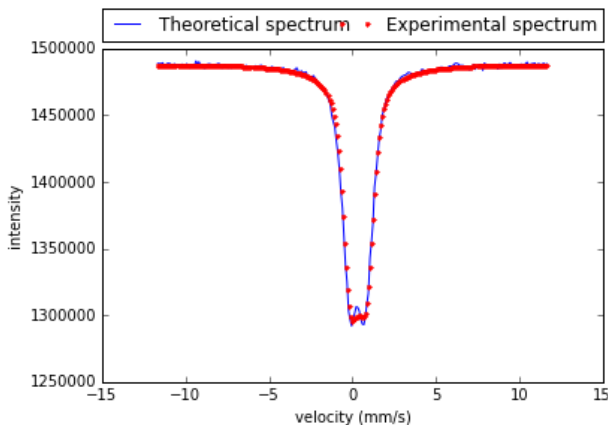
Source: The authors.

Figure 10 – Nickel ferrite Mössbauer spectrum at 180 K (CHI2 = 1.81).



Source: The authors.

Figure 11 – Nickel ferrite Mössbauer spectrum at 300 K (CHI2 = 2.51).



Source: The authors.

The values of CHI2 in the range [1.81 – 5.77] show that the model can reproduce the main features of the Mössbauer spectra, even in the situations when the thermally activated phenomena produce complex lineshapes. A good agreement between the experimental and theoretical spectra occurs in all temperatures in the range 4.2 K to 300 K, and the model describes the collapse of the hyperfine field at high temperatures due to superparamagnetic relaxation or magnetic transition temperature dependency on the particle diameter.

4 CONCLUSIONS

Nickel ferrite nanoparticles were successfully synthesized by the co-precipitation method, and their magnetizations are affected by the thermally activated phenomena predicted in the Pfannes-Higino model.

Effects like particle size distribution as well as a dependency of the magnetic transition temperature on particle diameter are very important to the analysis of the Mössbauer spectra of nanoparticles, and these effects can substitute the hyperfine field distributions, a statistical approach commonly used in the Mössbauer fitting programs.

Evolutionary algorithms and a theoretical model based on superparamagnetic relaxation phenomena and particle size distribution, as well as a dependency of the magnetic transition temperature on particle diameter, can be successfully used on Mössbauer spectra fits. The values of CHI2 are in the range [1.81 – 5.77]. Future works include modifications in the theoretical model and application of evolutionary algorithms on the fits of more complex Mössbauer spectra, taking into account other physical phenomena, e.g., interparticle interactions and surface effects.

5 ACKNOWLEDGMENTS

We are very thankful for the PPGMCS (Programa de Pós-graduação em Modelagem Computacional e Sistemas) and Unimontes actions of support.

REFERENCES

ALBUQUERQUE, A.S.; ARDISSON, J.D.; MACEDO, W.A.A.; LOPEZ, J.L.; PANIAGO, R.; PERSIANO, A.I.C.; **Structure and magnetic properties of nanostructured Ni-ferrite**. J. Mag. Magn. Mat., V. 226-230, p. 1379-1381, 2001.

BARBOSA, W.O. **Otimização de Parâmetros de Modelo Matemático da Forma de Linha Mössbauer Aplicado a Sistemas Magnéticos Granulares Nanométricos**. Dissertação (Mestrado em Modelagem Computacional e Sistemas) – Universidade Estadual de Montes Claros – Unimontes, Montes Claros, 2017.

- CHEN, Y.; YANG, D. **Mössbauer Effect in Lattice Dynamics**. WILEY-VCH Verlag GmbH & Co. KGaA, Weinheim, Deustcheland, 2007.
- CIANCHI, L.; MORETTI, P.; MANCINI, M.; SPINA, G. Rep. Progr. Phys, v. 49, p. 1243, 1986.
- CLAUSER, M.J.; BLUME, M. Phys. Rev. B, v. 3, n. 3, p. 583-591, 1971.
- FILHO, J.H.D. **Relaxação de Spin em Partículas Magnéticas Nanométricas**, Tese (Doutorado em Física) – Departamento de Física, Belo Horizonte, UFMG, 2001.
- GOLDANSKII, V.I.; HEBER R. **Chemical Applications of Mössbauer Spectroscopy**, New York, Academic Press, 1968.
- GÜTLICH, P.; BILL, E.; TRAUTWEIN, A. **Mössbauer Spectroscopy and Transition Metal Chemistry: Fundamentals and Application**, Berlin: Springer, 2011.
- JONES, D.H.; SRIVASTAVA, K.K.P. J. Mag. Magn. Mat., v. 78, p. 320, 1989.
- KODAMA, R.H.; BERKOWITZ, A.E. Phys. Rev. Lett. v. 77, p. 394, 1996.
- LÓPEZ, J. L.; PFANNES, H.D., PANIAGO, R. J. Mag. Magn. Mat., v. 1878, p. 226-230, 2001.
- MARTINS, M.L. **Síntese e Caracterização de Ferritas de Manganês e Zinco Visando Aplicacao como agente de Contraste em Diagnóstico Médico**. Trabalho de Conclusão de Curso - TCC. Universidade Estadual Júlio de Mesquita Filho, Instituto de Biociências, Campus de Botucatu, Botucatu, p. 77, 2008.
- MEDRANO, J.J.A.; et al. **Evidence of particle-particle interaction quenching in nanocomposite based on oleic acid-coated Fe₃O₄ nanoparticles after over-coating with essential oil extracted from Croton cajucara Benth**, J. Magn. Magn. Mat., V. 466, p. 359-367, 2018.
- PFANNES, H.D. et al. Hyperfine Interactions. V. 113, p. 507-515, 1998.
- PFANNES, H.D.; DIAS, J.H.; MAGALHAES-PANIAGO, R.; LOPEZ, J.L.; PANIAGO, R. **Mossbauer spectroscopy, superparamagnetism and ferrofluids**. Braz. J. Phys. vol 31, no.3, 2001.
- PIRES, M.J.M. **Espectroscopia Mössbauer: da Física Nuclear à verificação de efeitos relativísticos**, *Gazeta de Física*, v. 37, p. 10-13, 2014.
- RECHENBERG, I. **Cybernetic solution path of an experimental problem**, Relatório Técnico 1122, Franborough, Royal Aircraft Establishment, 1965.
- SAHA K.; BAJAJ A.; DUNCAN B.; ROTELLO V.M. **Beauty is skin deep: a surface monolayer perspective on nanoparticle interactions with cells and bio-macromolecules**, *Small (PMC)*, Jul 18, 7(14), p. 1903-1918, 2011.
- SCHWEFEL, H.P. **Evolutionsstrategie und numerische optimierung**, Tese de Doutorado, Berlin, Technical University of Berlin, 1975.
- TOURINHO, F.; FRANCK, R.; MASSART, R.; PERZYNSKY, R. **Prog. Colloid Polym.** V. 79, p. 128, 1999.
- YOSHIDA, Y. et al. **Mössbauer Spectroscopy – Tutorial book**, Nova Iorque, Springer Verlag, 2013.

CHAPTER 12

EFFECT OF GRAPHITE NANOSTRUTURES ON THE VISCOSITY PROPERTIES OF BLENDS DIESEL-S10 AND BIODIESEL¹

Data de aceite: 15/05/2021

Túlio Begena Araújo

São Paulo State University
School of Technology and Sciences –
FCT/UNESP
Department of Chemistry and Biochemistry
Presidente Prudente – São Paulo
<http://lattes.cnpq.br/0094407519359060>

Marcos Augusto Lima Nobre

São Paulo State University
School of Technology and Sciences –
FCT/UNESP
Department of Physics
Presidente Prudente – São Paulo
<https://orcid.org/0000-0003-4843-3975>

ABSTRACT: The nanotechnology can be applied in the changing of specific properties of functional fluids as the lubricity in fuels. In fact, nanoparticles or nanostructures can modify parameters as thermal conductivity and acting as catalyst in fuels and biofuels. The biodiesel has been added to the diesel for the decreasing of the sulfur emission. Furthermore, the lubricity is also decreased. In this sense, the desulfurization process removes

¹ This chapter is the translation of the chapter published in the book: The great world of nanotechnology / Organizer Marcos Augusto Lima Nobre. – Curitiba, PR: Artemis, 2020, Cap. 5, p. 48.

molecules containing sulfur of diesel. However, both desulfurization and biodiesel addition can change the composition and diesel properties. A natural expectation is that the addition of graphite to a diesel/biodiesel composition the lubricity can be retrieved. Taking in account, diesel S10 and biodiesel, propriety can be changed via addition of graphite containing nanostructures. The viscosity of blends diesel S10/biodiesel/graphite is analyzed from rheological characterization.

KEYWORDS: Graphite nanostructures. Biodiesel. Diesel. Blends. Viscosity.

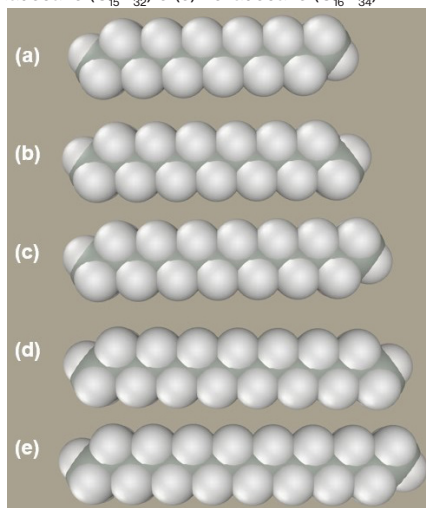
1 INTRODUCTION

Nanotechnology involving particles at the nanoscale can be used in advanced technologies for the development of mixtures of fossil fuel and biofuel. In fact, a nanoparticle can be defined as a particle that has any of its dimensions on a nanoscale, between 1 and 100 nm. Diluting nanoparticles in a liquid, a dispersion known in modern literature as nanofluids is obtained. Several properties of liquids can be modified, and improved, with the use of nanotechnology, such as the properties thermal conductivity and diffusivity, viscosity and lubricity. All of these properties are important when working with fuel mixtures, making it possible to increase the quality of combustion

and mass and heat transport through combustion systems. Some key factors influence the application of nanofluids and should be described in detail. Among them are: size of the nanoparticles and their shapes, their composition, agglomeration, work temperature, use of surfactants and interactions at the solid-liquid interface. Fluid viscosity should be studied in conjunction with other rheological parameters. Rheology is an area of knowledge positioned between physics and chemistry. The etymology of that word has a Greek origin, specifically in the word *rheo*, which means to flow. The flow of a liquid compound is connected to the laws of physics (classical mechanics, thermodynamics, etc.) and to chemical parameters (molecular mass, molecular interactions based on secondary chemical bonds, etc.). Besides the flow of liquids, rheology comprises the deformation of solids.

In some cases, the separation between liquid and solid behaviors is not so simple. For example, when analyzing very viscous liquids, they end up behaving like solids, or in the case of solids that flow when subjected to a high enough shear stress. Many other fields of study depend directly on rheological studies for their development. Among them we have: lubricants, paints, mineral dispersions, body fluids, cosmetics, food, glass, polymer solutions, detergents, papers, among others. The importance of these studies ranges from the production and transport of the reagents to the final qualities of the product. Complex multiphase systems are part of the aforementioned applications, such as suspensions and emulsions. Considering a fossil fuel, diesel stands out as a global energy source. Despite the complex composition, which depends on its refinement process, desulphurization and the oil used, on average, has 75% saturated hydrocarbons and 25% aromatic hydrocarbons. The five predominant components in diesel are shown in Figure 1. Most diesel molecules have linear carbon chains, consisting of 12 to 16 carbons.

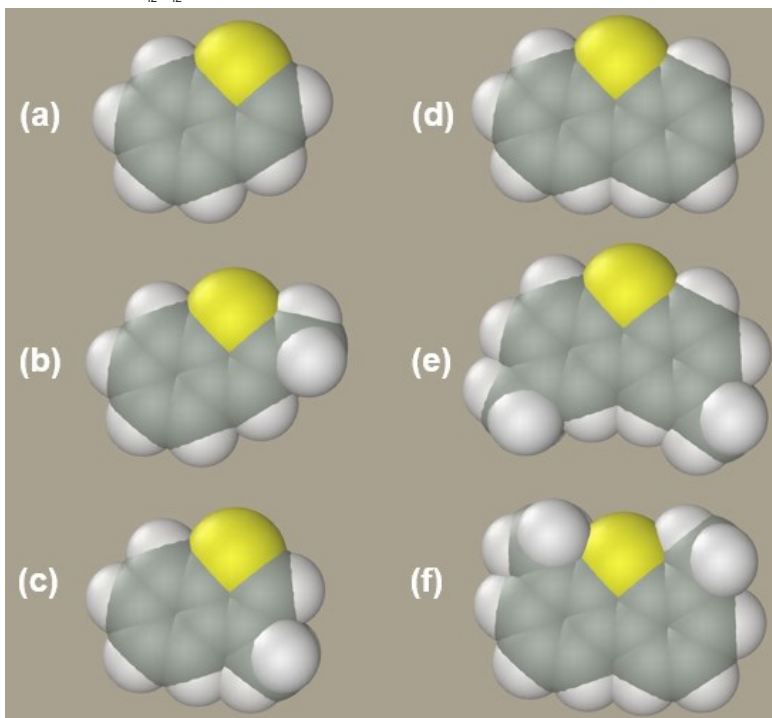
Figura 1 - Molecules of the five most abundant components in diesel: (a) dodecane ($C_{12}H_{26}$), (b) tridecane ($C_{13}H_{28}$), (c) tetradecane ($C_{14}H_{30}$), (d) pentadecane ($C_{15}H_{32}$) e (e) hexadecane ($C_{16}H_{34}$).



Source: designed by the author.

The preponderance of saturated hydrocarbons is accentuated by the desulfurization process. This process works to reduce the amount of sulfur compounds in the fuel. However, there are some deleterious effects such as the reduction of aromatic compounds and reduction of diesel lubricity. The sulfur molecules present in diesel are benzothiophenes, dibenzothiophenes and their derivatives. The molecules representing these groups are shown in Figure 2.

Figure 2 - Molecules of the main sulfur compounds of diesel: (a) benzotiofeno (C_8H_6S), (b) 2-metilbenzotiofeno (C_9H_8S), (c) 3-metilbenzotiofeno (C_9H_8S), (d) dibenzotiofeno ($C_{12}H_8S$), (e) 2,8-dimetildibenzotiofeno ($C_{12}H_{12}S$), e (f) 4,6-dimetildibenzotiofeno ($C_{12}H_{12}S$).

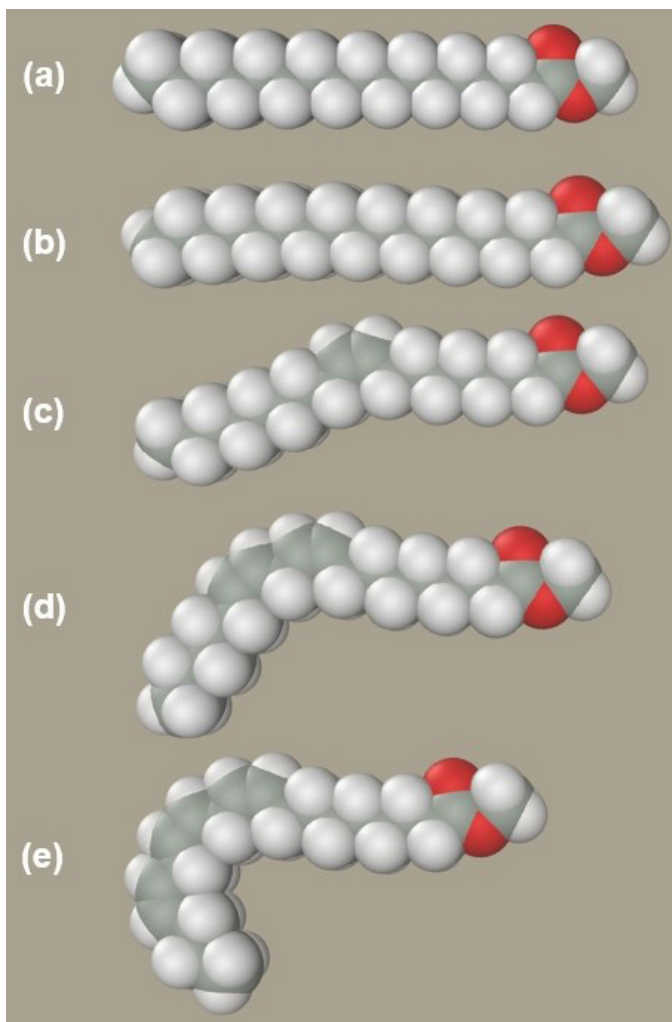


Fonte: designed by the author.

Biodiesel is produced from the transesterification of oils and fats, being composed of long chain esters, methyl or ethyl, derived from fatty acids. In Brazil, most of the biodiesel produced is derived from the transesterification of soy oil with methanol. This fuel is sold already added to the diesel.

The predominant components in biodiesel produced by methyl route are shown in Figure 3. Biodiesel molecules are, in general, larger than diesel molecules. Another important difference is that, for soy biodiesel, approximately half of its molecules are from unsaturated chains. These unsaturations cause the molecules to be non-linear, as one can see in Figure 3. In addition, one end of the ester molecules is polar, due to the bonds between carbon and oxygen atoms.

Figure 3 - Molecules of the five most abundant components in methyl soy biodiesel: (a) methyl palmitate ($C_{17}H_{34}O_2$), (b) methyl stearate ($C_{19}H_{38}O_2$), (c) methyl oleate ($C_{19}H_{36}O_2$), (d) methyl linoleate ($C_{19}H_{34}O_2$) e (e) methyl linolenate ($C_{19}H_{32}O_2$).



Fonte: designed by the author.

The effects of different proportions of nanostructured graphite particles on the viscosity of mixtures of complex fluids formed by the mixture of diesel S10 and biodiesel are discussed.

2 ANALYSIS OF VISCOSITY BY RHEOLOGY OF FLUIDS

The first rheological parameter to be defined in the study of fluids is viscosity. Viscosity is the resistance to the flow of a fluid derived from the internal friction of one

part of the fluid moving to another. Starting from Newton's proposal, it is possible to write Equation 1.

$$\tau = \eta\gamma \quad (1)$$

where τ is the shear stress, γ is the shear rate and η is the proportionality constant, denominated dynamic viscosity or viscosity. Not all fluids exhibit the behavior described by Eq. 1. Those that comply with Eq. 1 are called Newtonian fluids. Other fluids are non-Newtonian as they do not flow until a certain shear stress value is reached, known as yield stress. A fluid that behaves like Newtonian after the application of a minimum shear stress is denominated Bingham's plastic fluid. Equation 2 represents this behavior.

$$\tau = \tau_0 + \eta_p\gamma \quad (2)$$

where η_p is the plastic viscosity and τ_0 is the yield shear stress. Both types of fluids, Newtonian and Bingham plastics have constant viscosity values as a function of the shear rate. The Ostwald-De Waele (Equation 3) and Herschel-Bukley (Equation 4) models represent fluids in which the viscosity varies as a function of the shear rate.

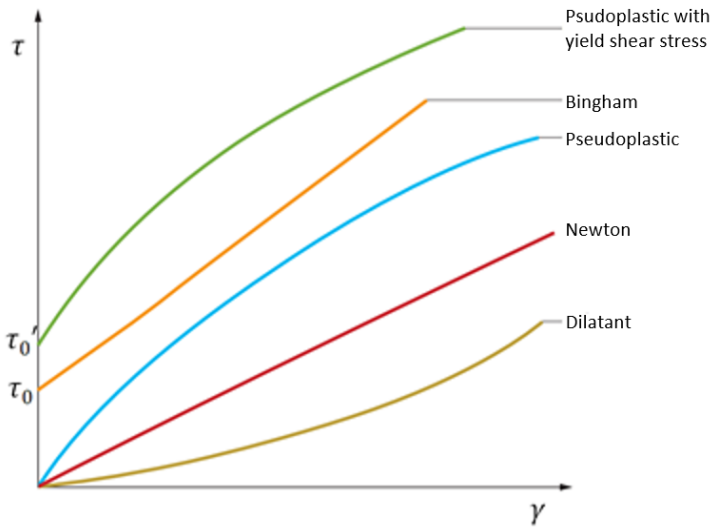
$$\tau = K\gamma^n \quad (3)$$

$$\tau = \tau_0 + K\gamma^n \quad (4)$$

where K is the consistency index parameter and n is the flow behavior index. By Equations 3 and 4, it is noted that the Ostwald-De Waele model applies to fluids that do not need a minimum flow stress, similarly to Newtonian fluids, while the fluids that obey the Herschel-Bukley model are refer to liquids that require minimal tension, such as Bingham plastic types. The consistency index parameter is equal to the viscosity presented by the fluid subjected to a fixed shear rate, called apparent viscosity. Fluids that respect these models and have a flow behavior index less than 1 are denominated pseudoplastics and their apparent viscosities decrease with the increase in the shear rate to which they are subjected. Fluids with a flow behavior index greater than 1 are denominated dilatants, as their apparent viscosities increase with the increase in the shear rate. Figure 4 shows rheological curves typical of fluids modeled with Equations 1, 2, 3 and 4. Some fluids have a variable behavior over time. This phenomenon is known as thixotropy. Once subjected to a constant shear rate, thixotropic fluids have their viscosity decreasing as a function of time. When leaving such fluids at rest, their viscosities slowly return to the initial value, much higher than the minimum achieved with a fixed shear rate. Fluids called rheopetics have their viscosity increased, while they are subjected to a fixed value shear rate, which

is why they are also known as antithixotropic. Like thixotropic fluids, rheopetic fluids regenerate their initial viscosity values while remaining at rest. Fluids that exhibit these types of behavior are complex in terms of shaping a law of behavior.

Figure 4 - Typical fluid curves representing Newton, Bingham, Ostwald-De Waele and Hershel-Bukley models.



Source: Araújo, 2020.

3 FUNCTIONAL DISPERSIONS

Dispersion processes and rheology of liquids with dispersed particles are of great industrial interest, as for the production of paints and solid additives in fuels. In general, for diluted systems, that is, with a volume fraction of solids less than 0.01 (1%), Equation 5 (proposed by Albert Einstein) serves as a model, through which the value of the viscosity parameter can be calculated.

$$\eta_d = \eta(1 + 2,5\phi) \quad (5)$$

where ϕ represents the volumetric fraction of solids and η_d represents the viscosity of the dispersion from the viscosity η of the fluid. In the development of this model, however, the particles considered are spherical.

In more concentrated systems, interactions between particles must be taken into account. George Keith Batchelor built a model that considers such interactions, Equation 6.

$$\eta_d = \eta(1 + 2,5\phi + 6,2\phi^2) \quad (6)$$

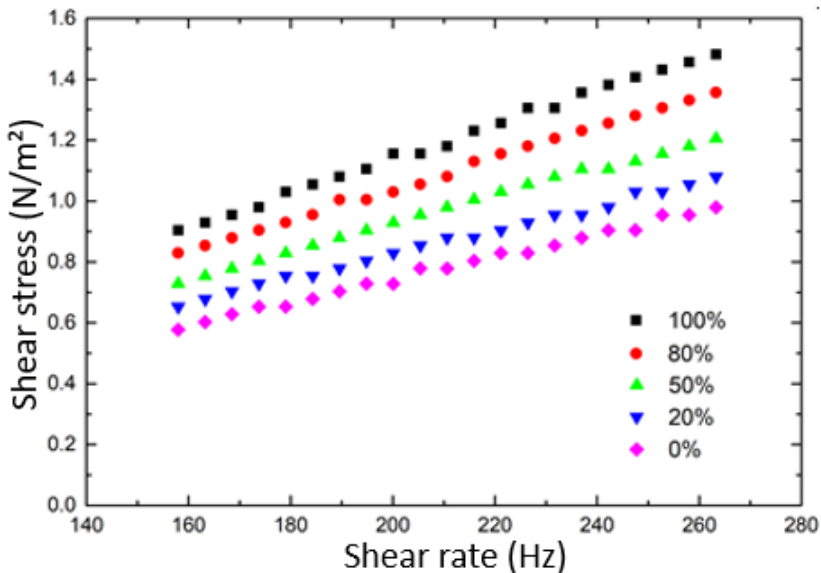
Several expressions have been proposed after Eq. 5 and 6 to describe the viscosity of dispersions. In common with each other and with Equations 5 and 6, the viscosity

parameter of a dispersion should increase with the increase in the concentration of added particles. Some studies have reported data that show results that do not fit these models.

In experiments involving complex fluids composed by blends of diesel S10 and biodiesel, with volumetric biodiesel fractions equal to 0%, 20%, 50%, 80% and 100% in the case, these show the behavior of Newtonian fluids for the shear rate range between 158 Hz and 263 Hz. This behavior is shown in Figure 5.

Figure 5 shows rheological curves, shear stress versus shear rate, for diesel S10, biodiesel and diesel S10/biodiesel blends. The shear stress varies linearly as a function of the shear rate of the blends.

Figure 5 - Shear stress versus shear rate for blends of diesel S10 and biodiesel, as a function of the volumetric fraction of biodiesel.



Source: Lanfredi, 2019.

Newtonian fluid behavior is as simple as possible for fluids. From the analysis of the behavior of the blends, it was possible to determine the values of their viscosities. These values are listed in Table 1. When adding nanostructured graphite particles to these blends, some results, even surprising, were obtained. To each of these samples, proportions of graphite powder equal to 0.2%, 0.4% and 0.8% by volume were added. All these quantities of graphite represent volumetric fractions suitable for the model proposed by Einstein. In the same experimental conditions, the dispersions maintained the behavior of Newtonian fluids, as can be seen in Figure 6. The results obtained for the viscosity values of all these samples are listed in Table 1.

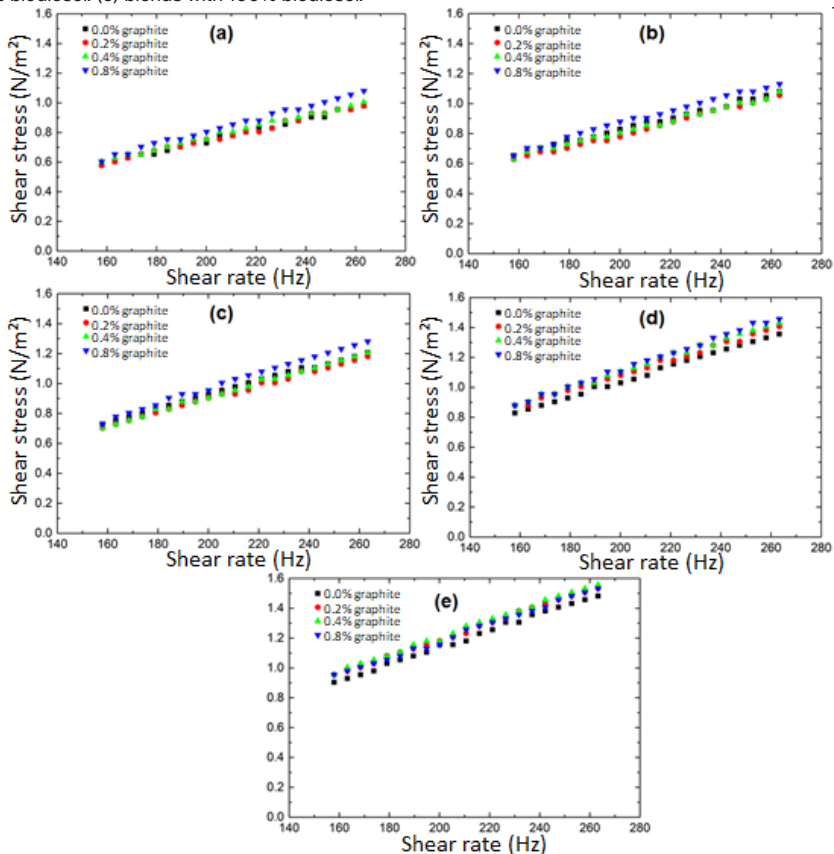
Table 1 - Viscosities in mPas of the binary blends of diesel S10 and biodiesel, with addition of graphite particles, at 293.15 K.

Volumetric fraction of biodiesel (%)	Volumetric fraction of graphite (%)			
	0.0	0.2	0.4	0.8
0	3.70±0.04	3.73±0.05	3.82±0.04	4.03±0.07
20	4.12±0.05	3.97±0.05	4.05±0.06	4.31±0.07
50	4.62±0.03	4.48±0.04	4.54±0.05	4.84±0.07
80	5.19±0.04	5.40±0.07	5.51±0.06	5.58±0.05
100	5.69±0.05	5.92±0.06	6.01±0.06	5.89±0.07

Source: Lanfredi, 2019.

According to the data listed in Table 1, some dispersions had lower viscosity values than solids-free fluids. This phenomenon occurs in four samples, those containing volumetric fraction of biodiesel equal to 20% and 50% and volumetric fraction of graphite equal to 0.2% and 0.4%. These results appear to conflict with Equation 5. However, graphite particles, due to their molecular structure, tend to have flattened structures, such as layers or sheets.

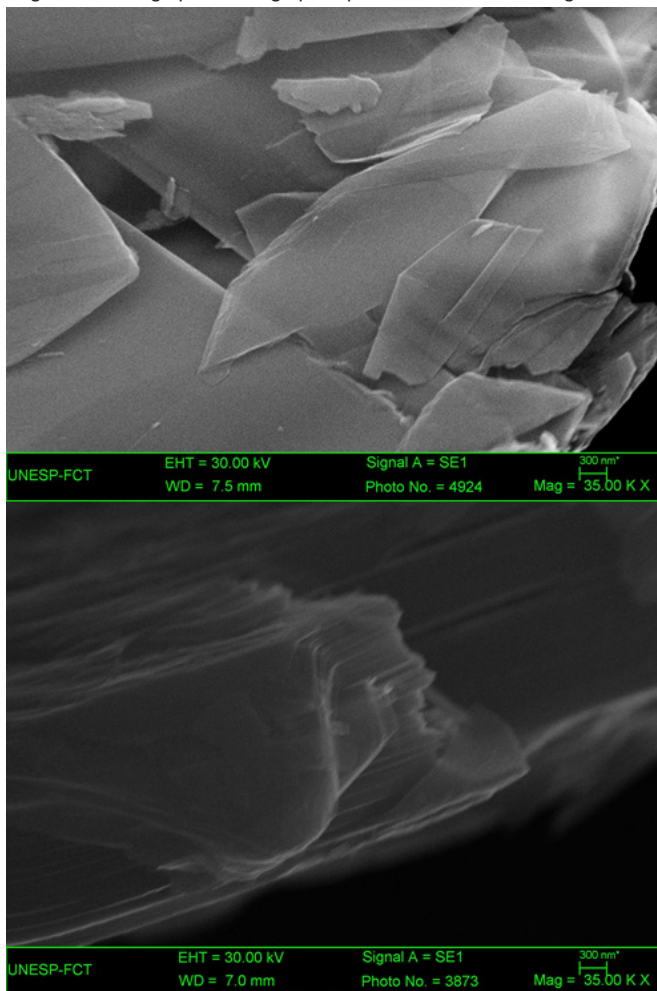
Figure 6 - Shear stress versus shear rate for blends of diesel S10 and biodiesel, as a function of the volume fraction of graphite. (a) blends with 0% biodiesel. (b) blends with 20% biodiesel. (c) blends with 50% biodiesel. (d) blends with 80% biodiesel. (e) blends with 100% biodiesel.



Source: Lanfredi, 2019.

Figure 7 shows micrographs of the graphite powder, obtained by scanning electron microscopy, in which it is possible to observe the nanostructures of the graphite particles. Thin blades can be identified with a 35000-fold magnification. In the upper image, extensive layers are identified with tenths of thickness of the size bar, 300 nm. In the bottom image of Fig. 7, an edge shows unequivocally that nanometric layers overlap.

Figure 7 - Micrographs of the graphite powder. 35000 times magnification.



Source: author.

According to scanning electron microscopy (SEM) micrographs, these graphite particles are composed of a nanostructure, composed of laminar structures of nanometric thickness. The model of action on the viscosity of the blends is not evident, but one idea is that the nanostructures of blades induce some type of lamellar order in the suspension. Thus, hypothetically, after the ordering of the system subjected to shear rates in a unidirectional way, there is a decrease in the viscosity of the analyzed complex fluids.

4 ACKNOWLEDGEMENTS

Authors acknowledge the FAPESP process 02/05997-9. Marcos A. L. Nobre (current CNPq-Researcher) acknowledges National Council for Scientific and Technological Development (CNPq) processes EU 481516/2010-7, PQ 311966/2017-9 and PQ 312122/2020-9. Túlio B. Araújo acknowledges the Coordination of Improvement of Higher Level Personnel (CAPES) for Grant and Small a fuel distributor for the diesel and biodiesel supplied.

REFERENCES

Araújo, T. B. **Caracterização de Propriedades de Excesso em Blendas Binárias e Ternárias de Misturas Combustíveis, no Sistema: Diesel/Etanol Anidro/Óleo de Palma**. 2020. 150f. Dissertação (Mestrado em Química) – Instituto de Biociências, Letras e Ciências Exatas, Universidade Estadual Paulista, São José do Rio Preto, 2020.

DEMIRBAS, A. **Biodiesel: A Realistic Fuel Alternative for Diesel Engines**. Springer-Verlag London, 2008. 208 p.

GVARAMIA, M. *et al.* **Tunable viscosity modification with diluted particles**: When particles decrease the viscosity of complex fluids. *Colloid and Polymer Science*, v. 297, p. 1507-1517, 2019.

IRGENS, F. **Rheology and Non-Newtonian Fluids**. Springer, 2014. 190 p.

KNOTHE, G.; KRAHL, J.; GERPEN, J. V. **The Biodiesel Handbook**. 2nd ed. Urbana, Illinois: AOCS Press, 2010. 494 p.

KNOTHE, G.; STEIDLEY, K. R. Kinematic viscosity of biodiesel fuel components and related compounds. Influence of compound structure and comparison to petrodiesel fuel components. *Fuel*, v. 84, n. 9, p 1059-1065, 2005.

LANFREDI, S.; Araújo, T. B.; Nobre, M. A. L. **Molecular-Interactions Effects on the Rheological Properties of Graphite Dispersions in Complex Binary Blends of Methyl Esters and Hydrocarbons**. Em: Brazil MRS Meeting, 18., 2019, Balneário Camboriú.

MALKIN, A. Y.; ISAYEV, A. **Rheology: Concept, Methods, and Applications**. 3rd ed. Toronto: ChemTec Publishing, 2017. 528 p.

MINKOWYCZ, W. J.; SPARROW, E. M.; ABRAHAM, J. P. **Nanoparticle Heat Transfer and Fluid Flow**. CRC Press, 2013. 342 p.

SINGH, S. P.; SINGH, D. **Biodiesel production through the use of different sources and characterization of oils and their esters as the substitute of diesel**: A review. *Renewable and Sustainable Energy Reviews*, v. 14, n. 1, p. 200–216, 2010.

STANISLAUS, A.; MARAFI, A.; RANA, M. S. Recent advances in the science and technology of ultra low sulfur diesel (ULSD) production. *Catalysis Today*, v. 153, n. 1-2, p. 1-68, 2010.

TADROS, T. F.; **Rheology of Dispersions**: Principles and Applications. Wiley-VCH, 2010. 219 p.

REMOCIÓN DE ARSÉNICO DE EFLUENTES ACUOSOS EMPLEANDO COMO ADSORBENTE MAGNETITA NANOESTRUCTURADA

Data de submissão: 05/04/2021

Data de aceite: 28/04/2021

Orfelinda Avalo Cortez

Universidad Nacional de Ingeniería
Escuela de Ingeniería Metalúrgica
Lima, Rímac, Perú
<https://orcid.org/0000-0002-6619-7227>

Luis Jean Carlo Cisneros García

Universidad Nacional de Ingeniería
Escuela de Ingeniería Metalúrgica
Lima, Rímac, Perú
<https://orcid.org/0000-0003-2423-0591>

David Pedro Martínez Aguilar

Universidad Nacional de Ingeniería
Escuela de Ingeniería Metalúrgica
Lima, Rímac, Perú
<https://orcid.org/0000-0001-6942-8273>

RESUMEN: La alta toxicidad del arsénico impulsa el interés y desarrollo de alternativas tecnológicamente viables y accesibles para remover el arsénico (As) presente en efluentes acuosos y por tanto constituye una necesidad apremiante para muchas comunidades que se ven afectadas por este problema. De acuerdo a la literatura las partículas magnéticas cumplen este

objetivo y pueden ser obtenidas a través de diversas rutas de síntesis. La coprecipitación es uno de los métodos más comunes para la obtención de magnetita a partir de una mezcla de sales ferrosa y férrica en medio altamente alcalino. En el presente trabajo se realizó la síntesis de magnetita a partir de sales precursoras como Sulfato Ferroso heptahidratado ($\text{FeSO}_4 \cdot 7\text{H}_2\text{O}$) y Nitrato Férrico nonahidratado ($\text{Fe}(\text{NO}_3)_3 \cdot 9\text{H}_2\text{O}$) en la proporción 1:1 y empleando el Hidróxido de Sodio (NaOH) para lograr un medio alcalino de $\text{pH}=12$. Se realizó la caracterización de la muestra final por Difracción de Rayos-X (DRX), Microscopia Electrónica de Barrido (MEB) y Análisis del área superficial (BET). El análisis de los difractogramas de DRX confirmaron que la muestra final era 100% magnetita con un tamaño de cristalito de aproximadamente 20nm. Las imágenes obtenidas por MEB mostraron que la magnetita estaba constituida por cristalitos cúbicos nanoestructurados. Los resultados del análisis BET arrojaron un valor de área superficial de $82.57 \text{ m}^2/\text{g}$ con un tamaño promedio de partícula de 72nm. Para evaluar la capacidad de remoción del Arsénico total presente en efluentes acuosos, se consiguió un efluente industrial con una concentración de As total inicial de 1.9 mg/L y con $\text{pH}=8.1$. Se hicieron pruebas de remoción empleando 0.4g de magnetita por litro de solución. La magnetita sintetizada demostró tener una excelente capacidad de remoción de

arsénico total en aguas ya que, en tiempos de contacto relativamente cortos, 10min, se logró remover el 99.99 % del As total.

PALABRAS CLAVE: Magnetita nanoestructurada. Adsorbente. Arsénico. Efluente.

ARSENIC REMOVAL OF AQUEOUS EFFLUENTS USING AS ADSORBENT NANOSTRUCTURED MAGNETITE

ABSTRACT: The high toxicity of arsenic drives the interest and development of technologically viable and accessible alternatives to remove the arsenic (As) present in aqueous effluents and therefore constitutes a necessity for many communities that are affected by this problem. According to the literature, magnetic particles meet this objective and can be obtained through various synthetic routes. Coprecipitation is one of the most common methods for obtaining magnetite from a mixture of ferrous and ferric salts in a highly alkaline medium. In the present work the synthesis of magnetite was carried out from precursor salts such as Ferrous Sulfate heptahydrate ($\text{FeSO}_4 \cdot 7\text{H}_2\text{O}$) and Ferric Nitrate nonahydrate ($\text{Fe}(\text{NO}_3)_3 \cdot 9\text{H}_2\text{O}$) in the proportion 1: 1 and using Sodium Hydroxide (NaOH) to achieve an alkaline medium of $\text{pH}=12$. The characterization of the final sample was performed by X-ray Diffraction (XRD), Scanning Electron Microscopy (SEM) and Surface Area Analysis (SAA). Analysis of the XRD diffractograms confirmed that the final sample was 100% magnetite with a crystallite size of approximately 20nm. The images obtained by SEM showed that the magnetite was made up of nanostructured cubic crystallites. The results of the SAA analysis showed a surface area value of 82.57 m^2/g with an average particle size of 72nm. To evaluate the removal capacity of total Arsenic present in aqueous effluents, was obtained a industrial effluent with an initial total As concentration of 1.9 mg/L and with $\text{pH} = 8.09$. Removal tests were made using 0.4g of magnetite per liter of solution. The synthesized magnetite proved to have an excellent capacity to remove total arsenic in water, because in relatively short contact times, 10 min, 99.99% of the total As was removed.

KEYWORDS: Nanoestructured magnetite. Adsorbent. Arsenic. Effluent.

1 INTRODUCCIÓN

La Agencia de Protección Ambiental de Estados Unidos (USEPA) clasifica al arsénico como cancerígeno en el grupo A, debido a la evidencia de sus efectos adversos sobre la salud. Ingerir niveles altos de arsénico puede causar oscurecimiento de la piel, y aumentar el riesgo de cáncer del pulmón, vejiga, hígado, riñón y de próstata (M.L. Castro de Esparza 2006). La presencia de arsénico en aguas de consumo ha ocasionado en todo el planeta la diseminación del hidroarsenicismo crónico regional endémico (HACRE), enfermedad crónica que se manifiesta principalmente por alteraciones dermatológicas como melanodermia, leucodermia y/o queratosis palmo-plantar, evolucionando hacia patologías más graves como distintos tipos de cáncer. Las poblaciones más afectadas son las de menores niveles de ingreso y, en América Latina, se estima que la población en riesgo supera los 14 millones de personas, si se toma como límite de concentración

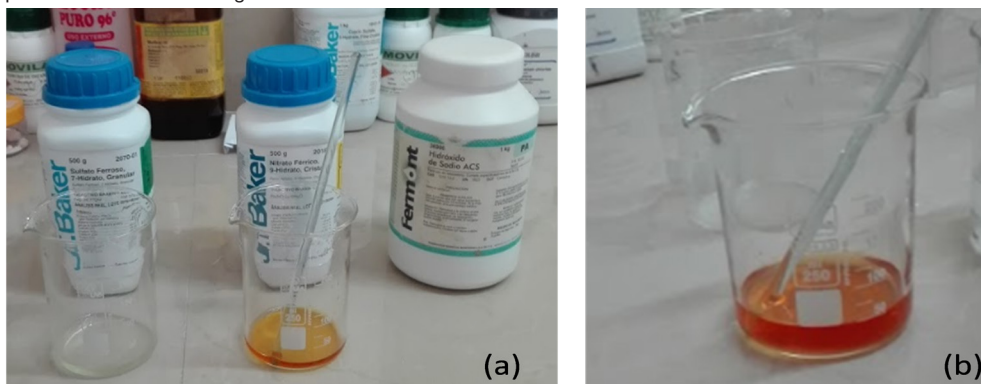
de arsénico en agua potable el recomendado por la Organización Mundial de la Salud (10µg/L) (World Health Organization, 2003).

Existen diversas tecnologías convencionales de tratamiento de agua contaminadas con arsénico (coagulación, precipitación, empleo de membranas como la osmosis inversa, adsorción, intercambio iónico) y las llamadas tecnologías emergentes (fitorremediación, electrocoagulación, empleo de nanomateriales). Las micro y macro partículas de óxidos de hierro son uno de los medios adsorbentes más eficaces (99.95% de As^{+5} y 98% de As^{+3}) y económicamente accesibles para la remoción del arsénico (Jochen Bundschuh et al, 2008) (J. Bundschuh, M.A. Armienta et al, 2009) (Marta I. Litter et al, 2010). En el presente trabajo se empleó la ruta química de coprecipitación, para sintetizar magnetita a partir de sales precursoras como Sulfato Ferroso ($FeSO_4 \cdot 7H_2O$) y Nitrato Férrico ($Fe(NO_3)_3 \cdot 9H_2O$) en la proporción 1:1 y empleando el Hidróxido de Sodio (NaOH) para lograr un medio alcalino de pH=12.

2 MATERIALES Y MÉTODOS

Los reactivos principales utilizados para la síntesis de la magnetita fueron Sulfato Ferroso ($FeSO_4 \cdot 7H_2O$), Nitrato Férrico ($Fe(NO_3)_3 \cdot 9H_2O$) e Hidróxido de Sodio (NaOH). Se trabajó con una relación molar 1 a 1 (0.005 moles para cada una de las sales) y con una concentración de 0.5M de NaOH. Se juntaron ambas sales, $FeSO_4 \cdot 7H_2O$ y $Fe(NO_3)_3 \cdot 9H_2O$ y luego se enrasó hasta 50 mL con agua destilada, tal como se muestra en la **Figura 1**.

Figura 1. (a) Reactivos empleados: $FeSO_4 \cdot 7H_2O$, $Fe(NO_3)_3 \cdot 9H_2O$ y NaOH (b) Solución conteniendo las sales precursoras disueltas en agua destilada.



La adición de NaOH se realizó lentamente y se fue anotando la variación del pH en función del volumen de NaOH en mL empleando un pHmetro digital (Marca OAKTON – Modelo pH 700) previamente calibrado, tal como se puede observar en la **Figura 2**. La

adición de NaOH se detuvo cuando se alcanzó pH=12, valor indicado en la literatura (Y. S. Lim, C. W. Lai, S. B. A. Hamid et al, 2014). Se decantó, se separó la solución sobrenadante y se lavó el precipitado de color negro con agua destilada 5 veces y la última lavada con alcohol. Finalmente se procedió a secar la muestra a una temperatura máxima de 50°C, La muestra finalmente fue colocada en un mortero con la finalidad de lograr desaglomerar las partículas y luego fue colocada en una luna de reloj que tenía un imán en la parte externa pudiéndose comprobar que se había logrado sintetizar una muestra magnética, tal como se puede observar en la **Figura 3**.

Figura 2. Secuencia experimental observada durante la adición de NaOH (a)pH=1.7 (b)pH=3-5 (c) pH=7-10 (d) pH=12 (e) equipo pH metro de mesa

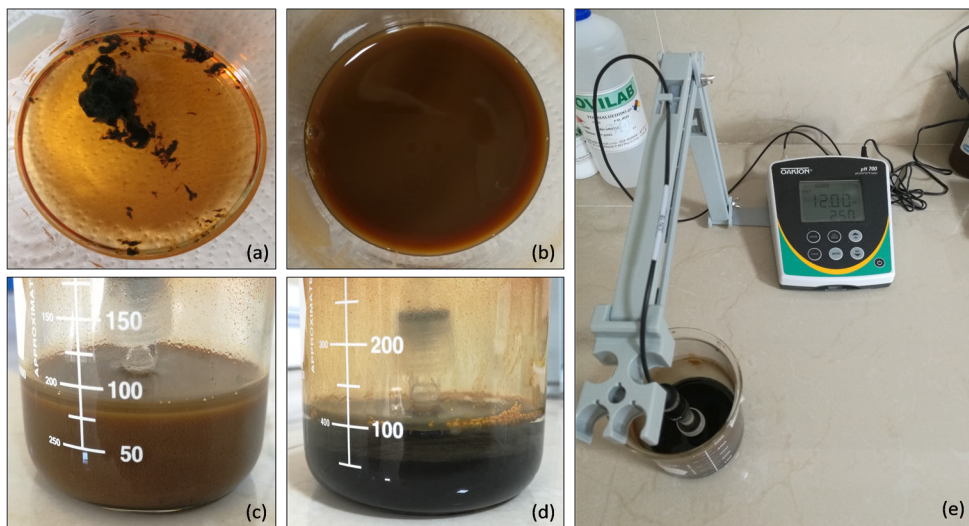


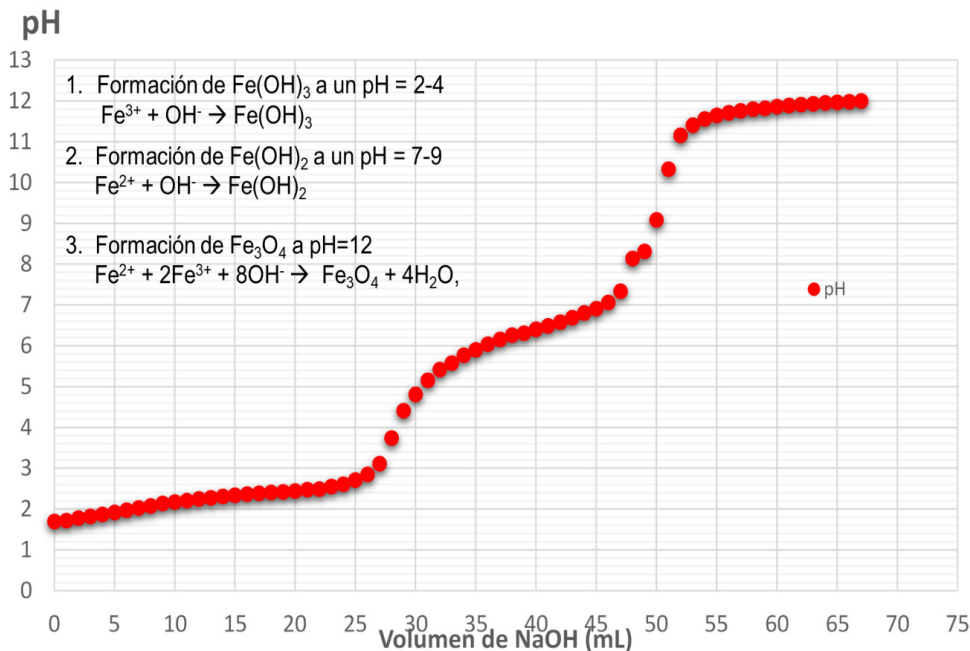
Figura 3. Decantación y lavado, secado, pesaje y muestra con imán.



De acuerdo al Diagrama de Pourbaix para el Sistema Fe-H₂O se predice que el Fe⁺³ será el primero en reaccionar con los iones OH⁻ provenientes del NaOH, a través de

la reacción: $\text{Fe}^{+3} + \text{OH}^- = \text{Fe}(\text{OH})_3$. A medida que se sigue adicionando NaOH a $\text{pH} > 6.5$ se formaría el $\text{Fe}(\text{OH})_2$, mediante la reacción: $\text{Fe}^{2+} + \text{OH}^- = \text{Fe}(\text{OH})_2$ y una vez formados ambos hidróxidos comenzaría a formarse el Fe_3O_4 a través de la reacción: $\text{Fe}^{2+} + 2\text{Fe}^{3+} + 8\text{OH}^- = \text{Fe}_3\text{O}_4 + 4\text{H}_2\text{O}$, llegándose a completar la reacción a un valor de $\text{pH}=12$, (Figura 4).

Figura 4. Curva de titulación de la mezcla de sulfato ferroso y nitrato ferrico con NaOH



3 ANÁLISIS DE LOS RESULTADOS

3.1 ANÁLISIS DE LOS RESULTADOS POR DIFRACCIÓN DE RAYOS X, DRX.

Se utilizó el Software PowderCell 2.4 para el análisis del difractograma DRX correspondiente a la muestra sintetizada y la comparamos con el difractograma patrón de la magnetita (**Figura 5**). El análisis cualitativo de la Difracción de Rayos X (DRX) mostró coincidencia en los picos en los planos HKL (111), (220), (311), (222), (400), (331), (422), (511), (440), (531), (442) que corresponden a los ángulos 2θ : 18.30°, 30.10°, 35.45°, 37.08°, 43.09°, 47.18°, 53.45°, 56.98°, 62.57°, 65.79°, 66.84°. Estos resultados muestran que se obtuvo magnetita pura (Fe_3O_4) y no otros óxidos de hierro. El software PowderCell2.4 también nos permitió determinar el tamaño de cristalito de la magnetita que fue de aproximadamente 20nm (**Figura 6**).

Figura 5. Difractogramas DRX de la muestra patrón de Fe₃O₄ (color rojo) y de la muestra sintetizada por coprecipitación (color negro). Software Powder Cell2.4.

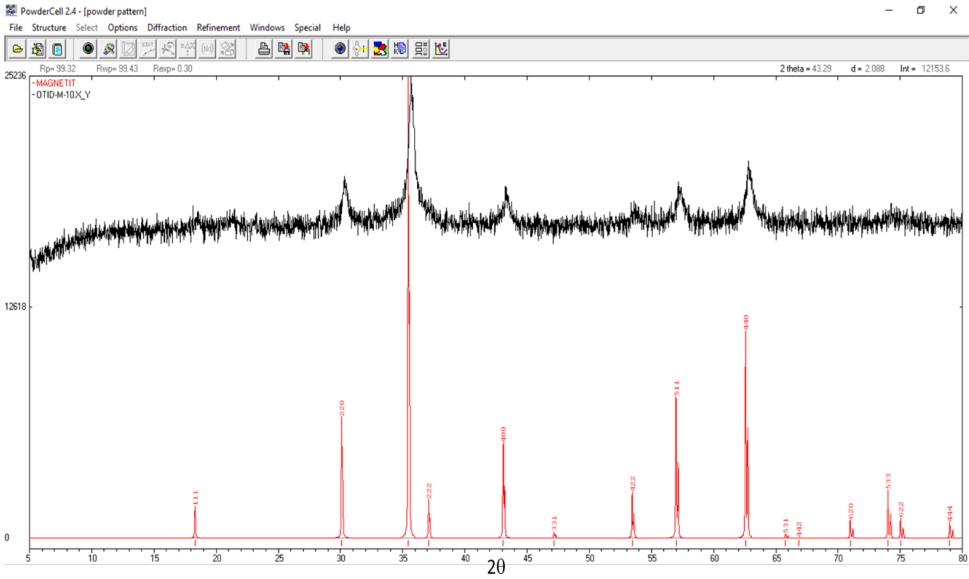
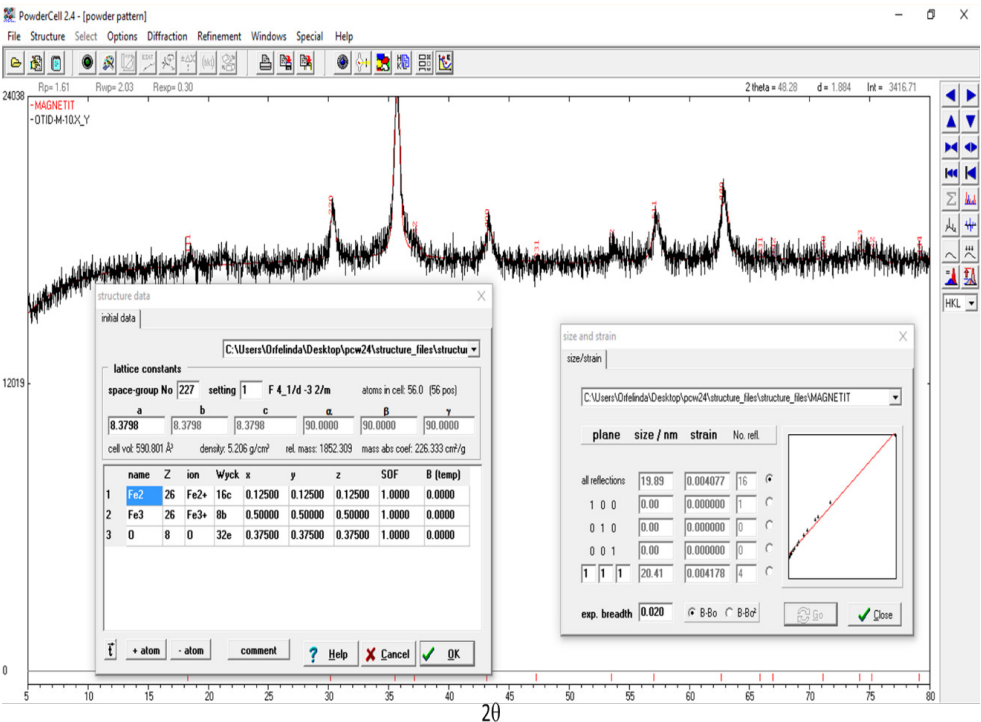


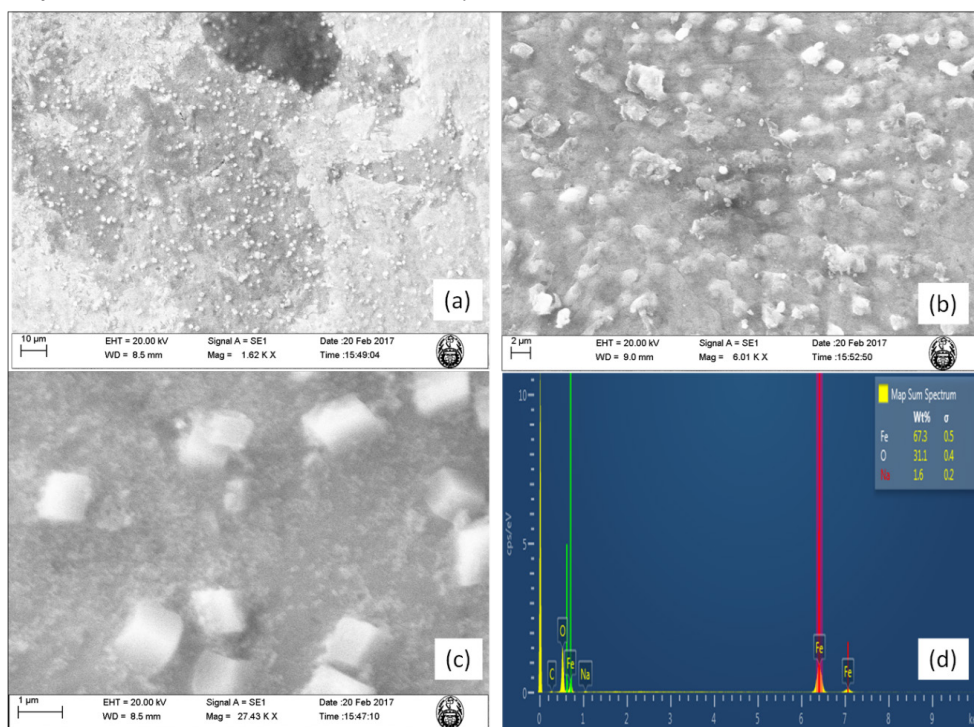
Figura 6. Determinación del tamaño de cristalito de la muestra sintetizada



3.2 ANÁLISIS DE LOS RESULTADOS DE MICROSCOPIA ELECTRÓNICA DE BARRIDO

Los resultados por Microscopia Electrónica de Barrido (MEB) mostraron la magnetita sintetizada fue de forma cúbica y con tamaños de partícula menores a 1µm. El análisis químico elemental por EDS (Espectrometría por Dispersión en Energía) acoplado al MEB, muestra que se tiene los porcentajes en pesos de Hierro y del Oxígeno, 67.3% y 31.1% respectivamente, que corresponde al Fe_3O_4 , pero también evidencia un valor de 1.6% de Sodio lo cual posiblemente sea algo de impureza que quedó durante la etapa de lavado incompleto (**Figura 7**).

Figura 7. Resultados del Análisis por Microscopia Electrónica de Barrido (MEB) a tres magnificaciones distintas (a, b, c) y resultados del análisis elemental de la muestra por EDS(d)



3.3 PRUEBAS DE REMOCIÓN DE ARSÉNICO POR ADSORCIÓN EN MAGNETITA

Para las pruebas de remoción de arsénico se emplearon dos tipos muestras, la M58 y la M67. La muestra M58 fue sintetizada utilizando 58mL de NaOH, mientras que la muestra M67 fue sintetizada empleando 67 mL de NaOH. Esta diferencia en las cantidades de NaOH empleadas se debió a que con 58 mL se alcanzó un pH=11.9 mientras que con 67 mL recién se logró alcanzar pH=12.

Los resultados del análisis de área superficial (BET) se muestran en la **Tabla 1** para las muestras M58 y M67. Se puede observar que la muestra de magnetita denominada M58 tiene mayor área superficial que la M67 y por tanto el tamaño de partícula de la M58 es menor a la M67, corroborando la relación inversa entre el tamaño de la partícula y el área superficial, es decir menor tamaño de partícula mayor área superficial.

Tabla 1. Resultados del análisis para la determinación del área superficial del Fe₃O₄ por el método BET.

Muestra	Tamaño de partícula (nm)	Área superficial (m ² / g)
M58	72.66	82.57
M67	92.06	65.17

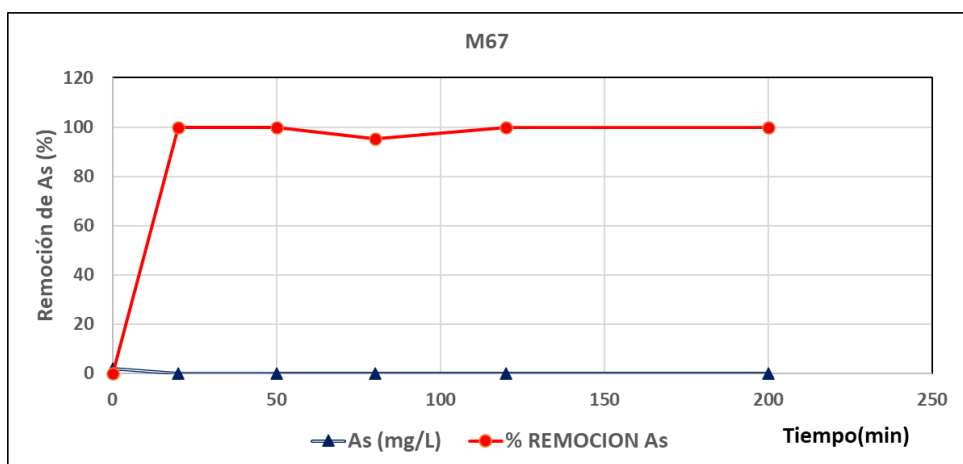
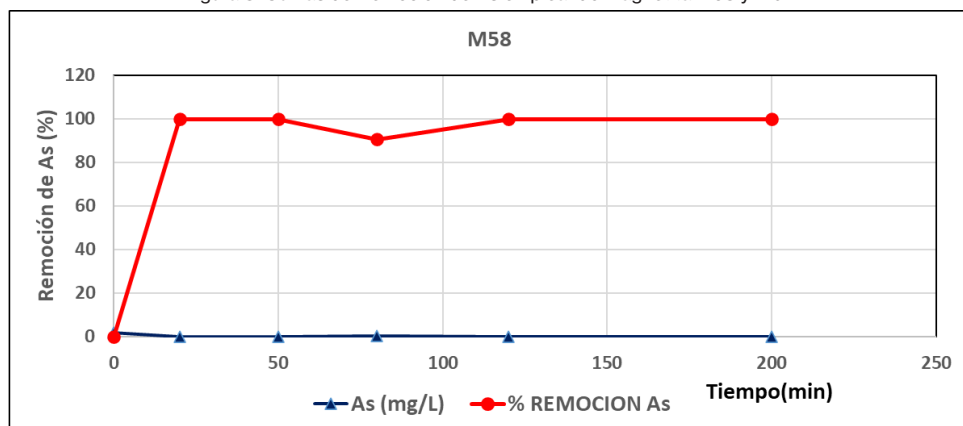
De acuerdo a la literatura (Saidur Rahman Chowdhury, Ernest K. Yanful, 2011) se empleó una concentración de magnetita de 0.4 g/L, es decir se pesaron muestras de 0.004g de magnetita y se colocaron en tubos de ensayo de 10 mL de agua conteniendo 1.9031 mg/L de arsénico. Se procedió a medir el pH de la muestra, obteniendo un valor de pH=8.09, es decir un agua ligeramente alcalina.

En la **Tabla 2** se puede observar los valores del tiempo (min), las concentraciones de As (mg/L) y los % de remoción de As en cada ensayo, empleando las muestras M58 y M67. La **Figura 8** muestra la relación entre el tiempo de contacto y la adsorción de As por la adsorbente magnetita. De acuerdo con la forma de la gráfica, la mayor cantidad adsorbida de arsénico se alcanza entre los 20 y 50 minutos, siendo este el tiempo de equilibrio del proceso para las condiciones experimentales fijadas.

Tabla 2. Resultados de las pruebas de remoción de As empleando las muestras de magnetita M58 y M67.

M58			M67		
Tiempo (min)	As(mg/L)	Remoción de As (%)	Tiempo (min)	As(mg/L)	Remoción de As (%)
0	1.9031	0	0	1.9031	0
20	0.0008	99.958	20	0.0006	99.968
50	0.0006	99.968	50	0.0005	99.974
80	0.1798	90.552	80	0.092	95.166
120	0.0003	99.984	120	0.0003	99.984
200	0.0003	99.984	200	0.0001	99.995

Figura 8. Curvas de Remoción de As empleando magnetita M58 y M67



Por la forma de la gráfica que se obtuvo el proceso de adsorción podría ser dividido en tres etapas: una primera etapa donde la cantidad adsorbida aumenta rápidamente en el tiempo, debido quizás a la difusión del sorbato desde el seno de la solución hasta la superficie del adsorbente. Una segunda etapa donde el proceso se hace muy lento y se desorbe algo de arsénico y una tercera etapa donde nuevamente se incrementa la cantidad adsorbida hasta lograr casi el 100% de remoción de arsénico. Se pudo observar que después de los 120 min casi no hay cambios, esto puede estar relacionado con la saturación de los sitios de adsorción del material y la llegada del sistema al equilibrio.

4 CONCLUSIONES

Se logró sintetizar nanopartículas de magnetita (Fe_3O_4) utilizando la ruta química de coprecipitación a partir de sulfato ferroso y nitrato férrico en medio alcalino. El análisis

por Difracción de Rayos X (DRX) mostró que se obtuvo 100 % de Magnetita (Fe_3O_4) con un tamaño de cristalito promedio de 20nm. La Microscopia Electrónica de Barrido (MEB) confirmó que la morfología de la magnetita sintetizada era de forma cúbica y menores a 1 μm , así como también el análisis EDS (acoplado al MEB) demostró que se tiene los porcentajes en pesos de Hierro y del Oxígeno de 67.3% y 31.1% respectivamente, que corresponden a una muestra de magnetita.

De acuerdo a los valores del Área Superficial obtenidos para las muestras M58 y M67 se puede concluir que a pH ligeramente menores a 12 (pH=11.9) se obtienen partículas de magnetita de menor tamaño y por tanto de mayor área superficial que las sintetizadas a pH=12. La magnetita sintetizada demostró tener una excelente capacidad de remoción de arsénico (As) en aguas ya que en tiempos de contacto relativamente cortos (20min) se logró remoción de casi 100% de As en aguas con concentraciones de 1.9 mg/L de arsénico.

REFERENCIAS

J. BUNDSCHUH, M.A. ARMIENTA, P. BIRKLE, P. BHATTACHARYA, J. MATSCHULLAT, A.B. MUKHERJEE, (2009). Natural Arsenic in Groundwater in Latin America, CRC Press/Balkema, Taylor & Francis Group, London, United Kingdom.

JOCHEN BUNDSCHUH, ALEJO PÉREZ CARRERA, MARTA LITTER. IBEROARSEN Distribución del arsénico en las regiones Ibérica e Iberoamericana, CYTED, 2008, volumen 1, capítulo 2.

MARTA I. LITTER, ANA MARÍA SANCHA, ANA MARÍA INGALLINELLA, IBEROARSEN Tecnologías económicas para el abatimiento de arsénico en aguas, 2010.

M.L. CASTRO DE ESPARZA, Presencia de arsénico en el agua de bebida en América Latina y su efecto en la salud pública. International Congress: Natural Arsenic in Groundwaters of Latin America, Mexico, 2006. Disponible en: <http://bvsper.paho.org/bvsacd/cd51/arsenico-agua.pdf>

SAIDUR RAHMAN CHOWDHURY, ERNEST K. YANFUL. Arsenic removal from aqueous solutions by adsorption on magnetite nanoparticles, Water and Environment Journal 25, 2011, 429-437.

WORLD HEALTH ORGANIZATION, Arsenic in drinking-water. Background document for preparation of WHO Guidelines for drinking-water quality. WHO, 2003, Geneva.

Y. S. LIM, C. W. LAI, S. B. A. HAMID, N. MUHD JULKAPLI, W. A. YEHYA, M. Z. KARIM, M. F. TAI & K. S. LAU. A study on growth formation of nano-sized magnetite Fe_3O_4 via coprecipitation method. Materials Research Innovations Vol. 18, Iss. Sup6, 2014, 457-461.

CHAPTER 14

AVALIAÇÃO DA MICRODUREZA DE NANOCOMPÓSITOS DE MATRIZ DE ALUMÍNIO REFORÇADOS COM ÓXIDO DE GRAFENO REDUZIDO

Data de aceite: 23/05/2021

Daniel Andrada Maria

Instituto de Engenharias Integradas
Universidade Federal de Itajubá
Campus Theodomirosantiago – Itabira - MG
<http://lattes.cnpq.br/4360044696999610>

Andreza de Sousa Andrada

Instituto de Engenharias Integradas
Universidade Federal de Itajubá
Campus Theodomirosantiago – Itabira - MG
<http://lattes.cnpq.br/8856252121271211>

Jordão Samuel Siqueira

Instituto de Engenharias Integradas
Universidade Federal de Itajubá
Campus Theodomirosantiago – Itabira - MG
<http://lattes.cnpq.br/1234922729106387>

Adelina Pinheiro Santos

Laboratório de Química de
Nanoestruturas de Carbono
Centro de Desenvolvimento da
Tecnologia Nuclear – Belo Horizonte - MG
<http://lattes.cnpq.br/6588263168885710>

Clascídia Aparecida Furtado

Laboratório de Química de
Nanoestruturas de Carbono
Centro de Desenvolvimento da
Tecnologia Nuclear – Belo Horizonte - MG
<http://lattes.cnpq.br/8253616889612034>

RESUMO: Este trabalho investiga o uso do óxido de grafeno reduzido (rGO) como reforço em nanocompósitos com matriz de alumínio (NCMAs), obtidos via metalurgia do pó. A moagem mecânica de uma mistura de pó de alumínio e rGO demonstrou ser capaz de formar compósitos homogêneos e altamente densificados, permitindo estabelecer uma interação efetiva entre a matriz e o reforço. O efeito do conteúdo de rGO (variando de 0,01 a 1,0% em massa) na microdureza dos NCMAs-rGO foi investigado. Um ganho de ~200% em microdureza para a composição de 0,5% em massa de rGO foi obtido.

PALAVRAS-CHAVE: Nanocompósitos. Nanotecnologia. Alumínio. Metalurgia do pó. Óxido de grafeno reduzido.

MICROHARDNESS EVALUATION OF NANOCOMPOSITES OF ALUMINUM MATRIX REINFORCED WITH REDUCED GRAPHEN OXIDE

ABSTRACT: This work investigates the use of reduced graphene oxide (rGO) as reinforcement in aluminum matrix composites (AMNCs) fabricated by powder metallurgy. Mechanical milling of a mixture of aluminium and rGO powders was able to form homogeneous and highly densified composites, allowing an effective interaction between matrix and reinforcement to establish. The effect of rGO content (ranging for 0.01 to 1.0 wt%) on the microhardness of

rGO-AMNCs was investigated. A gain of ~ 200% in microhardness for the 0.5 wt% rGO composition was obtained.

KEYWORDS: Nanocomposites. Nanotechnology. Aluminium. Powder metallurgy. Reduced graphene oxide.

1 INTRODUÇÃO

Depois apenas do aço e do ferro, o alumínio (Al) e suas ligas constituem os materiais mais utilizados em aplicações estruturais, em razão de excelentes propriedades como baixa densidade, elevada resistência mecânica específica, elevadas maleabilidade e ductibilidade e boa resistência à corrosão (ZHANG et al., 2019). Entretanto, apresentam algumas limitações, como, por exemplo, alto coeficiente de expansão térmica, propriedades tribológicas limitadas (STOJANOVIC; BUKVIC; EPLER, 2018), propriedades mecânicas sensíveis à temperatura, ao carregamento dinâmico e à presença de impurezas e uma maior susceptibilidade à corrosão (KAINER, 2006). Buscando contornar tais limitações, nas últimas décadas, materiais compósitos baseados em matriz de alumínio (CMAs) vêm sendo extensivamente investigados (KAINER, 2006).

Os CMAs podem ser obtidos pela combinação da matriz de alumínio com partículas de reforços cerâmicos ou não-metálicos. Dependendo do tipo de reforço utilizado, podem ser produzidos compósitos de matriz de alumínio com combinações incomuns de rigidez, resistência mecânica, ductibilidade e resistência à corrosão.

Os CMAs podem ser obtidos pela combinação da matriz de alumínio com partículas de reforços cerâmicos ou não-metálicos. Dependendo do tipo de reforço utilizado, podem ser produzidos compósitos de matriz de alumínio com combinações incomuns de rigidez, resistência mecânica, ductibilidade e resistência à corrosão. Contudo, não é sempre que a adição de partículas de reforço a uma matriz de alumínio leva a melhorias consideráveis em suas propriedades. Em alguns casos, as partículas de reforço podem constituir pontos de defeitos no material, resultando na falha prematura do compósito sob condições de carregamento mecânico. Adicionalmente, o tamanho das partículas de reforço tem um forte efeito sobre a resistência mecânica, a ductibilidade e o modo de falha do compósito resultante. Assim, as propriedades mecânicas dos CMAs podem ser melhoradas com a redução no tamanho das partículas de reforço da escala micrométrica para a escala nanométrica, dando origem aos nanocompósitos de matriz de alumínio (NCMAs).

Entre os nanomateriais de reforço utilizados na confecção dos NCMAs, os nanotubos de carbono (NTCs) e, mais recentemente, os materiais grafênicos (BIANCO et al., 2013; WICK et al., 2014), como o óxido de grafeno (GO), o óxido de grafeno reduzido (rGO), o grafeno de poucas camadas (FLG), as nanofolhas de grafeno (GNS) e a nanoplacas de grafeno (GNPs) têm sido considerados os melhores candidatos.

Quando comparados aos NTCs, os materiais grafênicos apresentam propriedades intrínsecas iguais ou superiores e vêm se mostrando especialmente adequados para produção de NCMA's. Diferente dos NTCs, os materiais grafênicos possuem uma estrutura plana capaz de suportar melhor as condições comuns ao processamento de materiais metálicos (elevadas temperatura e pressão) (NIETO et al., 2017). Adicionalmente, a elevada área superficial específica dos materiais grafênicos proporciona uma maior interação com a matriz, o que possibilita uma transferência mais eficaz de propriedades. E por fim, os materiais grafênicos podem ser obtidos a partir de fonte natural, o grafite, tornando-se relativamente mais barato e abundante.

Dessa forma, a dispersão homogênea de materiais grafênicos em uma matriz de alumínio pode conduzir à produção de NCMA's com propriedades mecânicas aprimoradas. Além disso, outras propriedades funcionais também podem ser esperadas em razão das propriedades notáveis do grafeno e seus derivados, como as propriedades autolubrificantes, o baixo coeficiente de expansão térmica e as elevadas condutividades térmica e elétrica. Na Tabela 1 são apresentadas algumas dessas propriedades para o grafeno e o rGO (objeto de estudo deste trabalho) e para o alumínio metálico (por motivo de comparação).

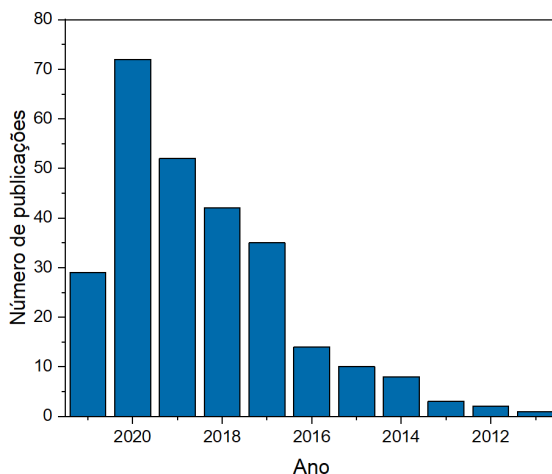
Tabela. 1 - Comparativo de propriedades entre o alumínio, grafeno e o rGO.

Propriedades	Alumínio (MACKENZIE; TOTTEN, 2003)	Grafeno (monocamada) (NIETO et al., 2017)	rGO
Resistencia à tração	40-700 MPa	130 GPa	360 MPa (Filme fino) (WAN et al., 2019).
Módulo de elasticidade	70 GPa	0,5-1 TPa	~300 GPa (ZHU et al., 2010)
Condutividade térmica	237 W.m ⁻¹ .K ⁻¹	4840- 5300 W.m ⁻¹ .K ⁻¹	30-2600 W m ⁻¹ K ⁻¹ (ZENG et al., 2019).
Coefficiente de expansão térmica	21-24x10 ⁻⁶ /K	-6x10 ⁻⁶ /K	-
Mobilidade de elétrons (298K)	12 cm ² .V ⁻¹ .s ⁻¹	15000 cm ² .V ⁻¹ .s ⁻¹	-
Transmitância		>95%	~83%
Área superficial específica		2630 m ² .g ⁻¹	~700 m ² .g ⁻¹ (seco)

Os estudos relacionados ao desenvolvimento de NCMA's reforçados com materiais grafênicos vem apresentando um crescimento exponencial na última década. Tal fato pode ser observado analisando o gráfico de barras apresentado na Figura 1,

construído por pesquisa à base de dados bibliográficos *ISI Web of Science* (<http://apps.webofknowledge.com>). Nesta pesquisa foram selecionados artigos publicados no período de 2011 a 2021, usando as palavras-chave “*graphene*”, “*composites*” e “*aluminum*”.

Figura 1 Número de artigos publicados por ano (incluindo artigos científicos e de revisão), no período de 2011 a 2021, usando as palavras-chave “*graphene*”, “*composites*” e “*aluminum*”.



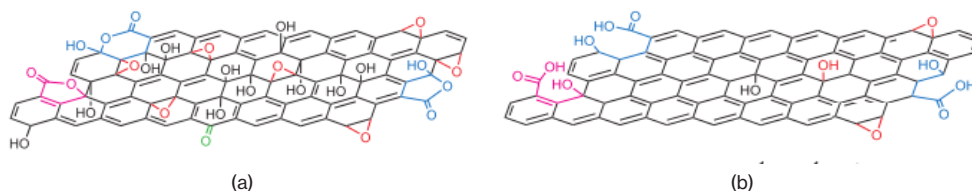
Os primeiros trabalhos que relataram a obtenção de NCMA's reforçados com materiais grafênicos (BARTOLUCCI et al., 2011) datam de quase uma década após o isolamento do grafeno em 2004 (NOVOSELOV, 2004). Tal atraso é frequentemente atribuído ao período de levantamento das propriedades dos novos materiais e à relativa facilidade para obtenção dos nanocompósitos de matriz polimérica quando comparados aos nanocompósitos de matriz metálica (TJONG; CHIN, 2013). Apesar da taxa absoluta anual ser arbitrária e depender da escolha das palavras-chave utilizadas na pesquisa é possível verificar que há uma tendência crescente do número de trabalhos que envolvem a obtenção de NCMA's reforçados com materiais grafênicos, apresentando-se como um novo paradigma no contexto dos nanocompósitos de matriz metálica e alavancando as pesquisas nessa área.

Por conseguinte, várias abordagens para sintetizar materiais grafênicos em grandes quantidades têm sido desenvolvidas. Estas podem ser divididas em duas grandes categorias: (i) as abordagens *bottom-up* (do inglês, de baixo para cima), que incluem o crescimento epitaxial por decomposição térmica de carbeto de silício e a deposição química em fase vapor de grafenos em superfícies metálicas; e (ii) as abordagens *top-down* (do inglês, de cima para baixo), que incluem os métodos de esfoliação mecânica (ANTISARI et al., 2006; PARK; RUOFF, 2009; ZHAO et al., 2010), a esfoliação química do

grafite em líquidos (PARK; RUOFF, 2009; VALLÉS et al., 2008; GHAFARZADEH, 2018) e a oxidação do grafite seguida pela sua redução (NOVOSELOV, 2004; PARK; RUOFF, 2009; PEI; CHENG, 2011; REINA et al., 2008).

Este último tem sido um método importante por sua relativa simplicidade e baixo custo, alto grau de esfoliação e quantidade de material obtido (STANKOVICH et al., 2006). O produto das reações de oxidação do grafite e redução do óxido é chamado frequentemente de óxido de grafite reduzido, que, quando esfoliado ou disperso, torna-se óxido de grafeno reduzido (rGO). O processo de redução química remove parcialmente defeitos e grupos funcionais (carboxila, hidroxila, epóxi, carbonila) da rede hexagonal do GO, tornando, assim, as propriedades do rGO mais próximas daquelas do grafeno (Tabela 1). A estrutura do GO e do rGO são apresentadas esquematicamente na Figura 2.

Figura 2 - Modelo esquemático para a estrutura química de uma única camada de óxido de grafeno (a) e do óxido de grafeno reduzido (b).



O desenvolvimento dos nanocompósitos baseados em matriz de alumínio e materiais grafênicos enfrenta principalmente os seguintes desafios: (i) a dispersão não homogênea do material grafênico; (ii) a ligação interfacial fraca e a formação de carbetos; e (iii) a degradação do ordenamento cristalino das fases durante o processamento. Para superar tais dificuldades, muitas estratégias têm sido desenvolvidas nos últimos anos (KHANNA; KUMAR; BANSAL, 2021), inclusive a avaliação de diferentes métodos de processamento, como a metalurgia líquida, a metalurgia do pó, a liga mecânica por fricção, a deposição eletroquímica, entre outros novos métodos que dependem da dispersão das fases em líquidos, como, por exemplo, a mistura em nível molecular. Dentre esses métodos, a metalurgia do pó se destaca, em razão da sua simplicidade e flexibilidade, alta produtividade e baixos custos relativos (ALRASHEEDI, 2016; BAIG et al., 2018; BARTOLUCCI et al., 2011; DASARI et al., 2018; ELGHAZALY; ANIS; SALEM, 2017; KHAN et al., 2017; LATIEF et al., 2011; LI; XIONG, 2017a; LI et al., 2018a; LIU et al., 2016a; PÉREZ-BUSTAMANTE et al., 2014; RAJ et al., 2020; SUN et al., 2017; SYED NASIMUL ALAMN, 2016; TURAN; AYDIN, 2020; WANG et al., 2019).

Neste trabalho, a metalúrgica do pó foi utilizada na obtenção de um nanocompósito de matriz de alumínio reforçado com rGO (NCMA-rGO). O efeito da concentração de rGO na microdureza do nanocompósito foi avaliado.

2 EXPERIMENTAL

2.1 OBTENÇÃO DA AMOSTRA DE rGO

A amostra de grafite utilizada nesse estudo foi fornecida pelo Nacional de Grafite LTDA, Brasil. Possui partículas com diâmetro médio de 50 μm , espessura de camadas da ordem de 50 nm e pureza maior que 99,9%. Todos os solventes e reagentes foram de grau analítico e utilizados sem purificação adicional. Outros reagentes químicos de análise foram fornecidos pela Sigma-Aldrich.

O procedimento de obtenção do GO (método Hummers modificado) foi baseado no trabalho de Abdolhosseinzadeh e colaboradores (ABDOLHOSSEINZADEH; ASGHARZADEH; KIM, 2015). A amostra sólida final foi triturada manualmente e peneirada em uma malha de 40# para obtenção de uma amostra em pó homogênea.

A reação de redução foi realizada em uma segunda etapa que iniciou-se com o preparo de uma dispersão aquosa da amostra de GO (1 mg. mL^{-1}). Em seguida, foi adicionada solução aquosa de NaOH 1,0 M para ajustar o pH \approx 9-10 e, finalmente, adicionou-se solução de ácido ascórbico (L-AA) 0,45 M numa quantidade equivalente a 10 vezes a massa inicial de GO. O produto sólido foi separado por filtração em membrana hidrofílica, de policarbonato, de 0,47 μm (Millipore®) e lavado com água deionizada e etanol anidro. O produto final foi seco em estufa à vácuo em temperatura inferior a 40 ° C durante 48h.

2.2 OBTENÇÃO DO NCMA-rGO

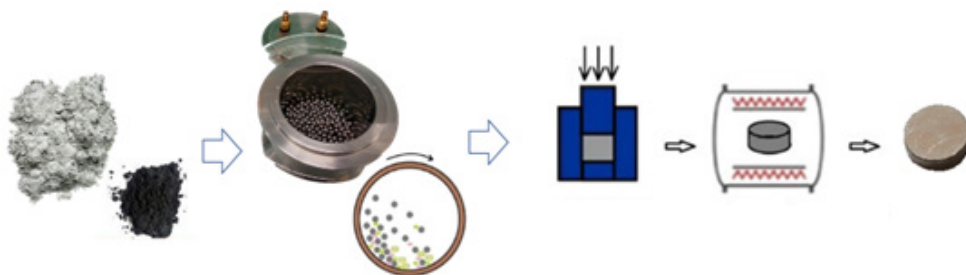
Pós de Al puros (> 99,7% de pureza) obtidos pela técnica de atomização foram cedidos pela ALCOA – Poços de Caldas – MG. Os pós possuem tamanho médio de partículas de 10 μm .

Para combinação de todos os pós e obtenção do NCMA-rGO utilizou-se inicialmente a moagem de alta energia para favorecer a dispersão homogênea das fases. Foi utilizado um moinho de bolas Restch PM 100 com a velocidade de 250 rpm. A moagem foi realizada durante 3 h em frasco de aço inoxidável de 250 ml com bolas de aço inoxidável de 2 mm de diâmetro, sob atmosfera inerte de N_2 ultrapuro. A moagem foi interrompida por 15 minutos a cada intervalo de 60 minutos para evitar o aquecimento excessivo da amostra. A proporção massa/carga foi mantida constante em 10:1. O metanol (CH_3OH -99,99%) foi utilizado como agente de controle do processo para minimizar a soldagem à frio das partículas de alumínio, numa proporção de 0,8% em massa em relação ao teor de alumínio.

Ao final do processo, a mistura foi mantida em um dessecador sob vácuo para permitir a passivação lenta do pó metálico por um período mínimo de 24 h. Em seguida, a mistura foi transferida para um frasco limpo e seco e devidamente selado para evitar

a contaminação e a absorção de umidade. Por fim, as amostras nanocompósitas foram adicionadas em uma matriz de aço de 10 mm de diâmetro e compactadas à frio a uma pressão de 550MPa e, em seguida, submetidas à sinterização utilizando um forno tubular horizontal (Fortelab, FT - 1200/HFL) em atmosfera de gás seco e inerte a 605 °C/10° C.min⁻¹, por 180 min. Uma representação esquemática do processo de obtenção dos NCMA's é apresentada na Figura 3.

Figura 3 - Representação esquemática das etapas de dispersão e consolidação dos CMMs.



Em relação à escolha da porcentagem mássica do reforço, de maneira geral, observa-se que nos NCMA's obtidos com porcentagens mássicas iguais ou superiores a 1% é comum verificar prejuízos nas propriedades mecânicas do material (LI; XIONG, 2017a; LI et al., 2015; LIAO; TAN, 2011; MORSI et al., 2010; STEIN et al., 2012). Portanto, para o presente trabalho, foram projetados NCMA's com as concentrações de 0,0, 0,01, 0,05, 0,5 e 1,0% em massa de rGO.

2.3 CARACTERIZAÇÃO

Medidas de densidade aparente e densidade real foram realizadas usando a técnica de picnometria à hélio em diversas etapas da manufatura dos NCMA's, buscando compreender aspectos relacionados à consolidação das amostras. A técnica de difração de raios X (DRX) foi empregada com a finalidade de identificar e avaliar alterações na microestrutura das amostras na forma de pó. As medidas de microdureza foram realizadas utilizando-se um microdurômetro Vickers Wilson – 402 MVD com carga de 0,2 kgf e tempo de 15 segundos. As amostras foram previamente limpas e polidas de acordo com norma ASTM E-384.

3 RESULTADOS E DISCUSSÃO

3.1 DENSIDADE E MICROESTRUTURA DOS NCMA'S

Os valores de densidade obtidos para os diferentes NCMA's estão apresentados na Tabela 2. As densidades experimentais (ρ_e) foram obtidas pelo método de Arquimedes

e as densidades teóricas foram calculadas (ρ_c) por meio da regra das misturas utilizando os valores de densidade do Al e do rGO puros obtidos experimentalmente ($2,698 \pm 0,006 \text{ g.cm}^{-3}$ e $1,651 \pm 0,019 \text{ g.cm}^{-3}$ para o Al e o rGO, respectivamente).

Tabela 2 – Valores médios de densidade obtidos experimentalmente e calculados por meio da regra das misturas para os diferentes NCMA-rGOs produzidos.

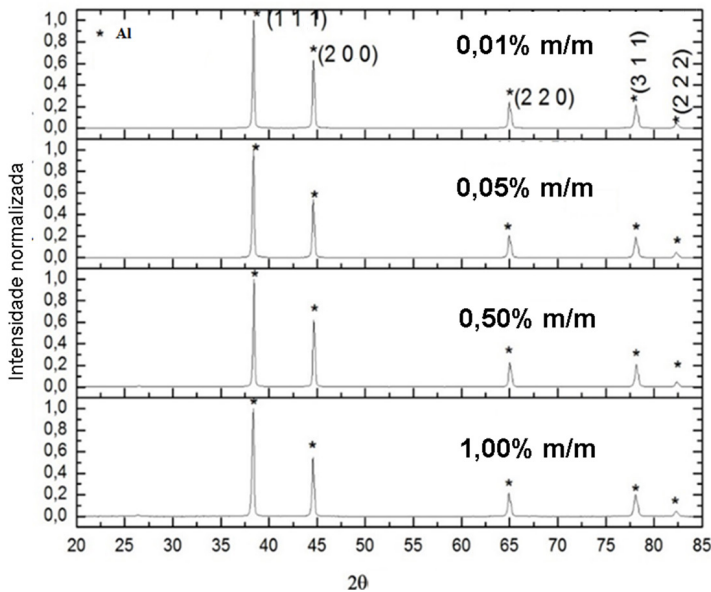
NCMA-rGOs		
$X_{m(\text{rGO})}$	$\rho_e \text{ (g.cm}^{-3}\text{)}$	$\rho_c \text{ (g.cm}^{-3}\text{)}$
0	$2,63 \pm 0,01$	2,698
0,0001	$2,63 \pm 0,02$	2,698
0,0005	$2,63 \pm 0,01$	2,697
0,005	$2,60 \pm 0,01$	2,689
0,01	$2,57 \pm 0,01$	2,681

Para os NCMA-rGOs, a incorporação dos materiais de reforço tem o efeito de reduzir a densidade. Essa diminuição mostra-se significativa apenas acima de 0,5% m/m.

Para o alumínio puro observou-se um valor de ~98% em relação à densidade teórica, o que demonstra o alto nível de densificação alcançado utilizando a metodologia proposta. Este valor está de acordo com os relatados na literatura (CHAMPION, 2008; KHAN et al., 2017; RASHAD et al., 2014). Já para os NCMA-rGOs foi possível verificar níveis de densificação atingindo valores de ~97% e ~96% em relação aos valores máximos teóricos. Resultados semelhantes foram obtidos por Khan e colaboradores (KHAN et al., 2017), que utilizaram metodologia semelhante à usada nesse trabalho, e em outros estudos que utilizaram variações do método de processamento (BISHT et al., 2017; LI; XIONG, 2017b). Para os NCMA-rGOs, observou-se a diminuição da densidade com a incorporação de rGO em concentrações acima de 0,5% em massa. As diferenças encontradas entre os valores experimentais e os valores calculados, em particular nas amostras com teor de reforço de 0,5 e 1,0% em massa devem-se, provavelmente, a fatores como a porosidade e à formação de aglomerados do material de reforço na amostra.

Os resultados de difração de raios X dos pós após a etapa de moagem são apresentados na Figura 4. É possível verificar que, para todas as proporções estudadas, apenas as reflexões mais intensas (111), (200), (220), (311) e (222) referentes à estrutura do alumínio (ICDD No. 89-4037) foram identificadas.

Figura 4 – Difratomogramas dos pós após a etapa de dispersão por moagem de alta energia.



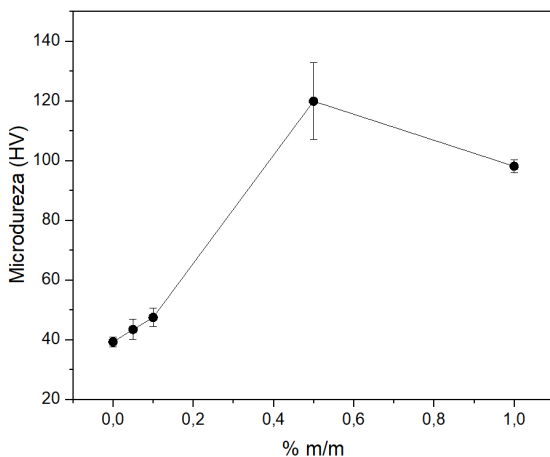
Devido à baixa concentração ($\leq 1\%$ em massa) do rGO e em razão de sua estrutura de poucas camadas, a reflexão (002) típica da estrutura tridimensional de materiais gráficos, comumente utilizada para identificar essa fase, não foi detectada nos difratogramas. Este resultado sugere que o processo de moagem possa ter favorecido a distribuição homogênea das fases e a sua concomitante inserção ao volume das partículas metálicas. Resultados semelhantes foram relatados na literatura (LIU et al., 2016b; ZHOU et al., 2019a, 2019b).

Outra observação importante é que o pico em $\sim 31^\circ$ não foi detectado nos difratogramas. Este pico é referente à fase Al_4C_3 conhecida por causar fragilização no Al e deteriorar as propriedades mecânicas dos NCMAs (AGARWAL; BAKSHI; LAHIRI, 2016). Isso pode ser devido à ausência dessa fase no nanocompósito ou devido ao limite de detecção da técnica.

3.2 MICRODUREZA DOS NCMAS

Os valores obtidos para a microdureza dos NCMAs-rGO em função do percentual em massa de rGO são apresentados na Figura 5. É possível notar que o rGO tem um efeito significativo no valor da microdureza dos NCMAs em comparação com o alumínio puro. Um aumento discreto foi verificado para a incorporação de rGO nas concentrações de 0,05 e 0,1% em massa. Já para a concentração de 0,5% em massa de rGO, observou-se um ganho real em microdureza de ~ 3 vezes em relação à do alumínio puro, de ~ 39 HV a ~ 120 HV (Figura 5).

Figura 5 - Resultados médios de microdureza para as amostras NCMA-rGO em função da % em massa do material de reforço.



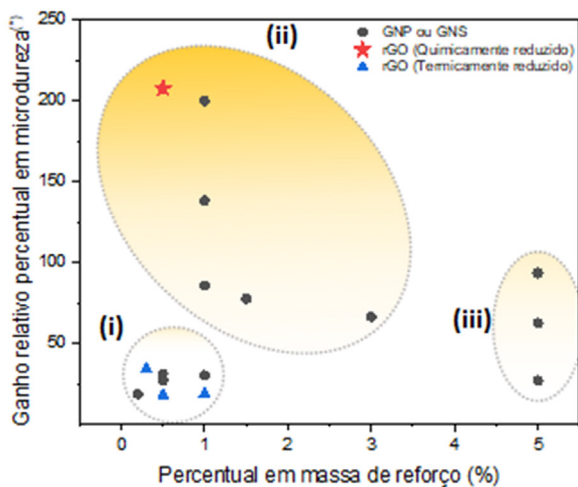
Para a concentração de 1% em massa de rGO, observou-se uma redução nos valores de microdureza, sugerindo um possível efeito de inhomogeneidade da dispersão, que pode induzir à formação de aglomerados, maior porosidade e menor efetividade da interação interfacial entre o Al e a fase carbono. Resultados semelhantes foram obtidos em outros estudos (BISHT et al., 2017; LI et al., 2015) onde proporções acima de 1% em massa provocaram degradação nas propriedades mecânicas de uma forma geral.

A Figura 6 a seguir reúne os melhores resultados encontrados na literatura para a microdureza dos NCMA's reforçados com rGO e com outros materiais grafênicos (por motivo de comparação). Nessa figura a microdureza encontra-se expressa em termos do ganho percentual relativo (comparação com o alumínio não reforçado), permitindo assim uma melhor comparação entre os diferentes trabalhos. A seleção dos trabalhos utilizados nesta comparação foi baseada na semelhança em termos de metodologia de processamento (metalurgia do pó/moagem de alta energia) (ALRASHEEDI, 2016; BAIG et al., 2018; BARTOLUCCI et al., 2011; DASARI et al., 2018; ELGHAZALY; ANIS; SALEM, 2017; KHAN et al., 2017; LATIEF et al., 2011; LI; XIONG, 2017a; LI et al., 2018a; LIU et al., 2016a; PÉREZ-BUSTAMANTE et al., 2014; RAJ et al., 2020; SUN et al., 2017; SYED NASIMUL ALAMN, 2016; TURAN; AYDIN, 2020; WANG et al., 2019.

Em função de não haver outros trabalhos na literatura até o momento que apresentem resultados de microdureza para NCMA's reforçados com rGO quimicamente reduzido, foi incluído nessa comparação os resultados de microdureza para o NCMA-rGO termicamente reduzido e NCMA reforçado com outros materiais grafênicos (GNPs ou GNS), como detalhado na legenda da Figura 6. Verifica-se nesta Figura, em função

da distribuição dos resultados, algumas regiões delimitadas que sugerem tendências, identificadas como (i), (ii) e (iii).

Figura 6 – Ganho relativo percentual⁽¹⁾ da microdureza em função do percentual em massa do reforço. ⁽¹⁾ $(HV_{(a)} - HV_{(b)}) / HV_{(b)} \times 100$. $HV_{(a)}$: microdureza do NCMA, $HV_{(b)}$: microdureza do alumínio puro em iguais condições de processamento.



No grupo (i) encontram-se reunidos os resultados com menores ganhos relativos na microdureza. Tal fato pode ser atribuído à pobre dispersão da fase de reforço e da baixa interação do reforço com a matriz metálica.

No grupo (iii) encontram-se agrupados resultados onde foram utilizadas maiores frações mássicas de reforço na confecção dos NCMA-rGO. Como mencionando, um dos maiores obstáculos para obter um NCMA-rGO com propriedades mecânicas aprimoradas é a distribuição homogênea do material de reforço, que se torna um desafio cada vez maior à medida que a quantidade relativa de reforço aumenta. A elevada energia de superfície desses materiais é responsável pela forte tendência de aglomeração de suas partículas, que, conseqüentemente, leva à redução nas suas propriedades mecânicas.

Por fim, o grupo (ii), onde o resultado do presente estudo se situa, reúne os trabalhos que apresentam melhor desempenho no ganho em microdureza. É possível dizer que os trabalhos incluídos nesse grupo são aqueles onde verifica-se uma combinação sinérgica entre as propriedades da matriz e do reforço. A faixa de concentração em massa em torno de 0,5-1,0% se destaca na obtenção de NCMA-rGO com melhores propriedades mecânicas, utilizando a metodologia de metalurgia do pó, concordando com outros trabalhos relatados na literatura (LI; XIONG, 2017a; LI et al., 2015; LIAO; TAN, 2011; MORSI et al., 2010; STEIN et al., 2012).

Ainda na Figura 6 é possível verificar que entre todos os trabalhos envolvendo o uso de rGO como reforço, o presente trabalho que utilizou o rGO reduzido quimicamente

(em vermelho) foi o que ofereceu melhor desempenho em aumento de microdureza. Cabe ressaltar que dos três estudos que investigaram a utilização do rGO reduzido termicamente (em azul), um deles refere-se ao primeiro estudo realizado em 2011 por Bartolucci e colaboradores (BARTOLUCCI et al., 2011) e outro, mais recente (RAJ et al., 2020), embora tenha apresentado desempenho inferior no aumento em microdureza, apresentou um valor absoluto expressivo de ~160 HV (para 0,5% em massa de rGO). Entretanto, nesse trabalho os autores utilizam a liga de alumínio 7075 que já possui dureza elevada.

Estudos teóricos recentes (CHEN et al., 2021; LI et al., 2018b; ZHANG; WANG, 2021) têm demonstrado que grafenos mais “defeituosos” (que apresentam maior densidade de defeitos pontuais e hibridização sp^3), GO ou rGO por exemplo, podem ser considerados materiais mais promissores para serem utilizados como fase de reforço em NCMA. De acordo com esses estudos, a energia de ligação interfacial Al-C é quase 4 vezes superior à esperada para um NCMA reforçado com “grafeno ideal” (GNP ou GNS, por exemplo), o que pode proporcionar, portanto, melhorias nas propriedades mecânicas dos NCMA.

4 CONCLUSÕES

Nanocompósitos NCMA-rGO, com concentração de rGO entre 0,01 e 1,0% em massa de rGO, foram obtidos utilizando a moagem de alta energia para promover a dispersão e combinação das fases. Os NCMA-rGO apresentaram elevado grau de densificação, verificando-se ganhos em microdureza de ~200% com frações mássicas de 0,5%. A fase Al_4C_3 , cuja formação pode levar a perdas em propriedades mecânicas dos NCMA, não foi detectada nos pós por DRX, evidenciando que as condições de moagem selecionadas podem ter sido adequadas para evitar danos excessivos ao material grafênico e, conseqüentemente, a sua formação. Em um estudo comparativo, frações mássicas de 0,5-1,0% apresentaram ganhos relativos em microdureza significativos, sugerindo um guia para estudos futuros.

5 AGRADECIMENTOS

Este trabalho teve o apoio do Instituto Brasileiro de Nanocarbono, do Programa SisNano e das agências brasileiras CNPq, CAPES, FAPEMIG e CNEN. Os autores gostariam de agradecer à Alcoa e à Nacional de Grafite LTDA pelo fornecimento das amostras.

REFERÊNCIAS

ABDOLHOSSEINZADEH, S.; ASGHARZADEH, H.; KIM, H. S. Fast and fully-scalable synthesis of reduced graphene oxide. **Scientific Reports**, v. 5, p. 1-7, 2015.

- AGARWAL, A.; BAKSHI, S. R.; LAHIRI, D. **Carbon nanotubes: Reinforced metal matrix composites**. 1. ed. CRC Press, 2016.
- ALRASHEEDI, N. H. Facile Synthesis and Characterization of Aluminum/Graphene Nanosheets Composites. **Arabian Journal for Science and Engineering**, v. 41, n. 11, p. 4391–4395, 2016.
- ANTISARI, M. V. et al. Low energy pure shear milling: A method for the preparation of graphite nanosheets. **Scripta Materialia**, v. 55, n. 11, p. 1047–1050, 2006.
- BAIG, Z. et al. An efficient approach to address issues of graphene nanoplatelets (GNPs) incorporation in aluminium powders and their compaction behaviour. **Metals**, v. 8, n. 2, p. 1–16, 2018.
- BARTOLUCCI, S. F. et al. Graphene-aluminum nanocomposites. **Materials Science and Engineering A**, v. 528, n. 27, p. 7933–7937, 2011.
- BIANCO, A. et al. All in the graphene family - A recommended nomenclature for two-dimensional carbon materials. **Carbon**, v. 65, p. 1–6, 2013.
- BISHT, A. et al. Strengthening mechanism in graphene nanoplatelets reinforced aluminum composite fabricated through spark plasma sintering. **Materials Science & Engineering A**, 2017.
- CHAMPION, Y. Powder metallurgy of nanometric aluminium powders. **Powder Metallurgy**, v. 51, n. 2, p. 125–132, 2008.
- CHEN, Y. et al. The interface properties of defective graphene on aluminium: A first-principles calculation. **Computational Materials Science**, v. 188, n. December 2020, p. 110157, 2021.
- DASARI, B. L. et al. Mechanical properties of graphene oxide reinforced aluminium matrix composites. **Composites Part B: Engineering**, v. 145, n. October 2017, p. 136–144, 2018.
- ELGHAZALY, A.; ANIS, G.; SALEM, H. G. Effect of Graphene Addition on the Mechanical and Tribological Behavior of. **Composites Part A**, 2017.
- GHAFFARZADEH K. IDTechEX. **Graphene, 2D Materials and Carbon Nanotubes: Markets, Technologies and Opportunities 2018–2028**. Available online: <https://www.idtechex.com/research/reports/graphene-2d-materials-and-carbon-nanotubesmarkets-technologies-and-opportunities-2018-2028-000603.asp>, 2018
- KAINER, K. U. **Basics of Metal Matrix Composites**. 1. ed. Forschungszentrum, Geesthacht: Wiley, 2006.
- KHAN, M. et al. Microstructural evolution, mechanical profile, and fracture morphology of aluminum matrix composites containing graphene nanoplatelets. **Journal of Materials Research**, v. 32, n. 11, p. 2055–2066, 2017.
- KHANNA, V.; KUMAR, V.; BANSAL, S. A. Mechanical properties of aluminium-graphene/carbon nanotubes (CNTs) metal matrix composites: Advancement, opportunities and perspective. **Materials Research Bulletin**, v. 138, n. April, 2021.
- LATIEF, F. H. et al. Journal of Analytical and Applied Pyrolysis Fabrication of exfoliated graphite nanoplatelets-reinforced aluminum composites and evaluating their mechanical properties and corrosion behavior. **Journal of Analytical and Applied Pyrolysis**, v. 92, n. 2, p. 485–492, 2011.
- LI, G.; XIONG, B. Effects of graphene content on microstructures and tensile property of graphene-nanosheets / aluminum composites. **Journal of Alloys and Compounds**, v. 697, p. 31–36, 2017a.

- LI, G.; XIONG, B. Effects of graphene content on microstructures and tensile property of graphene-nanosheets / aluminum composites. **Journal of Alloys and Compounds**, v. 697, p. 31–36, 2017b.
- LI, J. L. et al. Microstructure and tensile properties of bulk nanostructured aluminum/graphene composites prepared via cryomilling. **Materials Science and Engineering A**, v. 626, p. 400–405, 2015.
- LI, M. et al. Microstructure evolution and properties of graphene nanoplatelets reinforced aluminum matrix composites. **Materials Characterization**, v. 140, n. April, p. 172–178, 2018a.
- LI, Z. et al. Graphene quality dominated interface deformation behavior of graphene-metal composite: The defective is better. **International Journal of Plasticity**, v. 111, p. 253–265, 2018b.
- LIAO, J.; TAN, M. Mixing of carbon nanotubes (CNTs) and aluminum powder for powder metallurgy use. **Powder Technology**, v. 208, n. 1, p. 42–48, 2011.
- LIU, J. et al. Powder processing methodology for production of graphene oxide reinforced aluminium matrix composites. **Advances in Materials and Processing Technologies**, v. 0698, n. October, p. 1–14, 2016a.
- LIU, J. et al. Graphene oxide and graphene nanosheet reinforced aluminium matrix composites: Powder synthesis and prepared composite characteristics. **Materials and Design**, v. 94, p. 87–94, 2016b.
- MACKENZIE, D. S.; TOTTEN, G. E. **Handbook of aluminum**. 1. ed. New York: Marcel Dekker, 2003.
- MORSI, K. et al. A Spark plasma extrusion (SPE) of ball-milled aluminum and carbon nanotube reinforced aluminum composite powders. **Composites Part A**, v. 41, n. 2, p. 322–326, 2010.
- NIETO, A. et al. Graphene reinforced metal and ceramic matrix composites : a review. **International Materials Reviews**, v. 62, n. 5, p. 241–302, 2017.
- NOVOSELOV, K. S. Electric Field Effect in Atomically Thin Carbon Films. v. 666, n. 2004, 2004.
- PARK, S.; RUOFF, R. S. Chemical methods for the production of graphenes. **Nature Nanotechnology**, v. 4, n. 4, p. 217–224, 2009.
- PEI, S.; CHENG, H. The reduction of graphene oxide. **Carbon**, v. 50, n. 9, p. 3210–3228, 2011.
- PÉREZ-BUSTAMANTE, R. et al. Microstructural and hardness behavior of graphene-nanoplatelets / aluminum composites synthesized by mechanical alloying. **Journal of Alloys and Compounds**, v. 615, p. S578–S582, 2014.
- RAJ, R. R. et al. Effect of graphene addition on the mechanical characteristics of AA7075 aluminium nanocomposites. **Carbon Letters**, n. 0123456789, 2020.
- RASHAD, M. et al. Effect of Graphene Nanoplatelets addition on mechanical properties of pure aluminum using a semi-powder method. **Progress in Natural Science: Materials International**, v. 24, n. 2, p. 101–108, 2014.
- REINA, A. et al. Large Area, Few-Layer Graphene Films on Arbitrary Substrates by Chemical Vapor Deposition. **Nano Letters**, v. 9, n. 1, p. 30–35, 2008.
- STANKOVICH, S. et al. Graphene-based composite materials. **Nature**, v. 442, n. 7100, p. 282–286, 2006.
- STEIN, J. et al. Mechanical reinforcement of a high-performance aluminium alloy AA5083 with homogeneously dispersed multi-walled carbon nanotubes. **Carbon**, v. 50, n. 6, p. 2264–2272, 2012.

- STOJANOVIC, B.; BUKVIC, M.; EPLER, I. Application of aluminum and aluminum alloys in engineering. **Applied Engineering Letters**, v. 3, n. 2, p. 52–62, 2018.
- SUN, Y. et al. Reduced Graphene Oxide Reinforced 7075 Al Matrix Composites: Powder Synthesis and Mechanical Properties. **Metals**, v. 7, n. 11, p. 499, 2017.
- SYED NASIMUL ALAMN, L. K. A Mechanical properties of aluminium based metal matrix composites reinforced with graphite nanoplatelets. **Materials Science & Engineering A**, v. 667, p. 16–32, 2016.
- TJONG, S. C.; CHIN, S. Recent progress in the development and properties of novel metal matrix nanocomposites reinforced with carbon nanotubes and graphene nanosheets. **Materials Science and Engineering R: Reports**, v. 74, n. 10, p. 281–350, 2013.
- TURAN, M. E.; AYDIN, F. Improved elevated temperature mechanical properties of graphene-reinforced pure aluminium matrix composites. **Materials Science and Technology (United Kingdom)**, v. 36, n. 10, p. 1092–1103, 2020.
- VALLÉS, C. et al. Solutions of negatively charged graphene sheets and ribbons. **Journal of the American Chemical Society**, v. 130, n. 47, p. 15802–15804, 2008.
- WAN, S. et al. Ultrastrong Graphene Films via Long-Chain π -Bridging. **Matter**, v. 1, n. 2, p. 389–401, 2019.
- WANG, J. et al. Effect of the graphene content on the microstructures and properties of graphene/aluminum composites. **Xinxing Tan Cailiao/New Carbon Materials**, v. 34, n. 3, p. 275–285, 2019.
- WICK, P. et al. Classification framework for graphene-based materials. **Angewandte Chemie - International Edition**, v. 53, n. 30, p. 7714–7718, 2014.
- ZENG, Y. et al. Thermally Conductive Reduced Graphene Oxide Thin Films for Extreme Temperature Sensors. **Advanced Functional Materials**, v. 29, n. 27, p. 1–7, 2019.
- ZHANG, J. et al. A review of selective laser melting of aluminum alloys: Processing, microstructure, property and developing trends. **Journal of Materials Science and Technology**, v. 35, n. 2, p. 270–284, 2019.
- ZHANG, X.; WANG, S. Interfacial strengthening of graphene/aluminum composites through point defects: A first-principles study. **Nanomaterials**, v. 11, n. 3, p. 1–16, 2021.
- ZHAO, W. et al. Preparation of graphene by exfoliation of graphite using wet ball milling. **Journal of Materials Chemistry**, v. 20, n. 28, p. 5817–5819, 2010.
- ZHOU, W. et al. In situ formation of uniformly dispersed Al₄C₃ nanorods during additive manufacturing of graphene oxide/Al mixed powders. **Carbon**, v. 141, p. 67–75, 2019a.
- ZHOU, W. et al. Interfacial reaction induced efficient load transfer in few-layer graphene reinforced Al matrix composites for high-performance conductor. **Composites Part B: Engineering**, v. 167, p. 93–99, 2019b.
- ZHU, Y. et al. Graphene and graphene oxide: Synthesis, properties, and applications. **Advanced Materials**, v. 22, n. 35, p. 3906–3924, 2010.

CHAPTER 15

ROTA ECOLOGIA PARA SÍNTESE DE ELETRODO NANOESTRUTURADO DE ZnO PARA SUPERCAPACITOR

Data de submissão: 03/04/2021

Data de aceite: 26/04/2021

Bruna Rodrigues de Lima

Comissão Nacional de Energia Nuclear
Instituto de Pesquisas
Energéticas e Nucleares
Centro de Ciências e
Tecnologia dos Materiais
São Paulo – SP
<http://lattes.cnpq.br/6522156417116366>

Eguiberto Galego

Comissão Nacional de Energia Nuclear
Instituto de Pesquisas
Energéticas e Nucleares
Centro de Ciências e
Tecnologia dos Materiais
São Paulo – SP
<http://lattes.cnpq.br/4818030985379074>

Rubens Nunes de Faria Junior

Comissão Nacional de Energia Nuclear
Instituto de Pesquisas
Energéticas e Nucleares
Centro de Ciências e
Tecnologia dos Materiais
São Paulo – SP
<http://lattes.cnpq.br/8776524631256060>

Marilene Morelli Serna

Comissão Nacional de Energia Nuclear
Instituto de Pesquisas
Energéticas e Nucleares
Centro de Ciências e
Tecnologia dos Materiais
São Paulo – SP
<http://lattes.cnpq.br/7397656667247795>

Tatiane Yumi Tatei

Comissão Nacional de Energia Nuclear
Instituto de Pesquisas
Energéticas e Nucleares
Centro de Ciências e
Tecnologia dos Materiais
São Paulo – SP
<http://lattes.cnpq.br/8691251600229151>

RESUMO: Capacitores de dupla camada elétrica (EDLC) tem sido amplamente pesquisados devido as suas várias aplicações em dispositivos elétricos e eletrônicos, devido a alta densidade de potência e número de ciclos de carga e descarga. O óxido de zinco é um candidato promissor para emprego em eletrodos de supercapacitores. O ZnO é usado largamente em eletrodos de baterias com uma densidade de energia de cerca de 650 A g^{-1} , mas tem a desvantagem de apresentar formação de dendritas devido a ciclagem constante, as quais reduzem a vida útil. Neste trabalho, reportamos um método relativamente simples, ecológico e de baixo

custo para preparar eletrodos de ZnO que consiste em duas etapas. Inicia-se com a deposição de uma camada semente pelo método das deposição de camadas iônicas adsorvida e por reação sucessivamente (SILAR). Subsequentemente, a deposição em banho químico (CBD) foi usada para crescimento de nanoestruturas de ZnO. O método SILAR foi usado neste trabalho em substituição a métodos que utilizam alta temperatura e alto vácuo, tal como a deposição por vapor químico, para criar uma interface entre o coletor condutivo de aço inoxidável ou alumínio e o filme nanoestruturado de ZnO. A microscopia eletrônica de varredura ou empregada para caracterização morfológica dos eletrodos. A performance eletroquímica dos eletrodos nanoestruturados foi investigada por voltametria cíclica. A capacitância dos capacitores simétricos foi medida pelo método da carga descarga. O uso de diferentes complexantes resultou na formação de nanoestruturas com diferentes morfologias. Os voltamogramas mostraram bandas características de reações faradaicas, próprias de pseudocapacitores. Os resultados de capacitância indicam mostram que os fatores de maior influência para a capacitância foram a massa depositada e a morfologia da nanoestrutura de ZnO.

PALAVRAS-CHAVE: Supercapacitores. Métodos químicos. ZnO. Nanoestruturas.

GREEN SYNTHESIS OF ZnO NANOSTRUCTURED ELECTRODE FOR SUPERCAPACITOR

ABSTRACT: The electrical double layer capacitor (EDLC) has been extensively investigated for its many applications in electric and electronic devices, due to high power density and long-life cycle. Zinc oxide (ZnO) is a promising candidate for the electrochemical supercapacitor electrode. ZnO is well known to be an active battery material with a high energy density of about 650 A g^{-1} , but it has the disadvantage of dendrites formation during consecutive cycling, which decreases life cycle. In this paper, we report a relatively straightforward, environmentally friendly and low-cost method for preparing ZnO electrodes that consists in two steps. Starting with a ZnO seed layer onto a steel substrate employing the successive ionic layer adsorption and reaction (SILAR) method. Subsequently, a chemical deposition bath (CBD) was used for the nanostructured ZnO growth. A low temperature SILAR method was used in this study, replacing high temperature and vacuum methods, such as chemical vapor deposition or sputtering, to create an interface region between the conductive steel current collector and the nanostructured ZnO electrode. Scanning electronic microscopy has been employed in the characterization of the two-step produced nanostructured ZnO electrodes. The electrochemical performance of the nanocomposite electrodes has investigate using cyclic voltammetry. Capacitance was measured by charge-discharge curve. Different complex ions result in morphologies with different aspects. Cyclic voltammetry exhibited a broad redox peak indicative of typical reversible redox reaction responsible for the faradaic reactions in the supercapacitor. These results indicated indicating that de mass and morphologies were influenced in the capacitance.

KEYWORDS: Nanostructure. ZnO. Chemical method. SILAR. Supercapacitor.

1 INTRODUÇÃO

A quantidade de estudos empregando materiais abundantes, baratos, atóxicos e ecológicos, para fins de armazenamento de energia elétrica tem aumentado

significativamente nestes últimos anos. Dentro deste contexto, o ZnO, além de apresentar as características descritas acima, possui propriedades físicas que o torna um material promissor para emprego em: lasers na faixa do ultravioleta, diodos foto-emissores, diodos fotossensíveis, transdutores e atuadores piezoelétricos, armazenadores de hidrogênio, sensores químicos e bioquímicos, guias de ondas acústicas, células fotovoltaicas e supercapacitores (Conte, 2010; Lau et al., 2017).

Este amplo campo de aplicação do ZnO decorre das propriedades físicas e químicas, tais como: *band gap* de 3,37 eV, energia de ligação de 60 MeV e polarização espontânea de $-0,57 \text{ C/m}^2$, condutividade elétrica de até $5 \cdot \text{cm}^{-1}$, alta densidade de energia $650 \text{ A}\cdot\text{h}\cdot\text{g}^{-1}$ (Wang, 2004; Zhang, 2009; DING, 2014). O ZnO apresenta outra característica importante: devido a sua estrutura cristalina ser hexagonal é possível obtê-lo com características nano-morfológicas variadas.

A estrutura cristalina do ZnO pode ser descrita como o empilhamento de tetraedros coordenados por átomos de Zn^{2+} e O^{2-} ao longo do eixo *c* de uma estrutura hexagonal. A estrutura do ZnO não é centrossimétrica, resultando em um óxido piezoelétrico e piroelétrico. Outra importante característica do ZnO é possuir superfícies polares, que permitem a adesão superficial por meio de ligações de Van der Waals, sendo a mais comum destas superfícies os planos basais. A oposição dos íons nestes planos produz superfícies carregadas positivamente ($\text{Zn}-(0001)$) e negativamente ($\text{O}^-(000\bar{1})$), resultando em um momento de dipolo e na polarização espontânea ao longo do eixo *c*, assim como um divergente na superfície de energia (Wang, 2004).

Devido às características de sua estrutura cristalina, o ZnO possui três direções preferenciais de crescimento: $(01\bar{1}0) (\pm[01\bar{1}0], \pm[10\bar{1}0], \pm[1\bar{1}00])$ e $\pm[0001]$. Além destas direções preferenciais é possível, a partir do controle da taxa de crescimento das superfícies polares, promover várias outras direções de crescimento dos cristais.

O emprego de materiais nanoestruturado tem sido pesquisado para uso em supercapacitores do tipo pseudocapacitores (Yu et al., 2014; Zhang et al., 2009). Os pseudocapacitores armazenam cargas através de rápidas reações reversíveis de superfície ou reações do tipo redox próxima à superfície do material. Como essas reações redox geralmente ocorrem em óxidos metálicos, onde os íons metálicos possuem múltiplos estados de valência, óxidos como: MnO_2 , NiO_x , e CoO_x são excelentes candidatos para o emprego na construção dos pseudocapacitores.

Zhang et al (2009a) pesquisaram supercapacitores compostos por nanotubos de carbono impregnados com ZnO nanoestruturado como eletrodos, conseguindo capacitores de até $323,9 \text{ F g}^{-1}$. Os mesmos autores substituíram o grafeno obtendo capacitâncias da ordem de $11,3 \text{ F g}^{-1}$.

Sdihu e Rastogi (2014) estudaram supercapacitores planares empregando o ZnO do tipo nanotubo como nucleador de poli-pirrole (um tipo de polímero orgânico condutor). Segundo os autores as capacitâncias conseguidas foram na ordem de 130 mF cm^{-2} .

A síntese de nanoestruturas de ZnO para emprego em supercapacitores é realizada por diversos métodos. Alguns destes métodos são de alto custo, além de não se caracterizarem como técnicas de baixo impacto ecológico. Ou de menor custo são estudados objetivando a obtenção de nanoestruturas de alto desempenho (Haldorai, Voit, Shim, 2015; Raj et al., 2017).

A deposição por banho químico ou CDB (*chemical bath deposition*) é um método barato e simples para a obtenção de nanoestruturas de ZnO, o que o torna um método ecologicamente correto. Entretanto, a adesão de filmes nanoestruturados obtidos por CBD apresentam pouca aderência ao substrato, esta dificuldade foi sanada pelo crescimento de uma camada semente, em geral, utilizando técnicas com alta temperatura e alto vácuo, com a desvantagem destas técnicas serem mais agressivas ao meio ambiente.

A utilização do método SILAR (*Sucessive Ionic Layer Adsorption and Reaction*), que consiste na adsorção dos cátions em um CDB e a reação de formação do composto alvo em outro banho químico. Galego et al (2013) desenvolveram uma adaptação do método SILAR para crescimento de sementes de ZnO utilizando dois banhos catiônicos resultando em uma camada densa e aderente.

Os métodos SILAR/CBD em conjunto apresentam-se como uma rota simples, econômica e ecologicamente correta para a obtenção de eletrodos de ZnO.

Este estudo objetiva avaliar a influência do tipo de substrato na morfologia da semente e a influência de agentes complexantes no CDB na formação de filmes nanoestruturados. Estes eletrodos foram utilizados na montagem de supercapacitores simétricos e caracterizado suas propriedades elétricas.

2 MÉTODOS EXPERIMENTAIS

2.1 ELETRODOS

A composição química dos substratos, aço inoxidável 304 AISI e alumínio AA-1050, foi determinada por fluorescência de raios X, empregando-se o método dos parâmetros fundamentais (EDX-720, Shimadzu). As fases cristalinas presentes foram identificadas por difração de raios X utilizando radiação Cu - $K\alpha$ (PW1700, Philips).

Ao substrato pré-preparado para a elaboração do eletrodo foi adicionando um terminal de fio de Ni-Cr, através do processo de solda ponto, para futura aplicação e realização de medidas. O conjunto foi submetido a limpeza, seguindo a seguinte

seqüência: detergente Extran®, acetona, álcool isopropílico e água bidestilada, todos em banho de ultrassom, por 180 s. Após o processo de limpeza, a superfície foi decapada mergulhando-se o substrato por 1 s em solução ácida de $\text{H}_3\text{PO}_4\text{:HNO}_3\text{:H}_2\text{O}$ na proporção 5:1:5. A face externa do eletrodo, que contém o terminal soldado, foi isolada empregando-se uma camada de tinta esmalte.

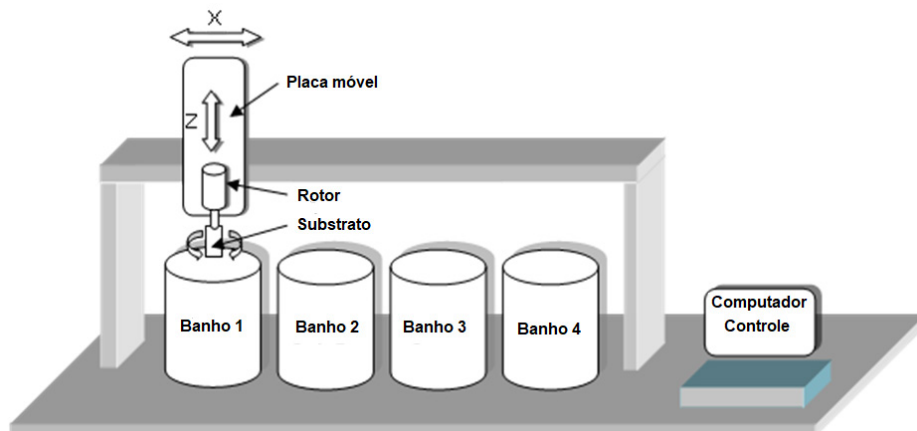
2.2 CRESCIMENTO NANOESTRUTURAS

A camada semente de ZnO foi crescida pelo método SILAR. A Tab. I mostra a seqüência, temperatura e tempo de imersão de cada banho. Para se conseguir uma boa camada de cobertura de sementes crescidas no eletrodo foi empregado 40 ciclos desta seqüência (Galego et al.,2013). O esquema do aparato empregado para efetuar os ciclos pode ser visto na Fig. 1. Após o crescimento da semente, os substratos foram mantidos na estufa por 8 h a 80 °C.

Tabela I: Seqüência utilizada pelo método SILAR, para crescimento da semente de ZnO.

Seqüência (#)	Banho (tipo)	Temperatura (K)	Tempo (s)
01	$\text{Zn}(\text{NO}_3)_2$	323	10
02	H_2O	363	5
03	Enxague (H_2O)	Ambiente	5
04	Acetato de Zn	323	40
05	H_2O	363	10
06	Enxague (H_2O)	Ambiente	5
07	Secagem (N_2)	Ambiente	20

Figura 1: Esquema do aparato utilizado para crescimento das sementes de ZnO sobre os substratos.



As diversas direções de crescimento do ZnO podem ser ativadas pelas condições do processo de crescimento. No caso dos métodos químicos, as principais

variantes são a concentração molar de íons de Zn^{2+} , a temperatura e os complexantes utilizados. Os complexantes utilizados neste estudo foram: hexametiletenotetramina ($(CH_2)_6N_4$ ou (HMT); ureia (NH_2CONH_2) e; etilenodiaminotetraacético dissódico ($(HO_2CCH_2)_2NCH_2CH_2N(CH_2CO_2H)_2$) ou (EDTA).

O crescimento das nanoestruturas de ZnO foi realizado pelo método CBD, em banho alcalino, com adição de NH_4OH . A composição mais adequada para cada um dos complexantes utilizados foi determinada por estudos anteriores. Na Tab. II são apresentadas as composições e concentrações dos complexantes utilizadas neste estudo. As amostras foram posicionadas com a face das sementes direcionadas para baixo por 8 h, sendo que os banhos foram substituídos a cada 2 h, devido a evaporação e degradação.

Tabela II: Composição química dos banhos utilizados para crescimento de ZnO nanoestrutura pelo método CBD.

Substrato – complexo	Composição – concentração		
Aço – EDTA	Zn(Ac) – 20 mM	NH_4OH – 1:20	EDTA – 2 mM
Aço – HMT	Zn(Ac) – 20 mM	NH_4OH – 1:20	HMT – 40 mM
Aço – Ureia	Zn(Ac) – 20 mM	NH_4OH – 1:20	Ureia – 40 mM
Al – EDTA	Zn(Ac) – 10 mM	NH_4OH – 1:20	EDTA – 2 mM

A morfologia das nanoestruturas de ZnO foram observadas por microscopia eletrônica de varredura convencional (XL-30, Philips) e por emissão de campo (JSM 6510, Jeol).

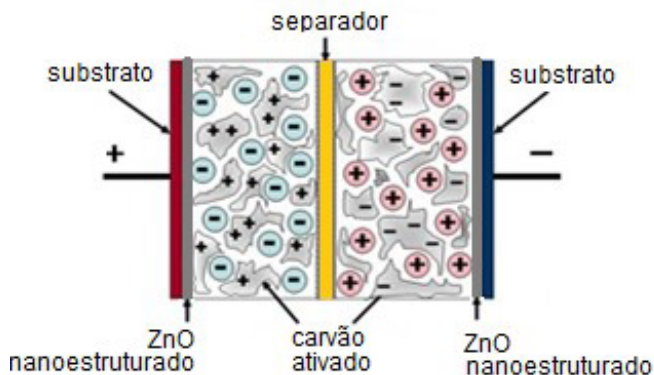
A voltametria cíclica (SP-50, BioLogic) foi utilizada para a caracterização do comportamento eletroquímico do substrato metálico recoberto com a nanoestrutura de ZnO. Os parâmetros eletroquímicos utilizados foram: a) eletrodo de referência: Ag/AgCl; b) velocidade de varredura: 50 mV s^{-1} e; c) solução do eletrólito: 0,1 M de Na_2SO_4 .

2.3 SUPERCAPACITOR

Os supercapacitores foram montados de modo simétrico (Chui et al., 2014) onde cada um dos eletrodos foi montado com o substrato/ZnO nanoestruturado e uma camada adicional (carvão ativado). Uma vez montados compuseram o dielétrico do supercapacitor. Esta camada adicional foi composta por: 100 mg de carvão ativado; 12,5 mg de negro de fumo e 40 mg de politetrafluoretileno (PTFE). A mistura foi homogeneizada e separada em duas porções com mesma massa. Em seguida foram prensadas com uma matriz de diâmetro menor que o do eletrodo, com uma pressão de 1000 Kg cm^{-2} por 5 min. Para o separador foi utilizado papel de filtro do tipo quantitativo. Um esquema da montagem

do supercapacitor pode ser vista na Fig. 2. Para garantir a integridade da montagem foi utilizado uma pinça isolante que manteve pressão suficiente para um contato elétrico. Em seguida, a montagem foi mergulhada em um eletrólito de Na_2SO_4 a 0,1 M. As medidas elétricas foram feitas depois de decorridos 12 horas dentro do eletrólito.

Figura 2: Esquema da montagem do supercapacitor.



O método de carga e descarga foi utilizado para determinação da capacitância. O ciclo consiste em: carga sob corrente constante até chegar no valor nominal de tensão, platô de tempo de estabilização e descarga sob corrente constante. A medida foi realizada na descarga anotando-se tempo decorrido entre de 80% e 40% do valor da tensão obtida na carga após o platô.

A equação (1) foi utilizada para o cálculo da capacitância:

$$C_{SD}(F) = I_{const}(A) \cdot \frac{\Delta t(s)}{\Delta v(V)} \quad (1)$$

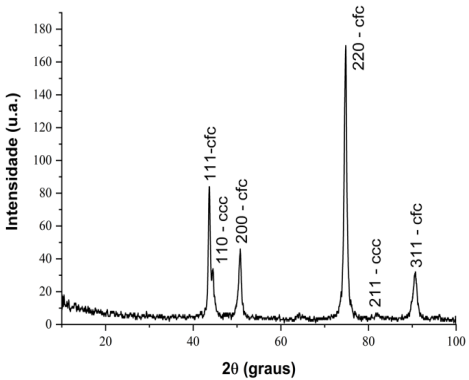
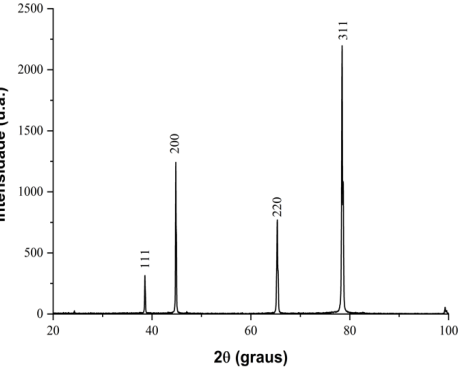
onde: C_{SD} é capacitância; I_{const} é a corrente constante utilizada na descarga; Δt é o tempo decorrido e Δv a variação de tensão.

Para a medida foi utilizada uma corrente constante de 1 mA, tanto para carga como para descarga. O platô foi de 30 min e tensão nominal para carga de 1 V (Andreas, 2014).

3 RESULTADOS

As condições superficiais dos substratos são cruciais para a formação de uma camada semente densa e bem aderida aos substratos. A Tab. III apresenta as características dos substratos utilizados na elaboração dos eletrodos aqui estudados.

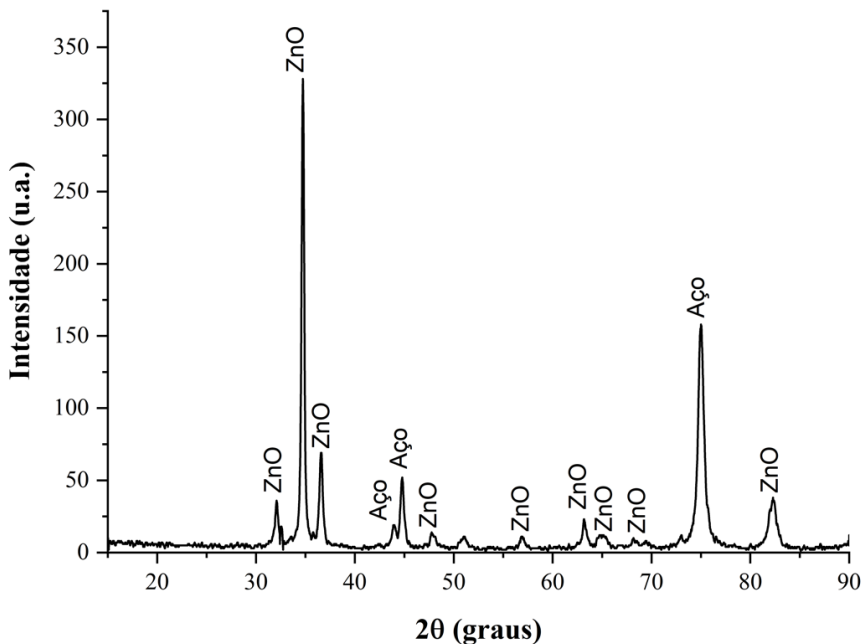
Tabela III: Características dos substratos utilizados para preparo de eletrodos com de ZnO nanoestruturado.

Material	Composição química (% em peso)	Estrutura cristalina	Espectro de difração de raios X
Aço	Fe – 71,60 Cr – 18,28 Ni – 8,74 Mn – 1,38 S – 0,02	FCC/BCC	 <p>The XRD pattern for the steel substrate shows several diffraction peaks. The y-axis is labeled 'Intensidade (u.a.)' and ranges from 0 to 180. The x-axis is labeled '2θ (graus)' and ranges from 20 to 100. The peaks are labeled as follows: 110 - ccc (at ~45°), 111 - cfc (at ~48°), 200 - cfc (at ~50°), 211 - ccc (at ~78°), 220 - cfc (at ~75°), and 311 - cfc (at ~90°).</p>
Alumínio	Al – 99,59 Fe – 0,37 Ti – 0,03 Zn – 0,02	FCC	 <p>The XRD pattern for the aluminum substrate shows four distinct diffraction peaks. The y-axis is labeled 'Intensidade (u.a.)' and ranges from 0 to 2500. The x-axis is labeled '2θ (graus)' and ranges from 20 to 100. The peaks are labeled as follows: 111 (at ~38°), 200 (at ~45°), 220 (at ~65°), and 311 (at ~78°).</p>

Uma característica dos metais laminados, caso dos metais utilizados neste estudo, é a presença de orientação preferencial de determinados planos cristalinos. Os espectros de difração de raios X apresentados na Tab. III mostra que o substrato de aço apresenta as fases cúbica de corpo centrado (CCC) e cúbica de face centrada (FCC), ambas com orientação da família de planos $\langle HK0 \rangle$. No substrato de alumínio, estrutura FCC, a orientação preferencial foi observada na família de planos $\langle 311 \rangle$.

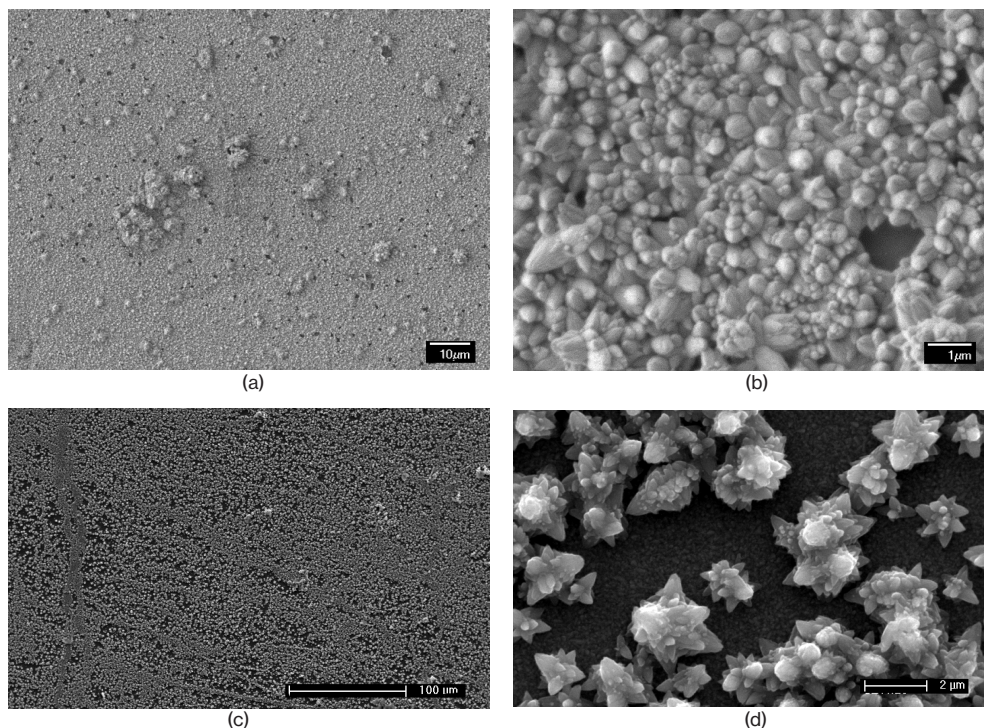
O método SILAR utilizado para o crescimento da semente de ZnO proporcionou uma interação forte entre o substrato e o ZnO e, as baixas temperaturas utilizadas nos diversos banhos foram suficientemente altas para a formação da fase cristalina hexagonal do ZnO e inibição de formação de Zn(OH)_2 , Fig. 3.

Figura 3: Espectro de difração de raios X da camada semente sobre o substrato de aço e alumínio.



A utilização de métodos químicos para crescimento de filmes finos de ZnO, principalmente com utilização de amônia, tende a promover o crescimento do ZnO na direção do plano basal da estrutura hexagonal. Entretanto, no caso da camada semente há influência da estrutura cristalina do substrato. No método SILAR, o crescimento dá-se íon por íon que tem a capacidade de acomodar, no caso a estrutura cristalina do ZnO, nas diferentes estruturas cristalinas da superfície do aço e do alumínio, pelo ajuste das diferentes direções preferenciais de crescimento do ZnO. Na micrografia, com menor aumento, Fig.4(a) e Fig. 4(c), observa-se: a) o recobrimento quase total da superfície do substrato; b) a presença de alguns aglomerados, com tamanho máximo de 10 μm pequenas e; c) áreas sem recobrimento devido a presença de ponto corroídos na superfície do substrato. Com maior aumento, Fig. 4(b) e Fig. 4(d), ficou evidente a heterogeneidade do filme de ZnO depositado, indicando que a acomodação da estrutura cristalina do ZnO nas estruturas cristalinas dos substratos favoreceu o crescimento do ZnO nas diversas direções preferenciais, com morfologia preponderante de nanorods coalescidos lateralmente.

Figura 4: Micrografia de varredura por emissão de campo da camada semente obtida pelo método SILAR utilizando HMT como agente complexante. Substrato aço: (a) menor magnificação e (b) maior magnificação. Substrato de alumínio: (c) menor magnificação e (d) maior magnificação.

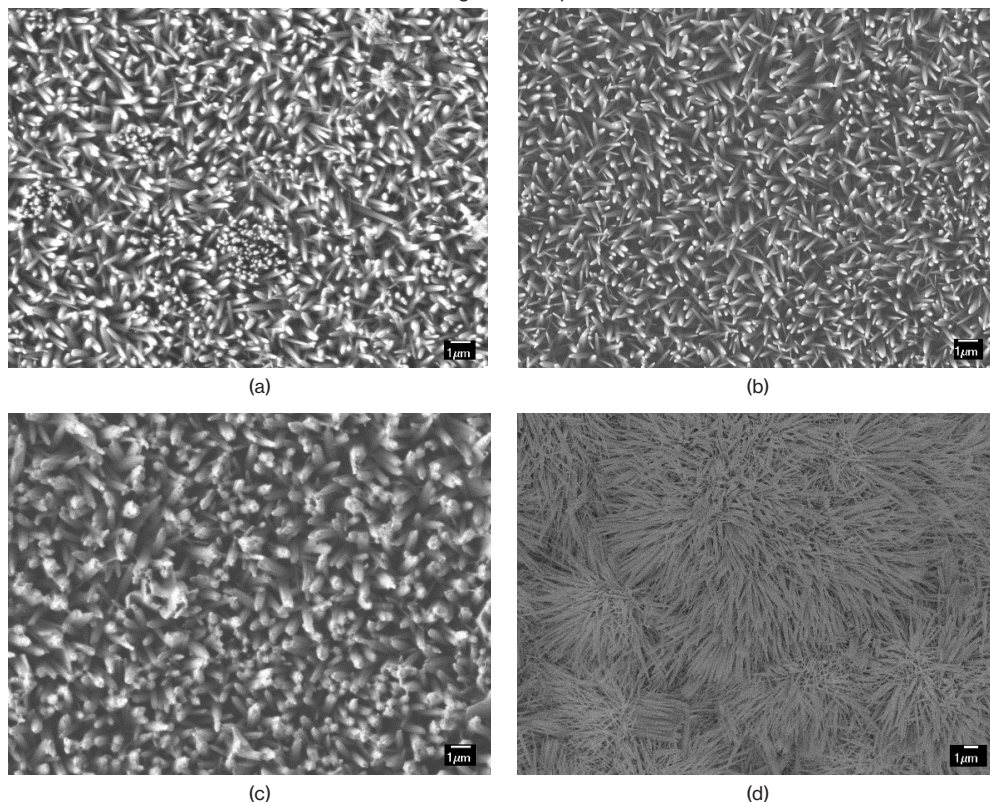


Por outro lado, sobre o substrato de alumínio o crescimento de nanoestruturas de ZnO não apresentou um crescimento com a mesma densidade observada no substrato de aço. Na Fig. 4 (d), observou-se que as nanoestruturas apresentam crescimento nas diversas direções de crescimento, com morfologia parecido com pétalas de flores.

Os filmes de ZnO nanoestruturados obtidos pelo crescimento pelo método CBD estão apresentados nas Fig. 5 (a), (b), (c) e (d). Nas micrografias apresentadas observou-se a influência da morfologia da semente comparando-se as nanoestruturas formadas sobre os substratos de aço inoxidável e alumínio. No caso, do substrato de aço inoxidável, Fig.5(a), (b) e (c), houve o predomínio da morfologia de nanobastões orientados preferencialmente em relação a direção do plano basal, observou-se também que os diferentes complexantes promoveram pequenas diferenças na morfologia. Já sobre o substrato de alumínio, Fig.5(d), a morfologia apresentada pode ser descrita como nanofios longos, que ao serem retirados do banho de crescimento e com o retorno do substrato a posição normal não se sustentaram na posição vertical. Esta morfologia pode ser atribuída a formação de uma semente com morfologia de

flores com um centro orientado da direção do plano basal e estarem distribuídas esparsamente sobre o substrato.

Figura 5: Micrografia, obtida por microscopia de varredura de elétrons, dos filmes nanoestruturados crescidos por CDB sobre diferentes substratos e com diferentes agentes complexantes.

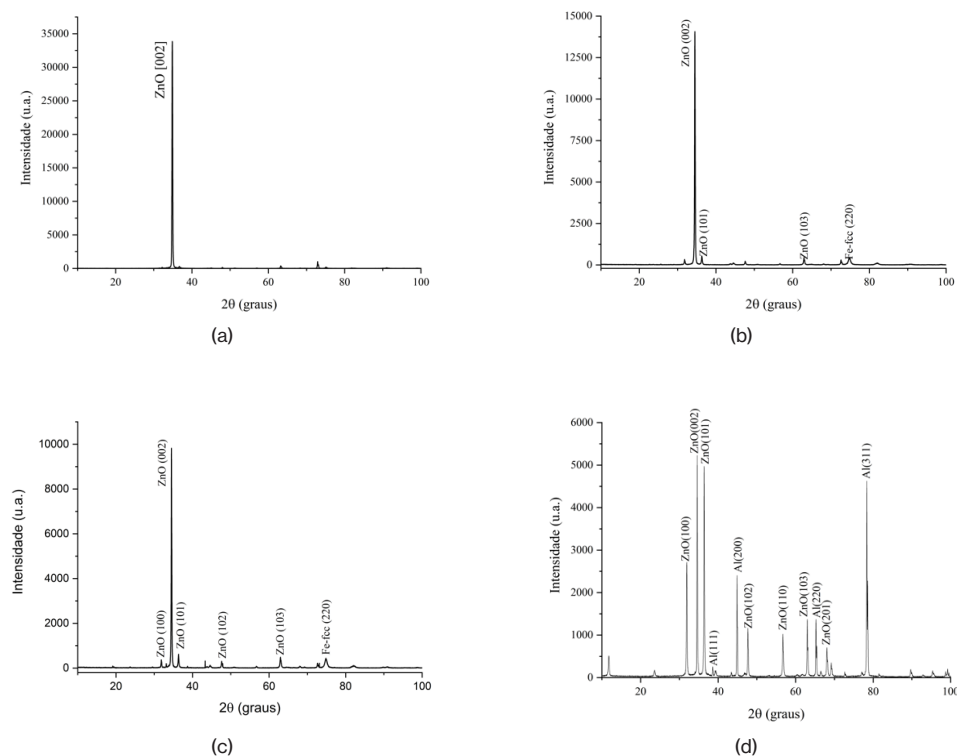


A densidade superficial de ZnO nanoestruturado formado, também, foi influenciada pelos complexantes no crescimento do filme por CDB. Os valores da massa depositada foram calculados pelo método da camada depositada por fluorescência de raios X, que estão apresentados na Tab. IV.

Tabela IV: Massa de ZnO depositada segundo o complexante.

Complexante	Massa de ZnO ($\mu\text{g}/\text{cm}^2$)
Aço - EDTA	1192,0
Aço - HMT	578,0
Aço - ureia	476,6
Al - EDTA	1443,6

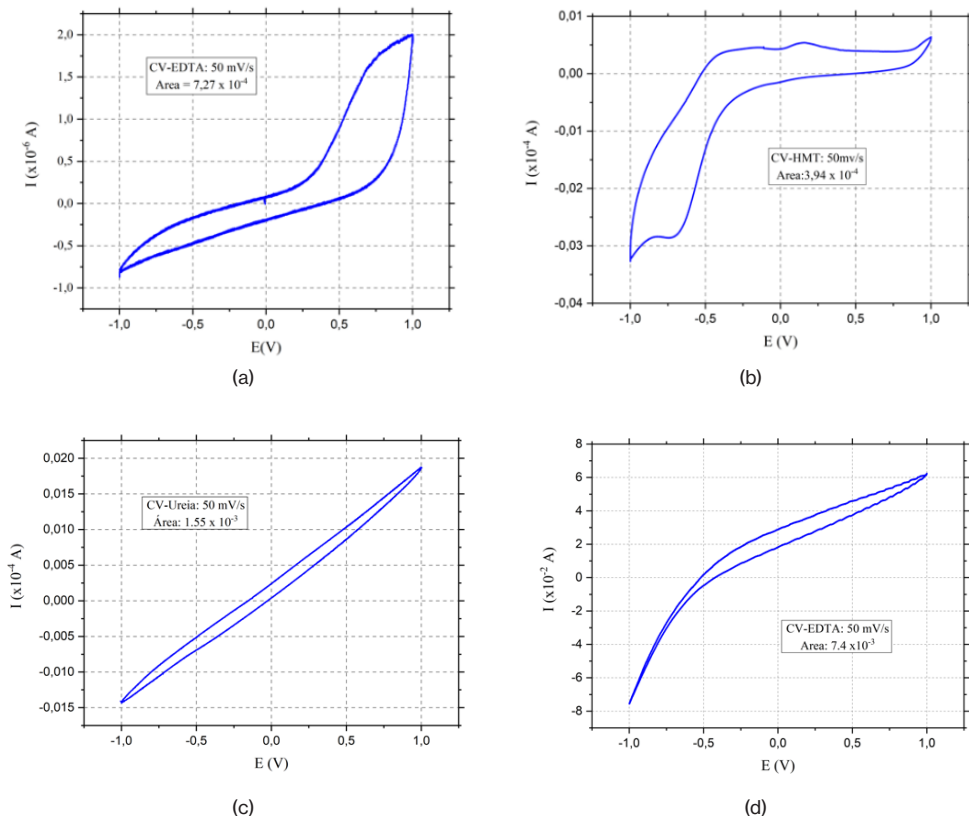
Figura 6: Espectros de difração de raios X obtidos com radiação de Cu K α dos filmes nanoestruturados obtidos com diferentes agentes complexantes: (a) aço - EDTA, (b) aço - HMT, (c) aço - ureia e (d) alumínio - EDTA.



Observa-se nos espectros de raios X dos substratos de aço inoxidável, Figs: 6 (a), 6 (b) e 6 (c), a alta intensidade do pico referente a direção do plano basal (002) da estrutura cristalina do ZnO, indicando forte orientação preferencial, também, observada nas micrografias. Nota-se, entretanto, a presença de outras reflexões nas Figs: 6 (b) e 6(c), considerando-se as massas depositadas, há um forte indicativo que próximo ao substrato ocorreu um crescimento de maior aleatoriedade que posteriormente coalesce e predomina o crescimento na direção do plano basal (002). Quanto a Fig. 6 (d), substrato de alumínio, a quantidade de massa depositada e ausência de uma orientação preferencial corroboram a hipótese sugerida acima. Como observado, houve a formação de nanofios de ZnO finos e longos o suficiente para inclinar-se ao ser retirado do CBD, dando o formato, como observado, de tufo de grama, explicando a orientação preferencial do plano basal (002) mesmo que esta não seja tão predominante como a observada nos substratos de aço inoxidável.

As características elétricas do conjunto substrato com ZnO nanoestruturado depositado foram avaliadas por voltametria cíclica. Os voltamogramas, medidos nas condições informadas na secção 2.2, estão apresentados nas Fig. 7 (a), (b), (c) e (d).

Figura 7: Voltamogramas obtidos para o conjunto substrato/ZnO obtidos por CBD com agentes complexantes: (a) EDTA; (b) HMT, (c) ureia e (d) substrato de alumínio.



Nos pseudocapacitores a energia é armazenada na dupla camada de Helmholtz e por reações de oxirredução nos eletrodos e suas proximidades. A forma dos voltamogramas apresentados nas Fig. 7 (a), (b), (c) e (d), indica o carácter pseudocapacitivo dos conjuntos estudados devido a presença de reações eletroquímicas (Lee et al., 2021; Guerra, 2019).

A Tab. V apresenta a avaliação dos supercapacitores, montados conforme seção 2.3.

Tabela V: Capacitância medida pelo método da carga/descarga.

Complexante	Massa total (g·10 ⁻³)	Capacitância C _{SD} (F)	Capacitância por massa (F·g ⁻¹)
Aço - EDTA	151,77±0,05	0,5±0,1	3,1±0,1
Aço - HMT	149,80±0,05	5,1±0,1	33,9±0,1
Aço - ureia	150,08±0,05	2,4±0,1	16,2±0,1
Al - EDTA	148,70±0,05	3,0±0,1	20,1±0,1

4 CONCLUSÕES

Os resultados mostraram que a morfologia das sementes foi influenciada pela estrutura cristalina do aço inoxidável e do alumínio; esta influência se reflete nas nanoestruturas crescida por CBD.

Os complexantes estudados promoveram crescimento de estruturas morfologicamente semelhantes; porém, voltametria cíclica mostrou um comportamento eletroquímico diferente para as morfologias obtidas com diferentes complexantes.

A influência na capacitância medida apresentou maiores diferenças; para o substrato de aço os maiores valores de capacitância foram obtidos para os eletrodos com menor massa de ZnO (Tab. IV) e com menor orientação preferencial obtidos utilizando HMT e ureia. O EDTA promoveu o maior crescimento e com maior orientação preferencial, porém com baixa capacitância. Para o substrato de alumínio com o crescimento de menor orientação preferencial e com massa semelhante ao do aço-EDTA, a capacitância foi da ordem dos supercapacitores de HMT e de ureia, isto é, com uma ordem de grandeza maior. Estes resultados mostram que os fatores de maior influência para a capacitância foram a massa depositada e a morfologia da nanoestrutura de ZnO.

Vale ressaltar que, os valores de capacitância obtidos neste estudo são menores que os habitualmente reportados na literatura. Entretanto, a capacitância depende das características do eletrodo e do eletrólito. A proposta deste trabalho foi o estudo do emprego de materiais amigáveis ao meio ambiente. Assim como o ZnO, o eletrólito utilizado na caracterização elétrica, sulfato de sódio, é o reagente químico de maior produção mundial, atóxico e biocompatível. Valores maiores de capacitância (Tab. V) poderiam ser obtidos caso fosse aumentada a concentração molar do eletrólito Na_2SO_4 ou empregando-se eletrólitos como, por exemplo, o hidróxido de potássio (KOH) que tem características eletroquímicas superiores ao sulfato de sódio, com a desvantagem de ser mais agressivo ao meio ambiente.

REFERÊNCIAS

ANDREAS, H. Measurement techniques for performance evaluation on supercapacitor materials and systems. In **Nanostructured ceramic oxides for supercapacitor applications**. Ed: Balakrishnan, A.; Subramanian, K.R.V. Chapter 4, CRC Press, 71-118, 2014.

CONTE, M. Supercapacitors technical requirements for new applications. **Fuel Cells**, v.10, n.5, p.806-818, 2010.

GALEGO, E.; SERNA, M.M.; RAMANATHAN, L.V. A new route to grow ZnO seed layer using SILAR method. **Technical Proceedings of the 2013 NSTI Conference and Expo, NSTI-Nanotech 2013**, v. 03, p.509-512, 2013.

GUERRA, A.; ACHOUR, A.; VIZIREANU, S.; DINESCU, G.; MESSACI, S.; HADJERSI, T.; BOUKHERROUB, R.; COFFINIER, Y.; PIREAUX, J.-J. ZnO/Carbon nanowalls shell/core nanostructures as electrodes for supercapacitors. **Applied Surface Science**, v.481, p.926-932, 2019.

HALDORAI, Y.; VOIT, W.; SHIM, J.-J. Nano ZnO@reduced graphene oxide composite supercapacitor: Green synthesis in supercritical fluid. **Electrochimica Acta**, v.120, p.65-72, 2014.

KIM, B.C.; HONG, J.-Y.; WALLACE, G.G.; PARK, H.S. Recent progress in flexible electrochemical capacitors: electrode materials, device configuration, and functions. **Advanced Energy Materials**, v.5, p.1500959 (1-33), 2015.

RAJ C.J.; RAJESH, M.; MANIKANDAN, R.; SIM, J.Y.; YU, K.H.; PARK, S.Y.; SONG, J.H.; KIM, B.C. Two-dimensional planar supercapacitor based on zinc oxide/manganese oxide core/shell nano-architecture. **Electrochimica Acta**, v.247, p.949-957, 2017.

LAU, S.C.; LIM, H.N.; RAVOOL, T.B.S.A.; YAACOB, M.H.; GRANT, D.M.; MACKENZIE, R.C.I.; HARRISON, I.; HUANG, N.M. A three-electrode integrated photo-supercapacitor utilizing graphene-based intermediate bifunctional electrode. **Electrochimica Acta**, v.238, p.178-184, 2017.

LEE, K.S.; PHIRI, I.; PARK, J.H.; KO, J.M.; KIM, S.H. Novel structure of bacteria doped ZnO particles: Facile and green synthesis route to prepare hybrid material for supercapacitor electrodes. **Journal of Industrial and Engineering Chemistry**, in press, 2021.

SIDHU, N.K.; RASTOGI, A.C. Vertically aligned ZnO nanorod core-polypyrrole conducting polymer sheath and nanotube arrays for electrochemical supercapacitor energy storage. **Nanoscale Research Letters**, v.9:453, 2014.

WANG, Z.L. Zinc oxide nanostructures: growth, properties and applications. **Journal of Physics: Condensed Matter**, v.16, p.R829-R858, 2004.

YU, Z.; TETARD, L.; ZHAI, L.; THOMAS, J. Supercapacitor electrode materials: nanostructures from 0 to 3 dimensional. **Energy & Environment Science**, v.8, n.3, p.702-730, 2015.

ZHANG, Q.; DANDENEAU, C.S.; ZHOU, X.; CAO, G. ZnO nanostructures for dye-sensitized solar cells. **Advanced Material**, v.21, p.4087-4108, 2009.

ZHANG, Y.; LI, H.; PAN, L.; LU, T.; SUN, Z. Capacitive behavior of graphene-ZnO composite film for supercapacitors. **Journal of Electroanalytical Chemistry**, v.634, p.68-71, 2009.

ZHANG, Y.; SUN, X.; PAN, L.; LI, H.; SUN, Z.; SUN, C.; TAY, B.K. Carbon nanotube-ZnO nanocomposite electrodes for supercapacitors. **Solid State Ionics**, v.180, p.1525-1528, 2009a.

CHAPTER 16

MORFOLOGIA DE FILMES FINOS NANOESTRUTURADOS DE ZnO PRODUZIDOS PELO MÉTODO SILAR

Data de submissão: 05/04/2021

Data de aceite: 26/04/2021

Rubens Nunes de Faria Junior

Comissão Nacional de Energia Nuclear
Instituto de Pesquisas Energéticas e
Nucleares
Centro de Ciências e
Tecnologia dos Materiais
São Paulo – SP
<http://lattes.cnpq.br/8776524631256060>

Eguiberto Galego

Comissão Nacional de Energia Nuclear
Instituto de Pesquisas Energéticas e
Nucleares
Centro de Ciências e
Tecnologia dos Materiais
São Paulo – SP
<http://lattes.cnpq.br/4818030985379074>

Marilene Morelli Serna

Comissão Nacional de Energia Nuclear
Instituto de Pesquisas Energéticas e
Nucleares
Centro de Ciências e
Tecnologia dos Materiais
São Paulo – SP
<http://lattes.cnpq.br/7397656667247795>

Lalgudi Venkataraman Ramanathan

Comissão Nacional de Energia Nuclear
Instituto de Pesquisas Energéticas e
Nucleares
Centro de Ciências e
Tecnologia dos Materiais
São Paulo – SP
<http://lattes.cnpq.br/2938011667744143>

RESUMO: A utilização do ZnO no campo da nanotecnologia é ampla devido a características físicas únicas tais como, banda proibida (~3,37 eV), energia de ligação de éxciton de 60 MeV, atóxico e de baixo custo. A estrutura cristalina hexagonal permite obter uma ampla diversidade de morfologias e isto permite sua utilização em: lasers de UV, cristais piezoelétricos, sensores químicos, sensores de gás, diodos emissores de luz, foto detectores e células solares. Uma das possíveis morfologia do filme fino de ZnO é um arranjo unidimensional submicrométrico de bastões, nanobastões e nanofios, o qual tem atraído muito interesse devido a alta área superficial e a alta proporção de aspecto, que são nanopartículas com um comprimento muitas vezes maior do que sua largura. Neste trabalho foi estudada a influência dos parâmetros do método de adsorção de camada iônica e reação sucessivas (SILAR) na obtenção de filmes de ZnO nanoestruturados sobre substrato

de vidro recoberto com óxido de estanho dopado com flúor ($\text{SnO}_2\text{:F}$). Na temperatura de 90°C ocorreu a formação de ZnO e o aumento de nanoestruturas formadas. A quantidade de ciclos é responsável pela densidade superficial, o crescimento acelera-se após se atingir a densidade superficial crítica. O tempo de permanência no banho de nucleação não tem influência significativa, já no banho de crescimento com o aumento do tempo ocorreu coalescimento das nanoestruturas. O uso do cloreto de zinco como precursor no banho de nucleação apresentou crescimento mais lento para concentrações molares baixas, o aumento da concentração molar resultou em filmes porosos. Os resultados obtidos neste estudo mostraram que alterações simples nas variáveis do processo SILAR para obtenção de ZnO permitiram desde a obtenção de nanoestruturas individuais a filmes compactos ou porosos.

PALAVRAS-CHAVE: Óxido de zinco. SILAR. Nanoestruturas. Filmes finos. DSSC.

MORPHOLOGY OF NANOSTRUCTURED THIN FILMS OF ZnO FABRICATE FROM SILAR METHOD

ABSTRACT: The utilization of ZnO in the nanotechnology is widely spread due its superior properties, such as wide direct band gap (~ 3.37 eV), high exciton binding energy of 60 meV, non-toxicity and low cost. The hexagonal crystalline structure allows obtaining a large diversity morphology and this allows its utilization in: UV lasers, piezoelectric crystal, chemical sensor, gas sensor, light emitting diode, photo detectors, and solar cells. One such morphology of ZnO thin film is the one-dimensional (1D) sub-micron rods or nanorods and nanowires which has attracted interest due to a large surface area and high aspect ratio. In the solar area the ZnO has been utilized in the electrode for dye-sensitized solar cell. In this study, ZnO nanostructured thin films were prepared by successive ionic layer adsorption and reaction (SILAR) method, on $\text{SnO}_2\text{:F}$ coated glass substrate. In this procedure, the substrate is immersed in successive aqueous baths containing zinc nitrate or zinc chloride/HMT and zinc acetate. The pH solution was adjusted by addition of ammonium hydroxide. ZnO is formed at temperature of 90°C and large nucleus on the substrate. The time in the nucleation bath has no significant influence, whereas in the growth bath with the increase in time, the nanostructures coalesced. The use of zinc chloride as a precursor in the nucleation bath showed a slower growth at low molar concentrations, the increase in the molar concentration resulted in porous films. The results obtained in this study showed that simple changes in the SILAR process variables to obtain ZnO allowed from obtaining individual nanostructures to compact or porous films.

KEYWORDS: Zinc oxide. SILAR. Nanostructure. Thin film.

1 INTRODUÇÃO

O ZnO é um semicondutor do tipo n com excelentes características físicas e químicas, tais como: banda proibida (*band gap*) de 3,37 eV, energia de ligação de éxciton de 60 meV, resistividade controlável na faixa de 10^{-3} a $10^5 \Omega$, alta mobilidade $200 \text{ cm}^2 \text{ V}^{-1} \text{ s}^{-1}$, estabilidade eletroquímica, atóxico, grande abundância na natureza. Estas características têm permitido seu emprego em: células solares sensibilizadas por corante (DSSC,

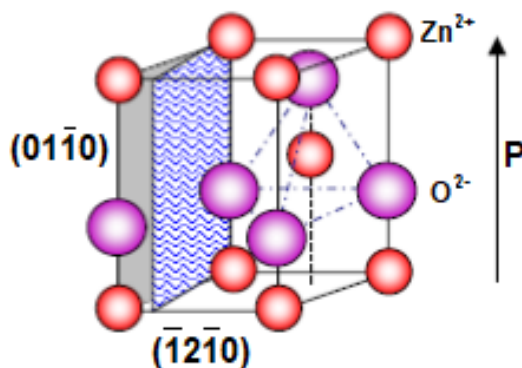
Dye Sensitized Solar Cell), filmes condutores transparentes, sensores de gás, material luminescente, transdutores, biosensores, detectores de ultravioleta, diodos emissores de ultravioleta, lasers semicondutores (Cheng, Chen, Lee, 2006; Wang, 2004).

No estado estequiométrico o ZnO apresenta alta resistividade, porém a vacância de átomos de oxigênio na rede cristalina produz um semicondutor natural do tipo n. Semicondutores do tipo p, obtidos a partir da incorporação de outra espécie atômica, têm sido estudados, porém sua obtenção e aplicação ainda são raras (Khranovskyy e Yakimova, 2012).

A estrutura hexagonal, do ZnO é semelhante à da wurtzita (grupo espacial C6mc) com parâmetros de rede da ordem de $a = 0.3296$ nm e $c = 0.52065$ nm. Esta estrutura pode ser descrita como o empilhamento alternado, em relação ao eixo c, de tetraedros de Zn^{2+} e O^{2-} (Fig.1), este arranjo resulta em uma estrutura não centro simétrica com faces polares e não polares. A presença de faces polares em cristais cria um momento de dipolo na estrutura resultando em um divergente da energia superficial, que para o emprego na DSSC favorece a adesão do corante por meio de ligações de Van der Walls. Entretanto, em cristais com faces polares a estabilidade, em geral, é obtida pela reconstrução ou faceting da superfície do cristal. Porém, o ZnO é um óxido que não apresenta esta característica, o que permite melhor controle sobre a morfologia dos cristais no crescimento (Wang, 2004).

O ZnO possui os planos basais polares, sendo o plano (0001) formado por íons de Zn^{2+} , enquanto o plano (000 $\bar{1}$) formado é por íons de oxigênio, resultando em um momento de dipolo e polarização espontânea ao longo do eixo “c” devido a alta energia destes planos. Os planos de menor energia são: $\{2\bar{1}\bar{1}0\}$ e $\{01\bar{1}0\}$ (Wang, 2004).

Figura 1: Esquema representativo da estrutura cristalina do ZnO (WANG, 2004).



O controle dos parâmetros experimentais durante o crescimento permite obter morfologias como: flores simples (*single flowers*) (Mane et al, 2008; Jiménez-Garcia et al, 2011; Gao et al, 2008), nanobastões (*nanorods*) (Tak e Yong, 2005; Wu et al, 2008), nanofios (*nanowires*) (Law et al, 2005), pirâmides (*pyramidal*), nozes ovaladas (*ground-nut-shaped*)

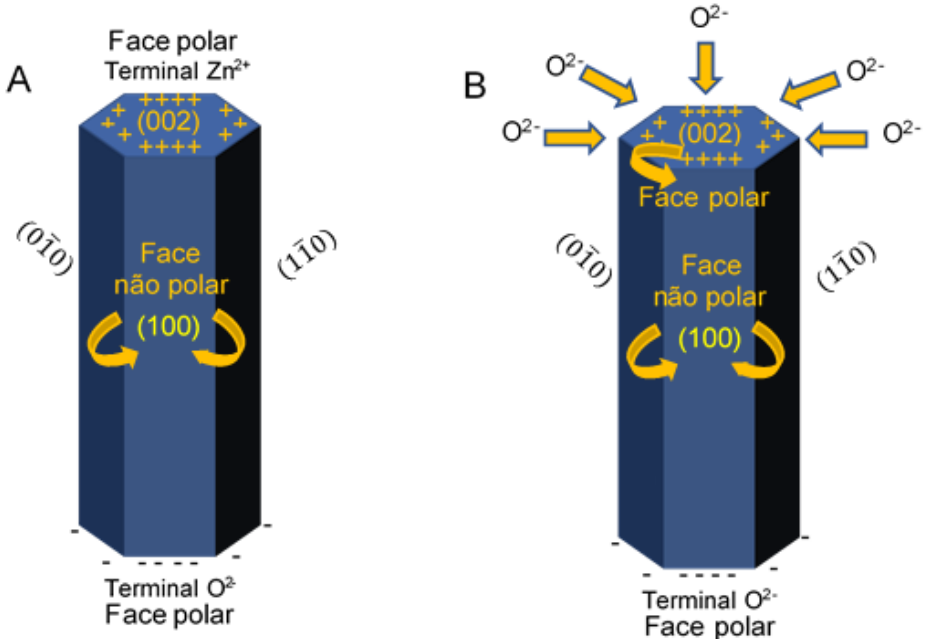
(Kanmani, 2012), raios de sol (*starburst*) (Lockett et al, 2012), nanoplacas (*nanosheets*) (Wang, Xie e Zeng, 2005), flores de arroz (*rice-like*) e nanoespinhas (*nanospines*), prestando-se cada uma destas morfologias a um tipo determinado de aplicação.

As faces polares são energeticamente instáveis e não podem existir sem um mecanismo de redistribuição das cargas superficiais que permita o abaixamento da energia livre. As faces polares podem ser estabilizadas por: (1) reconstrução da superfície ou *faceting*; (2) transferência de cargas entre superfícies (relaxação); ou (3) formação de superfícies não estequiométricas: por formação de vazios ou adsorção de moléculas (Greene et al, 2005).

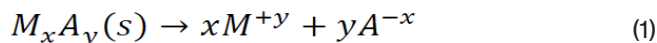
A instabilidade das faces polares (Fig.2A) promove a adsorção dos íons a estas faces (Fig.2B) resultando no aumento da taxa de crescimento ao longo da direção (002). Consequentemente, o controle da velocidade de crescimento ao longo desta direção é a chave para o controle da morfologia deste óxido; o ZnO possui três direções de crescimento preferenciais que podem ser controladas: $\pm [0001]$, $(2\bar{1}\bar{1}0)$ ($\pm[2\bar{1}\bar{1}0]$, $\pm[\bar{1}2\bar{1}0]$, $\pm[\bar{1}\bar{1}20]$) e $(01\bar{1}0)$ ($\pm[01\bar{1}0]$, $\pm[10\bar{1}0]$, $\pm[1\bar{1}00]$) (Gurav et al, 2011).

O uso de agentes complexantes, associado a existência de faces polares e não polares, permitem favorecer o crescimento orientado em diversas direções cristalográficas. Os íons complexos ligam-se, preferencialmente, as faces polares em detrimento das não polares que tendem a se ligar aos agentes quelantes não polares.

Figura 2: Esquema das superfícies polares e apolares da estrutura cristalina do ZnO [adaptado de Gurav et al, 2011].



Nos métodos de crescimento químicos em soluções aquosas a formação de fase sólida ocorre quando o produto iônico é maior que o produto de solubilidade. Assim sendo, no caso de um sal metálico temos inicialmente a dissolução do mesmo:



em uma solução em equilíbrio:

$$K' = \frac{[M]^x[A]^y}{[M_xA_y]} \quad (2)$$

como a concentração de uma substância em fase sólida pura é constante:

$$K'[M_xA_y] = [M]^x[A]^y \quad (3)$$

escrevendo:

$$K_{ps} = K'[M_xA_y] \quad (4)$$

o produto de solubilidade fica assim definido como:

$$K_{ps} = [M]^x[A]^y \quad (5)$$

nesta expressão o termo:

$$K_{ps} = [M]^x[A]^y \quad (6)$$

é chamado de produto iônico (Mane e Lokhande, 2000).

A condição do produto iônico para a formação de fase sólida em soluções aquosas não saturadas ocorre a partir de dois mecanismos distintos: por nucleação homogênea ou heterogênea. Na nucleação homogênea os núcleos formam-se no seio da solução, a partir da coagulação de íons complexos devido a agitação molecular. Enquanto, que a nucleação heterogênea necessita de um suporte que atuará na condensação do íon da solução pela formação de ligações químicas entre os íons superficiais do substrato e os íons em solução. Assim, é fácil perceber que a probabilidade de ocorrência da nucleação heterogênea é maior que da homogênea. Os três principais fatores que influenciam o produto de solubilidade são: temperatura, solvente e tamanho do núcleo da fase sólida.

O método de deposição de camadas sucessivas por adsorção e reação (SILAR) é uma técnica de crescimento em banho químico que pode ser considerada como um método de crescimento íon por íon ou camada por camada, assemelhando-se aos métodos de alto vácuo. Este método foi proposto originalmente por Nicolau em 1985 para o crescimento de filmes de sulfeto de zinco. Na sua proposta original, o processo básico

do método consistia na imersão do substrato em um banho químico para a adsorção dos íons de zinco sobre o substrato, seguida pela imersão do substrato em um segundo banho onde ocorria a reação química de formação do sulfeto.

Ristov et al [1987] foram os primeiros a utilizar o método para a deposição de filmes de ZnO. Reportando a importância da amônia para o aumento da taxa de crescimento e entre os sais de zinco estudados a lenta taxa de crescimento apresentada pelo cloreto de zinco.

A essência do SILAR é a obtenção de monocamadas catiônicas, deste modo o tempo de permanência do substrato imerso no banho catiônico é um dos fatores determinante para seu sucesso, conseqüentemente a automatização do método, foi descrita por Jiménez-González et al (1995), proporcionou o desenvolvimento do método com a inclusão de novas etapas no processo, tais como: lavagem entre banhos (Lokhande et al, 2014), utilização de ultrassom no banho aniônico (Gao et al, 2004, 2004(a), 2006 e 2007), ultrassom para lavagem (Kumar et al, 2008, 2010).

Portanto, o número de variáveis a serem otimizadas no SILAR é bastante elevado, tais como: temperaturas dos banhos catiônicos, aniônico e de lavagem, tempo de permanência em cada banho, seqüência e número de repetições do processo, composição dos banhos, processos de secagem. Este estudo objetivou avaliar algumas destas variáveis, como: a influência da temperatura do banho aniônico; do tempo de permanência nos banhos catiônicos; da concentração molar e; da razão $Zn^{2+}:NH_4^-$. Estas variáveis influenciam morfologia de nanoestruturas de ZnO para obtenção de um filme para utilização como camada semente para posterior crescimento de nanoestruturas de ZnO.

2 MÉTODOS EXPERIMENTAIS

Este estudo foi conduzido utilizando-se como substrato lâmina de vidro recoberta com SnO_2 dopado com flúor (FTO), normalmente utilizado nas DSSCs. Todo o processo de limpeza do substrato foi realizado em banhos ultrassônicos, por 180 s cada, na seguinte seqüência: Extran®; água deionizada; acetona; álcool isopropílico e; água deionizada. Como última etapa da limpeza foi realizada a secagem sob fluxo de N_2 , para ativação da superfície recoberta com SnO_2 . Tanto a face não recoberta por SnO_2 , quanto as bordas da lâmina, as mesmas foram recobertas com fita de PTFE, para evitar crescimento de sementes de ZnO nestas superfícies.

O processo SILAR utilizado para a obtenção de nanoestruturas de zinco foi descrito por Galego et al (2013). Neste estudo foram avaliadas a influência de tempo, temperatura e concentração dos banhos catiônicos e aniônico descritos na Tab. 1.

Tabela 1: Condições básicas do processo SILAR utilizadas neste estudo.

Sequência	Banho (espécie química)	Temperatura (°C)	Tempo (s)	Rotação (rpm)
1	Catiônico 1 (Nitrato)	50	10	Estático
2	Aniônico	90	10	Estático
3	Lavagem	Ambiente	5	30
4	Catiônico 2 (Acetato)	40	40	Estático
5	Aniônico	90	10	Estático
6	Lavagem	Ambiente	5	30
7	Secagem - fluxo de N ₂		30	30

A determinação das fases cristalinas obtidas foi realizada por difração de raios X, utilizando radiação Cu - K α , no difratômetro Brucker AXS.

A microscopia eletrônica de varredura (MEV) foi utilizada para estudo das nanoestruturas crescida. Foram feitas observações superfícies e em superfície de fratura com inclinação de 75° em relação ao feixe de elétrons, utilizando-se o microscópio Philips – XL30.

3 RESULTADOS E DISCUSSÕES

No processo SILAR, para obtenção de ZnO, a temperatura mais elevada é a do banho aniônico onde ocorre a reação química de formação do ZnO, trabalhar em temperatura baixa torna o método mais atrativo do ponto de vista ecológico e econômico; entretanto podem ocorrer a formação do hidróxido de zinco, fazendo-se necessário a realização de tratamento térmico. Além disso, a temperatura do banho aniônico, também influencia na densidade superficial de núcleos de ZnO formados na superfície do substrato. Nas Figs. 3 (a), (b) e (c) são apresentadas micrografias obtidas por MEV das nanoestruturas de ZnO utilizando o banho aniônico a temperatura de 60 °C, 70 °C e 90 °C; observa-se que a formação dos núcleos sobre o substrato aumenta com o aumento da temperatura, influenciando diretamente o recobrimento do substrato. Na Fig.3(b) foi possível perceber o crescimento de alguns núcleos, enquanto na temperatura de 90°C (Fig.3(c)) ocorreu um aumento significativo dos núcleos na superfície e também houve crescimento na direção basal.

A análise do espectro por difração de raios X indicou a formação da fase cristalina do ZnO nas temperaturas estudadas, na Fig.4 é apresentado o espectro da difração de raios X obtido para a amostra com banho aniônico a temperatura de 90 °C, onde foi possível identificar as fases do SnO₂ do filme condutor e a fase cristalina do ZnO com orientação preferencial na direção do plano basal; nos métodos por banho químico observa-se que o coalescimento da nanoestrutura resulta na orientação preferencial dos planos (100), (101) e (002) sendo este o de preferência conforme o crescimento prossegue e a nanoestrutura

adquiriu o hábito cristalino de um nanobastão; esta sequência de crescimento ocorre de acordo com a energia livre superficial dos planos do ZnO $G_{100} = -2,0013 \text{ kJ mol}^{-1}$, $G_{101} = -2,1067 \text{ kJ mol}^{-1}$ e $G_{001} = -2,8102 \text{ kJ mol}^{-1}$ (Shinde et al., 2005; Khranovsky, et al., 2012).

Figura 3: Micrografias obtidas por MEV das nanoestruturas de ZnO obtidas utilizando banho aniônico a temperatura: (a) 60 °C; (b) 70°C e (c) 90°C.

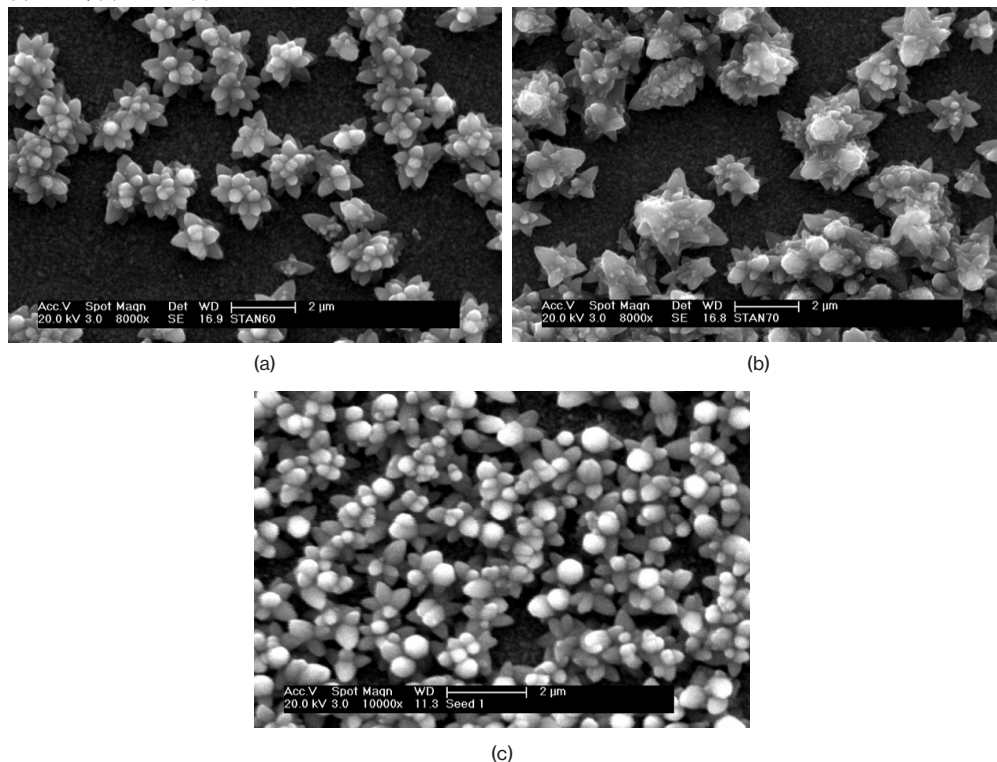
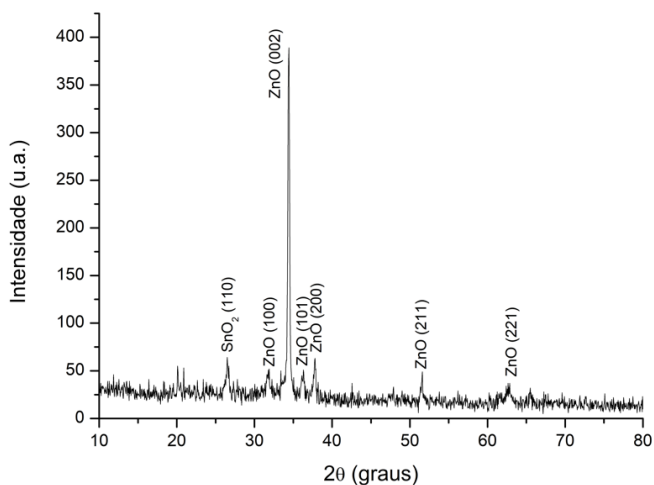
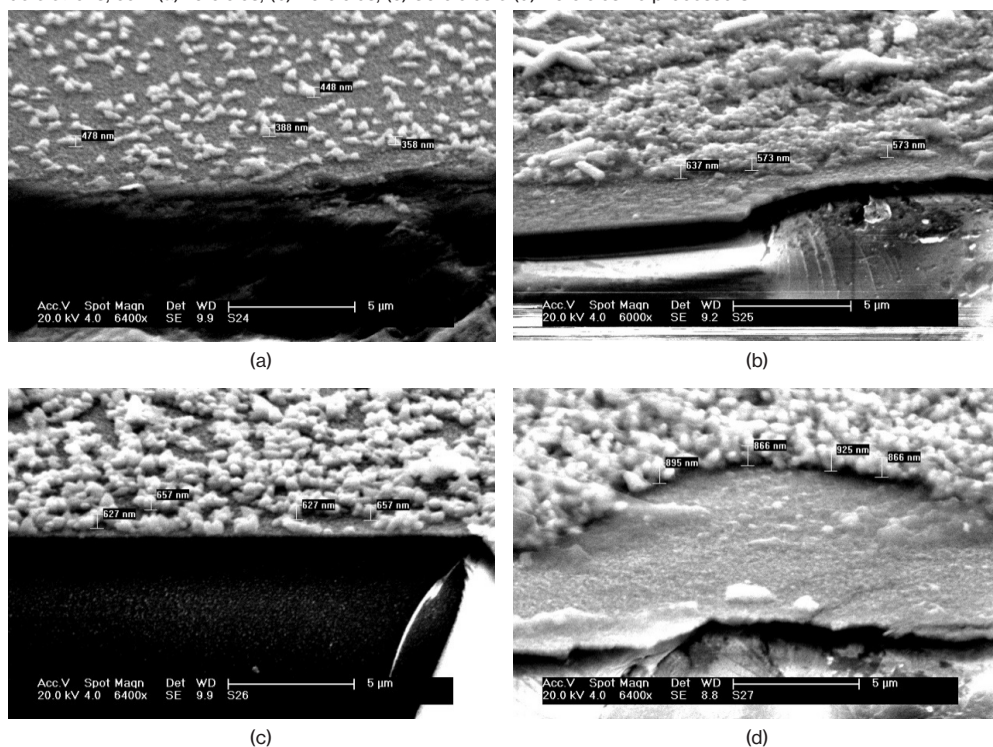


Figura 4: Espectro de difração de raios X da amostra obtida pelo método SILAR com banho aniônico a 90°C



Estabelecida a temperatura do banho aniônico, a próxima etapa foi o estudo do número de ciclos do processo SILAR necessários para a obtenção de um recobrimento uniforme do substrato. As micrografias, obtidas por MEV, apresentadas nas Fig. 5 (a), (b) (c) e (d), foram realizadas em região de fratura e com as amostras inclinadas a 75 ° em relação ao feixe de elétrons, nestas pode-se ver que o processo utilizado promove a nucleação na superfície do substrato, assim como o crescimento dos núcleos formados. Estudos anteriores realizados por Galego et al. (2013) indicam que a nucleação superficial ocorre no banho catiônico de solução de nitrato de zinco/HMT, enquanto o crescimento dos núcleos ocorre preferencialmente no banho catiônico de solução de acetato/amônio. O gráfico apresentado na Fig. 6 apresenta da taxa de crescimento em função do número de ciclos utilizado no processo SILAR.

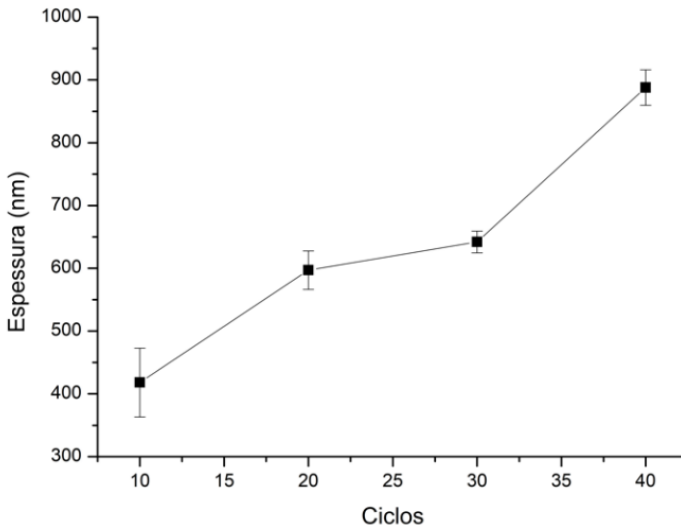
Figura 5: Micrografias obtidas por MEV do filme de ZnO, na região de fratura e inclinadas a 75° em relação ao feixe de elétrons, com (a) 10 ciclos; (b) 20 ciclos; (c) 30 ciclos e (d) 40 ciclos no processo SILAR.



Estes resultados mostraram que em cada ciclo, nas condições estudadas, ocorreu nucleação e crescimento de núcleos até o trigésimo ciclo, pode-se inferir pelo gráfico apresentado na Fig.6 que nos ciclos posteriores ocorreu preferencialmente o

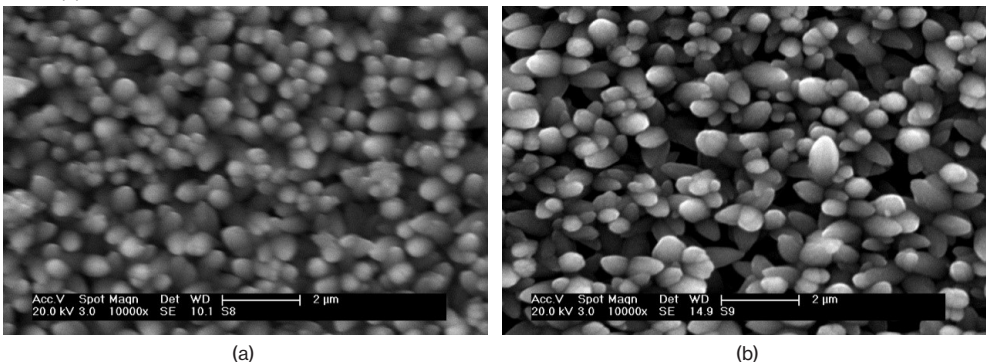
crescimento dos núcleos já aderidos ao substrato, este resultado também foi descrito por Amalraj e Senguttuvan (2014).

Figura 6: Gráfico da taxa de crescimento da camada de ZnO em relação ao número de ciclos de repetição empregado no SILAR.

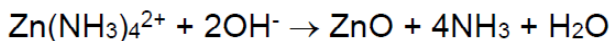


A adsorção dos íons Zn^{2+} é regida pelo produto de solubilidade local, entretanto em soluções insaturadas pode ocorrer a dissolução do núcleo formado, nas Figs. 7 (a) e (b) são apresentadas as micrografias da superfície de ZnO obtidas com tempo de permanência de 10 s e 20 s da amostra no banho catiônico de nitrato de zinco/HMT foi possível avaliar que não houve alterações significativas na densidade superficial de núcleos aderidos a superfície, indicando a não ocorrência de dissolução dos núcleos.

Figura 7: Micrografia obtidas por MEV da superfície de ZnO crescidas com permanência no banho de ZnO de (a) 10 s e (b) 20 s.

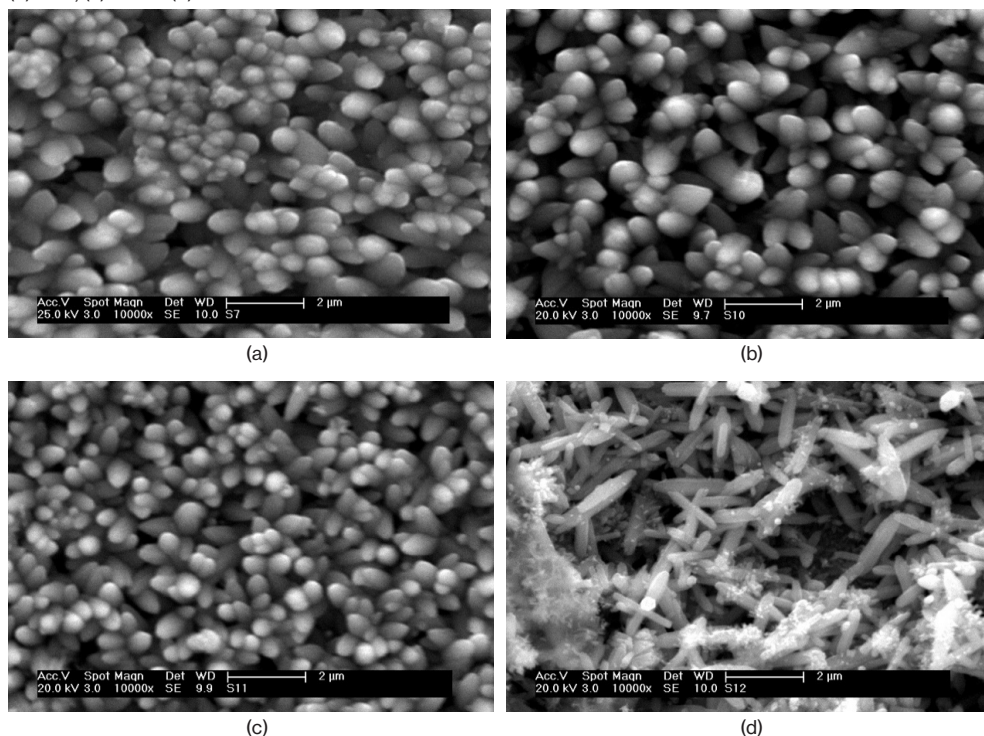


O tempo de permanência do substrato no banho catiônico é um dos fatores mais cruciais do método SILAR. Portanto, o ideal é determinar o tempo necessário para que apenas um íon seja adsorvido em cada sítio disponível e que não ocorra adsorção ou ligações entre os íons de zinco adsorvidos na superfície, a reação de formação, para íons complexados é:



A presença do amônio na solução do banho pode ser obtida pela adição de hidróxido de amônia ou sais geradores de amônio em seu processo de decomposição. Alguns autores sugerem que as ligações entre os íons complexados são fracas e que a inclusão de uma etapa de lavagem entre o banho catiônico e aniônico, permite eliminar este tipo de ligação e, também, de íons fracamente adsorvidos na superfície. Entretanto, outros autores sugerem que nesta etapa ocorre a formação de $\text{Zn}(\text{OH})_2$, e que posteriormente no banho a alta temperatura é convertido em ZnO (Zhang et al., 2010; Taner et al., 2011).

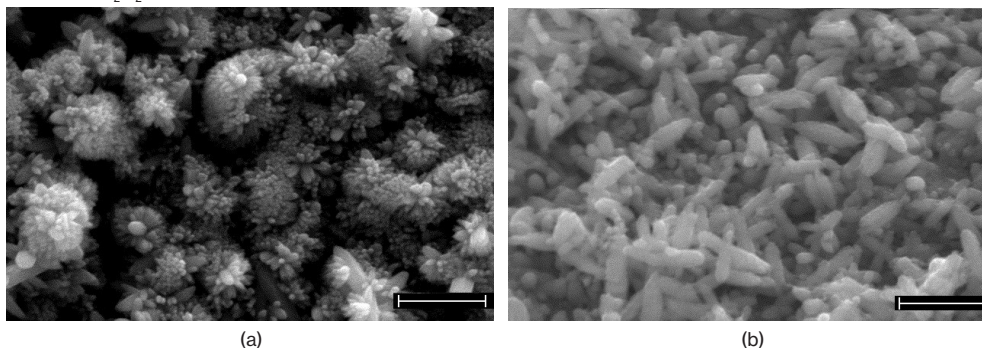
Figura 8: Micrografias da superfície das nanoestruturas, obtidas por MEV, com tempo de permanência de: (a) 10 s, (b) 30 s, (c) 40 s e (d) 60 s.



O mesmo estudo, de tempo de permanência de amostra no banho catiônico, foi realizado para o crescimento no acetato de zinco. As micrografias Fig.8(a) e Fig.8(b) mostraram que os núcleos depositados no banho de nitrato de zinco sofreram um crescimento acentuado nos planos apolares resultado em uma estrutura mais compacta. No entanto, com o aumento do tempo de permanência observou-se que ocorreu o crescimento preferencial nas direções dos planos polares, Fig.8(c) e Fig.8(d). Durante o processo SILAR não foi possível impedir completamente a nucleação homogênea, principalmente no banho aniônico. Assim, foi possível observar que o aumento do tempo de permanência para 60 s implicou na formação de nanoestruturas no seio da solução que foram aderidas fracamente a superfície do filme de ZnO tornando o crescimento dos nanobastões em direções aleatórias.

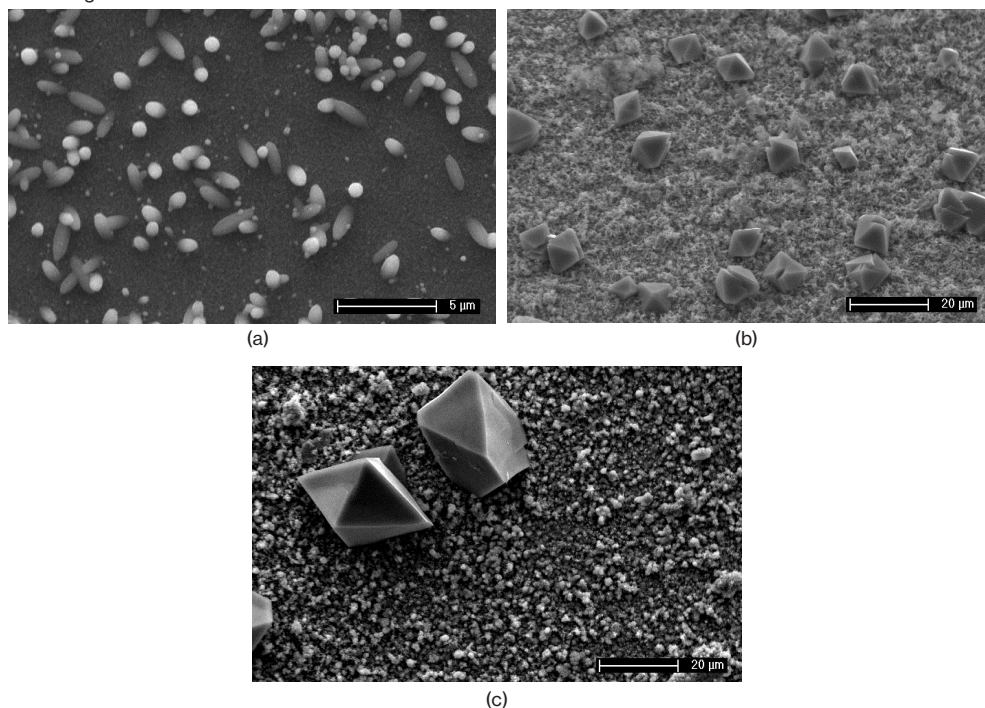
O principal objetivo do estudo das variáveis do método SILAR, aqui realizado, foi determinar a sequência com a menor temperatura e tempo de execução, tornando deste modo o processo atrativo do ponto de vista econômico e ecológico. Temperaturas muito baixas que a ambiente necessitam de um sistema de resfriamento, portanto o ideal foi trabalhar com temperaturas de aquecimento próximas a temperatura ambiente para os banhos catiônicos. Gurav et al. (2011) estudaram o efeito da adição de peróxido de hidrogênio ao banho aniônico, mostrando que houve aumento de espessura do filme e maior orientação preferencial na direção do plano basal. A Fig.9 apresenta a camada de ZnO formada com a adição de 1% de peróxido de hidrogênio ao banho aniônico, com o objetivo de aumentar a taxa de reações de formação do ZnO, este aditivo promoveu maior crescimento do ZnO, mas as custas de menor orientação cristalina das nanoestruturas nas condições usadas neste estudo.

Figura 9: Micrografias obtidas por MEV que mostram a ação do H_2O_2 sobre a morfologia: (a) adição de 1% em volume de H_2O_2 ; (b) sem adição.



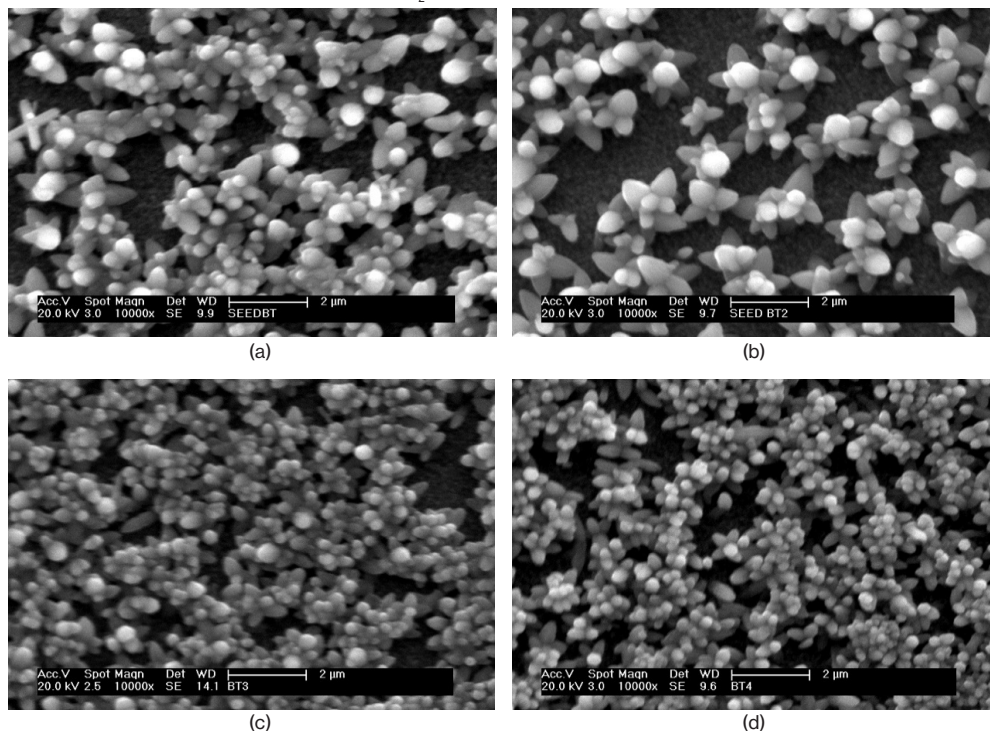
A Fig.10 apresenta as micrografias, obtidas por MEV, da superfície da camada de ZnO com e sem a etapa do banho de lavagem, observou-se a adesão de nanopartículas nucleadas homogêneas e crescidas no banho aniônico. As etapas de lavagem durante o processo SILAR são responsáveis pela retirada dos íons fracamente ligados, promovendo o crescimento de nanoestruturas mais aderentes ao substrato e com menores defeitos estruturais.

Figura 10: Nano e microestruturas de ZnO observada por MEV na superfície da camada de ZnO: (a) estrutura dos núcleos após a etapa de lavagem, (b) e (c) adesão de microestruturas formadas no banho catiônico em processo sem lavagem.



A influência da concentração molar em ambas as soluções dos banhos catiônicos e da proporção $Zn^{2+}:NH_4^-$ no banho de crescimento foram estudadas com a finalidade de buscar nanoestruturas com diferentes morfologias. Os filmes nanoestruturados obtidos pelo método SILAR podem ser empregados em diversos tipos de sensores, assim a morfologia será determinada pelo tipo de aplicação. Outro uso deste filme é atuando como semente para posterior crescimento de estruturas micrométricas, neste caso a morfologia do filme nanoestruturado terá grande influência na morfologia das estruturas de ZnO crescidas posteriormente.

Figura 11: Micrografia obtidas por MEV da superfície de filmes nanoestruturados obtidos com diferentes concentrações no banho de nucleação de $ZnCl_2$: (a) 0,01 M, (b) 0,02 M, (c) 0,04 M e (d) 0,06 M.



Nas Figs. 11 (a), (b) (c) e (d) são apresentadas as micrografias, obtidas por MEV, para os filmes nanoestruturados de ZnO obtidos utilizando com sal precursor de cloreto de zinco nas concentrações molares de: 0,01 M, 0,02 M, 0,04 M e 0,06 M como banho de nucleação. Analisando o conjunto das micrografias pode-se ver, que diferentemente da solução utilizando nitrato de zinco, o uso de cloreto de zinco não produziu uma densidade superficial de núcleos capaz de recobrir completamente o substrato. A micrografia da Fig.11(a) mostra a predominância de núcleo aderidos ao substrato com poucos crescimentos significativos.

A velocidade de formação do ZnO utilizando como precursor o cloreto de zinco é menor que a do nitrato de zinco, observando a Fig.11(b) onde a concentração molar dos dois sais de zinco estudados foi a mesma observa-se o menor recobrimento do substrato com o uso do cloreto de zinco. Nas Fig. 11(c) e Fig. 11(d) observa-se que não há influência significativa da concentração molar na formação do filme nanoestruturado, sugerindo que o aumento da concentração molar promove o crescimento dos núcleos já formados em detrimento da nucleação de novos núcleos resultando em um filme poroso.

4 CONCLUSÕES

Os resultados obtidos neste estudo mostraram que alterações simples nas variáveis do processo SILAR para obtenção de ZnO permitiram desde a obtenção de nanoestruturas individuais a filmes compactos ou porosos. A maioria dos parâmetros estudados exerceu em maior ou menor grau influência sobre a morfologia das nanoestruturas crescidas sobre o FTO. Esta ampla gama de morfologias e filmes se presta aos mais diversos usos deste versátil semicondutor.

REFERÊNCIAS

AMALRAJ, A.S.; SENGUTTUVAN, G. Effect of multiple dipping of SILAR deposited ZnO thin films by physic-chemical process. **Journal of Materials Science: Materials in Electronics**, v.25, p.2035-2040, 2014.

CHENG, H-C.; CHEN, C-F, LEE, C-C. Thin film transistors with active layer of zinc oxide (ZnO) fabricated by low temperature chemical bath method. **Thin Solid Films**, v.498, p.142-145, 2006.

GALEGO, E.; SERNA, M.M.; RAMANATHAN, A new route to grow ZnO seed layer using the SILAR method. **Technical Proceedings of the 2013 NSTI Nanotechnology Conference and Expo**, NSTI-Nanotech, v.3, p.509-512, 2013.

GAO, X.D.; LI, X.M.; YU, W.D. Preparation, structure and ultraviolet photoluminescence of ZnO films by novel chemical method. **Journal of Solid State Chemistry**, v.177, p.3830-3834, 2004.

GAO, X.D.; LI, X.M.; YU, W.D. Synthesis and optical properties of ZnO nanocluster porous films deposited by modified SILAR method. **Applied Surface Science**, v.229, p.275-281, 2004a.

GAO, X.D.; LI, X.M.; YU, W.D.; LI, L.; PENG, F.; ZHANG, C-Y. Microstructure analysis and formation mechanism of ZnO nanoporous film via the ultrasonic irradiation mediated SILAR method. **Journal of Crystal Growth**, v.291, p.175-182, 2006.

GAO, X.D.; LI, X.M.; YU, W.D.; LI, L.; QIU, J-J.; PENG, F. Low temperature deposition of transparent ZnO films by the ultrasonic-mediated stepwise method. **Solar Energy Materials and Solar Cells**, v.91, p.467-473, 2007.

GAO, Y. -F.; MIAO, H.-Y.; LUO, H.-J.; NAGAI, M. Precipitation of ZnO powders from aqueous solutions with water-soluble polymers. **Crystal Growth & Design**, v.8, n.7, p.2187-2193, 2008.

GREENE, L.E.; LAW, M.; TAN, D.H.; MONTANO, M. GOLDBERGER, J.; SOMORJAI, G.; YANG, P. General route to vertical ZnO nanowire arrays using textured ZnO seeds. **Nanoletters**, v.5, n.7, p.1231-1236, 2005.

GURAV, K.V.; PATIL, U.M.; PAWAR, S.M.; KIM, J.H.; LOKHANDE, C.D. Controlled crystallite orientation in ZnO nanorods prepared by chemical bath deposition: effect of H₂O₂. **Journal of Alloys and Compounds**, v.509, p.7723-7728, 2011.

JIMÉNEZ-GARCIA, F.N.; ESPINOSA-ARBELÁEZ, D.G.; VARGAS-HERNÁNDEZ, C.; DEL REAL, A.; RODRÍGUEZ-GARCÍA, M.E. Characterization of nanostructures of ZnO and ZnMnO films deposited by successive ionic layer adsorption and reaction method. **Thin Solid Films**, v.519, p.7638-7643, 2011.

KANMANI, S.S.; RAMACHANDRAN, K. Role of aqueous ammonia on the growth of ZnO nanostructures and its influence on solid-state dye sensitized solar cells. **Journal Materials Science**, v.48, v.5, p.2076-2091, 2013.

- KHRANOVSKYY, V.; YAKIMOVA, R. Morphology engineering of ZnO nanostructures. **Physica B**, v.407, p.1533-1537, 2012.
- KHRANOVSKYY, V.; YAKIMOVA, R.; KARLSSON, F.; SYED, A.S.; HOLTZ, P-O.; URGESSA, Z.N.; OLUWAFEMI, O.S.; BOTHA, J.R. Comparative PL study of individual ZnO nanorods, grown by APMOCVD and CBD techniques. **Physica B**, v.407, p.1538-1542.
- KUMAR, P.S.; RAJ, A.D.; MANGALARAJ, D.; NATARAJ, D. Growth and characterization of ZnO nanostructured thin films by a two step chemical method. **Applied Surface Science**, v.255, p.2382-2387.
- KUMAR, R.S.; SATHYAMOORTHY, R.; MATHESWARAN, P.; SUDHAGAR, P.; KANG, Y.S. Growth of novel ZnO nanostructures by soft chemical routes. **Journal of Alloys and Compounds**, v.506, p.351-355, 2010.
- LAW, M.; GREENE, L.E.; JOHNSON, J.C.; SAYKALLY, R.; YANG, P. Nanowire dye-sensitized solar cells. **Nature Material**, v.4, p.455-459, 2005.
- LOCKETT, A.M.; THOMAS, P.J.; O'BRIEN, P. Influence of seeding layers on the morphology, density, and critical dimensions of ZnO nanostructures grown by chemical bath deposition. **The Journal of Physical Chemistry C**, v.116, p. 8080-8094, 2012.
- MANE, R.S.; LOKHANDE, C.D. Chemical deposition method for metal chalcogenide thin films. **Materials Chemistry and Physics**, v.65, p.1-31, 2000.
- MANE, R.S.; LEE, W-J.; LOKHANDE, C.D.; CHO, B.W.; HAN, S-H. Controlled repeated chemical growth of ZnO films for dye-sensitized solar cells. **Current Applied Physics**, v.8, p.549-553, 2008.
- NICOLAU, Y.F. Solution deposition of thin solid compound films by a successive ionic-layer adsorption and reaction process. **Applications of Surface Science**, v.22-23, p.1061-1074, 1985.
- RISTOV, M.; SINADINOVSKI, G.J.; GROZDANOV, I. MITRESKI, M. Chemical deposition of ZnO films, **Thin Solid Films**, v.149, p.65-71, 1987.
- SHINDE, V.R.; LOKHANDE, C.D.; MANE, R.S.; HAN, S-H. Hydrophobic and textured ZnO films deposited by chemical bath deposition: annealing effects. **Applied Surface Science**, v.245, p.407-413, 2005.
- TANER, A.; KUL, M.; TURAN, E.; AYBEK, A.S.; ZOR, M.; TASKÖPRÜ, T. Optical and structural properties of zinc oxide films with different thicknesses prepared by successive ionic layer and reaction method. **Thin Solid Films**, v.520, p.1358-1362, 2011.
- TAK, Y.; YONG, K. Controlled growth of well-aligned ZnO nanorod array using a novel solution method. **Journal of Physics and Chemistry B**, v.109, p.19263-19269, 2005.
- WANG, Z.L. Zinc oxide nanostructures: growth, properties and applications. **Journal of Physics: Condensed Matter**, v.16, p.R820-R858, 2004.
- WANG, H.; XIE, C.; ZENG, D. Controlled growth of ZnO by adding H₂O. **Journal of Crystal Growth**, v.277, p.372-375, 2005.
- WU, W.; HU, G.; CUI, S.; ZHOU, Y.; WU, H. Epitaxy of vertical ZnO nanorods arrays on highly (001)-oriented ZnO seed monolayer by a hydrothermal route. **Crystal Growth & Design**, v.8,n.11, p.4014-4020, 2008.
- ZHANG, D.; ZHANG, J.; WU, Q.; MIU, X. Ultraviolet emission of ZnO nano-polycrystalline films by modified successive ionic layer adsorption and reaction technique. **Journal of Sol-Gel Science and Technology**, v.54, p.165-173, 2010.

CHAPTER 17

OBTENÇÃO E CARACTERIZAÇÃO DE NANOCRISTAIS DE CELULOSE A PARTIR DE PAPEL RECICLADO VIRGEM E PÓS-CONSUMO

Data de submissão: 05/04/2021

Data de aceite: 26/04/2021

Jean Brito Santos

Universidade Federal da Bahia
Salvador, BA

<http://lattes.cnpq.br/4192432710216149>

Emanoel Igor da Silva Oliveira

Instituto Federal da Bahia
Salvador, BA

<http://lattes.cnpq.br/0262590272550573>

Nádia Mamede José

Universidade Federal da Bahia
Salvador, BA

<http://lattes.cnpq.br/5940246341994507>

RESUMO: Papel reciclado virgem e pós-consumo foram avaliados para obtenção de nanocristais de celulose. As amostras picotadas foram pré-tratadas por lavagem a quente com água, tratamento com NaOH(aq) e branqueamento com NaClO(aq). Os papéis branqueados foram hidrolisados com H₂SO₄(aq) 55% para obtenção dos nanocristais. Os perfis de DRX dos papéis não tratados apresentaram, além dos picos de celulose I, picos referentes a aditivos

presentes no papel, índice de cristalinidade na faixa de 70-80%, similar à celulose microcristalina. O fluxo de birrefringência das suspensões permitiu inferir que nanopartículas foram obtidas, sendo que aquelas obtidas do papel virgem ($\xi = -24,6 \pm 0,3$ mV) apresentaram-se mais dispersas em relação ao pós-consumo ($\xi = -13,8 \pm 0,5$ mV). FTIR em conjunto com análise térmica indicam pigmento residual que influenciam na estabilidade térmica dos nanocristais obtidos. Para os nanocristais sem pigmento, verificou-se maior temperatura de degradação da celulose em comparação a nanocristais comerciais avaliados em comparação.

PALAVRAS-CHAVE: Nanocristais. Nanopartículas. Celulose. Papel reciclado.

OBTENTION AND CHARACTERIZATION OF CELLULOSE NANOCRYSTALS FROM VIRGIN AND POST-CONSUMER RECYCLED OFFICE PAPER

ABSTRACT: Virgin and post-consumer recycled office paper were evaluated to obtain cellulose nanocrystals. The shredded samples were boiled with water prior the alkali treatment with NaOH(aq) and bleaching with NaClO(aq). The bleached papers were hydrolyzed with 55% H₂SO₄(aq) to obtain the nanocrystals. The XRD profiles of untreated papers showed, in addition to the cellulose peaks, peaks related to additives present in

the paper, as well crystallinity index in the range of 70-80%, similar to microcrystalline cellulose. The birefringence flow of the suspensions made it possible to infer that nanoparticles were obtained, and those obtained from virgin paper ($\xi = -24.6 \pm 0.3$ mV) were more dispersed in relation to post-consumer ($\xi = -13.8 \pm 0.5$ mV). FTIR spectra deals with thermal analysis and indicates some remaining ink that influences the thermal stability of the obtained nanocrystals. Impure nanocrystals displayed higher degradation temperature than commercial nanocrystals assumed as standards.

KEYWORDS: Nanocrystals. Nanoparticles. Cellulose. Recycled paper.

1 INTRODUÇÃO

Nanocristais de celulose são nanopartículas promissoras para diversas aplicações em virtude de suas boas propriedades mecânicas, elevada cristalinidade e versatilidade para modificação química (DUFRESNE, A., 2013). Esse tipo de nanomaterial pode ser obtido de diversas fontes celulósicas, contudo, diante das atuais demandas ambientais, o aproveitamento de resíduos para esse fim constitui-se como uma abordagem desejável. O Brasil é um dos maiores produtores mundiais de papel (TEIXEIRA, M. B. D.; OLIVEIRA, R. A.; GATTI, T. H.; P. A. Z., 2017) gerando, portanto, grandes quantidades desse material após o consumo que geralmente se acumulam ou são reaproveitados por reciclagem convencional. O objetivo desse trabalho foi avaliar o papel reciclado em sua forma virgem e pós-consumo como fontes para obtenção de nanocristais de celulose, o que poderia agregar maior valor ao resíduo em comparação à reciclagem.

2 METODOLOGIA

2.1 PRÉ-TRATAMENTO DOS PAPÉIS:

Cortou-se uma resma de papel virgem e um saco de papel pós consumo em pequenos pedaços e aferiu-se a massa do material obtido; Os pigmentos do papel pós-consumo foram extraídos com acetona para análise individual; Ferveram-se em água destilada os pedaços de papel durante 12 horas (DANIAL, W. H. et al., 2015) Triturou-se num liquidificador a massa úmida da etapa anterior para obter-se um material com aspecto de lama; Filtrou-se a vácuo e lavou-se o material com água destilada por diversas vezes; Separou-se parte da massa obtida para caracterização; Ferveu-se o sólido com NaOH(aq) 5% m/v, em proporção 2:1 mL de solução para massa (g) de papel, durante uma hora; Branqueou-se os papéis com NaClO(aq) 2% v/v juntamente com CH₃CO₂H(aq) 5% v/v e NaOH(aq) 5% m/v, numa proporção 2:1:1 mL, respectivamente por duas horas;

Filtrou-se a vácuo a solução e lavou-se o sólido por diversas vezes com água destilada até pH neutro; Separou-se amostras para caracterização.

2.2 CARACTERIZAÇÃO DOS PAPÉIS:

Os materiais de partida e aqueles obtidos no pré-tratamento foram caracterizados por Infravermelho (FTIR) e Difração de Raios-X (DRX).

2.3 OBTENÇÃO DOS NANOCRISTAIS:

5 g de papel branqueado foram hidrolisados com 50 mL de H_2SO_4 (aq) 55% v/v, a 50° C, por 2 h, sob agitação mecânica, sendo posteriormente o sistema centrifugado e a solução turva obtida dialisada até pH neutro.

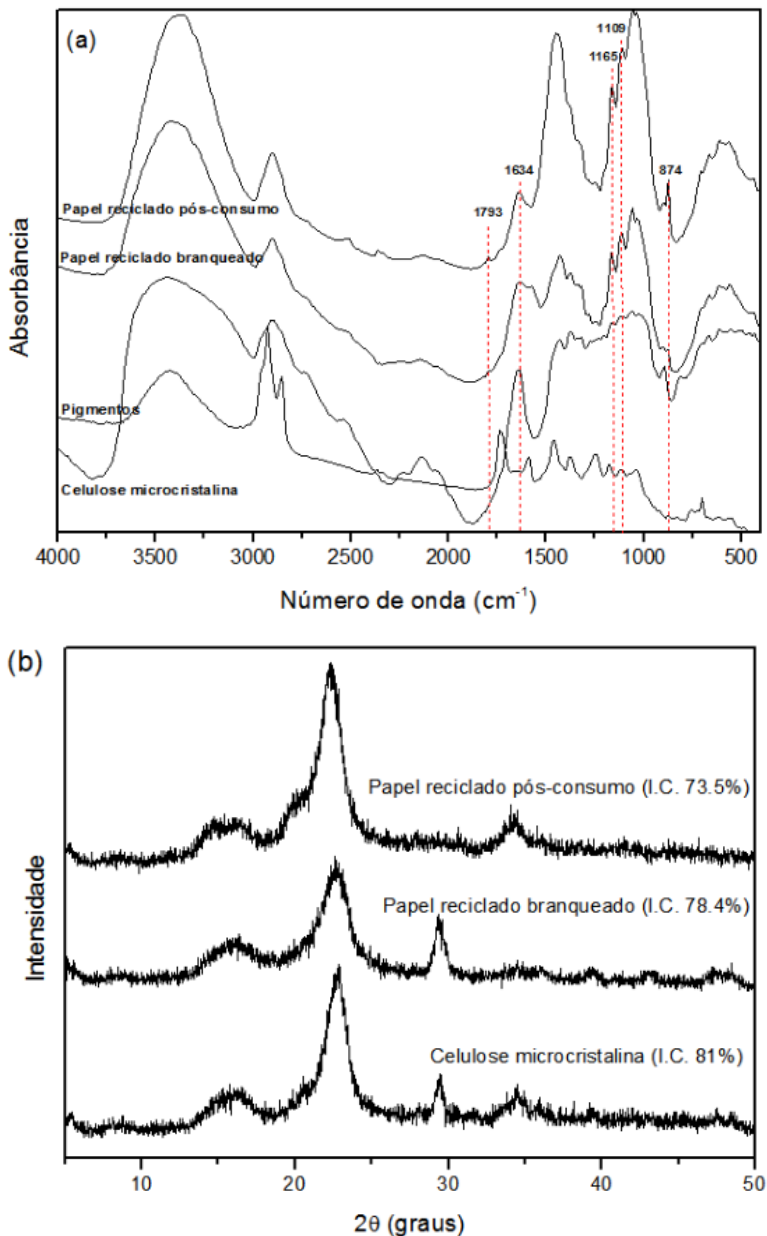
2.4 CARACTERIZAÇÃO DOS NANOCRISTAIS:

Os nanocristais obtidos foram caracterizados por Birrefringência, Espalhamento de luz eletroforético (ELS), Difração de Raios-X (DRX) e Análise térmica (TGA).

3 RESULTADOS E DISCUSSÃO

A Figura 1 apresenta os espectros de FTIR e os difratogramas de raios-X das amostras. A análise dos espectros de FTIR foi feita comparando-se os espectros dos papéis não tratados e branqueados com o espectro da celulose microcristalina para identificar as bandas provenientes da celulose e, posteriormente, comparando-se as bandas ausentes no espectro da celulose microcristalina, mas presentes no espectro dos pigmentos isolados. Segundo esse critério de análise, as bandas que aparentam ter contribuições dos pigmentos residuais presentes no papel branqueado foram destacadas com linhas tracejadas nos espectros. Esses dados indicam que os pré-tratamentos efetuados não foram suficientes para remover 100 % dos pigmentos, contudo as bandas de celulose permanecem como na referência. Nos difratogramas são observados picos de difração característicos da celulose do tipo I e picos de aditivos que são adicionados ao papel para conferir alvura e resistência, tais como dióxido de titânio, carbonato de cálcio, entre outros. Os pré-tratamentos empregados foram eficientes para remover as regiões amorfas da celulose e preservar as regiões cristalinas, contudo o desaparecimento do pico em torno de 34,5° sugere que algum ataque não desejado à região cristalina ocorreu.

Figura 1 – Espectros de infravermelho (a) e difratogramas de raios-X (b) do papel pós-consumo, branqueado, pigmentos extraídos e celulose microcristalina para comparação.



A Figura 2 apresenta o aspecto visual das suspensões obtidas, o fluxo de birrefringência observado e os respectivos potenciais Zeta, além das caracterizações relativas à cristalinidade e ao comportamento térmico.

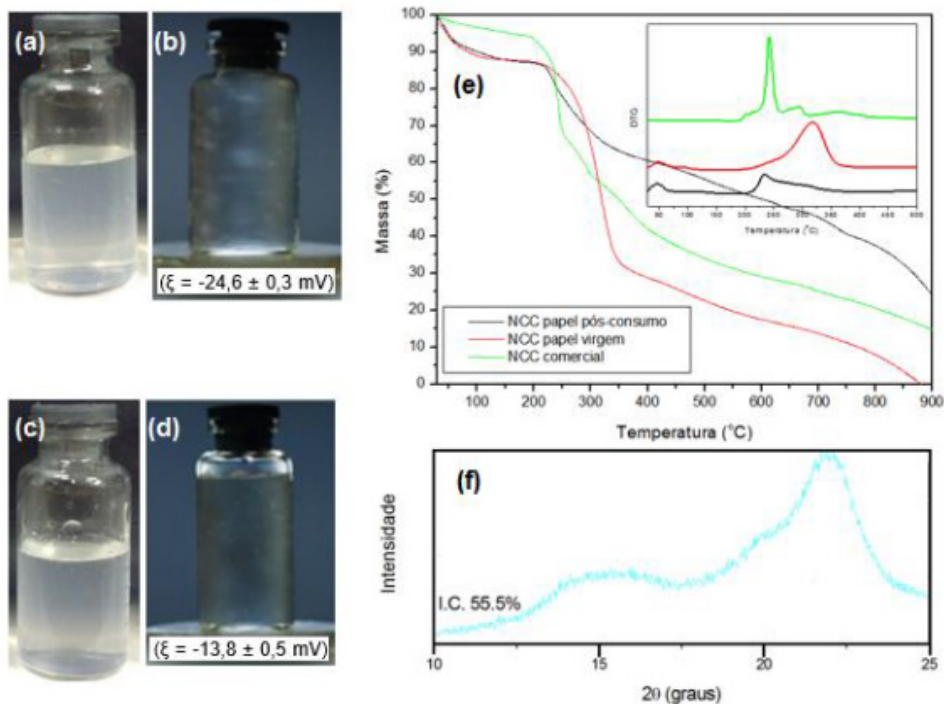
O aspecto turvo e opalescente das suspensões é típico de suspensões coloidais que contém nanopartículas de celulose. Observa-se que o fluxo de birrefringência foi

mais intenso para a suspensão obtida do papel reciclado virgem, o que indica uma maior dispersão das partículas em água e é corroborado pelo maior valor de potencial Zeta apresentado por essa suspensão.

O menor índice de cristalinidade em comparação ao papel branqueado e o desaparecimento do pico em 34,5° confirmam que, de fato, a hidrólise ácida ocorreu numa extensão maior do que a desejada, contudo o índice de cristalinidade na faixa de 55-60% está dentro dos valores de nanocristais obtidos de outras fontes relatadas na literatura.

Em relação ao comportamento térmico, observa-se que os nanocristais obtidos diferem bastante em relação aos nanocristais comerciais. Os eventos de degradação da celulose ocorrem todos na região compreendida entre 200 e 400 °C. Ao verificar o DTG, são identificados três eventos para o material de referência, cujas temperaturas de degradação dependem do grau de sulfatação e da acessibilidade às cadeias celulósicas. Verifica-se que tanto a T_{onset} quanto a $T_{\text{máx}}$ foram maiores para os nanocristais obtidos do papel virgem em comparação aos demais, indicando que a presença de pigmentos compromete essa estabilidade térmica, possivelmente por diminuir a energia de ativação para a degradação da celulose, tal como já bem relatado na literatura como efeito da sulfatação da celulose (MORIANA, R.; VILAPLANA, F.; EKA, M., 2016).

Figura 2 – Fluxo de birrefringência e potencial Zeta das suspensões aquosas de nanocristais de celulose obtidas a partir de: (a) e (b) papel reciclado virgem, (c) e (d) papel reciclado pós-consumo, (e) comportamento térmico dos nanocristais (f) Difratograma dos nanocristais obtidos do papel virgem.



4 CONSIDERAÇÕES FINAIS

Foi possível obter nanocristais de celulose, tanto a partir do papel reciclado de escritório virgem quanto pós-consumo. Os resultados mostraram que a presença de pigmentos residuais no nanomaterial implica em redução de estabilidade em meio aquoso e estabilidade térmica. O controle de hidrólise precisa ser mais bem ajustado para evitar a degradação das regiões cristalinas da celulose. Apesar dos problemas citados, a celulose obtida apresentou padrão de cristalinidade similar à celulose microcristalina, o que sugere que o papel reciclado pós-consumo é uma fonte em potencial para a cadeia de nanocelulose brasileira. Recente trabalho de revisão (KUMAR, V.; PATHAK, P.; BHARDWAJ, N. K., 2020) fortalece ainda mais o potencial dos papéis residuais como fonte alternativa de obtenção desse tipo de nanomaterial.

REFERÊNCIAS

1. DANIAL, W. H.; MAJID, Z. A.; MUHID, M. N. M.; TRIWAHYONO, S.; BAKAR, M. B.; RAMLI, Z. **The reuse of wastepaper for the extraction of cellulose nanocrystals.** Carbohydr. Polym. 118, 166, 2015.
2. DUFRESNE, A. **Nanocellulose: a new ageless bionanomaterial.** Mater. Today. 16, 220-227, 2013.
3. KUMAR, V.; PATHAK, P.; BHARDWAJ, N. K. **Waste paper: An underutilized but promising source for nanocellulose mining.** Waste Management 102, 281-303, 2020.
4. MORIANA, R.; VILAPLANA, F.; EKA, M. **Cellulose nanocrystals from forest residues as reinforcing agents for composites: a study from macro- to nano-dimensions.** Carbohydrate polymers, [S.L.], v. 139, p. 139-149, mar. 2016.
5. TEIXEIRA, M. B. D.; OLIVEIRA, R. A.; GATTI, T. H.; P. A. Z. **O Papel: Uma Breve Revisão Histórica, Descrição da Tecnologia Industrial de Produção e Experimentos para Obtenção de Folhas Artesanais.** Rev. Virtual Quim. 9, 1368, 2017.

ABOUT THE ORGANIZER

MARCOS AUGUSTO DE LIMA NOBRE: Assistant Professor and Researcher (2006 - present), with citation name M. A. L. Nobre, at the São Paulo State University (UNESP), School of Science and Technology, Department of Physics, campus at Presidente Prudente-SP. Head and Founder (2002) of the Laboratory of Functional Composites and Ceramics (LaCCeF acronym in Portuguese, the native idiom), Lab certified by PROPE-UNESP/National Council for Scientific and Technological Development/CNPq*. Grants from National Council for Scientific and Technological Development (CNPq), 2020-2023, 2019-2021 and 2010-2012. Granted with Young-Researcher scholarship by the São Paulo Research Foundation, FAPESP (São Paulo, São Paulo) (2002 - Summer of 2005). Postdoctoral fellow at the Polytechnic School of the University of Sao Paulo (POLI USP-SP) Metallurgy and Materials Science Department with FAPESP Scholarship (1999-summer of 2000). PhD in Science, CAPES Scholarship (Physical Chemistry 1999) by the Chemistry Department, UFSCar-SP. Master in Chemistry CNPq scholarship (Physical Chemistry 1995) by the Chemistry Department, UFSCar-SP. Licentiate degree (4-year of study) in Physics (1993) CNPq and CNPq-Rhae scholarships by the Physics Department, UFSCar-SP. Associate Editor of the Micro & Nano Letters - IET 2019-2020. Associate Editor of the Micro & Nano Letters-Wiley, 2020 - present. Ethical Editor of the Applied Mathematics Science (Reuse) m-Hikari and Modern Research in Catalysis, Irvine-CA, USA (2017- date). Editorial board member of the Artemis Editora, Brazil. Nowadays, have 02 patents. Has published 80 papers at 39 different indexed Journals of renowned Editors. In May/25/2021, has been cited 1379 times, at 76 papers (47 with citations), in according to the ResearchID actual Publons base having an H-index equal to 23. Academic Google score: H = 28, i10 = 45 and 2338 citations. Reviewer of more than three dozen of journals. Have more than 580 communications and presentation in National and International Congress and Symposiums, from these 150 has been published as Conference Paper. Author or co-author of 20 Chapters of book approaching Scientific Divulcation, Teaching of Physic and Chemistry for teachers actuating in the graduating degree. For this, the Nanoscience and Nanotechnology have been the first strategy. Received tens of National and International Awards, Honorable mentions and distinction mentions, as well as titles. Research skills: Materials Science, Advanced Ceramic Processing, Linear and Non-linear Advanced Dielectrics Materials, Solid state chemistry, Impedance spectroscopy of solids and fluids, Structural Characterization via Mid infrared Spectroscopy with Fast-Fourier-Transformed of solid and fluids, Structural and non-structural Phase Transitions in Semiconductor Ferroelectrics. Also, Molecular Interactions in Functional Fluids as biofuels and its blends, probed via mid infrared Spectroscopy. Research interests: New Functional Materials as

amorphous composite based on carbon/nanoparticles and Semiconductor Ferroelectrics.
Member of the Program of Post-Graduation in Chemistry at UNESP - Campus of São José
do Rio Preto, IBILCE UNESP – SP, Brazil.

INDEX

A

Adsorbente 172, 173, 179, 180

Alumínio 182, 183, 184, 186, 187, 189, 190, 191, 192, 193, 198, 200, 204, 205, 206, 208, 209, 210

Annealing 1, 2, 4, 5, 7, 9, 10, 227

Arsénico 172, 173, 174, 178, 179, 180, 181

AuNR dimer 12, 14, 16, 17, 18, 19

B

Biodiesel 162, 164, 165, 168, 169, 171

Blends 162, 168, 169, 170, 171

Bulk sensitivity 12, 14, 15, 16, 17, 18, 19, 73

C

Carboxymethylchitosan 125, 127, 128, 129, 132, 133, 136

Celulose 228, 229, 230, 231, 232, 233

Chemical composition of SS surface 109

Clay 125, 127, 128, 130, 131, 133, 136, 137

Comparison among Silica and reuse of waste 77

COMSOL 14, 15, 68

Conductive tubes 92, 93, 94, 95, 100, 102, 104, 106

Confined water 39, 40, 41, 42, 52, 55, 58, 59, 60, 61, 63, 65

D

DFT 21, 23, 35, 36, 49, 50, 63

Diesel 162, 163, 164, 165, 168, 169, 171

DSSC 213, 214, 217

E

Efluente 172, 173

Evolutionary strategies 151, 156

F

FEM 14, 68

Figure of merit 11, 12, 14, 15, 16, 17, 67, 68, 72, 73, 74

Filmes finos 205, 212, 213
Filter 125, 126, 127, 128, 131, 132, 134, 135, 136, 137
Fits on Mössbauer spectra 151
FoM 15, 16, 17, 18, 19, 68, 74

G

Graphite nanostructures 162

K

$\text{KSr}_2\text{Nb}_5\text{O}_{15}$ ceramic 138, 139, 141, 144, 146

M

Magnetita nanoestruturada 172, 173
Metalurgia do pó 182, 186, 191, 192
Métodos químicos 198, 201, 205
Micro and nano silica 76, 77, 78, 79, 84, 90

N

Nanocomposite 36, 37, 91, 125, 126, 127, 128, 132, 133, 134, 135, 136, 137, 161, 182, 183, 194, 195, 196, 198, 211
Nanocompósitos 182, 183, 185, 186, 193
Nanocristais 228, 229, 230, 232, 233
Nanoestruturas 182, 198, 200, 201, 202, 206, 210, 213, 217, 218, 219, 222, 223, 224, 226
Nanograins 1, 2, 3, 9, 138
Nanolithography 39, 40, 41, 42, 45, 50, 62, 64, 66
Nanopartículas 151, 180, 212, 224, 228, 229, 231
Nanostructures 2, 9, 12, 13, 14, 15, 17, 19, 21, 22, 23, 25, 38, 61, 68, 69, 70, 71, 72, 74, 138, 162, 170, 211, 213, 226, 227
Nanostructures surface 21, 22, 23
Nanotechnology 12, 20, 62, 66, 102, 106, 126, 138, 162, 183, 195, 213, 226
Nanotecnologia 182, 212
 NiFe_2O_4 nanoparticles 150, 151, 153

O

Oxidation 39, 40, 41, 42, 53, 55, 59, 64, 65, 91, 109, 117, 118, 121
Óxido de grafeno reduzido 182, 183, 186

Óxido de zinco 197, 213

P

Papel reciclado 228, 229, 232, 233

Perfectly matched layer 11, 12, 15, 68, 69

PIII in magnetic field 109

Plasma immersion ion implantation 92, 93, 94, 107, 108, 109, 122, 123, 124

R

RI 15, 16, 67, 68, 72, 73

Rice husk Silica 77

Rolling 1, 2, 3, 4, 5, 6, 7, 9

Rough rolls 1, 2, 3, 8, 9

S

SILAR 198, 200, 201, 204, 205, 206, 210, 212, 213, 216, 217, 218, 219, 220, 221, 222, 223, 224, 226

Silica Morphology 77, 83

Silver nanoparticles 74, 125, 127, 128, 129, 130, 132, 133, 136, 137

Supercapacitores 197, 198, 199, 200, 202, 209, 210

Surface 1, 2, 3, 4, 5, 6, 7, 8, 9, 10, 11, 12, 14, 19, 20, 21, 22, 23, 24, 27, 28, 29, 30, 31, 33, 34, 35, 36, 37, 38, 39, 40, 41, 42, 44, 45, 50, 52, 53, 54, 55, 57, 58, 59, 60, 63, 64, 65, 66, 68, 69, 70, 75, 77, 79, 80, 81, 82, 84, 85, 88, 91, 92, 93, 94, 95, 96, 98, 99, 100, 102, 103, 104, 105, 106, 107, 108, 109, 110, 111, 112, 113, 114, 116, 117, 118, 119, 121, 122, 129, 152, 160, 161, 173, 211, 213, 226, 227

Surface modification 37, 38, 92, 93, 106, 109, 110

U

Ultrananocrystalline Diamond Films 93, 108

V

Viscosity 89, 162, 163, 165, 166, 167, 168, 169, 170, 171

X

X-ray photoelectron spectroscopy 42, 92, 96, 103, 108, 109, 111, 123

Z

ZnO 21, 22, 23, 24, 25, 26, 27, 28, 29, 30, 31, 32, 33, 34, 35, 36, 37, 38, 197, 198, 199, 200, 201, 202, 204, 205, 206, 207, 208, 209, 210, 211, 212, 213, 214, 215, 217, 218, 219, 220, 221, 222, 223, 224, 225, 226, 227

ZnO nanocrystals 21, 23, 25, 35



**EDITORA
ARTEMIS**